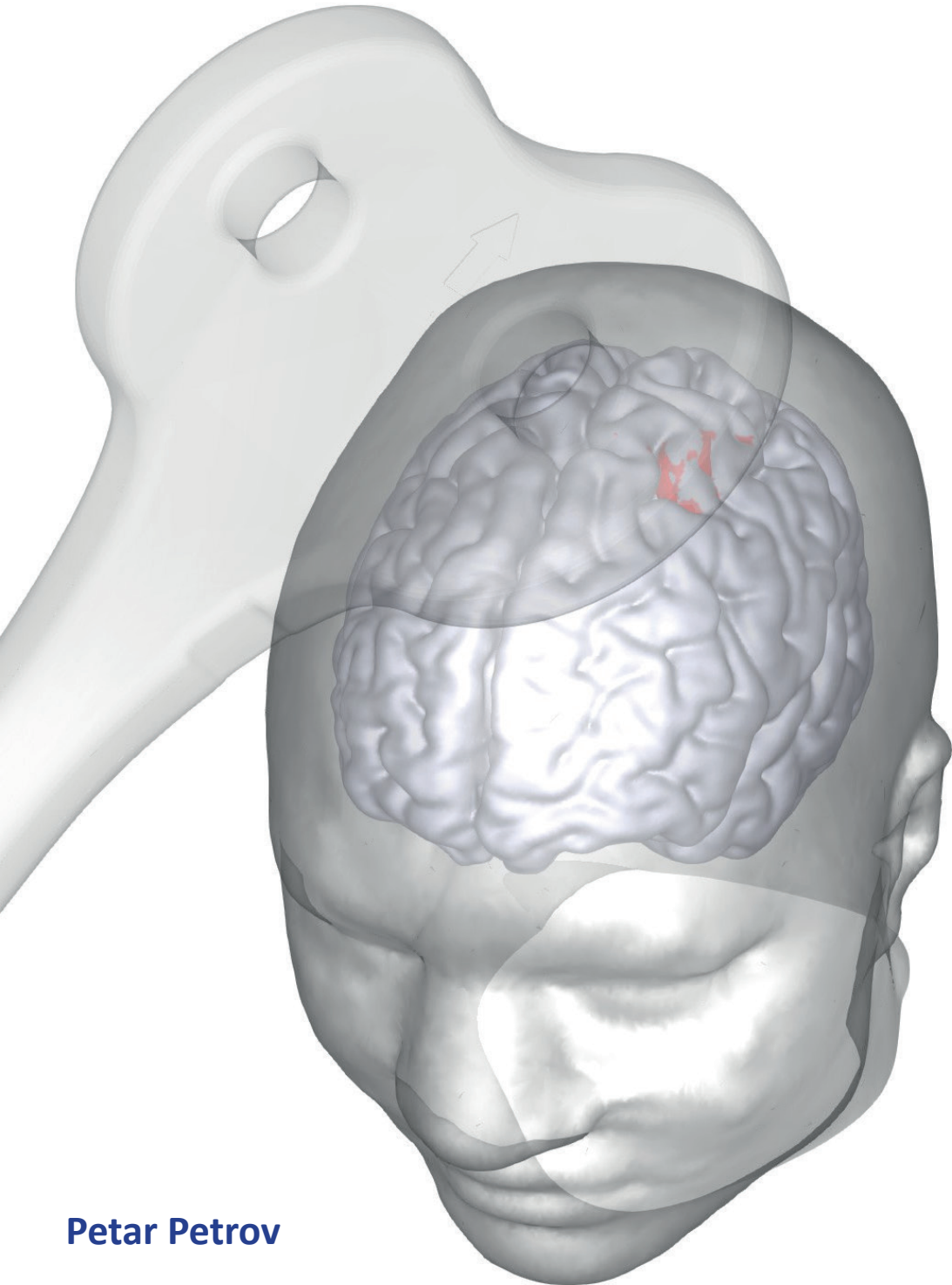


Virtual Neurostimulation

Computer-aided transcranial magnetic stimulation (TMS) guidance and dosimetry



Petar Petrov

Virtual Neurostimulation

Computer-aided transcranial magnetic stimulation (TMS) guidance and dosimetry

Petar Petrov

Colophon

Cover front: Visualization of the author's MR derived outer head contour as well as isolated cortex (gray matter). Software used: The Neural Navigator 3.6

Cover back: Visualization of the E-fields distribution as predicted from FEM. Reconstruction of the coil position and visualized using trivial approximation. Software used: Octave 6.1.0

The research described in this dissertation was performed at the Department of Psychiatry, Brain Center Rudolf Magnus and the Biomedical MR Imaging and Spectroscopy Group, Center for Image Sciences of the University Medical Center Utrecht.

Funding for this research was provided by the DeNeCor project (ENIAC project nr 324257) and the Netherlands Organization for Scientific Research (VICI 016.130.662), both awarded to the University Medical Center Utrecht, and by Brain Science Tools B.V., De Bilt, The Netherlands

Copyright © 2023 Petar Petrov

All right reserved. No part of this publication may be reproduced or transmitted in any form or by any means, without prior permission from the author.

ISBN: 978-94-93289-20-8 / NUR 981

Printed by: PrintSupport4U

Virtual Neurostimulation

Computer-aided transcranial magnetic stimulation (TMS) guidance and dosimetry

Virtuele neurostimulatie

Computerondersteunde transcraniële magnetische stimulatie (TMS) begeleiding en dosimetrie

(met een samenvatting in het Nederlands)

Proefschrift

ter verkrijging van de graad van doctor aan de Universiteit Utrecht
op gezag van de rector magnificus, prof. dr. H.R.B.M. Kummeling, ingevolge het
besluit van het college voor promoties in het openbaar te verdedigen op dinsdag 7
februari 2023 des middags te 14.15 uur

door

Petar Petrov

geboren op 10 september 1982

te Plovdiv, Bulgaria

Promoter: Prof. dr. R. M. Dijkhuizen

Co-promoter: Prof. dr. ir. C.A.T. van den Berg

Supervisor: Dr. S.F.W. Neggers

Publication of this manuscript was financially supported by:

Brain Science Tools B.V.

Content

Chapter I	Introduction	9
Chapter II	Imaging, Modeling, and Electromagnetic Simulation of Evoked Activity in the Human Brain (theoretical backgrounds)	33
Chapter III	How much detail is needed in modeling a transcranial magnetic stimulation figure-8 coil: measurements and brain simulations	59
Chapter IV	A validation approach for computational models of TMS induced brain currents using motor evoked potentials	91
Chapter V	Validating models of TMS effects with concurrent TMS/fMRI	115
Chapter VI	Temporal control of events in a novel concurrent TMS-fMRI setup tested on TMS of the prefrontal cortex!	139
Chapter VII	Design and evaluation of a rodent-specific TMS coil: an in silico and in vivo validation study	171
Chapter VIII	Summary and general discussion	199
Chapter IX	Nederlandse Samenvatting	225
Chapter X	Dankwoord	231
Chapter XI	Publications	239
Chapter XII	Curriculum Vitae	239

Biology is the study of the complex things in the Universe. Physics is the study of the simple ones.

Richard Dawkins,
1941 – present (Evolutionary Biologist)

Chapter I

Introduction

Introduction

Non-invasive neuro-stimulation, and in particular transcranial magnetic stimulation TMS, offers a remarkable new world of possibilities for brain research and diagnostic and therapeutic opportunities for brain-related health care. Yet its use is often surprisingly cumbersome and haphazard, and the opportunities are too often unexplored, to the detriment of science and health care. This is largely due to the lack of understanding of the interaction between magnetic fields and electrically active tissues in the brain and how neuronal signaling is affected as a result. This is the lacuna that has spurred the research on the basis of this thesis.

Outline

In this chapter, we provide a historical background of bioelectricity and neuronal stimulation as we introduce the notion of TMS. Next, we outline the relevance of TMS for certain clinical aspects of neurological and psychiatric disorders as well as showcase its excellent potential for exploring the central nervous system noninvasively, being exceptionally well-suited for experiments on a wide range of higher mammals including humans. This is followed by a brief overview of clinical applications of TMS and some of the limitations of current practices. Importantly, we propose computer models of how TMS induces brain activation as a useful tool in resolving some of the uncertainty surrounding the application of TMS. Finally, we provide a clear definition of TMS dosimetry and highlight the importance of well-validated models. We adopt a multi-modal imaging approach in our effort to link physiological response to electric-field calculations, which allows us to experimentally validate our computer models of TMS induced brain activation. We conclude with a summary of the thesis chapters that introduce, explore, and validate the use of our computer-guided TMS dosimetry models, as well as provide several examples of how we have successfully applied these new technologies.

Electricity and Bio-Electricity

Electricity is known to humankind since ancient times. Records from as early as Aristotle's time describe what is known today as static electricity. In about 600 BC, the Ancient Greeks discovered that rubbing fur on amber (fossilized tree resin) caused

an attraction between the two materials ¹. However, unsurprisingly, in that period the power of electricity was considered divine and thus left to the realm of the gods. It was not until 1600 AD that the physician William Gilbert used the Latin word “electricus” to describe the force that certain substances exert when rubbed against each other. A century later, the first practical scientific device capable of producing static electricity on demand was demonstrated in 1703 by Francis Houksbee under the supervision of the head of the British Royal Society, Sir Isaac Newton. About the same time (1729), another prominent scientist, Stephen Gray, an astronomer, discovered the phenomenon of static induction and defined two of the fundamental properties of electricity, namely conductance and resistance.

It is noteworthy that the realization of what we now consider bioelectricity was already present at the time of those initial scientific breakthroughs. In 1776, the English scientist Henry Cavendish experimented with torpedo fish, a fish from the family of electric rays, infamous among sailors for its ability to knock down a grown man by inflicting a short burst of up to 200V of electric discharge using its ray. However, it is the Italian physician and physicist Luigi Galvani who is recognized as the pioneer of bio-electromagnetism, following his experiments around 1780 with electrical stimulation of the nerve fibers of frogs [1]. He not only was able to demonstrate that discharging electricity along the lower limb of a frog can make it twitch, but even more remarkably doing so even in the absence of an external energy source, by simply short two points along two separate frog bodies he could achieve the same effect. Galvani postulated that all living things possess innate “animal-electricity”, an idea that was found preposterous by another prominent Italian scientist of that time, Alessandro Volta. Instead, Volta argued, there was a single electrical phenomenon, and the observations of Galvani were due to the differences in the metal conductance of his electrodes. Ironically, each of them was both right and wrong. While Volta had postulated correctly the singular nature of electricity, the work of Hodgkin and Huxley proved in 1952 that biological cells operate according to the same physical principles of electricity and that it is indeed intrinsic to all biological life, hence the term bio-electricity [2]. Later, Hodgkin and Huxley’s discovery of the ion-gated channels on virtually any biological cell membrane, was made by experimenting with the giant axon of the Atlantic squid, 1963 Nobel Prize in medicine.

By now we know for certain that there is only one physical phenomenon of electricity. However, there is also a clear distinction between electrical phenomena in man-made electrical circuits and living organisms alike. In contrast to bare wire (metal) conductance, where negatively charged electrons are responsible for current flow, it is ions that form the electrochemical gradients in biological tissues (Na⁺ Sodium and K⁺ Potassium create the ion-flux voltage gradient, while Cl⁻ Chlorine/Chloride is responsible for homeostasis, together giving rise to the resting cell membrane

1 <https://www.universetoday.com/82402/who-discovered-electricity/>

potential) [2] (see chapter 4). Furthermore, when talking about biological currents on a macro level, we often consider so-called eddy-currents that usually form in geometrically complex volume conductive media. Predicting the induced-current density in such media is not straightforward. Biological tissues have non-trivial DPs, which are also known to be very frequency sensitive.

However, again in contrast with passive cables, the effective neuronal signal velocity is considerably slower, since the mechanism of interneuron signal transmission involves slower, chemically driven reactions in the synapses between neurons instead. Additionally, it depends on the chemical concentrations of complex molecules, known as neurotransmitters, in the synaptic cleft between the axon of the sending neuron and the dendritic tree of the receiving neuron, which significantly modulate the rate and magnitude of action potentials in the postsynaptic membrane [2] (see chapter 5, page 96). Note that synaptic signaling is sometimes bridged by so-called gap junctions, a form of cytoplasmic continuation that allows to some degree direct electrical signaling over cells [2] (see chapter 5, pages 94-95).

History of Transcranial Magnetic Stimulation

The common history of the discoveries of electricity and bio-electricity is truly fascinating. However, an even more remarkable aspect of those historical records is the evidence of the use of electricity for experimental and therapeutic purposes long before the modern definition of electricity itself. One such account could be dated as far back as 46 AD when a Roman physician by the name of Scribonius Largus became known for treating a common headache with torpedo fish, which had previously shown promising results in the treatment of pain among soldiers. Another curious account of the use of the same torpedo fish comes from Persian philosopher Avicenna's Canon of Medicine (980–1037), in which it is mentioned as a therapy against melancholia and epilepsy. It was not until the Enlightenment period, however, that interest in electrical experiments on humans and animals grew more substantially [3] [4]. In the early 18th century, physicians were using so-called Leyden jars for a wide range of conditions such as headaches and hysteria [5]. Invented by the Dutch scientist Pieter van Musschenbroek from Leiden, the Leyden jar was the predecessor of modern batteries, capable of storing static electricity by means of a wire (electrode) with one end in a jar and the other attached to a Houksbee's generator. A serendipitous event involving such a Leyden jar and the prominent American scientist and politician Benjamin Franklin led to the discovery that electricity could be applied safely to the cranium. Another scientist, a Dutch by the name of Jan Ingenhousz, reported similar occurrences, further mentioning improved mental facilities shortly after the discharge; he speculated on the possibility to treat "mad men" and epilepsy and consequently proposed clinical trials [6]. While Galvani was well known for his physiological experiments with frogs, it was

his nephew Giovanni Aldini who experimented with direct current to treat psychiatric conditions with symptoms similar to those manifested in the condition known today as schizophrenia [7].

The first known account of magnetism, or rather the effect of electromagnetism, is considered the 1820 experiment carried out by the Danish physicist Hans Christian whereby through the switching on and off of the current running through a wire, he was able to influence the direction of a nearby compass needle (a static magnet). Doing so he was among the first scholars to demonstrate a clear connection between electricity and magnetism. Around the same time, in 1838, the English scientist Michael Faraday demonstrated for the first time the principle of induction: he wrapped two insulated coils of wire around an iron ring and found that upon passing a current through one coil, a momentary current was induced in the other coil; thus he discovered the core physical principle underlying TMS.

One of the earliest demonstrations of modern physiology, in particular nerve stimulation, came in 1896 from the remarkable experiments of the French physician and physicist Jacques-Arsène d'Arsonval wherein changing magnetic fields (induced by AC currents) were applied to the human body [8]. Yet, it was not until much later, circa 1965, that interest in neural stimulation by using the principle of pulsed magnetic fields was revived, by Bickford and Fremming [9]. Using a damped 500 Hz sinusoidal magnetic field, they demonstrated muscular stimulation in animals and humans. Almost two decades later, in 1982, Polson and Barker came up with a device capable of inducing peripheral nervous stimulation by applying a single short-time varying magnetic pulse near the trunk of a nerve [10]. Four years later, the device was successfully applied to the cranium with a clear physiological motor response of the hand [11]. Barker is considered the father of TMS since he demonstrated one very useful property of magnetic fields: they can penetrate the human skull with little attenuation and can thus induce inter-cranial stimulation in a non-invasive and safe manner. Thus the term trans-cranial magnetic stimulation TMS was introduced, and the device was firmly established as the most prominent of the noninvasive brain stimulation (NIBS) type of devices.

TMS as referred to in this thesis is not to be confused with other acronyms in life science/medicine, namely Tension Myositis Syndrome [12].

Clinical Relevance of Transcranial Magnetic Stimulation

Although TMS was initially adopted primarily as an investigational and diagnostic tool, it has made some strides since in the therapeutic treatment of some

common mental disorders such as major depression. Around the mid-1990s, researchers from the field of psychiatry started to experiment with repetitive TMS (rTMS; repeated TMS discharges at a certain frequency) and thus began to study the effect of such protocols on patients diagnosed with depression [13][14]. Experiments on rodents have also revealed biological (molecular) effects of rTMS similar to antidepressant [15]. Meanwhile, numerous clinical trials were conducted that ultimately led in 2008 to the FDA approval of rTMS for the treatment of MDD after a successful phase III study (randomized, sham-controlled, multi-site) on 301 medication-free patients with previously reported aversion and/or resistance to general medication [16]. The same group later demonstrated in 2010 [17] and 2014 [18] that the efficacy of left DLPFC rTMS was about ~30-40% of increased remission rate.

Currently, clinical paths for the use of TMS in the case of depression are approved only after initial pharmacological treatment has proved either to be ineffective or to lead to severe side effects, or – when neither is applicable – due to other counter-indications. Such cases constitute around 40% of patients suffering from major depression (MD) who are treated with antidepressant medications. For those patients, TMS offers an alternative consisting of daily 30–45-minute rTMS treatment sessions over the course of 2–3 weeks. The most cited counter indication of TMS is a personal or family history of epilepsy. However, the same report has demoted the same LF rTMS protocol when applied on the contra-lesional hemisphere during the chronic stage following a stroke (months to years after the incident) from class B (probable efficacy) to class C (possible efficacy). The effect of recovery was shown to be heterogeneous, and more subject-specific treatments were recommended [19].

Another very promising application of TMS is in the recovery process of patients who have recently suffered an ischemic stroke. In the developed world, with an increasingly aging population, stroke is one of the most common causes of death [20] together with other cardiovascular complications [21]. In a very recent review of evidence-based guidance of TMS, post-stroke sub-acute rTMS on the contra-lesional hemisphere has been promoted to class A (definite efficacy), for its benefits in the recovery of upper motor skills in the post-acute stage following a stroke (days to weeks after the incident) [22]. However, the same report demoted from class B (probable efficacy) to class C (possible efficacy) the same LF rTMS protocol applied on the contra-lesional hemisphere during the chronic stage of stroke (months to years after the incident). The effect of recovery has shown to be heterogeneous and more subject-specific treatments were recommended [23].

The possible therapeutic benefits of TMS are not limited to depression and stroke but span the wider spectrum of neurological and psychological disorders of the human central nervous system [24] [25] [26]. With somewhat lower efficacy, TMS has shown potential in the treatment of psychosis, PTSD, OCD, autism, dementia, and

tinnitus, all still rated at class-B evidence or lower. The benefits of TMS have been explored for some well-known degenerative diseases too, both as an investigational tool and as a possible therapeutic intervention. It has been proposed as a method of elevating deficits in upper motor functions of patients with Parkinson's disease [27]. Although the motor deficit associated with the disease becomes apparent at a later stage, degeneration and reorganization have been shown to occur at a much earlier stage already. With the help of TMS it is possible to discriminate between healthy and pathological responses, allowing for monitoring as the disease progresses. Also, EMG responses to TMS on the motor cortex in the form of MEPs have been proposed as a potential early biomarker of Alzheimer's disease [28].

The possibility to treat, diagnose, or otherwise intervene in such a diverse set of diseases has been accompanied by a fair share of uncertainty and misuse. Clinical practitioners keep providing evidence of the efficacy of TMS above and beyond our level of theoretical understanding of the underlying causality, as shown through fundamental neuroscience research and quantitative modeling. Unfortunately, studies are all too often hard to reproduce and the majority fail rigorous clinical-trial criteria such as including a well-designed control group, placebo stimulation (sham TMS) and often produce a relatively large number of non-responders (30–40%) [29]. Current protocols vary in their choice of target (mechanism of behavior) and type of neuronal response (inhibition vs. facilitation), for both depression and post-stroke recovery. No approach fits all cases, and clinicians alongside researchers are in constant search for more appropriate protocols for administering rTMS that are also more personalized. In this context, modern imaging combined with cutting-edge computer software can offer TMS practitioners an advanced tool to better target, control, and evaluate the outcome of a particular TMS session. The additional information and feedback given to the operator by such computer-aided individual TMS models should benefit patients considering the large degree of uncertainty associated with the current state of the art [30] [31]

Clinical Practices

Despite the increased application of TMS, current practices could be still considered crude and rudimentary. A good example is the current approach toward finding a suitable stimulation-target region. Frequently, simple methods are chosen to guide the place of TMS administration, for instance, the shape of the head or the place where movements can be evoked on the scalp. One of the most widely employed approaches, during the treatment of major depression, is the so-called rule of 5 cm of positioning the coil on the patient's Brodmann's area 46, the dorsolateral prefrontal cortex (DLPFC), which is simple but not quite accurate, as it is reported to miss the target one-third of the times [17][32] and on average to have a modest accuracy of

~2cm [33]. To administer TMS on a particular patient, one needs first to establish the motor hot spot, above the primary motor cortex (M1), through visually confirmed thumb twitches, and then shift the coil 5cm toward the anterior. For more general and for whole-head cortical targeting, the 10–20 EEG electrode-placement system has been suggested. The slightly better heuristic of BeamF3 has been suggested to locate F3 and F4 position electrode site of 10–20 EEG instead from three skull measurements alone: head circumference, nasion–inion distance, and left tragus–right tragus distance [34]. When compared to subject-specific MRI-based DLPFC-MNI coordinates, the CoG differences were <1.36cm 95% of the time and <0.65cm 50% of the time. Even more arbitrary is the only practical guidance for coil orientation after positioning, according to which, a seemingly arbitrary, 45° orientation relative to the central sulcus wall is recommended [35].

When compared to subject-specific MRI-based DLPFC-MNI coordinates, the CoG differences were <1.36cm 95% of the time and <0.65cm 50% of the time. Even more arbitrary is the only practical guidance for coil orientation after positioning, according to which, a seemingly arbitrary, 45° orientation relative to the central sulcus wall is recommended [36] [37]. In one longitudinal study with infants, using MRI, the authors report a clear, highly individual folding of the GM to emerge by the age of 2, even in twins [37].

One major advancement in the application of TMS was the introduction of frameless stereotaxic systems [38]. Also known as image guidance or neuronavigation, it requires MRI T1-weighted anatomical images that allow cortical target identification and TMS targeting with an overall spatial accuracy of <5 mm or better [39] [38]. It also supports real-time simultaneous coil-to-head placement and monitoring. Such image guidance can greatly benefit TMS applications. It has been shown that the number of participants required for TMS to achieve a statistically significant effect on behavior is lowered from ~47 without neuronavigation to 9 with neuronavigation using only anatomical MRI scans and 5 when combined with functional MRI (fMRI) [40]. A recent review has confirmed the superiority of fMRI functional guidance when compared to the center of gravity (CoG) of motor evoked potentials (MEP) coil guidance and has further confirmed the validity of using probabilistic atlas positions in cases where functional imaging is not available [41]. Furthermore, it has been demonstrated for rTMS treatment of major depression, that MRI guidance of coil placement on DLPFC achieves 30-50% more effective treatment as compared to the classic non-guided “5 cm rule” coil placement, measured in terms of depression symptom reduction [42][43]. Similar observations have been made for psychosis treatment [44] [45].

Regardless of the method of navigation, there is the need to conduct a short session to determine the so-called resting motor threshold (RMT), the TMS intensity threshold at which involuntary thumb movements or EMG responses start to emerge

[46]. Generally, RMT is considered a way to control TMS dose for individual differences in cortical excitability. The experimental or therapeutic stimulation intensity is then routinely set as a certain percentage of machine output corresponding to the RMT [46] ; commonly $\sim 110\text{-}120\%$ of RMT is used for TMS applications.

There are only two observable physiological responses to spTMS administration. When applied to the motor cortex with an intensity above the RMT, it results in a clear muscle twitch producing a quantitative MEP, measured with EMG. While application over the occipital lobe is known to produce reliably observable responses in the form of visual phosphenes, this can only be reported subjectively by the subject. Therefore, RMT is usually the choice of TMS dose calibration. An important assumption is that such threshold values can be easily translated to other cortical sites that are the target of TMS in a treatment, diagnostic, or research application. In support of such a proposition, a study conducted on 30 subjects comparing RMT to resting phosphene threshold RPT has reported a high correlation between RMT and RPT over subjects and a good match with a linear compensation factor based only on the distance to the cortex [47]. The factor predicting RPT from RMT in the aforementioned study was skull thickness, which is known to be highly variable in both intersubject and intrasubject. From the same group even emerged a metric for cross-site threshold determination based on RMT [48]. However, such black-box approaches are agnostic of the actual induced electric field shaped by the highly heterogeneously conductive brain with complex tissue boundaries. That particular study was conducted on simple head models, in which the influence of individual cortical morphology on induced cortical currents was completely ignored.

There are additional, more fundamental issues, with any approach that tries to translate dosage from one area to another, each with its own anatomical and functional distinctions. The mechanism of action underlying the mode of probing might differ significantly. One good example is the acceptance in general that TMS acts excitatory on the motor cortex while phosphenes are linked to an inhibitory process in the visual cortex [49].

We believe that only more general and physically realistic models of induced current, taking into account individual head and brain morphology, allow the correct setting and control of TMS dose.

Computer-Guided Dosimetry and Targeting

It is important to define what we mean by dosimetry in the context of the computer-guided application of TMS. We refer to dosimetry as the set of variables that TMS practitioners can influence in a hypothetical parameter space (DoF) that have shown to be significant factors in the efficacy of stimulation. Examples of such aspects

are the position of the coil and its orientation relative to anatomical landmarks and most importantly adjusting the intensity of stimulation as a certain percentage of TMS machine output (MO). This is by far not an exclusive list of all configurable parameters. For instance, devices exist that offer some level of pulse-shape adjustment (cTMS), however, such devices are rare and still considered largely exotic and almost exclusively applied in research. There are two commonly available types of TMS devices delivering monophasic and biphasic pulse shapes capable of injecting either unidirectional or bidirectional currents in the tissue underneath the coil. In general, one phase of strongly increasing current is followed by a slightly slower decrease in the opposite direction. We conducted experiments with both types of devices, in which we looked exclusively at spTMS stimulation. Although rTMS is more relevant clinically, our focus is on investigating the mechanism of action underlying induced currents directly evoked by a TMS pulse, for which spTMS is preferable. In fact, during an experimental design, we intentionally try to avoid any LTP and LTD effect associated with rTMS, transient or long-term plasticity modulation of the cortex [50]. Only when one truly understands how and where exactly a current is evoked in the brain by a single pulse from a TMS coil can one begin to describe the effects of rTMS provoking longer-lasting effects achieved by preferential cortical excitability modulation.

The application of a single-pulse protocol is better suited for the investigation of isolated responses in the brain and the correlation with predictions based on induced electrical-field calculations. At the same time, the insights from such predictions are equally useful for rTMS when it comes to navigation and coil guidance with the purpose to inflict a change in neuronal tissue at a required dose and location. We acknowledge, however, the implication of pulse shape and especially in combination with the direction of the currents for the future development of more effective stimuli predictions [51] [52], although this is not a topic of investigation in this thesis.

In our opinion, the key advantage computer models could offer for subject-specific TMS treatment is to assist in coil orientation. This limits the degrees of freedom when we try to control dosimetry and helps to resolve arguably one of the most critical problems related to TMS efficiency. There is a substantial amount of evidence to support the notion of induced current direction sensitivity when it comes to the effectiveness of neuronal stimulation. Such dependence has been demonstrated *in vivo* experimentally on both micro(μ)- and macro(mm)-levels.

For example, single-cell and population-recording studies of neurons using extracellular electrophysiology (EEP) microelectrode recordings have reported responses dependent on current direction, which were recorded on layer V M1 neurons of a rodent shortly after a single TMS pulse (0.8–1s epoch) [53]. Modern functional neuroimaging evidence on the influence of TMS coil orientation on directly induced neuronal activation is scarce. We are not aware of a concurrent TMS/fMRI study systematically investigating the effects of coil orientation. There is one PET study in

which this was attempted [54] : it tried to evaluate what directional components of modeled E-fields local to the cortical explained PET activation. The results were somewhat inconclusive. Inward- and outward-pointing E-fields (relative to the cortical surface) did explain aspects of PET activation better than the strength of the total E-field did, but the field's degree of orthogonality relative to the cortical sheet (in a symmetric manner) did not explain PET activation any better than the total E-field (see chapter 2 for more details).

The evidence from EMG recordings of muscle responses induced by TMS through the corticospinal tract suggests that for maximal responses, the direction of induced currents (in parallel with the coil handle) should be perpendicular to the central sulcus. There is a clear dependence of MEP responses on coil orientation in combination with pulse shape [55] [52] [35] [56]. The evidence from EMG muscle responses MEPs induced by TMS through the corticospinal tract suggests that for maximal responses, the direction of induced currents (in parallel with the coil handle) should be perpendicular to the central sulcus. There is a clear dependence of MEP responses on coil orientation in combination with pulse shape [57]. However, the distinction is neither clear nor simplistic, if we look at the empirical evidence from experimental human research. The majority of studies have shown some degree of dependence on the effects of TMS and coil orientation, but details greatly differ. This implies a more complex interaction between induced current direction and the activity of neurons in the cortical sheet, possibly involving a complex interplay between inhibitory and excitatory sub-circuits. Additionally, while most studies focus on hand muscle groups, one study conducted on the foot has revealed less sensitivity to coil direction [58]. The authors have reported a higher range in the optimal angles found for the M1 ($\sim 60^\circ$) compared to that of the foot ($\sim 30^\circ$) and further statistically outlined the orthogonal component of the electrical field to be the significant factor in either case.

In conclusion, the influence of induced current direction with respect to the underlying neuronal organization on the induced neuronal activation influenced our adoption of "activation metrics" (see chapter 2). These metrics describe how an evoked current in the brain can excite neurons in the cortical sheet taking into account what we know about the overall organization of the cortical sheet. We propose several metrics on a macroscopic level that can discriminate between tangential and axial components of the E-field injected on the cortical sheet, instead of simply assessing the region of maximally induced E-field as most studies do. Additionally, we adopt simpler control metrics to serve as null hypotheses.

The long-term objective of the macroscopic models proposed in this thesis of how a TMS coil induces brain activation is to provide valuable feedback to the clinician in the form of an expected neuronal activation map projected on the outer cortex under the variable degrees of freedom (such as position, coil angle, and machine power). It would allow the TMS operator to control the induced current dose much more

precisely and as such make therapeutic and diagnostic TMS use more reliable. The possible benefit of such an integrated environment has been suggested in the community before [59] [60].

Electric Field Models

The previous sections elucidated how much uncertainty and crudeness still surround the application and research of TMS. Computer models for TMS have already been suggested and attempted by several scholars over the last decades in the hope of resolving some of the variability and uncertainty involving TMS. Numerical solutions that approximate the injected electrical currents can provide better control over dose and targeting and have been suggested as a tool for better TMS guidance.

Initial models of TMS were lacking in detail. They were largely inadequate in capturing the complex geometry of the human head, due not only to constraints of computing power but also to the unavailability of advanced imaging. Before 2000, approaches were limited to very simplistic concentric spheres forming shells with layers capturing only the most dominant tissue types (GM-Skull) [61][62][63]. Such models predicting very symmetric field distribution were quickly challenged by early models taking into account more realistic tissue-boundary geometry [64]. In more detailed individual head models, the contribution to the electric field magnitude of charge accumulation on realistic gray-matter tissue interfaces was estimated to be in the range of 20–35% [65]. It was also found to be in opposition to the initial E-field evoked by the TMS coil, thereby constraining it, which possibly led to a decrease in the effective area of stimulation [66]. The use of accurate conductivity values at the boundary of cerebral-spinal fluid (CSF) volumes and the inside of the skull in finite element modeling (FEM) models were highlighted as an important factor determining induced current distribution [67]. Computational FEM on brain-shaped templates results in up to 10mm difference in induced E-field CoG in relation to varying coil orientation over M1 [68]. The main reason for this spatial shift is a small space filled with CSF between the gyral crowns and the skull that caused local maxima in induced current through excessive accumulation of the secondary E-field. The possible implication of such small CSF spaces for E-field modeling has been studied in more detail [69]. The same group claims that the effect of rotating a coil on M1 of $<10^\circ$ steps has a negligently small spatial effect on the final E-field distribution [70].

Even more, elaborate head models using anisotropic conductivity values for the WM derived from diffusion-weighted imaging (DTI-MRI) have accounted for a complex microstructure in the form of WM fibers [71] [72]. The possibility of direct WM stimulation has been explored in such models and showed to be influenced not only by intensity but also by the direction of TMS-induced currents on the GM-WM

interface [73] and along a single tract [74] [75]. The strongest effect was found where currents were orthogonal to the underlying axonal fabric. However, this influence of WM anisotropy on TMS-evoked currents is so far purely theoretical; no empirical validation is available at present. Furthermore, one of the aims of this thesis is to understand neuronal activation in the cortical sheet (see chapter 2). Therefore, in the FEM models adopted here, we opted to model the WM tissue as isotropic conductivity.

The benefits of subject-specific E-field models derived from individual imaging have been demonstrated in several studies. In the research presented in this thesis, we exclusively focus on anatomically correct, subject-specific, volumetric conductance models derived from high-resolution MR images. The numerical method of choice is FEM and the available literature provides the values for the isotropic conductivity of each major tissue type. In chapter 2, we further elaborate on and provide the theoretical background behind our individual FEM models of TMS-induced currents. We also outline the physical principles underlying TMS and touch on some fundamental neuro-electrical coupling models that allow me to estimate the neuronal response to the fields predicted by the FEM models. We propose several macroscopic metrics dependent on current orientation relative to the orientation of the outer cortical sheet (GM). We investigate whether the addition of such metrics, on top of the modeled E-field as predicted by FEM, is a better predictor of neuronal responses to TMS than the mere magnitude of the evoked E-field, in two empirical validations.

Model Validation

The focus of the research underlying this thesis was the construction of anatomically realistic finite-element-based head models of conductive tissues and realistic models of TMS coils, as well as implementing macroscopic models of electro-neuronal couplings in the cortex and validating these models empirically. To this end, we conducted in-vivo experiments to quantitatively compare the aforementioned TMS activation models derived from MRI scans of a group of human volunteers with the measured elicited physiological responses to TMS in the same group of people. We exclusively looked into two already established noninvasive techniques that have shown to be effective and safe to use concurrently with TMS. The first one is motor-evoked potentials (MEPs), which are the responses to a TMS pulse on the motor cortex derived from electromyographic (EMG) measurements from surface electrodes on muscles, which are a popular proxy for motor cortical neuronal activation. The second one, using concurrent TMS-fMRI, is observing the BOLD response to TMS stimulation of the motor cortex that arises due to the metabolic needs of the activated populations of neurons. Both methods rely on a proxy to indirectly relate direct neuronal firing with the measured physiological response. In chapters 4 and 5, more details on the validation experiments are provided, and results are presented.

The benefits of combining non-invasive imaging with TMS are well-known [76]. Modalities, such as EEG and fMRI, may be used to guide TMS in so-called close-loop protocols. This way, the spatial and temporal parameters determining the potential TMS efficacy could be dynamically adapted, continuously, or in steps during a session. At the beginning of a session, it is already possible to automatically determine the resting motor threshold (RMT) using EMG, employing MEP criteria of 50 μ V peak-to-peak in at least five of ten consecutive trials (≥ 30 repetitions) [77]. Arguably the more intriguing aspect of imaging is the ability to validate to some extent the predictions from E-field distributions resulting from FEM models.

It is important to note that two distinct approaches exist toward evaluating the response to TMS via imaging: immediately after application (online effect) and shortly after a session (offline effect). While the latter could be useful for the investigation of plasticity-induced (LTP/LTD) lasting effects of rTMS, the former is better suited to studying the effects of spTMS.

We started the body of work presented in this thesis by evaluating the accuracy of our models of the B-field induced by the TMS coil by themselves. The uncertainty that we studied was on the level of detail required to capture the geometrical shape of the coil windings in order to achieve realistic distribution of the computed fields. We developed in-house numerical computation algorithms that we verified against B-field mapping in an MR scanner (see chapter 3).

One of the most common physiological measurements often conducted with spTMS is the combination with EMG. This is no surprise since the clearest and measurable physiological response of TMS is the mechanical control of movements. TMS is also generally cheap, easy to use, and readily available from a variety of vendors. However, its effects can span the complete cortico-spinal tract, complicating interpretation and making the translation less straightforward [78]. It involves complex inhibition and excitation pathways from the stimulated cortex to the muscles, including, for example, loops through the basal ganglia and nodes in the spinal cord. The decoupling of the different contributions from the cortico-cortical, cortico-spinal, and cortico-thalamic circuits to the final MEP is challenging. This further limits MEPs as a means of evaluating the direct effect of TMS on the cortex. We propose tailored MEP mappings with more variable coil directions rather than coil positions around and on M1 from fMRI while maintaining a similar magnitude on the hotspot by varying the TMS power. This novel approach helps to establish the current direction as a prime factor of variability since the E-field magnitude is maintained roughly the same.

As a second validation experiment, we use functional MRI concurrently with TMS (see chapter 5). Functional MRI allows for whole-head recording at a relatively high, 3mm resolution, using echo-planar imaging (EPI) sequences. The method we adopt results in maps of voxels with either a positive (excited) or negative (inhibited)

response. Clear relationships between TMS dosage MO (machine output) to BOLD signal responses have been demonstrated before [79] [80]. However, the extent to which TMS-evoked E-fields correlate to TMS-evoked fMRI activation maps is as of yet unclear. Unlike EMG, the combination of fMRI with TMS is significantly more challenging. It requires an elaborate setup, in which several inherited limitations to combining with magnetic devices need to be addressed first [80] [81]. Only a handful of research centers have developed such custom solutions, which often require some collaboration with TMS manufacturers. In chapter 6, we focus on the technical setup that we developed and used for the research presented in this thesis and cover the requirements of and impediments to combining TMS and fMRI in more detail.

Summary

The history of electrical and magnetic stimulation of biological tissues and the discovery of the pure physical phenomenon of electromagnetism are intertwined. In particular, experiments involving the non-invasively injection of a current based on the principle of induction eventually led to Barker's demonstration of modern TMS in 1982. Although it has gained wide adoption in both clinical and research settings, we still lack good control over dosimetry and a clear idea of the exact mechanism of current flow and interaction with neuronal tissue. TMS studies are plagued by issues of reproducibility and suffer from large variability in responses and outcomes. We propose that computer models of induced electric fields and initial implementations of models describing the interaction between induced currents and neuronal signaling in the stimulated tissue could help improve the efficacy and further aid the application of TMS in addition to current state-of-the-art navigation systems.

The body of the work informing this thesis involves a multimodal approach validating the models that we developed for TMS-induced currents using in-vivo experiments. The focus is on comparing the predicted TMS-induced E-field intensity and spatial distribution from computer numerical models, combined with first models of electric currents and their interaction with neurons in the cortical layers, with measurable physiological responses. For this purpose, we developed a sophisticated framework capable of producing subject-specific 3D models.

This thesis not only develops such models but also validates them empirically in several experiments mainly on human volunteers (and one on rodents), which is an effort seldom made by other groups, who mainly report modeling results without much empirical validation. The technical advances that were needed for this empirical work are also presented (chapter 6).

Finally, we also present the first application of my modeling work, in the form of a miniature, liquid-cooled, rodent TMS coil, which was constructed based on my

initial models and is useful in translational TMS research involving the treatment of stroke (chapter 7).

Thesis outline

The history of electrical and magnetic stimulation of biological tissues and the discovery of the pure physical phenomenon of electromagnetism are intertwined. In particular, experiments involving the non-invasively injection of a current based on the principle of induction eventually led to Barker's demonstration of modern TMS in 1982. Although it has gained wide adoption in both clinical and research settings, we still lack good control over dosimetry and a clear idea of the exact mechanism of current flow and interaction with neuronal tissue. TMS studies are often plagued by issues concerning reproducibility and suffer from large variability in responses and outcomes (chapter 1). We propose that computer models of induced electric fields and initial implementations of models describing the interaction between induced currents and neuronal signaling in the stimulated tissue could help improve the efficacy and further aid the application of TMS in addition to current state-of-the-art navigation systems.

The more technical details concerning theory, model construction, and methods were cut from the original publications, as presented in chapters 3, 4, 5, 7, and consolidated in one theoretical background chapter (chapter 2). The content was extended and a few key aspects were elaborated further in more detail, such as FEM construction; elector-magnetic theory; underlying neuronal coupling. We took such, a more unconventional approach, not only to make the rest of the text concise but also more accessible than the typical Ph.D. thesis. With less distraction in the way, we expect the reader to have a better chance and opportunity to appreciate the contribution to the life sciences in general and innovative neuro-stimulation and modulation in particular.

The arguably more trivial part of TMS modeling and virtual simulation is that of the coil, compared to the human head. Nevertheless, the geometric and numeric detail required to have an accurate enough E-field calculation was largely unknown. Therefore, we focused our initial effort on exploring exactly that question under rigorous MR-based experiments on a dummy phantom (chapter 3). This gave us the much-needed confidence to employ the coil model we developed (in-house) for the rest of the computer simulation presented in the following chapters (chapters 3, 4, 5, 7).

A central aim of our research was to develop a practical, multi-modal approach toward validating computational models of TMS using in-vivo experiments. The focus was on comparing the predicted E-field intensity and spatial distribution, derived from

numerical simulations, to measurable physiological responses. In the process, we had to suggest some trivial activation metrics to evaluate the potential neuronal response to externally injected current following a successful administration of single-pulse TMS. We conducted two small-size studies on healthy human subjects (shared cohort). In one of the studies, we decided to employ MEPs from EMG as the quantitative physiological measurement in response to the subtle changes in the direction of the injected currents (coil orientation) on and around the primary motor cortex M1 (chapter 4). In the other we relied on modern functional MRI to evaluate any proximal (close to the coil) as well as potentially distant areas of activation (change in BOLD) (chapter 5).

Our group contributes to the previously developed experimental setup of combining concurrent TMS with MRI was significant with the introduction of very precise temporal control and synchronization. Because of this and its relevance to chapters 3 and 5 we decided to dedicate a chapter only on the experimental setup by extending the methodological section of previously published work from our group (chapter 6).

Finally, we present another practical application of our modeling work in the effort to create a miniature rodent TMS coil. We were able to provide an initial coil design where essential performance parameters were optimized virtually, before the construction of any physical prototypes. Such an innovative rodent coil is proving useful in translation research involving TMS and post-stroke recovery (chapter 7).

We conclude with the general discussion (chapter 8) where we address some of the limitations of our experiments, suggest future improvements and most importantly reflect on the results. We also look into alternative modalities such as EEG having the potential to contribute to our understanding of TMS by providing additional physiological measurement. With special dedication, we cover the extension to activation metrics we proposed with eventual macro-level (population-level) synthetic neuronal models. It is recommendation for the future advancement of the research presented here.

References

- [1] M. Bresadola, “Medicine and science in the life of Luigi Galvani (1737-1798),” *Brain Res. Bull.*, vol. 46, no. 5, pp. 367–380, 1998.
- [2] D. Purves, *Neuroscience Third Edition*, vol. 3. 2004.
- [3] P. KELLAWAY, “THE PART PLAYED BY ELECTRIC FISH IN THE EARLY HISTORY OF BIOELECTRICITY AND ELECTROTHERAPY,” *Bull. Hist. Med.*, vol. 20, no. 2, pp. 112–137, Jul. 1946.
- [4] G. Tsoucalas, M. Karamanou, M. Lymperi, V. Gennimata, and G. Androutsos, “The ‘torpedo’ effect in medicine,” *Int. Marit. Health*, vol. 65, no. 2, pp. 65–67, 2014.
- [5] C. Dorsman and C. A. Crommelin, *The Invention of the Leyden Jar*. Brill, 1957.
- [6] S. A. Beaudreau and S. Finger, “Medical electricity and madness in the 18th century: The legacies of Benjamin Franklin and Jan Ingenhousz,” *Perspect. Biol. Med.*, vol. 49, no. 3, pp. 330–345, 2006.
- [7] T. G. Bolwig and M. Fink, “Electrotherapy for Melancholia,” *J. ECT*, vol. 25, no. 1, pp. 15–18, Mar. 2009.
- [8] J. D. Grabow, “Magnetic Stimulation in Clinical Neurophysiology,” *Mayo Clin. Proc.*, vol. 65, no. 9, pp. 1283–1285, Sep. 1990.
- [9] B. D. Bickford, R. G., Freeming, “Neuronal stimulation by pulsed magnetic fields in animals and man.,” 1965.
- [10] M. J. Polson, A. T. Barker, and I. L. Freeston, “Stimulation of nerve trunks with time-varying magnetic fields.,” *Med. Biol. Eng. Comput.*, vol. 20, no. 2, pp. 243–4, Mar. 1982.
- [11] A. T. Barker, R. Jalinous, and I. L. Freeston, “Non-invasive magnetic stimulation of human motor cortex.,” *Lancet (London, England)*, vol. 1, no. 8437, pp. 1106–7, May 1985.
- [12] L. I. Sank, “Traumatic masturbatory syndrome.,” *J. Sex Marital Ther.*, vol. 24, no. 1, pp. 37–42.
- [13] A. Pascual-Leone, B. Rubio, F. Pallardó, and M. D. Catalá, “Rapid-rate transcranial magnetic stimulation of left dorsolateral prefrontal cortex in drug-resistant depression,” *Lancet*, vol. 348, no. 9022, pp. 233–237, 1996.

- [14] M. S. George *et al.*, “Daily repetitive transcranial magnetic stimulation (rTMS) improves mood in depression,” *Neuroreport*, vol. 6, no. 14, pp. 1853–1856, 1995.
- [15] M. E. Keck *et al.*, “Neuroendocrine and behavioral effects of repetitive transcranial magnetic stimulation in a psychopathological animal model are suggestive of antidepressant-like effects,” *Neuropsychopharmacology*, vol. 24, no. 4, pp. 337–349, 2001.
- [16] J. P. O’Reardon *et al.*, “Efficacy and Safety of Transcranial Magnetic Stimulation in the Acute Treatment of Major Depression: A Multisite Randomized Controlled Trial,” *Biol. Psychiatry*, vol. 62, no. 11, pp. 1208–1216, 2007.
- [17] M. S. George *et al.*, “Daily left prefrontal transcranial magnetic stimulation therapy for major depressive disorder: A sham-controlled randomized trial,” *Arch. Gen. Psychiatry*, vol. 67, no. 5, pp. 507–516, 2010.
- [18] M. S. George, J. J. Taylor, and E. B. Short, “The expanding evidence base for rTMS treatment of depression,” *Curr. Opin. Psychiatry*, vol. 26, no. 1, pp. 13–18, 2013.
- [19] S. Rossi, M. Hallett, P. M. Rossini, and A. Pascual-Leone, “Safety, ethical considerations, and application guidelines for the use of transcranial magnetic stimulation in clinical practice and research,” *Clin. Neurophysiol.*, vol. 120, no. 12, pp. 323–330, 2012.
- [20] Q. Yang *et al.*, “Vital Signs: Recent Trends in Stroke Death Rates - United States, 2000-2015.,” *MMWR. Morb. Mortal. Wkly. Rep.*, vol. 66, no. 35, pp. 933–939, Sep. 2017.
- [21] E. J. Benjamin *et al.*, “Heart Disease and Stroke Statistics-2017 Update: A Report From the American Heart Association.,” *Circulation*, vol. 135, no. 10, pp. e146–e603, 2017.
- [22] J. P. Lefaucheur *et al.*, “Evidence-based guidelines on the therapeutic use of repetitive transcranial magnetic stimulation (rTMS) (2018 UPDATE),” *Clin. Neurophysiol.*, vol. 125, no. 11, pp. 2150–2206, 2014.
- [23] T. Morishita and F. C. Hummel, “Non-invasive Brain Stimulation (NIBS) in Motor Recovery After Stroke: Concepts to Increase Efficacy,” *Curr. Behav. Neurosci. Reports*, vol. 4, no. 3, pp. 280–289, 2017.
- [24] M. Kobayashi and A. Pascual-Leone, “Transcranial magnetic stimulation in neurology,” *Lancet Neurol.*, vol. 2, no. 3, pp. 145–156, 2003.
- [25] P. M. Rossini and S. Rossi, “Transcranial magnetic stimulation: Diagnostic, therapeutic, and research potential,” *Neurology*, vol. 68, no. 7, pp. 484–488, 2007.

- [26] P. M. Rossini *et al.*, “Non-invasive electrical and magnetic stimulation of the brain, spinal cord, roots and peripheral nerves: Basic principles and procedures for routine clinical and research application: An updated report from an I.F.C.N. Committee,” *Clin. Neurophysiol.*, vol. 126, no. 6, pp. 1071–1107, 2015.
- [27] C. L. Chung and M. K. Y. Mak, “Effect of Repetitive Transcranial Magnetic Stimulation on Physical Function and Motor Signs in Parkinson’s Disease: A Systematic Review and Meta-Analysis,” *Brain Stimul.*, vol. 9, no. 4, pp. 475–487, 2016.
- [28] A. Guerra *et al.*, “Transcranial magnetic stimulation studies in Alzheimer’s disease,” *Int. J. Alzheimers. Dis.*, vol. 2011, 2011.
- [29] J. A. Yesavage *et al.*, “Effect of repetitive transcranial magnetic stimulation on treatment-resistant major depression in US veterans: A randomized clinical trial,” *JAMA Psychiatry*, vol. 75, no. 9, pp. 884–893, 2018.
- [30] A. Thielscher, A. Antunes, and G. B. Saturnino, “Field modeling for transcranial magnetic stimulation: A useful tool to understand the physiological effects of TMS?,” *Proc. Annu. Int. Conf. IEEE Eng. Med. Biol. Soc. EMBS*, vol. 2015-Novem, pp. 222–225, 2015.
- [31] S. F. W. Neggers, P. I. Petrov, S. Mandija, I. E. C. Sommer, and C. a. T. van den Berg, “Understanding the biophysical effects of transcranial magnetic stimulation on brain tissue: The bridge between brain stimulation and cognition,” *Prog. Brain Res.*, no. Computational Neurostimulation, pp. 1–31, 2015.
- [32] U. Herwig, F. Padberg, J. Unger, M. Spitzer, and C. Schönfeldt-Lecuona, “Transcranial magnetic stimulation in therapy studies: Examination of the reliability of ‘standard’ coil positioning by neuronavigation,” *Biol. Psychiatry*, vol. 50, no. 1, pp. 58–61, 2001.
- [33] R. Ahdab, S. S. Ayache, P. Brugières, C. Goujon, and J.-P. Lefaucheur, “Comparison of ‘standard’ and ‘navigated’ procedures of TMS coil positioning over motor, premotor and prefrontal targets in patients with chronic pain and depression,” *Neurophysiol. Clin. Neurophysiol.*, vol. 40, no. 1, pp. 27–36, 2010.
- [34] A. Mir-Moghtadaei *et al.*, “Concordance between BeamF3 and MRI-neuronavigated target sites for repetitive transcranial magnetic stimulation of the left dorsolateral prefrontal cortex,” *Brain Stimul.*, vol. 8, no. 5, pp. 965–973, 2015.
- [35] J. P. Brasil-Neto, L. G. Cohen, M. Panizza, J. Nilsson, B. J. Roth, and M. Hallett, “Optimal focal transcranial magnetic activation of the human motor cortex: effects of coil orientation, shape of the induced current pulse, and stimulus intensity,” *Journal of clinical neurophysiology: official publication of the American Electroencephalographic Society*, vol. 9, no. 1, pp. 132–136, 1992.

- [36] C. Wachinger, P. Golland, W. Kremen, B. Fischl, and M. Reuter, “BrainPrint: A discriminative characterization of brain morphology,” *Neuroimage*, vol. 109, no. 1, pp. 232–248, Apr. 2015.
- [37] D. Duan *et al.*, “Individual identification and individual variability analysis based on cortical folding features in developing infant singletons and twins,” *Hum. Brain Mapp.*, no. December 2019, pp. 1985–2003, 2020.
- [38] S. F. W. Neggers *et al.*, “A stereotactic method for image-guided transcranial magnetic stimulation validated with fMRI and motor-evoked potentials,” *Neuroimage*, vol. 21, no. 4, pp. 1805–1817, 2004.
- [39] J. Ruohonen and J. Karhu, “Navigated transcranial magnetic stimulation.,” *Neurophysiol. Clin.*, vol. 40, no. 1, pp. 7–17, 2010.
- [40] A. T. Sack, R. Cohen Kadosh, T. Schuhmann, M. Moerel, V. Walsh, and R. Goebel, “Optimizing Functional Accuracy of TMS in Cognitive Studies: A Comparison of Methods,” *J. Cogn. Neurosci.*, vol. 21, no. 2, pp. 207–221, 2009.
- [41] R. Sparing, D. Buelte, I. G. Meister, T. Pauš, and G. R. Fink, “Transcranial magnetic stimulation and the challenge of coil placement: A comparison of conventional and stereotaxic neuronavigational strategies,” *Hum. Brain Mapp.*, vol. 29, no. 1, pp. 82–96, 2008.
- [42] P. B. Fitzgerald *et al.*, “A Randomized Trial of rTMS Targeted with MRI Based Neuro-Navigation in Treatment-Resistant Depression,” *Neuropsychopharmacology*, vol. 34, no. 5, pp. 1255–1262, Apr. 2009.
- [43] M. Klirova *et al.*, “Individualized rTMS neuronavigated according to regional brain metabolism (18FDG PET) has better treatment effects on auditory hallucinations than standard positioning of rTMS: A double-blind, sham-controlled study,” *Eur. Arch. Psychiatry Clin. Neurosci.*, vol. 263, no. 6, pp. 475–484, 2013.
- [44] A. Aleman, I. E. Sommer, and R. S. Kahn, “Efficacy of Slow Repetitive Transcranial Magnetic Stimulation in the Treatment of Resistant Auditory Hallucinations in Schizophrenia,” *J. Clin. Psychiatry*, vol. 68, no. 03, pp. 416–421, Mar. 2007.
- [45] C. Freitas, F. Fregni, and A. Pascual Leone, “Meta-analysis of the effects of rTMS on negative and positive symptoms in schizophrenia,” *Schizophr. Res.*, vol. 108, no. 1–3, pp. 11–24, 2010.
- [46] D. J. L. G. Schutter and J. van Honk, “A standardized motor threshold estimation procedure for transcranial magnetic stimulation research.,” *J. ECT*, vol. 22, no. 3, pp. 176–178, 2006.

- [47] M. G. Stokes *et al.*, “Biophysical determinants of transcranial magnetic stimulation: effects of excitability and depth of targeted area,” *J. Neurophysiol.*, vol. 109, no. 2, pp. 437–444, 2013.
- [48] M. G. Stokes, “Simple Metric For Scaling Motor Threshold Based on Scalp-Cortex Distance: Application to Studies Using Transcranial Magnetic Stimulation,” *J. Neurophysiol.*, vol. 94, no. 6, pp. 4520–4527, 2005.
- [49] T. Kammer, K. Puls, H. Strasburger, N. J. Hill, and F. a. Wichmann, “Transcranial magnetic stimulation in the visual system. I. The psychophysics of visual suppression,” *Exp. Brain Res.*, vol. 160, no. 1, pp. 118–128, 2005.
- [50] A. J. Butler and S. L. Wolf, “Putting the brain on the map: use of transcranial magnetic stimulation to assess and induce cortical plasticity of upper-extremity movement,” *Phys. Ther.*, vol. 87, no. 6, pp. 719–36, Jun. 2007.
- [51] I. Delvendahl, N. Gatteringer, T. Berger, B. Gleich, H. R. Siebner, and V. Mall, “The role of pulse shape in motor cortex transcranial magnetic stimulation using full-sine stimuli,” *PLoS One*, vol. 9, no. 12, pp. 1–22, 2014.
- [52] R. Hannah and J. C. Rothwell, “Pulse Duration as Well as Current Direction Determines the Specificity of Transcranial Magnetic Stimulation of Motor Cortex during Contraction,” *Brain Stimul.*, vol. 10, no. 1, pp. 106–115, 2017.
- [53] A. B. Li, J. Virtanen, A. Oeltermann, and C. Schwarz, “Lifting the veil on the dynamics of neuronal activities evoked by transcranial magnetic stimulation,” *Elife*, vol. 6, p. e30552, 2017.
- [54] T. D. Krieg, F. S. Salinas, S. Narayana, P. T. Fox, and D. J. Mogul, “Computational and experimental analysis of TMS-induced electric field vectors critical to neuronal activation,” *J. Neural Eng.*, vol. 12, no. 4, p. 046014, 2015.
- [55] V. H. Souza, T. M. Vieira, A. S. C. Peres, M. A. C. Garcia, C. D. Vargas, and O. Baffa, “Effect of TMS coil orientation on the spatial distribution of motor evoked potentials in an intrinsic hand muscle,” *Biomed. Eng. / Biomed. Tech.*, vol. 0, no. 0, 2017.
- [56] T. Kammer, S. Beck, A. Thielscher, U. Laubis-Herrmann, and H. Topka, “Motor thresholds in humans: a transcranial magnetic stimulation study comparing different pulse waveforms, current directions and stimulator types,” *Clin. Neurophysiol.*, vol. 112, no. 2, pp. 250–258, Feb. 2001.
- [57] M. Hamada, J. M. Galea, V. Di Lazzaro, P. Mazzone, U. Ziemann, and J. C. Rothwell, “Two Distinct Interneuron Circuits in Human Motor Cortex Are Linked to Different Subsets of Physiological and Behavioral Plasticity,” *J. Neurosci.*, vol. 34, no. 38, pp. 12837–12849, 2014.

- [58] L. Richter, G. Neumann, S. Oung, A. Schweikard, and P. Trillenber, “Optimal Coil Orientation for Transcranial Magnetic Stimulation,” *PLoS One*, vol. 8, no. 4, 2013.
- [59] M. Stenroos and L. M. Koponen, “Real-time computation of the TMS-induced electric field in a realistic head model,” *bioRxiv*, p. 547315, 2019.
- [60] A. Paffi *et al.*, “A Computational Model for Real-Time Calculation of Electric Field due to Transcranial Magnetic Stimulation in Clinics,” *Int. J. Antennas Propag.*, vol. 2015, no. Im, pp. 23–27, 2015.
- [61] B. J. Roth, J. M. Saypol, M. Hallett, and L. G. Cohen, “A theoretical calculation of the electric field induced in the cortex during magnetic stimulation,” *Electroencephalogr. Clin. Neurophysiol. Potentials Sect.*, vol. 81, no. 1, pp. 47–56, 1991.
- [62] J. D. Weissman, C. M. Epstein, and K. R. Davey, “Magnetic brain stimulation and brain size: relevance to animal studies,” *Electroencephalogr Clin Neurophysiol*, vol. 85, no. 3, pp. 215–219, 1992.
- [63] P. Ravazzani, J. Ruohonen, F. Grandori, and G. Tognola, “Magnetic Stimulation of the Nervous System: Induced Electric Field in Unbounded, Semi-infinite, Spherical, and Cylindrical Media,” vol. 24, pp. 606–616, 1996.
- [64] T. a Wagner, M. Zahn, A. J. Grodzinsky, and A. Pascual-Leone, “Three-dimensional head model simulation of transcranial magnetic stimulation.,” *IEEE Trans. Biomed. Eng.*, vol. 51, no. 9, pp. 1586–98, Sep. 2004.
- [65] F. S. Salinas, J. L. Lancaster, and P. T. Fox, “3D modeling of the total electric field induced by transcranial magnetic stimulation using the boundary element method.,” *Phys. Med. Biol.*, vol. 54, no. 12, pp. 3631–3647, 2009.
- [66] R. Salvador and P. C. Miranda, “Transcranial magnetic stimulation of small animals: a modeling study of the influence of coil geometry, size and orientation.,” *Conf. Proc. IEEE Eng. Med. Biol. Soc.*, vol. 2009, pp. 674–7, Jan. 2009.
- [67] A. Thielscher, A. Opitz, and M. Windhoff, “Impact of the gyral geometry on the electric field induced by transcranial magnetic stimulation.,” *Neuroimage*, vol. 54, no. 1, pp. 234–43, Jan. 2011.
- [68] I. Laakso, A. Hirata, and Y. Ugawa, “Effects of coil orientation on the electric field induced by TMS over the hand motor area.,” *Phys. Med. Biol.*, vol. 59, no. 1, pp. 203–18, Jan. 2014.
- [69] A. M. Janssen *et al.*, “The influence of sulcus width on simulated electric fields induced by transcranial magnetic stimulation.,” *Phys. Med. Biol.*, vol. 58, no. 14, pp. 4881–96, 2013.

- [70] A. M. Janssen, T. F. Oostendorp, and D. F. Stegeman, “The coil orientation dependency of the electric field induced by TMS for M1 and other brain areas,” *J. Neuroeng. Rehabil.*, vol. 12, no. 1, pp. 1–13, 2015.
- [71] P. C. Miranda, M. Hallett, and P. J. Basser, “The electric field induced in the brain by magnetic stimulation: a 3-D finite-element analysis of the effect of tissue heterogeneity and anisotropy,” *IEEE Trans. Biomed. Eng.*, vol. 50, no. 9, pp. 1074–85, Sep. 2003.
- [72] M. De Lucia, G. J. M. Parker, K. Embleton, J. M. Newton, and V. Walsh, “Diffusion tensor MRI-based estimation of the influence of brain tissue anisotropy on the effects of transcranial magnetic stimulation,” *Neuroimage*, vol. 36, no. 4, pp. 1159–70, Jul. 2007.
- [73] A. Nummenmaa *et al.*, “Targeting of White Matter Tracts with Transcranial Magnetic Stimulation,” *Brain Stimul.*, vol. 7, no. 1, pp. 80–84, 2014.
- [74] N. De Geeter, G. Crevecoeur, a Leemans, and L. Dupré, “Effective electric fields along realistic DTI-based neural trajectories for modelling the stimulation mechanisms of TMS,” *Phys. Med. Biol.*, vol. 60, no. 2, pp. 453–471, 2015.
- [75] N. De Geeter, L. Dupré, and G. Crevecoeur, “Modeling transcranial magnetic stimulation from the induced electric fields to the membrane potentials along tractography-based white matter fiber tracts,” *J. Neural Eng.*, vol. 13, no. 2, p. 026028, 2016.
- [76] T. O. Bergmann, A. Karabanov, G. Hartwigsen, A. Thielscher, and H. R. Siebner, “Combining non-invasive transcranial brain stimulation with neuroimaging and electrophysiology: Current approaches and future perspectives,” *Neuroimage*, vol. 140, pp. 4–19, 2016.
- [77] K. Cuypers, H. Thijs, and R. L. J. Meesen, “Optimization of the transcranial magnetic stimulation protocol by defining a reliable estimate for corticospinal excitability,” *PLoS One*, vol. 9, no. 1, 2014.
- [78] S. Bestmann and J. W. Krakauer, “The uses and interpretations of the motor-evoked potential for understanding behaviour,” *Exp. Brain Res.*, vol. 233, no. 3, pp. 679–689, 2015.
- [79] D. E. Bohning *et al.*, “Combined TMS / fMRI Study of Intensity-Dependent TMS Over Motor Cortex,” *Ratio*, vol. 45, no. 4, pp. 385–394, 1999.
- [80] D. E. Bohning *et al.*, “Bold-fMRI response to single-pulse transcranial magnetic stimulation (TMS),” *J. Magn. Reson. Imaging*, vol. 11, no. 6, pp. 569–574, 2000.

[81] S. Bestmann, J. Baudewig, and J. Frahm, “On the synchronization of transcranial magnetic stimulation and functional echo-planar imaging,” *J. Magn. Reson. Imaging*, vol. 17, pp. 309–316, 2003.

Chapter II

Imaging, Modeling, and Electromagnetic
Simulation of Evoked Activity in the Human
Brain

(theoretical backgrounds)

Theoretical Background

In this chapter, we will cover the theoretical background behind the computational models we develop and use in the later chapters. Please, keep in mind that sub-sections of the materials and methods chapters were omitted from the original publications (chapters 3, 4, 5, and 7). Instead, we present in this chapter a slightly extended version of the same material with more comprehensive coverage of some key topics.

We start by looking at what a TMS device is from an engineering point of view and how we can produce accurate estimates of the electromagnetic fields generated by the TMS coil. Then we cover the challenge of the construction of complex volume conductor models of the human head derived from anatomical MRI images. Finally, the combination of the two constitutes what we refer to as Finite Element Models (FEM) of TMS-induced currents, in the form of an approximation of the final electric field distribution in the cortex.

Further, knowing the shape and magnitude of injected eddy currents, allows us to elaborate more on the underlying principle of the neuronal coupling with such extracellular electric fields which is the foundation of the effect TMS has on neuronal stimulation. We propose several metrics of ‘activation’ at a macroscopic level that we use as a local model of neuronal stimulation, which we employ later in our experimental work validating the models we propose in this chapter. Ultimately, such models could be used for proper dose control of TMS administration. This chapter will be referred to often in the chapters to come that will have fewer methodological details than the published papers.

Magnetic Stimulator Unit

A typical TMS device is surprisingly simple from a hardware point of view (even instructions for home-made (DIY) TMS devices can be found on the internet ²). A therapeutic rTMS (bi-phasic) setup consists of the main unit, sometimes with additional power booster and/or coil cooling units, that is connected to a coil using a thick about 1.5m long cable. Based on the polarity of the discharged currents through the coil and consequently the direction of the injected currents we have two major variants: mono and bi-phasic stimulators, resulting in mono- and biphasic pulse shapes,

2 <https://www.instructables.com/id/Transcranial-Magnetic-Stimulation-TMS-Device/>

respectively. The former is commonly used for diagnostic purposes while the latter is often the pulse shape of choice for treatment purposes. The size and shape of the coil are also important to consider. Although some exotic variants exist, the figure-0 (circular) and figure-8 shaped coils remain the most prevalent ones in clinical settings. Generally speaking, figure-0 coils are preferred in the case of peripheral neuronal stimulation, where a larger target area is covered with less accuracy. In contrast, the figure-8 shaped coils are the common choice for cortical stimulation as stimulation is more focused and accuracy higher. In particular, the angled figure-of-8 coil seems to provide a good design where focality and depth of stimulation are optimal [1]. See section 2 (coil modeling) below for further insights in coil design and manufacturing.

A typical operator would only need to adjust the machine power output (MO or MPO) expressed as a value between 0 and 100%, of the maximum magnetic field that a particular combination of device&coil can deliver. A representative device would be able to deliver a 1700V maximum driving current of about 5000A through a coil of around 15uH induction that is capable of delivering up to 200V/m secondary electric field into the human cortex. Such enormous primary currents exist only for a fraction of a second, (0.2-0.4ms), and even then heat accumulation especially in the case of repetitive TMS (rTMS) is a concern that needs to be dealt with by appropriate cooling mechanisms such as mineral oil or air cooling systems. Based on the polarity of the discharged currents in the coil and the resulting direction of injected secondary currents there are two main types of TMS devices, mono-phasic and bi-phasic. The former produces a single rising phase of the voltage, generating a unidirectional field, while the latter has two phases of rising and slightly less powerful falling pulse in opposing directions one after another, generating a current in the wires with 2 phases (approximately sinusoidal in shape). Although variable pulse shape devices exist on the market (cTMS), they are still considered primarily valuable for investigational use. Due to its more effective pulse shape for neuronal interference [2], bi-phasic stimulators are the dominant choice for clinical treatment, as is the case with depression. The mono-phasic pulse shape is often employed for precise electrophysiological mapping studies and is hence more common for neurological diagnostic use due to the cleaner physiological response it evokes, such as electromyographical (EMG) responses in the muscles.

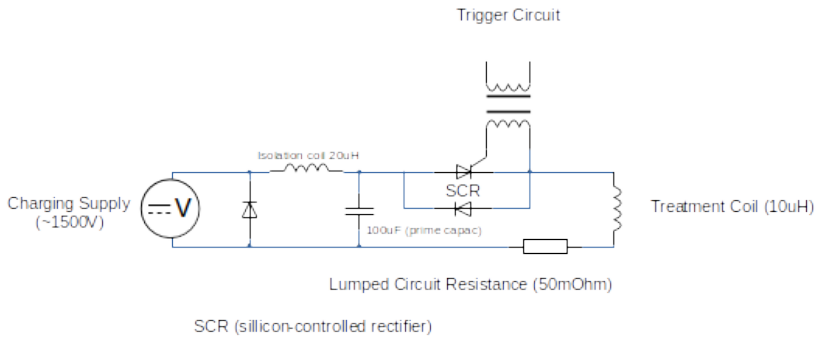


Figure 1: TMS circuit diagram of a biphasic stimulator

The inside of the main unit of a typical TMS device reveals a relatively simple design of an electronic scheme. In Figure 1 you can see a slightly idealized electrical schematic of a bi-phasic stimulator with only the most relevant components shown. We can further generalize the schematic in question to a classical CLR electrical circuit, where the major induction L is coming from the externally connected coil. Then the internal resistance of all electronics R and the huge capacitance C , usually in the shape of banks of capacitors. A thyristor with an inductive decoupled (transformer) control pin is used for triggering the discharge of the capacitors through the main circuit. It is interesting to note that the second phase of a bi-phasic device is in the form of a reused power coming from the collapse of the magnetic field of the first pulse and partially recharges the capacitors before a secondary discharge. The diode, connected in parallel to the coil, the main purpose is to drive away such reverse currents.

TMS Coil EM-Fields Modeling

The accuracy of numerical coil field modeling has received relatively little attention in comparison to FEM aspects of currents induced in the head. Modeling currents in the human head includes full head 3D meshing of MRI images and especially the derivation of the electric field to explore its effects on the cortex, arguably the most intriguing from a life science perspective. This difference in focus is not surprising considering that the derivation of the primary electric field evoked by a TMS coil depends on well-established electromagnetic theory and common engineering principles. There are several computational methods proposed in the literature [3] [4] [5] and they are all straightforward to implement in the form of simple discrete models. They have shown to be capable of approximating, accurately enough, the induced magnetic and electric fields induced by a discharging coil. One such

common approach involves the piece-wise current integration of small segments along the wire [6]. These segments form a curve that follows the profile of the general shape of multiple copper winding. To numerically quantify the magnetic and electric fields produced by TMS the following discrete forms of the general Biot-Savart equations are used, for the magnetic field and magnetic vector potential respectively [7] (chapter 6.4) :

$$B(\vec{r}) = \frac{I\mu_0 w}{4\pi} \int \frac{\partial l \times \vec{r}}{|\vec{r} - \vec{r}_0|^3} \quad (\text{B-field})$$

$$A(\vec{r}) = \frac{I\mu_0 w}{4\pi} \int \frac{\partial l}{|\vec{r} - \vec{r}_0|} \quad (\text{E-field})$$

allowing us to derive the fields at a point \mathbf{r} as a result of current running through a wire segment $d\mathbf{l}$ at a distance $\mathbf{r} - \mathbf{r}_0$ away from it, where $\mathbf{r} \gg d\mathbf{l}$ and μ_0 is the magnetic permeability of free space at a distance \mathbf{r} from the source. Finally, the w symbol in the equations is added to aid the numerical tuning by providing a linear weight factor per line segment to help us calibrate better the spacial distribution of the fields.

To accomplish a complete numerical evaluation following the formulation just given, we first need to be able to evaluate the current running through the coil at the moment of discharge. Doing so will in turn require we have a good approximation of the geometry of the coil and some strategy for integrating the current along that geometry. Splitting a circle into sufficient piece-wise line segments and taking the (infinitesimal) small steps of integration along that segment will ensure we will have an accurate estimation of the magnitude of the fields. At the same time, the distribution of the field will be entirely governed by our success in approximating the overall shape of the magnetic flux produced through the induction of each particular coil. This might not necessarily follow the shape of the coil case as seen from the outside. Finally, we need to consider the combination of each integration point along the geometry of the coil model to each node of our FEM model of the head and solve the before mention equations to produce complete field distribution in our domain following the principle of superposition of the magnetic fields.

The method just described is the one adopted for the rest of our research. Key benefits are the possibility to generalize any shape and geometry while simultaneously being relatively easy to realize numerically albeit more costly computationally wise compared to alternatives [8]. Another method to model the magnetic field of a TMS coil that we can encounter often in common literature involves the use of magnetic dipole moments where a collection of dipoles is arranged in rings to resemble the general shape of the TMS coil geometry and their moment is taken as proportional to the current magnitude flowing through the coil windings [5] .

Although more trivial than modeling induced currents in the head with FEM, the modeling of a coil is not without challenges. To approximate well enough (<10% discrepancy with measurements) both the field shape and its magnitude demands additional intuition and at least some trial and error. For instance, both the piece-wise wire approach as well as the multi-dipoles approach heavily rely on current weighting applied for each stack of windings for the former and the number of dipoles and ring contribution factors and self-induction for the latter [9] [10]. This in combination with the fact that many studies have opted for simple single-loop geometries, to model generic TMS coils, motivated us to look into how much geometrical detail and tuning is required to come up with reliable models. Previous work of Salinas et. al. [11] have already demonstrated the significance of the coil geometrical complexity, in scale applicable to both humans and small rodents.

We set out to model TMS coils with the proposed piece-wise Biot-Savart method in varying levels of detail and compared those models with measured incident fields evoked by an actual TMS coil inside an MRI scanner, using a novel phase mapping approach at low stimulation intensities. The detailed models and empirical validation of our coil modeling approach are presented in chapter 3 where we validate the accuracy of our coil modeling approach that we use for the rest of the work presented here. In summary, the coil model providing sufficient detail and a good match to magnetic field measurements (see chapter 3) was the spiral piece-wise model of the figure-of-8 coil, which is used in the other modeling chapters 4 and 5. See a coil wire model below in figure 2.

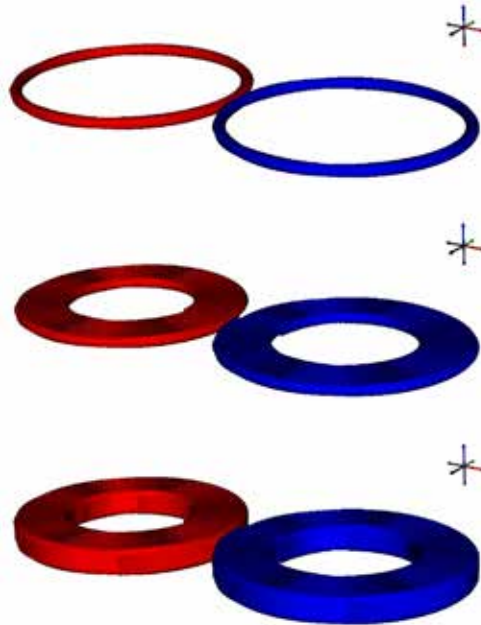


Figure 2: Several coil models with progressive complexity in geometry. Top: Single loop using outer radius with 4mm winter-wing gap; Middle: Spiral profile of 9 turns; Bottom: Similar to the previous coil but with added 10 layers with 1mm spacing;

We further concluded that taking into account the exact spiral profile is not required to model measured fields effectively, not surprisingly considering the construction of most coils in the form of tightly wound wires compactly packed in a ring shape. Instead, our experiments showed the cumulative surface for each coil wing to be the main contributing factor to accuracy at a distance depth of $\sim 3\text{cm}$ for a coil with a 5cm wide ring surface.

So far we have only addressed coil modeling in the context of assessing the field induced by a complete coil in a homogeneous medium, and its potential impact on brain research studies. However, other studies have focused exclusively on modeling for better design and engineering of TMS coils [12]. The work we present later in chapter 7 is one example of such an attempt to influence the design and ultimate production of several rodent-tailored TMS coils.

Now we know the shape and magnitude of the B-field of the coils used in our modeling and validation approach, we will continue to establish how such B-fields induce currents in a human head with complex morphology.

Estimating induced currents in the head: a problem formulation

When the magnetic field (B-field) generated by a coil is known, in theory, it is possible to estimate the induced electric field (E-field) current in a conductive medium under the coil, in our case the head. First, we will try to formalize this problem of induced fields in the head with the appropriate physical laws.

Theoretically, the problem of estimating the distribution of the electrical currents injected into the brain by a TMS coil is in the category of forward mathematical models where the source is well-defined and we only need to estimate the field distribution on an accurately shaped 3D model under realistic LF tissue dielectric properties. An exogenous electric field in biological tissues will introduce currents with ohmic (resistive) and displacement (capacitive) components. While the former emerges from the free movement of charged particles (ions) in the extra-cellular space in biological tissue (outside the cell plasma membrane), the latter is caused by the polarization of the medium itself. Ionic double layers that surround a cellular membrane, and even some embedded within macro-molecules, can be seen as paired charges that in principle can be polarized. How easy that polarization can be is governed by the electrical permittivity ϵ .

We here consider the magnetic field \mathbf{B} induced by the TMS coil and the primary electrical field \mathbf{E}_p that is in turn induced in the head by that B-field. Both electrical and magnetic fields are fully described by Maxwell's equations (in differential form):

$$\nabla \times \bar{\mathbf{E}} = -\frac{\partial \bar{\mathbf{B}}}{\partial t}$$

Formula 1: Faraday's Law

$$\nabla \times \bar{\mathbf{H}} = \bar{\mathbf{J}} + \frac{\partial \bar{\mathbf{D}}}{\partial t}$$

Formula 2: Amper's Law

$$\nabla \cdot \bar{\mathbf{D}} = \rho$$

Formula 3: Gauss's law

$$\nabla \cdot \bar{\mathbf{B}} = 0$$

Formula 4: Gauss's Law

where \mathbf{E} [volts;V/m] is the induced electric field, \mathbf{B} [teslas;T] the magnetic flux density induced by the coil, while \mathbf{H} [amperes;A/m] is the magnetic field, then \mathbf{J} [amperes over area, A/m²] the current density, \mathbf{D} [coulombs;C/m²] the dielectric displacement and ρ [coulombs; C/m³] the electric charge density. Also, we know how the current density relates to the electric field according to the generalized Ohm's law, where σ represents the medium conductivity tensor:

$$\bar{\mathbf{J}} = \bar{\sigma} \bar{\mathbf{E}}$$

Formula 5: Ohm's Law

The law of induction simply states that a time-varying magnetic field will introduce an equivalent electric field in the orthogonal direction. The primary induced electric field comes as a direct result of the current running through a coil and is considered the primary force behind neuro-stimulation. There is a secondary effect caused by the charge accumulation on the border of domains, due to the law of conservation, additionally influencing the final E-field. The complete definition of the total induced electric field is given as the sum of both the primary and secondary electrical fields:

$$\mathbf{E}_t = \mathbf{E}_p + \mathbf{E}_s = -\frac{\partial \bar{\mathbf{A}}}{\partial t} - \nabla \cdot \phi$$

Formula 6: Total Induced Electric Field

where \mathbf{A} is the magnetic vector potential from the coil induction alone and ϕ is the scalar potential distribution. The divergence of the scalar potential produces the secondary electric field, which distribution is determined by the electrical properties of each tissue type, which constitute the conductivity σ (sigma) and the relative permittivity ϵ (epsilon).

Under quasi-static approximation, the medium could be described as purely resistive and any capacitive currents that are proportional to ϵ could be safely ignored, that is no additional displacement currents exist [7] (chapter 9.2) that might cause phase difference [13]. The quasi-static assumption is commonly adopted in the field due to the following observations: relatively low frequency of stimulation (1-10 kHz); the ratio between the displacement and ohmic current for biological tissue properties ($\omega \ll 1$) in the range of ~5kHz ranges $\sigma \sim 1$ (CSF) – $\sigma \sim 0.004$ (SKULL) and $\epsilon \sim 10^6$ F/m [14]. This allows us to decouple the spatial and temporal components of the electric field under the low-freq dielectric properties of the medium. As a result, Maxwell's equations become simpler by eliminating any time-varying component for \mathbf{H} and \mathbf{E} allowing us to define the secondary E-field as the divergence of the scalar potential: $\mathbf{E}_s = -\nabla \cdot \phi$

It is easy to show that the divergence of formula 2 (Amper's Law) yields $\nabla \cdot \vec{J} = \nabla \cdot \nabla \times \vec{H} = 0$ because the divergence of the curl of a vector field is zero. Keeping in mind that and combining the general Ohm's law with the definition of electric field stemming from the divergence of the scalar potential leads to the final equation:

$$\nabla \cdot (\bar{\sigma} \nabla \phi) = \nabla \cdot \vec{J}$$

Formula 7

This gives us the final forward problem definition assuming the Neumann boundary condition defining the fluid-like flow of current denoted by:

$$|\bar{\sigma} E| \cdot \vec{n} = 0 \text{ on } \partial \Omega$$

Formula 8

and the Poisson equation defining the potential field under quasi-static approximation

$$\nabla \cdot (\bar{\sigma} \nabla \phi) = I_s \in \Omega$$

Formula 9

Although commonly adopted, the quasi-static treatment of the problem is not exclusive and some authors have raised concerns in the validity of the underlying assumptions [15] [16]. There is an excellent theoretical treatment of the alternative where the high-frequency component of TMS is considered as well [17] (chapter 9.10).

Estimating induced currents in the head: computer simulation

The numerical calculation of the TMS-induced total electric field in the otherwise highly heterogenous medium, that is the human head, is a key part of our modeling approach. The generation of the subject-specific head mesh together with the derivation of the primary electric field of the coil were the most challenging steps undertaken in the process of creating a complete computer simulation.

In principle, many physical phenomena could be described in the form of differential equations or more often in a system of complex governing partial differential equations (PDEs). Electricity is no exception, the derivation of the secondary field could be expressed as a linear system of basis equations defined per element (tetrahedron) of the modeled domain, which we present as an MRI-derived 3D head mesh. The Finite Element Model (FEM) method involves discretization (thus finite), breaking a complex domain into smaller and simpler geometry with simpler solutions to solve that, put together globally, yield a final approximate solution of the

entire problem. One caveat is that a direct solution to such a linear system of equations $\mathbf{A} \cdot \mathbf{x} = \mathbf{B}$, where \mathbf{A} and \mathbf{B} are fixed square matrices and \mathbf{x} is a column vector, the unknown, is usually not possible since \mathbf{A} is often not invertible, that is no direct solution exists for $\mathbf{x} = \mathbf{A}^{-1} \cdot \mathbf{B}$. Instead, we rely on iterative numerical routines to eventually converge to acceptable accuracy to the guess for the unknown variable. In our case, the iterative optimization algorithm is the bi-conjugate gradient decent method [18] with the Jacobian matrix per-conditioner (providing the initial starting estimate). In more traditional FEM literature, \mathbf{A} is referred to as the stiffness matrix and is given by fixed property of the material for each element of the mesh and \mathbf{B} as the stress vector (e.g. applied force), since FEM was initially adopted for mechanical simulations.

In our case, \mathbf{A} is constructed using the conductivity values and \mathbf{B} is the primary electric field induced by the TMS coil. After the derivation of the PDE (formula 9) and its boundary conditions (formula 8), the forward problem can be formulated in the following way. Given a certain source configuration, represented by the right-hand side of (formula 9), compute the potential distribution ϕ in the domain Ω . At this point, it becomes apparent that for the forward calculations a source model and a description of the head as a volume conductor is needed. The software suite we used to conduct the FEM simulations is SCIRun 4.7. At the moment of the writing of this theses, a SCIRun 5.0 stable is publicly available.

Head Modeling

In order to perform FEM modeling of currents in a medium, one must somehow compartmentalize the medium in regions of similar conductivity. Generally, tetrahedrons are used to accomplish this.

The challenge in this compartmentalization is the often complex shape of the conductive medium in a head. Any higher mammal species but in particular the human brain possess an astonishingly high level of complexity in both structure and inter-regional organization. The part of the head most relevant for TMS FEM modeling is the neo-cortex, which is a narrow sheet of layers of neuronal cell bodies encompassing the brain and hence located superficially, about 2 to 4 cm below the scalp. The detail to which we can structurally model the neocortex it is limited by the spatial imaging resolution, in the case of MRI. Furthermore, the factor impacting the numerical simulations needed for FEM most, is how accurately the surface boundaries between the gray matter (GM) and cerebral-spinal fluid (CSF) and to a lesser extent between gray and white matter (WM) are captured by the volumetric description (3D head mesh) of those tissues as derived from an MRI scan. However, the intricate folding pattern of the GM presents us with the highly convoluted outer sheet as arguably the

most significant boundary surface for the FEM head mesh, which makes this separation of relevant tissues a serious challenge.

It is paramount that the spatial layout of an MRI volume including air, tissues in the head such as skin, skull, cerebral spinal fluid (CSF), and gray and white matter (GM, WM) are described volumetrically in such a way that they capture the electromagnetic properties (especially electrical conductivity) well. The processing of an original MRI image into a volumetric description of the space occupied by the relevant tissue types is performed sequentially in a series of steps that are described below.

First, MRI images need to be subdivided into regions of similar electrical properties. This process is generally referred to as image segmentation. For all other studies presented in this thesis, a T1 weighted MRI scan (TR/TE of 10.0/4.6 ms, a flip angle of 8°, voxel size of 0.75x0.75x0.8 mm³, scan duration of 11.3 min, 225 slices with a slice gap of 0 mm) was obtained at a Philips Achieva 3T MRI scanner for all participants. This MRI image was converted into the Nifti 1.1 format, and segmented into air, skin, skull, CSF, GM, and WM using the ‘unified segmentation’ algorithm as implemented in SPM12 with Bayesian prior tissue maps. This generally results in viable segmentation for each major tissue type in the form of a probability map where voxel values indicate the probability of belonging to a certain tissue class. For each voxel in the volume, it was then determined what the most likely tissue type was (i.e, which tissue probability map had the highest value at that location, where the ‘winning’ tissue type had to be at least 0.3 likelihood). For each voxel, an index was saved into a new volume indicating the associated tissue type (a so-called ‘index map’). Subsequently, the index maps were further processed to guarantee a set of requirements per tissue type. The CSF index values were stored first and dilated by a voxel, such that no holes were present between GM and CSF that can occur for spurious intensities in the MRI images. Next, in the same fashion, the WM values are inserted into the volume. The other tissue indexes were added after that, overwriting previously inserted voxels. The indexes where: 1 = GM, 2 = WM, 3=CSF, 4 = Skull/Skin, 5=air. Note that skull and skin were treated as one tissue type, as mainly the inner boundary of the skull is relevant for current flow in FEM, and the unified segmentation algorithm we use artificially results in a very convoluted skull/skin boundaries with many archipelagos of skin tissue types in the skull and vice versa.

We inspected the indexed image visually slice by slice for every single participant included in the study, and occasionally manually removed voxels erroneously classified as GM deeper inside sulci that ‘clogged’ a sulcus (causing the GM voxels across a sulcus to ‘connect’). Such ‘clogging’ would have caused the 2 banks of a sulcus to artificially connect in a computed volumetric mesh, which is known to result in spurious currents when used for FEM modeling. See figure 3a for a visualization of this manual editing process.

In figure 3-b the entire MRI image processing pipeline leading to a 3D meshed head is depicted and further elaborated upon.

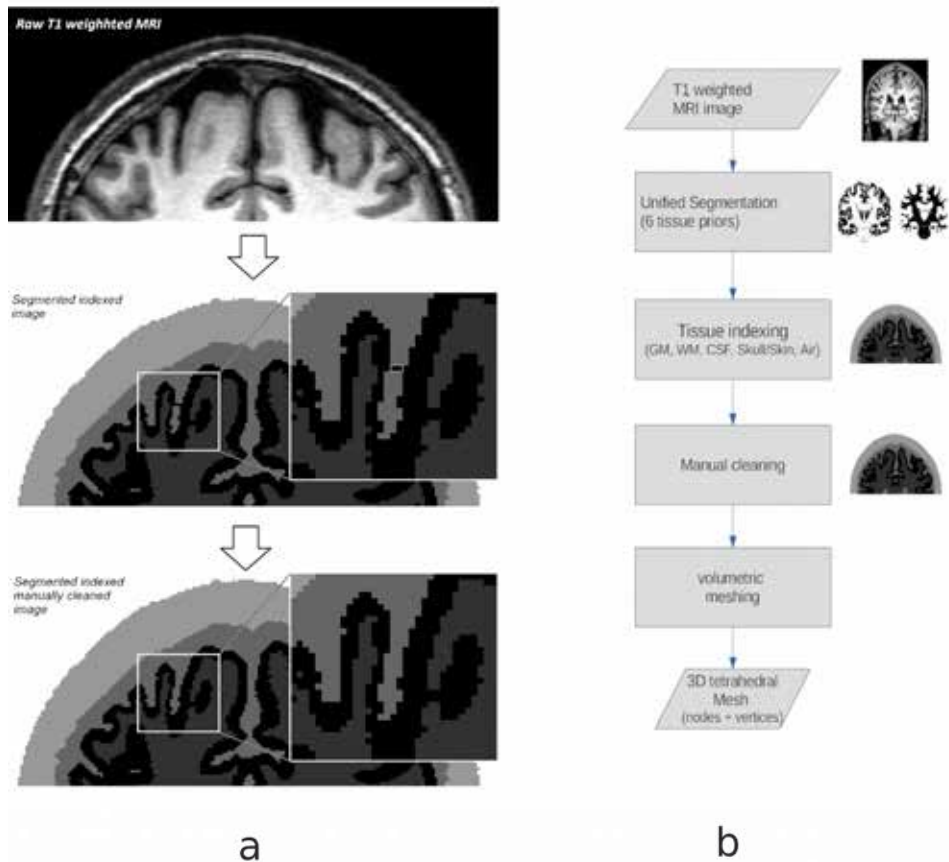


Figure 3: On the left (a) : From top to bottom a coronal cut from anatomical T1 weighted MRI to binary partitioned tissue classification map. On the right (b): Typical steps involved in image processing pipelines from raw scanner images to final volumetric 3D model.

After the automatic segmentation, indexing, and manual corrections, index maps remain that are suitable for deriving parametric volumetric representations (the 3D meshes) describing the tissues that can be used for FEM modeling. 3D meshing is the process of describing a volume (in this case tissue type) with elementary shapes, in our case tetrahedrons. To guarantee rather smooth boundaries on the interface between different compartments, we first adopted an iterative smoothing routine of alternating

inflation-deflation operations in image space. Those images were processed by our meshing algorithm one per tissue type to produce the final FEM mesh using Cleaver2: A Multi-Material Tetrahedral Meshing Library and Application (Scientific Computing and Imaging Institute (SCI), University of Utah, The USA) [<https://github.com/SCIInstitute/Cleaver2>].

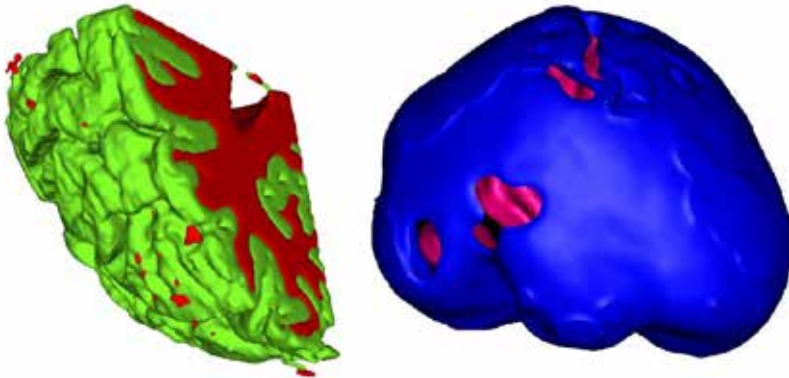


Figure 4: Two most common artifacts encountered during mesh creation. On the left: small disconnected islands of misclassified tissues; On the right: peeling of thin layers and the creation of sharp discontinuities

In addition, for FEM modeling to work, our meshes must have a smooth flow and the divergence of the field should be close to zero. This imposes several restrictions on the quality of the tissue interfaces in particular and the volumetric 3D mesh in general. In FEM the error of the numeric solution is strictly governed by the quality of the mesh [19]. A good quality mesh will have as smooth as possible boundary interface with no holes or discontinuities, forming a so-called water tight 3D mesh for each compartment, with a distinct homogeneous conductivity. Producing such meshes can be challenging. Two of the most common causes of degraded meshes come from merged boundaries, disappearing interfaces, and the formation of holes between different compartments and the erroneous isolation of disconnected usually small volume (islands) compartments. The cause for a missing interface is usually due to aggressive smoothing of the segmented and indexed image, a process used by many mesh algorithms including ours. Using an aggressive amount of image smoothing, however, might merge parts of otherwise anatomically distinct structures, such as the physical separation between CSF and GM near the sulcal walls, a gap that can be as small as 1mm or less that sometimes remains just under the MR spatial resolution. The effect of such artificial merges on FEM simulation is the introduction of current leakage between otherwise separated compartments, leading to spurious results in the resulting simulated current patterns. This is exactly the reason why we took great care

to separate especially sulcal walls through manual cleaning (see figure 3a and description above). The effect of distinct compartments merging due to excess smoothing or low image spatial resolution causes the partial omission of boundary surface interfaces.

As the accuracy of simulations is closely related to the quality of the mesh and in particular the well-defined shape for each of its constituent elements, we employed several metrics to evaluate the quality of the generated tetrahedral elements. Further, we refined such non-conforming elements by splitting or merging them with adjacent ones. The most common case of degenerate elements are all vertices too close together that give almost zero volume; have very sharp or wide angles between edges; wrong order of vertex indices giving negative volume.

Neuronal Coupling

The above sections elucidate in detail and quantitatively how a TMS device generates a current through a set of windings forming a coil, how this coil generates a magnetic field in the head, how this magnetic field in turn generates a current in the tissues in the head, including in the cortical layers containing most neurons. However, how the assembly of connected neurons in the cortical layers responds to this locally induced field is as of yet not discussed.

For reference: the most common figure-of-8 coils provide a relatively focal ($4 \times 2 \text{cm}^2$) superficially at a depth of 2 to 4 cm along the central iso-line of the B-field induced by the TMS coil. That depth conveniently includes the folded adult human cortex up to about 1 cm below the dura mater.

In order to understand the neuronal consequences of an induced current in the cortical sheet, we need to take a closer look at the organization of different types of neurons found within the cortical sheet.

The neuronal column is a fundamental principle of neuronal organization within the cortical sheet where the main axes of neurons are oriented in small functional columns perpendicular to the cortical sheet [20] (Hubel & Wiesel, 1979). Those main pyramidal neurons are found in many of the cortical layers, receiving afferent input from other regions, sending efferent output to other regions, and are interconnected horizontally with different types of inter-neurons. See figure 5 below for an overview.

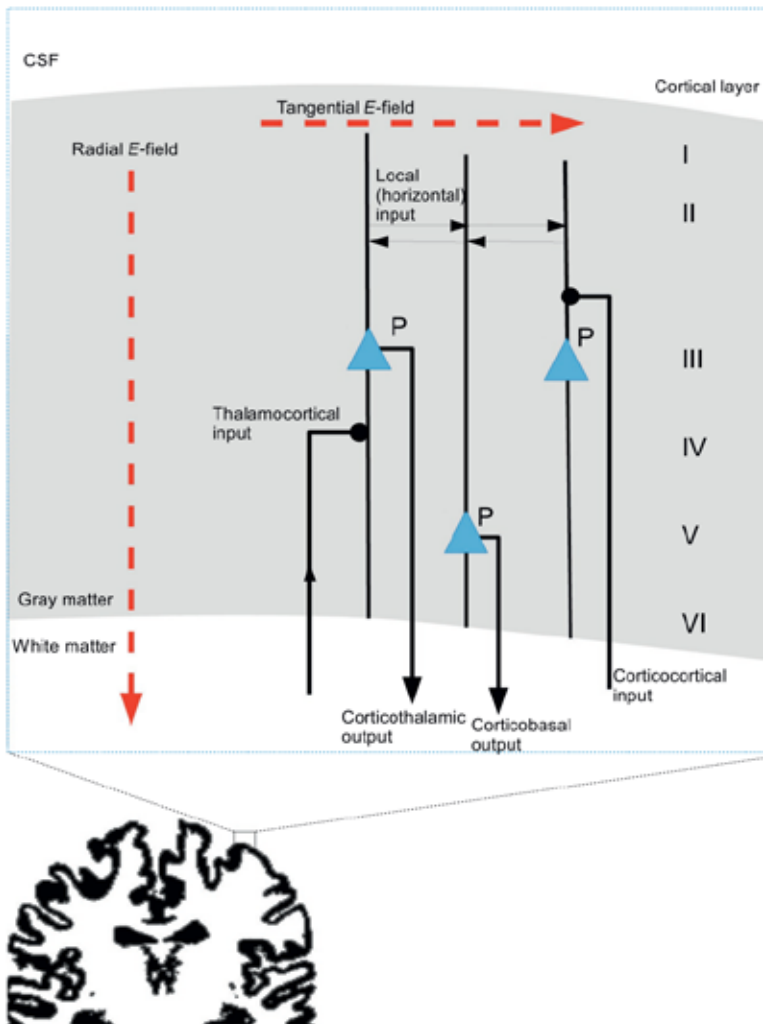


Figure 5: The cortical sheet is depicted below as black tissue (derived from a slice through an MRI scan segmented into a gray matter map). In the enlarged window, it is depicted how the cortical sheet consists of six layers, with pyramid cells (P), inhibitory inter-neurons and granule cells (not shown), and afferent and efferent fibers arriving from and connecting to other brain areas. The radial (perpendicular to the cortical sheet) and tangential component (parallel to the cortical sheet) of a TMS-induced incident E-field are shown as red (dark gray in the print version) arrows. For a full explanation, see Section 2.1 of Neggers et. al. 2015.

Traditionally in TMS modeling studies, only the magnitude of the E-field, $|E|$, has been considered in the estimating of the potential region of activation [10] [21] which in principle neglects any contribution due to the direction of the injected currents relative to the neuronal sheet. This also neglects the influence of the type of pulse shape, mono or bi-phasic, which is known to have a profound effect on TMS-induced neuronal activation. More importantly, when only assessing the induced E-

field magnitude one completely ignores the underlying micro structure and organization of the human cortex, which also is known to have a profound effect on how a TMS pulse generates neuronal activation [22], [23]. To take the local morphology of the cortical sheet into account, after experiments with functional PET imaging in combination with TMS (at the same time) the group of Peter Fox proposed a current dependent metric where currents orthogonal to the cortical sheet are most effective, and currents in parallel with the cortical surface much less so [24]–[26]. They proposed the cosine hypothesis for the relationship between a local electrical field and neuronal activation, or simply C3, where the neuronal activation from a certain piece of cortical tissue is proportional to the cosine of the angle between the local induced electrical field and the normal vector to that same local patch of the cortical sheet. This metric has been quite influential and could explain several empirical findings related to the angle of induced currents in the brain and neuronal activation.

Interestingly, the C3 metric already results in a potential contradiction, which recently spurred a lively debate in the field (for a good summary, see the discussion of [27]). The strongest induced field is always stronger closer to the coil, which naturally favors the gyral crown as most likely site of stimulation. Alternatively, the C3 cosine hypothesis would suggest that despite the lower intensity regions deeper within the sulcal wall are preferentially targeted as the TMS-evoked currents flow largely parallel to the scalp, orthogonal to the deeper sulcal walls [24] [26].

Those two hypotheses suggest alternative mechanisms of how the action of activation is achieved on the macro neuronal level based on our current understanding of the layered cortical wiring of the human cortical sheet. The first proposes an indirect pathway from vertically oriented L2/3 cells and L5 PT (pyramidal tract) at the crown as the most likely network, which could explain the occurrence of I-waves and D-waves through inter-neuron connectivity. The second study proposed the “cosine” hypothesis suggesting that only cells along the PT (pyramidal tract) pick up the majority of the electrical flux and as result more are the direct source of feed-forward propagation of events. Such a hypothesis could explain the difference in RMT for PA and AP injected currents, considering PT tracts along the long axis of the cortical column but in the opposite directions [28][2][29].

Fox and colleagues claim empirical evidence in the observation of an activation preference in the medial surface deeper in a sulcus with PET and supra-threshold TMS [24] or by the ability to explain the angular dependency of coil orientation relative to gyral orientation [22] [23] [30]. The same model was demonstrated numerically (FEM) and supported with functional PET imaging, as a piece of strong evidence for this hypothesis [25]. However, the cosine model is also criticized with indirect empirical evidence [27]. Based on FEM models combined with the aforementioned C3 metric [27], albeit through indirect evidence of comparing results from a model to previously reported functional imaging studies, Bungert et al

have confronted the notion that any prime component of the E-field relative to the outer cortical layer can be a good estimator alone.

Finally, one can argue that the cosine model proposed by Fox and colleagues ignores the fact that many of the main glutamatergic excitatory neurons in the cortical columns are interconnected horizontally by GABAergic inhibitory interneurons [31]. This implies that the TMS-induced E-field polarizing and hence inhibiting such inhibitory inter-neurons could contribute to a maximal release of inhibition on and subsequent activation of then dis-inhibited cortical column neurons. This in turn would predict the opposite of the C3 model, namely activation preferentially in gyral crowns where E-fields are parallel to the main orientation of inter-neurons, and much less deep in the sulci.

The debate in the TMS modeling and empirical literature as summarized above demonstrates that it is far from established how a TMS-induced current evokes activation in the human cortical sheet. Therefore, in the next section, we introduce several neuronal activation metrics that we developed concerning the aforementioned alternative theoretical considerations, that can compute a macroscopic pattern of expected activation on a patch of the cortical surface. Most notably, the role of other organizational principles of the neuronal sheet, such as the contribution of horizontal interneurons and the polarity of ascending and descending fibers. This allows us to further validate these activation models and integrate them into models for dose-response characteristics of TMS. The angular dependence between induced electric fields and the underlying neuronal organization is a central point of the investigations described in this thesis.

Neuronal Activation Metrics

In this section, we set out 5 different models for the coupling between a TMS-induced E-field and neurons in the cortical sheet. The different views surrounding this topic have been discussed in the previous section.

Metric C3. When approximating the cortical surface with a triangular surface mesh, as depicted in figure 7 per metric, a surface patch with a set of triangles would experience the total ‘activation’ of the inner product between the surface normal of each triangle and the total E-field through that triangle (maximal for a local E-field aligned with the surface normal), multiplied by the surface of that triangle S , yielding the term $|\vec{E} \cdot \vec{n}|S$, summed over all triangles in a patch. The absolute value is used because we assume a symmetric interaction for inward and outward E-fields (see below), due to the bi-phasic stimulator we employ

There is empirical support for this model for the coupling between the induced E-field and neuronal activation. It has been established that brain activation, as estimated by proxy through measured electromyograms (EMG) as a response to TMS on the motor cortex (motor evoked potential or MEP), is affected by the direction of the underlying central sulcus [22]. Currents induced perpendicular to the central sulcus evoke maximal MEPs, but to evoke MEPs with the same amplitude, a larger current magnitude was needed for currents evoked parallel to the central sulcus. Similar observations were made for the direction of current relative to major sulci in the visual cortex in terms of evoked phosphene thresholds (a visual illusion) [32]. Such observations led to assumptions that neuronal axons oriented perpendicular to the cortical sheet, potentially descending tracts, cause the majority of evoked activations by TMS, and hence are stimulated optimally with currents perpendicularly to the cortical sheet. This has been dubbed the ‘C3’ metric for the relationship between currents and neuronal activation [24]. See figure 7C for a graphical depiction. However, there also is ample debate about this metric [27], and we hence also adopted other potential metrics that might explain neuronal activation induced by a local current.

Metric C2. It could also be that local horizontal connections between pyramid cells in the cortex, through inhibitory interneurons [31], produce most of the activation induced by local fields. In such a case, currents in parallel to a cortical tissue would evoke maximal neuronal activation (or suppress it maximally). This metric we dub C2 is also sketched in figure 7b. For C2, a cortical sheet approximated by surface with a set of triangles would experience the total ‘activation’ of the length of the outer product between the surface normal of each triangle and the total E-field through that triangle (maximal for a field perpendicular to the normal), again multiplied by the surface of that triangle S , yielding the term $|\vec{E} \otimes \vec{n}| S$, summed over all triangles in a patch. The absolute value is used because we assume a symmetric interaction for inward and outward E-fields.

Metric CE. We further adopt the notion that perhaps the mix of neuron types found in the cortex is too complex for such a simple and crude neuronal metric of activation, and that the best predictor for activation is simply the magnitude of the local E-field without taking into account its direction, as is the classic approach in human TMS E-field modeling (see section 6). We describe this metric as ‘CE’. A surface patch representing the cortical sheet would for this simple metric contribute $|\vec{E}| S$ per triangle, where S is the surface of each triangle. This metric is depicted in figure 7a.

Metrics C4 and C5. Note that one could argue that the E-field’s polarity also should be taken into account. For example, for metric C3, this would mean that currents pointing inward from CSF into a sulcus, would evoke a negative (or minimal) signal, and pointing outwards a maximal signal, which would equate to $\vec{E} \cdot \vec{n} S$. Note

that this idea holds true for a monophasic TMS pulse shape, for biphasic pulse shapes there is a current in opposing directions in short succession per stimulus and the net contributions probably add up. Therefore we can not distinguish between a symmetric or asymmetric coupling between E-field and neuronal sheet in our validation experiments using biphasic pulse shapes (using concurrent TMS-fMRI, see chapter 5). Hence we assumed a symmetric interaction and implement this notion with the absolute value of the inner product between the E-field and the surface normal, or $|\vec{E} \cdot \vec{n}|$ for C3, and in a similar fashion for C2. However, for validation experiments using TMS and EMG (MEPs) as described in chapter 4, we consider both polarities for a C3-like metric, with one metric maximal for inward pointing E-fields (C4) and one maximal for outward-pointing E-fields (C5).

In summary, the 5 metrics discussed above describing macroscopic models of how a local electrical field interacts with cortical neuronal tissues are mathematically described as follows:

$$\begin{aligned}
 C_e &= \int_{\Omega\%} |\vec{E}_t| A \quad \text{The E-field magnitude;} \\
 C_2 &= \int_{\Omega\%} |\vec{E}_t \circ (n \otimes \hat{E}_t)| A \quad \text{Symmetric E-field tangential;} \\
 C_3 &= \int_{\Omega\%} |\vec{E}_t \circ n| A \quad \text{Symmetric E-field orthogonal;} \\
 C_4 &= \int_{\Omega\%} \vec{E}_t \circ n^{-1} A \quad \text{Asymmetric E-field orthogonal outward;} \\
 C_5 &= \int_{\Omega\%} \vec{E}_t \circ n A \quad \text{Asymmetric E-field orthogonal inward;}
 \end{aligned}$$

The integral over the domain is simply the sum over each triangle of the isolated tri-surface patches of our ROIs, where A is its area. In figure 6, the C2, C3, C4, C5, and CE metrics are depicted, including how to compute them for a triangulated surface mesh we use to describe the cortex for sake of simplicity. We have used those metrics to empirically validate our complete models set out in this chapter using concurrent TMS/fMRI BOLD measurements (see chapter 5) and TMS-MEP experiments (see chapter 6).

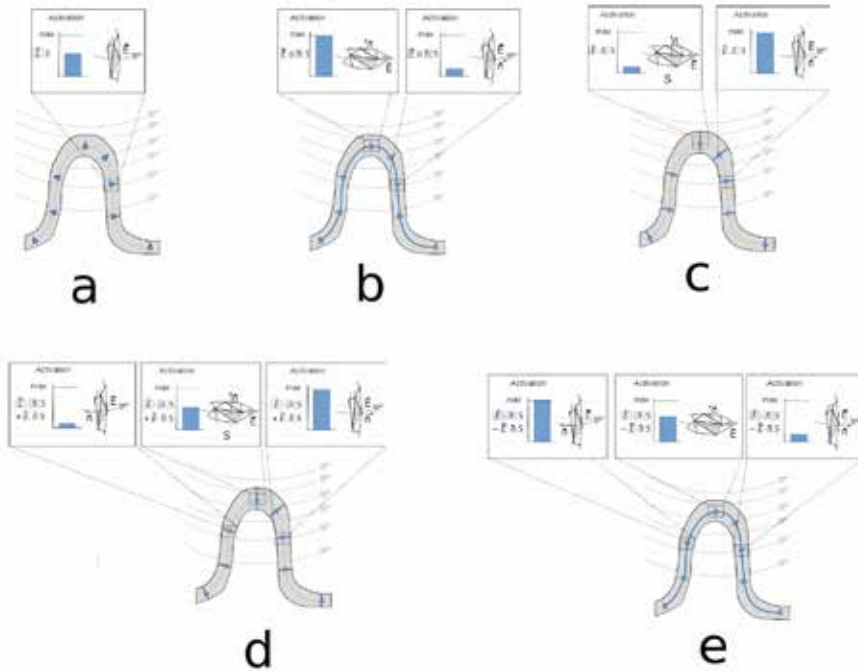


Figure 6: Conceptual illustration of the effect of each metric on the final estimate of the effectiveness of stimulation on a highly idealized folded cortical surface of a human cortex in 2D, for one gyrus in 3 situations. The curved grey lines denote the E-field \mathbf{E} evoked by a TMS stimulus, S is the area of a surface patch, and \mathbf{n} is the surface normals. The panels depict the geometrical relationship between a surface polygon normal \mathbf{n} and the estimated E-field, given for the center of the polygon. (a) metric CE: the activation per surface mesh element equals the size of the E-field times the area of the surface it passes through, independent from the current direction. (b) metric C3: for each surface element, the resulting activation is the product of the surface area and the size of the vector product of the E-field and surface normal (size of both vectors times the cosine of the angle between them). This is maximal for a surface patch along the sulcal wall and minimal for a surface patch on the gyral crown. (c) metric C2: for each surface element, the resulting activation is the product of the surface area and the size of the cross product of the E-field and surface normal (size of both vectors times the sine of the angle between them). This is minimal for a surface patch along the sulcal wall and maximal for a surface patch on the gyral crown. (d) metric C4 and (e) C5 : similar to C3 but flavoring outward or inward injected E respectively.

Summary

In this chapter, we have set out our main computational framework to predict neuronal responses in the brain of an individual as a response to a magnetic field pulse generated by a given TMS coil. To accomplish this, we first developed a method to

quantitatively derive the magnetic field generated by a set of coil windings constituting a given TMS coil, using piece-wise Biot-Savart modeling. We then developed a method to represent the most relevant tissue types in the human head in a 3D volumetric description (the volume mesh) of the space covered by such tissues in an individual MRI scan. After that, we adopted a finite element model that allows the estimation of the current evoked in the head by the modeled TMS coil, taking into account the individual morphology of each subject's brain. Finally, we approximated the macroscopic neuronal activation patterns in the cortical sheet that would result from such a current, using different considerations derived from literature and our ideas, that reflect how neuronal tissue in the cortical sheet is organized.

Taken together, this complete model allows one to model the B-field generated by any TMS coil shape, estimate the induced current of such a coil in each head for which a high-quality MRI scan is available, and approximate the induced neuronal activation according to competing local models of the current-to-neuronal coupling. This is a powerful generic approach allowing many different applications of dose and location-controlled TMS.

However, important parts of this computational framework necessarily rely on assumptions and simplifications. Therefore, in the next chapters of this thesis, we will experimentally validate this framework on several levels: the magnetic field generated by the TMS coil will be measured with a special setup in an MRI scanner using phantom objects, the induced activation will be validated indirectly using motor evoked potentials in the hand muscles, and more directly using concurrent TMS-fMRI.

Importantly, these validations can reveal what assumptions and simplifications were valid or where we need to reconsider our approach. This will be further elucidated in the discussion of this thesis in chapter 8.

References

- [1] R. M. Hardwick, E. Lesage, and R. C. Miall, "Cerebellar Transcranial Magnetic Stimulation: The Role of Coil Geometry and Tissue Depth," *Brain Stimul.*, vol. 7, no. 5, pp. 643–649, 2014.
- [2] I. Delvendahl, N. Gattinger, T. Berger, B. Gleich, H. R. Siebner, and V. Mall, "The role of pulse shape in motor cortex transcranial magnetic stimulation using full-sine stimuli," *PLoS One*, vol. 9, no. 12, pp. 1–22, 2014.
- [3] P. C. Miranda, M. Hallett, and P. J. Basser, "The electric field induced in the brain by magnetic stimulation: a 3-D finite-element analysis of the effect of tissue heterogeneity and anisotropy.," *IEEE Trans. Biomed. Eng.*, vol. 50, no. 9, pp. 1074–85, Sep. 2003.
- [4] M. De Lucia, G. J. M. Parker, K. Embleton, J. M. Newton, and V. Walsh, "Diffusion tensor MRI-based estimation of the influence of brain tissue anisotropy on the effects of transcranial magnetic stimulation.," *Neuroimage*, vol. 36, no. 4, pp. 1159–70, Jul. 2007.
- [5] P. Ravazzani, J. Ruohonen, F. Grandori, and G. Tognola, "Magnetic Stimulation of the Nervous System: Induced Electric Field in Unbounded, Semi-infinite, Spherical, and Cylindrical Media," vol. 24, pp. 606–616, 1996.
- [6] E. Ball, "Calculation of field from an arbitrary shape of coil by numerical vector integration," *Proc. Inst. Electr. Eng.*, vol. 122, no. 12, p. 1456, 1975.
- [7] EDWARD M. PURCELL, *Electricity and Magnetism (Berkeley Physics Course, Vol. 2) 2nd Edition*. 1985.
- [8] M. Carley, "Evaluation of Biot-Savart integrals on tetrahedral meshes," pp. 1–8, 2007.
- [9] A. Thielscher and T. Kammer, "Electric field properties of two commercial figure-8 coils in TMS: calculation of focality and efficiency.," *Clin. Neurophysiol.*, vol. 115, no. 7, pp. 1697–708, Jul. 2004.
- [10] A. Thielscher and T. Kammer, "Linking Physics with Physiology in TMS: A Sphere Field Model to Determine the Cortical Stimulation Site in TMS," *Neuroimage*, vol. 17, no. 3, pp. 1117–1130, Nov. 2002.
- [11] F. S. Salinas, J. L. Lancaster, and P. T. Fox, "Detailed 3D models of the induced electric field of transcranial magnetic stimulation coils.," *Phys. Med. Biol.*, vol. 52, no. 10, pp. 2879–2892, May 2007.

- [12] L. M. Koponen, J. O. Nieminen, T. P. Mutanen, M. Stenroos, and R. J. Ilmoniemi, "Coil optimisation for transcranial magnetic stimulation in realistic head geometry," *Brain Stimul.*, vol. 10, no. 4, pp. 795–805, 2017.
- [13] P. C. Miranda, *Physics of effects of transcranial brain stimulation*, 1st ed., vol. 116. Elsevier B.V., 2013.
- [14] R. Plonsey and D. B. Heppner, "Considerations of quasi-stationarity in electrophysiological systems," *Bull. Math. Biophys.*, vol. 29, no. 4, pp. 657–664, 1967.
- [15] T. a Wagner, M. Zahn, A. J. Grodzinsky, and A. Pascual-Leone, "Three-dimensional head model simulation of transcranial magnetic stimulation.," *IEEE Trans. Biomed. Eng.*, vol. 51, no. 9, pp. 1586–98, Sep. 2004.
- [16] T. Wagner *et al.*, "Impact of brain tissue filtering on neurostimulation fields: A modeling study," *Neuroimage*, vol. 85, no. 0 3, pp. 1048–1057, Jan. 2014.
- [17] R. M. Gulrajani, *Bioelectricity and Biomagnetism*. Wiley, 1998.
- [18] J. Shewchuk, "An introduction to the conjugate gradient method without the agonizing pain," 1994.
- [19] L. J. Gomez, M. Dannhauer, L. M. Koponen, and A. V. Peterchev, "Conditions for numerically accurate TMS electric field simulation," *Brain Stimul.*, vol. 13, no. 1, pp. 157–166, 2019.
- [20] D. H. Hubel and T. N. Wiesel, "Brain Mechanisms of Vision," *Sci. Am.*, vol. 241, no. 3, pp. 150–162, Sep. 1979.
- [21] M. Windhoff, A. Opitz, and A. Thielscher, "Electric field calculations in brain stimulation based on finite elements: an optimized processing pipeline for the generation and usage of accurate individual head models.," *Hum. Brain Mapp.*, vol. 34, no. 4, pp. 923–35, Apr. 2013.
- [22] J. P. Brasil-Neto, L. G. Cohen, M. Panizza, J. Nilsson, B. J. Roth, and M. Hallett, "Optimal focal transcranial magnetic activation of the human motor cortex: effects of coil orientation, shape of the induced current pulse, and stimulus intensity.," *Journal of clinical neurophysiology: official publication of the American Electroencephalographic Society*, vol. 9, no. 1. pp. 132–136, 1992.
- [23] T. Kammer, M. Vorwerk, and B. Herrmberger, "Anisotropy in the visual cortex investigated by neuronavigated transcranial magnetic stimulation," *Neuroimage*, vol. 36, no. 2, pp. 313–321, 2007.
- [24] P. T. Fox *et al.*, "Column-Based Model of Electric Field Excitation of Cerebral Cortex," *Hum. Brain Mapp.*, vol. 22, no. 1, pp. 1–14, 2004.

- [25] T. D. Krieg, F. S. Salinas, S. Narayana, P. T. Fox, and D. J. Mogul, "Computational and experimental analysis of TMS-induced electric field vectors critical to neuronal activation," *J. Neural Eng.*, vol. 12, no. 4, p. 046014, 2015.
- [26] T. D. Krieg, F. S. Salinas, S. Narayana, P. T. Fox, and D. J. Mogul, "PET-based confirmation of orientation sensitivity of TMS-induced cortical activation in humans," *Brain Stimul.*, vol. 6, no. 6, pp. 898–904, 2013.
- [27] A. Bungert, A. Antunes, S. Espenhahn, and A. Thielscher, "Where does TMS Stimulate the Motor Cortex? Combining Electrophysiological Measurements and Realistic Field Estimates to Reveal the Affected Cortex Position," *Cereb. Cortex*, no. September, pp. 1–12, 2016.
- [28] M. Hamada, J. M. Galea, V. Di Lazzaro, P. Mazzone, U. Ziemann, and J. C. Rothwell, "Two Distinct Interneuron Circuits in Human Motor Cortex Are Linked to Different Subsets of Physiological and Behavioral Plasticity," *J. Neurosci.*, vol. 34, no. 38, pp. 12837–12849, 2014.
- [29] R. Hannah and J. C. Rothwell, "Pulse Duration as Well as Current Direction Determines the Specificity of Transcranial Magnetic Stimulation of Motor Cortex during Contraction," *Brain Stimul.*, vol. 10, no. 1, pp. 106–115, 2017.
- [30] P. I. Petrov, S. Mandija, I. E. C. Sommer, C. A. T. van den Berg, and S. F. W. Neggers, "How much detail is needed in modeling a transcranial magnetic stimulation figure-8 coil: Measurements and brain simulations.," *PLoS One*, vol. 12, no. 6, p. e0178952, 2017.
- [31] R. Tremblay, S. Lee, and B. Rudy, "GABAergic Interneurons in the Neocortex: From Cellular Properties to Circuits," *Neuron*, vol. 91, no. 2, pp. 260–292, 2016.
- [32] T. Kammer, K. Puls, H. Strasburger, N. J. Hill, and F. a. Wichmann, "Transcranial magnetic stimulation in the visual system. I. The psychophysics of visual suppression," *Exp. Brain Res.*, vol. 160, no. 1, pp. 118–128, 2005.

Chapter III

How much detail is needed in modeling a transcranial magnetic stimulation figure-8 coil: measurements and brain simulations

Abstract

Despite TMS wide adoption, its spatial and temporal patterns of neuronal effects are not well understood. Although progress has been made in predicting induced currents in the brain using realistic finite element models (FEM), there is little consensus on how a magnetic field of a typical TMS coil should be modeled. Empirical validation of such models are limited **and** subject to several limitations.

We evaluate and empirically validate models of a figure-of-eight TMS coil that are commonly used in published modeling studies, of increasing complexity: simple circular coil model; coil with in-plane spiral winding turns; and finally one with stacked spiral winding turns. We will assess the electric fields induced by all 3 coil models in the motor cortex using a computer FEM model. Biot-Savart models of discretized wires were used to approximate the 3 coil models of increasing complexity. We use a tailored MR based phase mapping technique to get a full 3D validation of the incident magnetic field induced in a cylindrical phantom by our TMS coil. FEM based simulations on a meshed 3D brain model consisting of five tissues types were performed, using two orthogonal coil orientations.

Substantial differences in the induced currents are observed, both theoretically and empirically, between highly idealized coils and coils with correctly modeled spiral winding turns. Thickness of the coil winding turns affect minimally the induced electric field, and it does not influence the predicted activation.

TMS coil models used in FEM simulations should include in-plane coil geometry in order to make reliable predictions of the incident field. Modeling the in-plane coil geometry is important to correctly simulate the induced electric field and to correctly make reliable predictions of neuronal activation

Introduction

In neuroscience and medicine, Transcranial Magnetic Stimulation (TMS) is increasingly used to investigate brain function as well as for diagnostic and therapeutic purposes. During TMS administration a rapid, short-lasting magnetic field is generated which induces a relatively focal electric field in the cortex. Such externally induced electric field can cause depolarizations or hyperpolarization of the ion-channels in the cell membranes of cortical neurons, leading to alterations in neuronal activation or ultimately in neuronal plasticity. This is exploited in various ways both in research and in clinical settings to modulate human behavior, to diagnose and to treat conditions affecting the central nervous system [1].

However, the spatial and temporal pattern of the actual effect of a TMS pulse on the brain tissue is not well understood, let alone the ensuing changes in activity patterns of ensembles of neurons. The interaction of a rapidly changing magnetic field with the brain tissue is complex and depends on the exact cortical morphology, realistic tissue conductivity, and last but not least the exact geometry of the TMS coil and the current running through it.

The increasing adoption of TMS has recently inspired several groups to computationally evaluate the induced electric fields in the human brain [2,3]. A variety of computational models of TMS induced currents in the brain exists, such as Finite Element Modeling (FEM), Boundary Element Modeling (BEM) [4,5] and Impedance Methods (IM) [6]. The aforementioned studies focus on how different brain tissues, anisotropy and shape influence the induced electric fields. However, there is little consensus on the preferred method how to model the magnetic field of a typical TMS coil, which serves as an input to the just mentioned numerical methods. Approaches vary significantly from simple idealized coil models [3,6] to detailed models of realistic stacked coil winding turns [2,5]

One quite common approach towards modeling a typical TMS coil is to adopt simplified geometries in the form of idealized circular shapes (one per 'wing' in case of figure-of-8 coil). The idealized dipole models on a single layer disk [7], elliptic integration on a perfect circular contour [3] or piecewise Biot-Savart law integration over each line segment of a single circular thin wire [8] are just a few examples of such idealized coils. Others have experimented with more elaborate designs where the detailed geometrical properties of the coils are better captured. The Biot-Savart law, which provides the magnetic field around a straight wire piece, can be applied in

principle to any shape of packed coil winding turns. It was applied on a thin wire with elliptic geometry by [9], while [5] [10] additionally incorporated wire width, wire height and number of turns to model even more geometrically realistic coils. By improving the idealized dipole model of [7], a more detailed and better shaped dipole model was then proposed and adopted by Thielscher and colleagues [11,12] [2].

Although results from these studies show realistic currents patterns in the crowns and lips of the cortical gyri, they often lack direct empirical validation of the adopted coil models. This makes further predictions of ensuring neuronal activation rather problematic, since the reported results directly depend on the accuracy of the magnetic field predictions.

One exception is the work presented by Salinas et. al. [5]. They have not only looked at the discrepancy between simplistic and detailed coil geometries, for four commercially available coils, but also compared results against empirical measurements. Those measurements were conducted using field pickup coil probes and an oscilloscope, measured at a couple of control points. Their results show that differences between simplistic and detailed coil models diminish at distances of 3 cm or more away from the coil, while the biggest discrepancy of 32% can be observed close to the coil surface ($< 2\text{cm}$). They concluded that coil model details have a minor impact when TMS is applied on humans, but it might be rather significant when applied on small animals. They also highlight the need to further determine and evaluate the complete electric field.

An alternative approach to modeling a TMS coil is suggested by [13][14]. The proposed method of measuring, mapping and storing the magnetic vector potential in a data base circumvents the need of modeling the coil all together. The need of inner design knowledge for each coil type and manufacturer vanishes too. It can also be used for validating purposes in place of the MR imaging methods adopted in our study. One obvious advantage of our method is its non-invasive nature that would be beneficial in case of future in-vivo experiments with human subjects.

A previously demonstrated, MR measurements [15] [16] can be utilized to reconstruct the TMS magnetic field from the acquired phase maps [17]. Those studies serve as proof of concept, but lack either a realistic stimulator or/and coil, which is a major limitation when it comes to validation of TMS coil models (see section Material and Methods → Theoretical Background). We have developed a novel setup to allowing successful application of both a real TMS stimulator and TMS coil inside a clinical 3T MR scanner [18].

We consider three distinct models to represent a typical figure-of-8 TMS coil. We start with the arguably the most often adopted in common literature model, the single loop of thin wire with the outer most radius for each wing. Then we gradually introduce more geometrical detail to such an idealized model to better match its geometry to the shape of the physical coil. The second model consist of several spiral winding turns and the third one has a few stacked layers of the same spiral windings. We adopt BiotSavart integration to numerically predict the induced magnetic field of each model and we compare it against MR field measurements. The focus of our study is not to find the most accurate model for a given TMS coil but rather to assess the validity of geometric approximation used in published TMS literature, most notably the very simplistic in our opinion coil, where each wing is modeled using only a single wire/winding turn.

To estimate the relevance of detailed TMS coil modeling for actual brain stimulation , we extrapolate the predictions of the three coil models to the human brain. In particular, we focus our attention on a small cortical patch in the motor cortex near M1 (the 'hand knob' area) using FEM. We devise a simple metric to quantify potential differences in prediction of cortical excitation for each of the coil models. These simulations should allow one to relate our findings on appropriate TMS coil models to actual brain stimulation experiments, as one will have a simple scalar 'activation' measure per coil model to compare between coil models.

This exploration can offer guidance for realistic TMS induced current simulations in a human brain that are increasingly suggested to have the potential to improve TMS treatment planning [19,20]. Unraveling the influence of the TMS coil model may help to bring TMS models into clinical practice.

Materials and Methods

In the sections below we present the 3 different coil models of increasing geometric complexity that we investigate, the most detailed being close to an actual MR safe TMS figure-of-8 coil. Next, we will describe how the Biot-Savart method is implemented and proceed with the empirical validation of the predicted fields by comparing the simulated against the measured TMS induced magnetic field. Finally we describe simulations of the electric fields induced by the coil models on a realistic human brain model. This will allow us to assess the impact of each model in a more realistic context where we look to quantify the potential of neuronal activation.

We investigated three different figure-of-8 coil models of increasing complexity. Coil BSM-811 is the most trivial of all, a single layer with two circular loops of a single wire with opposite currents running in each. Then coil BSM-819 is a more elaborated coil, a single layer of nine spiral winding turns per coil wing. Finally, the most complex coil BSM-879 constitutes of seven layers each having nine spiral winding turns per coil wing. Here, BSM stands for Biot-Savart-Method and 8 refers to the general geometric shape of what we refer to as a typical figure-of-8 TMS coil. See Fig.3A for an overview of the three coil models.

We developed in-house a few additional modules to SCIRun 4.7 (A Scientific Computing Problem Solving Environment (Scientific Computing and Imaging Institute (SCI), Utah, USA)). The following modules were introduced to generate the geometry for each model: Modules → TMS → ModelTMSCoilSimple for coil model BSM-811; Modules → TMS → ModelTMSCoilSpiral for coil models BSM-819 and BSM-879. The underlying algorithm for both modules is unified, implemented as half circle generator of points (mesh nodes) in the range $0-\pi$ with angular step equal to the range / #elements (number of segments Table 1) at offset R from the origin. The spiral shape of BSM-819/879 was realized simply as half-circles with planar (x-axis) offset of the origin and radius, $R_n + dr/2 = R_{n+1}$ and $O_n + dr/2 = O_{n+1}$ where $dr = (R_{outer} - R_{inner} / \# \text{winding turns})$ and n is winding index. The amount of current in the wire is provided explicitly and assigned on each element of the wire mesh (segment) as a scalar value [+/-]. To compute numerically the induced magnetic fields in accordance to the Biot-Savart formulation (see eqs 2 and 3) we introduced one final module to SCIRun, Modules → Math → SolveBiotSavartContour, when provided with a SCIRun mesh of type 'curve-mesh' it iterates over each segment and accumulate the contribution on each to the final field in discrete steps interpolated along n to n+1 nodes (see Table 1 integration step). It treats negative sign for the current as a hint to reverse the direction of integration on each segment, causing a flip in interpolation from n+1 to n. This last addition conveniently helps in composing wire segments independent of topology (order of segments/nodes in the mesh) thus making the job of the generator-modules more trivial.

The source code for the additional modules that we developed in-house for this study is available online at:

<https://github.com/pip010/scirun4plus/releases/tag/v4.7.2>

DOI: 10.5281/zenodo.160114

Table 1. Geometrical details of the three modeled coils.

Coil Type	Segments Per Wing	Integration Step	Radius Innermost Winding	Radius Outermost Winding	Outer Interwings Distance	#Layers	#Winding turns
BSM-811	92	0.025 mm	44 mm	44 mm	2 mm	1	1
BSM-819	763	0.012 mm	26 mm	44 mm	2 mm	1	9
BSM-879	5341	0.04 mm	26 mm	44 mm	2 mm	7	9

Overview of the three coil models, geometrical dimensions and additional modeling details.

Theoretical background

The E-field produced by a TMS machine has a primary and secondary component[3]. The primary component \vec{E}_p arise from the TMS coil magnetic vector potential \vec{A} , which solely dependent on the coil geometry, inductance and pulse shape. The secondary component \vec{E}_s is related to the gradient of the scalar potential of the volumetric conductive medium Φ , which contains the portion of the electric field actually linked to the resistive brain tissues. This latter electric field can be related to charge accumulation at tissue boundaries caused by gradients in the electric tissue conductivity. Under the quasi-static approximation the total electric field \vec{E}_t induced by TMS is given in eq. 1.

$$\vec{E}_t = \vec{E}_p + \vec{E}_s = -\frac{\partial \vec{A}}{\partial t} - \nabla \Phi \quad (1)$$

To numerically evaluate the magnetic vector potential we used the Biot-Savart formulation, which gives the magnetic field distribution around a current flowing through a wire segment dl at a distance r-r₀ away, where r >> dl .

$$A(\vec{r}) = \frac{I \mu_0 w}{4 \pi} \int \frac{\partial l}{|\vec{r} - \vec{r}_0|} \quad (2)$$

Here w is a scalar weighting factor specific for each coil model (reported in Table 2) and μ_0 is magnetic permeability of free space at a distance r from the source. The total vector potential field is used as input to our FEM simulation to derive the

approximate solution for \vec{E}_s in eq. 1 (see section 'Human Brain Simulation' subsection 'Finite Element Simulation').

The piecewise Biot-Savart method we adopt to compute the magnetic field of our coil models is as follows:

$$B(\vec{r}) = \frac{I\mu_0 w}{4\pi} \int \frac{\partial l \times \vec{r}}{|\vec{r} - \vec{r}_0|^3} \quad (3)$$

Equation 3 was used to compute the magnetic field for all three coil models. Only the magnetic field was considered for validation purpose (see section 'empirical validation of coil models').

The integral in eq. 2 and eq. 3 was approximated via step summation over discrete line segments, what we refer to as integration step is the uniform length taken along each segment. In order to eliminate any significant variation due to numerical computational inaccuracy we performed a tuning procedure to determine the maximal accepted integration step. The magnetic field is well known anywhere along the mid-line passing through the center of perfectly shaped circular wire according to the following analytical formula:

$\vec{B} = \frac{I\mu_0}{2\sqrt{(R^2/Z^2 + R^2)^3}}$, where I is the delivered current, R is the radius of the circular coil, Z is an offset along its central/middle axis. For a single circular coil of radius 44mm composed of 64 segments we kept the error within 1% at a distance of 1 cm from its center. The adopted integration step for each of the three coil models is reported in Table 1.

The TMS stimulator we used in the validation experiments produces a short 0.4 ms bipolar pulse (5 KHz ,0.2 ms per cycle see Fig. 2 A. For 100% MO (machine output) , the peak current and voltage amounts to 5500 A and 1650 V respectively, as reported by manufacturer.

Since the readings of our experimental setup are based on MR phase accumulation images and the result will depend on the reconstruction procedure it is important to clarify key aspects first. The recordings are MR phase images in the interval +/- π per pixel. Those raw images were then post-processed through unwrapping algorithm. The resulting phase patterns represent the net (time average

over the TMS pulse) MR phase contribution. In theory, if the bipolar TMS current running in the coil would have the same amplitude and duration for both the current polarities, the total MR phase contribution would be zero. In practice, however, since the current running in the TMS coil is a damped bipolar pulse, the phase contribution given by the first current polarity is not fully compensated by the phase contribution of the second current polarity, thus leading to a measurable MR signal. In principle, the same phase contribution can be given by a static DC current running in the TMS coil for the same duration as the actual bipolar TMS current. We call this DC current as equivalent TMS current.

To approximate the TMS pulse to its equivalent DC current, we calculated the time averaged integral of the current shape normalized to 1% MO , see Fig. 1 B. For each coil model, the obtained values of DC current used to compute both the incident magnetic field and magnetic vector potential is reported in Table 2. We choose 1% MO to avoid image artifacts (signal loss due to excessive intra-voxel dephasing) near the coil during the MRI measurements [18].

Table 2. Coil current values used in simulation.

Coil Type	Phantom Experiment (1% MO)	Human FEM Model (70% MO)	Current Distribution Factor (w)
BSM-811	25032 [mA]	288.75 E10 ⁶ [A]	* 7
BSM-819	3576 [mA]	38.5 E10 ⁶ [A]	* 1
BSM-879	511 [mA]	5.5 E10 ⁶ [A]	/ 7

Currents used for each coil model for both empirical phantom experiments and the human FEM simulation

The current distribution factor is a compensation factor to the net current provided for each model to account for any discrepancy due to pure geometrical differences between the three coil models. For example coil BSM-819 is considered closest to the real geometry of the actual physical coil, nine winding turns of thin wire for each wing,,where the current for coil BSM-811 is 7 times the one for BSM-819, roughly equal to the ratio in the wire length between the two models. Finally, for coil BSM-879 the current is split equally among each of the seven layers.

To compute the secondary electric field induced in brain tissues during a TMS experiment, i.e. the field produced by the charge accumulation at tissue boundaries, the input to drive the FEM simulations should be the maximum dI/dt . This ratio refers to the first half frame of the current shape in Fig. 1 B. Considering a typical MO for TMS experiments of 70%, the maximum dI/dt in our case will be 38.5×10^6 A/s. This value is in line with reported in literature values for 100% MO [21,22].

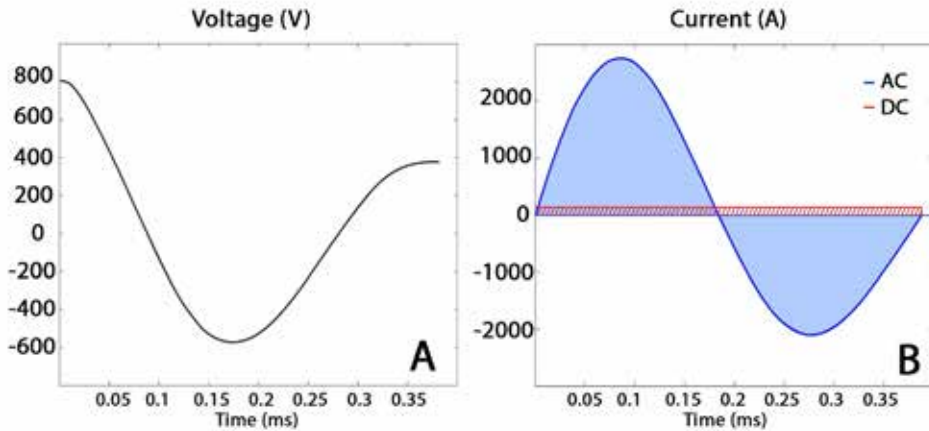


Figure 1. Coil current approximation.

On the left (Fig 1A) is shown the plot of the electric field of the coil, while on the right (Fig 1B) it is shown the resulting current profile. The DC approximation in red (shaded area) Fig 1B. Both subplots are idealized and given for 50% machine power.

Empirical validation of the coil models

In order to empirically validate the three coil models, we performed MR-based measurements. First, we introduce the apparatus adopted for the experiment. Then, we describe the MR acquisition protocol and data processing.

Apparatus

Experimental measurements were conducted inside a 3T MR scanner (Achieva, Philips Medical Systems, Best, The Netherlands). For TMS administration, we used the Magstim Rapid 2 TMS stimulator (MagStim, Whitland, UK) connected to an MR compatible TMS coil with ceramic casing. For all details of this setup see a previous report from our group [23]. Measurements were conducted on an agar

phantom (diameter 12.5 cm, height 20 cm filled with a solution of Agar 20 gr/L and NaCl 9.5 gr/L: conductivity 1.6 S/m at room temperature of 23° C and frequency 128 MHz). This phantom was placed into a custom built holder that allowed additional positioning of the TMS coil and MR elliptical surface coils (flex-L and flex-M) for signal reception.

To make the TMS coil visible in the acquired images, twelve additional markers filled with tap water were fixed on the posterior coil surface.

MRI acquisition and data analysis

For the purpose of TMS magnetic field mapping, a single echo Spin Echo sequence was performed, using the body coil in transmit and the MR-flex coils in receive mode. For this measurement the parameters were: repetition time TR = 1 s, echo time TE = 20 ms, field of view FOV = 160x160x2 mm³, voxel resolution RES = 1x1x2 mm³. The relative position of the TMS coil with respect to the phantom is depicted in Fig. 2.

By subtracting two phase images acquired with and without applying TMS pulses, it is possible to isolate the TMS contribution to the phase accumulation [18]. Due to the direct relationship between phase accumulation and the incident TMS magnetic field[15], it was possible to retrieve the TMS incident magnetic field. However, these maps reflect only the z-component of the total magnetic field. This is because, in an MR experiment, only the magnetic field component parallel to the main static magnetic field B₀ is measurable.

To reconstruct in simulation the position of the TMS coil with respect to the phantom, a reference T2 weighted turbo spin echo map of the phantom and the TMS coil was acquired : TR= 11 s, TE = 80 ms, FOV = 240x240x210 mm³, and RES = 1.5x1.5x3 mm³. Then we used a commercially available stereotactic navigation system “The Neural Navigator” (www.neuralnavigator.com, by Brain Science Tools BV, The Netherlands) to co-register the coil position and orientation from MR world space to simulation world space. The process involves capturing the position of several fluid capsules affixed on the coil casing, using 3D digitizing hardware. Those positions were then mapped to the location of the visible capsules in T2 MRI space via point cloud algorithm [24]. We achieved 1 mm precision for position and up to 4 degree precision for orientation. To compensate for the thickness of the coil case, a rigid body translation of 15 mm was applied as the last step. Further details on the coil position reconstruction method and precision can be found in an earlier paper of our group using the same method [23].

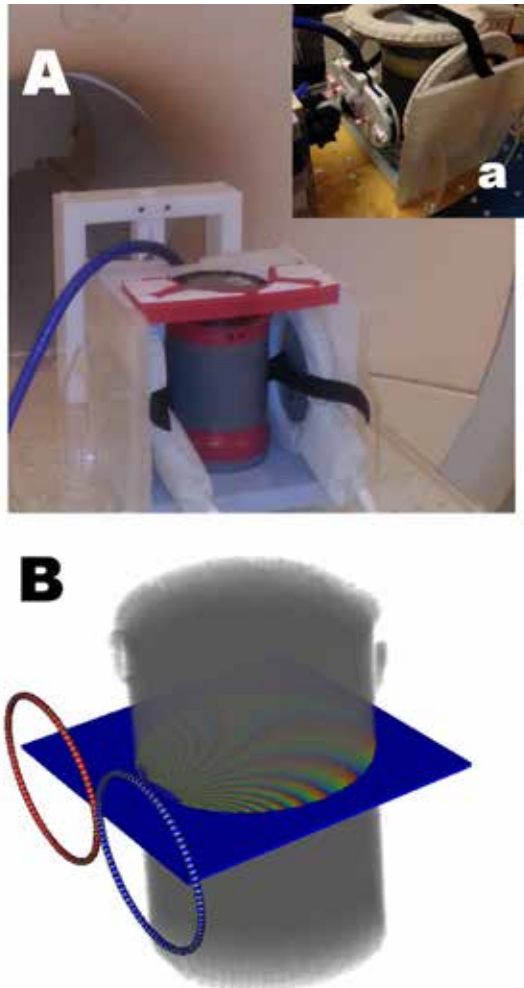


Figure 2. Experimental and virtual setup.

On top (Fig 2A) photo of physical phantom; holder; MR flex coils. Fig 2Aa, top right, the actual TMS figure-of-8 coil with capsules visible in red. On bottom (Fig 2B) is shown a visualization of the phantom T2, coil model BSM-811 as well as a single slice of MR phase accumulation measurements.

Human Brain Simulation

This study directly validates several models of increasing geometrical detail and complexity of the figure-of-8 TMS coil using MR techniques. However, to allow readers to interpret the differences between coil models for their actual brain stimulation experiments, we need to evaluate the electric field evoked by each model and how it interacts with brain regions of interest. In order to assess the consequences of TMS coil model detail for use in planning actual brain stimulation, we used a finite element model (FEM) of the human head. We estimated the electric field flux through a small region in the motor cortex. Finally, we adopt a crude metric for evoked brain stimulation, that takes into account individual cortical folding patterns.

This simulation is relevant for real TMS applications, as so called motor evoked potentials (MEPs), an electromyographic recording of the motor cortex response coming from the thumb muscle shortly after a TMS pulse, are commonly measured to assess motor cortical excitability in different forms and shapes. MEPs are known to be altered in several diseases affecting the central nervous system and investigated for potential diagnostic use. For an overview see [25].

This extrapolation of our findings to the human brain will allow researchers and computational modelers to get an idea how TMS coil model detail affects predictions in realistic situations, which in the future could allow for more accurate dosimetry. Below, we evaluate the simulation of the induced activation for the thumb area in the human motor cortex (M1).

Human Head Model

We used a 3D tetrahedral mesh of a real human head, that was previously reported in literature [26], to explore the expected effect of TMS. The mesh consists of 480,316 nodes and 2,785,034 elements. Generally the more nodes a model has the higher the numerical accuracy is and the more elements a model has the better the representation of the underlying structure is. The brain mesh is partitioned in 5 compartments : Scalp, Skull, CSF (Cerebral Spinal Fluid), GM (Cortical Gray Matter),

WM (Cortical White Matter). The following isotropic conductivity values were adopted for each tissue type: Scalp = 0.5 S/m; Skull = 0.02 S/m; CSF = 1.6 S/m; GM = 0.3 S/m and WM = 0.25 S/m, within average of reported values [21].

The CSF ↔ GM boundary surface is the most significant interface to consider when trying to evaluate the cortical effects of TMS [27]. The head model we employ has a relatively high quality GM outer surface with well conforming anatomically shape, see figure 3.

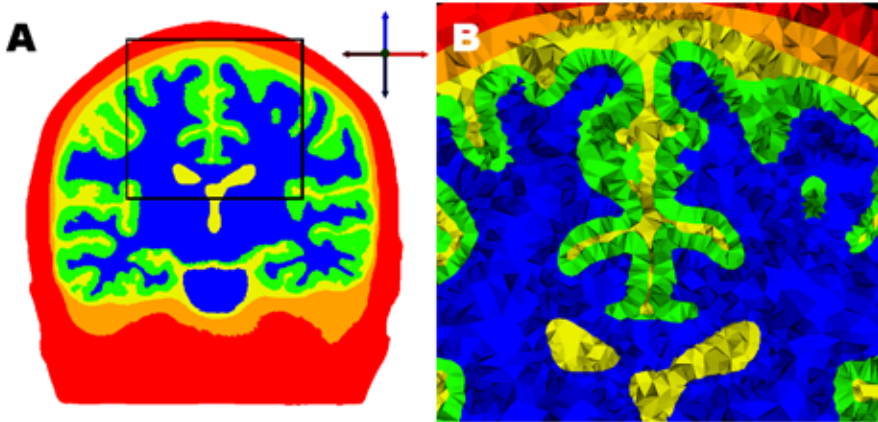


Figure 3. Volumetric tetrahedral mesh of the human head (FEM) model.

On the left (Fig 3A) a mid-coronal slice with well conforming to anatomy boundaries for each tissue. On the right (Fig 3B) a closer view of 3A, the black sided rectangle in Fig 3A, where individual pyramidal shapes for each tetrahedron are easy to discern.

Finite element simulation

The FEM calculations were carried out using version 4.7 of SCIRun: A Scientific Computing Problem Solving Environment (Scientific Computing and Imaging Institute (SCI), Utah, USA).

We used the SCIRun Math → SolveLinearSystem module with Jacobi preconditioner and the gradient bi-conjugate algorithm selected as solver with terminating residual target error RMS (Root Mean Square) set to 10^{-4} .

Two boundary conditions and one global requirement were imposed:

- The Neumann's boundary condition $\vec{J} \cdot \vec{n} = 0$ so no current leaves the head;
- The induced current density is continuous and obey flow property throughout the domain $\vec{J}_1 \cdot \vec{n}_1 = \vec{J}_2 \cdot \vec{n}_2$
- In the quasi-static limit the divergence of the current density to be zero $\nabla \cdot \vec{J} = 0$

Here J denotes the current density through a boundary element surface (triangle) having a normal n .

The solution of the FEM solver was the scalar potentials distribution. The gradient of the scalar potential produces the secondary in accordance with Eq. 1. Summed together with the time varying contribution of the magnetic vector potential it produces the total electric field E_t from Eq. 1.

Cortical Region of Interest (ROI)

To assess 'activation' in the brain resulting from TMS induced currents, we choose a region of interest (ROI) around M1 in the so called 'hand knob', the area in the motor cortex controlling the thumb. This region was manually drawn using MRICron (<http://www.nitrc.org/projects/mricron/>). The binary mask containing the ROI was fitted from the 1mm isotropic voxel grid onto the polygonal mesh building gray matter in our tetrahedral head model. Since we decided to focus only on the CSF \leftrightarrow GM boundary interface the procedure results in a small polygonal patch consisting of ~ 500 triangle faces, spanning an area of $\sim 4.5 \text{ cm}^2$. See Fig.7 A for the ROI rendered on top of the gray matter. The final value of the E-field for each polygon on the patch were extracted via linear interpolation from the tetrahedral mesh.

We decided to explore two orthogonal orientations of the TMS coil with respect to the central sulcus around M1, as it is known that MEPs are depending on the direction of induced current (which roughly runs parallel to the coil handle) with respect to the underlying central sulcus orientation [28]. An orientation parallel and orthogonal to the central sulcus near M1 were chosen to maximize the effect of coil orientation (responses are expected to be smallest for parallel orientations, see [1] for an overview). Our motivation for picking two orientation is not to study the effect of coil-orientation in general but rather to eliminate the coil orientation factor when drawing conclusions to our results.

The geometrical center of the surface of the modeled coils was positioned at a distance of 2 cm away from the GM surface. Besides visual inspection no additional aid was used for coil guidance and placement.

Cortical Evaluation Metric

We also take into account how the electric field induced by TMS interacts with neurons in the cortical layers, in a simplified scheme, and compare a metric (see below) of the resulting net electric field through the 'hand knob' between the two aforementioned orthogonal coil orientations for the 3 coil models.

As it is generally assumed [1] that pyramidal cells with their axons oriented orthogonally to the cortical layers are the main responders to TMS induced currents. We assumed that currents orthogonal to the cortical layers have a maximal effect, and currents parallel to it a minimal effect on an infinitesimally small surface patch. We hence devised a simple but physiologically plausible metric to evaluate the difference in potential for neuronal activation for each of the proposed coil models.

$$\vec{E}_c = \sum_{i=0}^M S_i |\vec{E}t_i \cdot \vec{n}_i| \quad (4)$$

The metric given in Eq. 4 accounts for the angle between the total electric field E_t and the normal n on each surface triangle of the patch (M number of triangles) weighted by its area S . Equation 4 will effectively favor electric field vectors perpendicular to the gray matter surface rather than parallel ones. Such an approach is motivated by the anatomical structure of the cortical layers, where axons of pyramidal neurons, running mostly perpendicular to the pial surface are assumed to pick up most of the induced current induced in the cortex [1]. Similar metric was proposed previously by Fox and colleagues [29], the cortical column cosine (C^3) model, that claims to be able to estimate effective stimulating electric field for TMS [30][31]. However, in addition we normalize the electric field by the are for each triangle to capture the electric field flux through the patch.

Importantly, we want to clarify that the purpose of using our formulation of the C^3 metric as given in (4) is not to construct the best model for local electric activation of

neuronal tissue by induced E-fields in all possible detail, or to validate such a model. The rather crude C^3 metric does not reflect details regarding electro-physiological processes on the cell membrane, pre- and post-synaptic hyper- and depolarization, inter- and into cortical layer connections etc. Work adequately modeling the interaction of \vec{B} and \vec{E} fields at this microscopic level is published elsewhere Rahman et al [32], for an overview, see De Berker et al [33]. Still, there is ample evidence that metrics like C^3 approximate macroscopic TMS evoked activation quite well at the neuronal level [29–31] as well as at the EMG and behavioral level Kammer et al [34].

Results

MRI field measurements

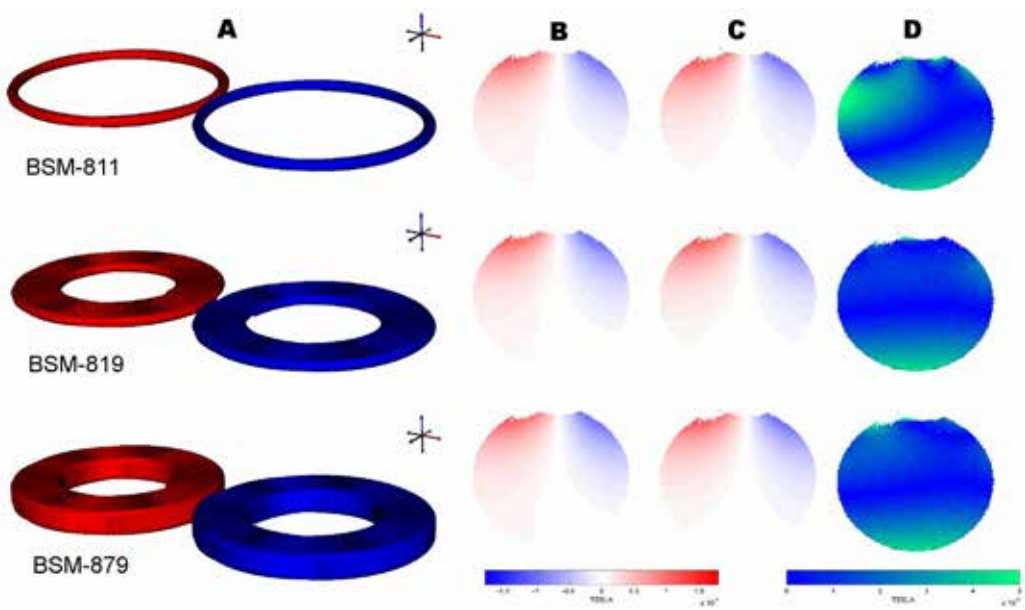


Figure 4. The three coil models and the empirical results.

From top to bottom BSM-811, BSM-819 and BSM-879 : Fig. 4A the 3D models of the three coils under investigation. Fig. 4B shows the B_z results, coming from MR measurements (all slices are the same). Fig. 4C shows the B_z results, coming from computer simulations. Finally, Fig. 4D gives the AD (absolute difference) metric for each coil model, between MR measurements (Fig. 4B) and numeric calculations (Fig.

4C). The slice views (Fig. 4 B, C and D) correspond to the 1mm thick slice depicted in Fig. 2B .

From Fig. 4 B one can observe the raw Bz measurements from the scanner and compare it to each of the 3 coil models. Note that Bz refers to the z component of the full magnetic vector field \mathbf{B} . In the same image we provide the absolute difference $AD = |B_z^{MRI} - B_z^{FEM}|$ of the same Bz field, between all coil models and the reference MRI measurement. For a distance of more than 8 cm away from the coil, the noise level becomes dominant. This is due to the low 1% machine power we employ for the empirical experiments.

Even at such low machine power and 1 mm in-plane scan resolution some signal is lost at 2cm or closer from the coil center (top view of slices in fig 4 B). Such signal drop-out is due to over-phasing of more than $\pm\pi$. This effectively increased the distance at which we were able to measure from 2.0 to 2.4 - 2.5 cm away from the coil. Nevertheless some spatial discrepancy between the simple, idealized BSM-811 coil and the more detailed BSM-819 and BSM-879 are still visible and easy to distinguish. Clear regions of over and under estimation of the simulated Bz for the BSM-811 exists in contrast to BSM-819 which has consistent error distribution (smooth gradient of the AD error metric in Fig. 4), while BSM-879 pattern was still better than BSM-811 do exhibit slight inconsistency compared to BSM-819. The relative error is hardly spatially consistent, it roughly equated to about 4-10% for BSM-811 and 1-5% for BSM-819.

Overall the difference between the three coils, Bz measurement, seems quite small judging from the graphs in Fig 5, that gives us the 1D profile along the dotted line in Fig.4, situated at a distance of 4cm away from the coil. Nevertheless, the trend that BSM-811 deviates most from measurements remains the same.

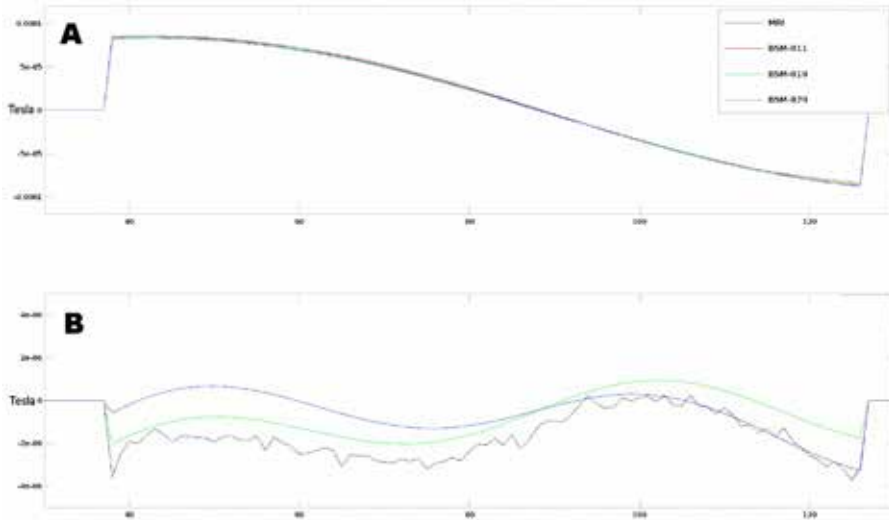


Figure 5. Plot of Bz field at distance 4cm away from the coil.

On top Fig. 5A absolute value of the measured magnetic field in the MRI and the predicted values for all three coil models. On bottom Fig. 5B The value of BSM-811 used as a baseline; MRI measures, BSM-819 and BSM-879 prediction relative to the baseline.

Cortical stimulation

On the left an overview image of the coil, the cortical gray matter sheet, semi-transparent skin rendering. On the right a close-up view (zoom-in) of the area just under the coil (M1 moto-cortex gyrus). Fig 6A coil model BSM-811 orthogonal to the M1 gyrus. Fig 6B coil model BSM-819 orthogonal to the M1 gyrus. Fig 6C coil model BSM-811 parallel to the M1 gyrus. Fig 6D coil model BSM-819 parallel to the M1 gyrus.

In Fig. 6 the cortical surface and induced E-field is shown for the simple coil BSM-811 and coil with realistic spiral winding turns BSM-819, for the direction of induced current parallel and orthogonal to the central sulcus.

The three models produce visually similar shape and magnitude of the total electric field E_t (eq 1). Only the single circular loop coil has a clear overestimation of the peak area under the coil, while the results from the detailed (spiral geometry) models are indistinguishable from each other. Those observation are in accordance

with the results from the empirical experiment conducted on the phantom at distance of ~ 3 cm and evaluated on the B_z field. The discrepancy between the predicted E_t field of (BSM-811) and (BSM-819) in the 'hot-spot' area under the coil is further amplified (15-20 % Relative Difference) at a distance of ~ 2 cm from the coil, see E_t on the cortical GM surface Fig. 6 and E_t on the small ROI patch (M1 hand knob area) Fig. 7.

More interestingly, however, once we carry E_t to our custom cortical evaluation metric E_c (eq. 4) we can see a relative difference of around 15% between the simple and more complex coil geometries in Fig. 7. The relative difference between BSM-811 and BSM-819 are 12.8% and 15.4% for the orthogonal and parallel orientation respectively. The results for BSM-879 are almost identical to the ones for BSM-819. The observed 15% relative difference between the simplified and the more complex geometries is consistent among both orientations. The relative difference of the reported metric for the two different orientations is around 33%, results are in accordance with other studies [19,35].

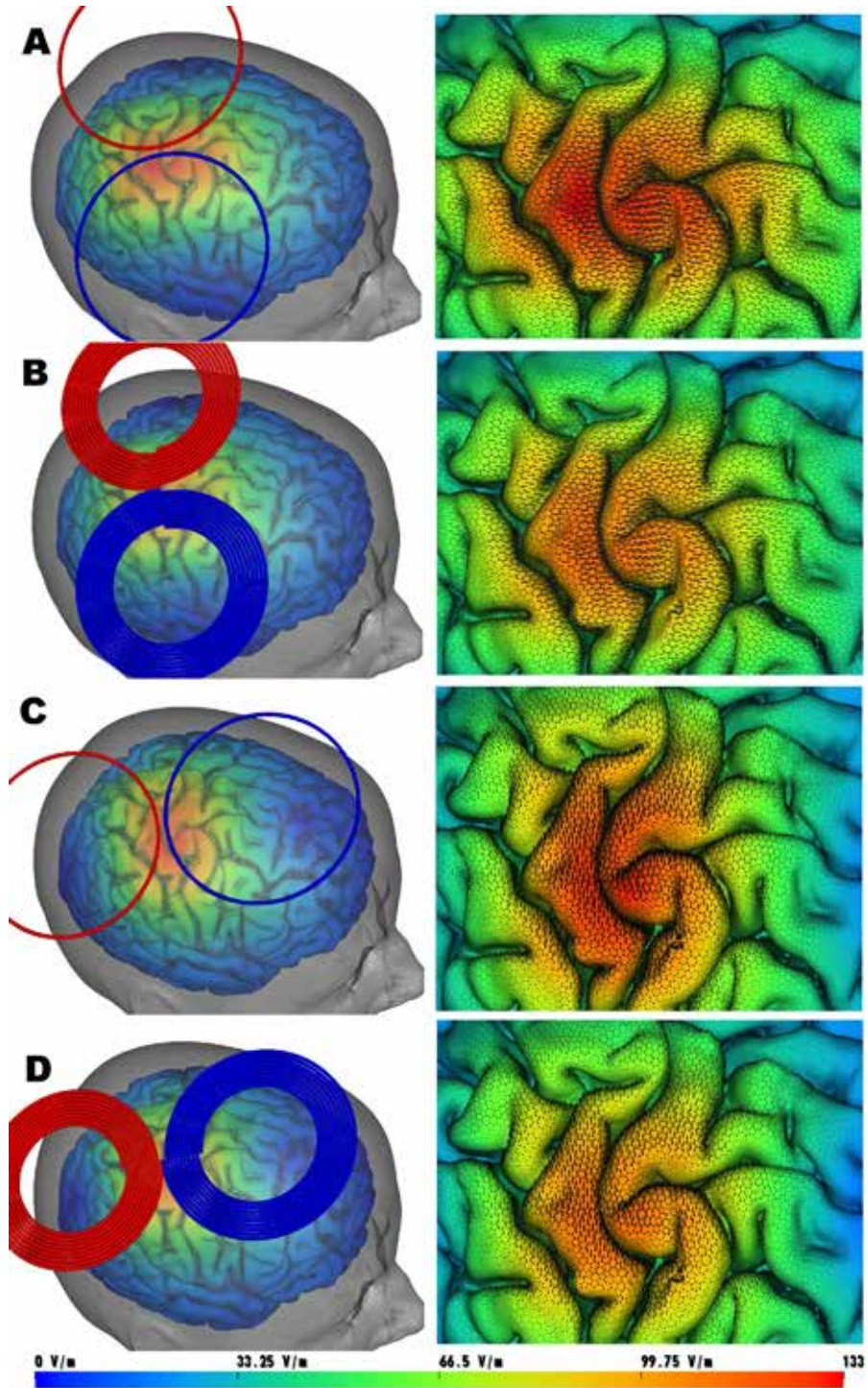


Figure 6. Total electric field results from FEM.

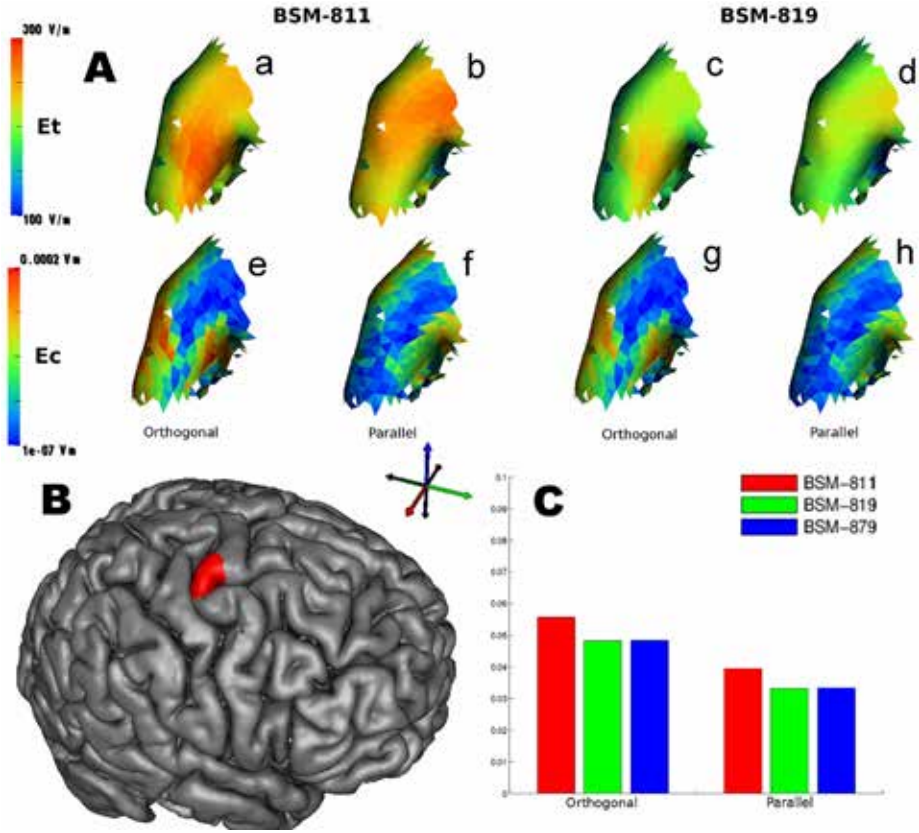


Figure 7. Results for the electric field(s) inside our ROI.

On top (Fig 7A) shows the total electric field (E_t) and custom electric field (E_c) metrics on our ROI patch for the simple coil BSM-811 and the spiral coil BSM-819 for the two primary orientations (parallel and orthogonal to M1 gyrus surface).

Fig 7A top row (abcd) is showing the total electric field \vec{E}_t and bottom row (efgh) is our custom electric field metric \vec{E}_c . On (Fig 7A) left half (abef) is for coil BSM-811 while the right half (cdgh) is for coil BSM-819. The two orientations are shown interleaved for each column of Fig 7A: (ae) is orthogonal; (bf) is parallel; (cg) is orthogonal; (dh) is parallel. On bottom left (Fig 7B) Gray Matter Cortex surface rendering with ROI patch colored in red. On bottom right (Fig 7C) bar-plot of our custom electric field metric \vec{E}_c for all three coils and the two orientations.

Discussion

In this study, we compared simulations to MR measurements of the magnetic field produced by a realistic figure-of-8 TMS coil using a real TMS stimulator and pulse shape. Three different coil models with increasing geometric complexity were considered. The 3 coil models were a simple circular pair of coils consisting of one winding, a spiraling wire per coil 'wing' with realistic dimensions and a coil model consisting of spiraling stacked wires to emulate the thickness of the wire packs. We observed that in the region where neurostimulation usually takes place (about 2.5 cm below the coil center), both spiraling wire coil models best predicted the actual field (RE < 5%). Instead the single circular wire coil deviated from MR measurements up to 10% RE. The difference in prediction quality between the thin and the stacked spiraling coil models was negligible.

One of the main challenges we faced was due to intrinsic limitations of the hardware we used to conduct the empirical work we presented so far. In particular, our ambition to position the coil as close as possible to the phantom while maintaining realistic machine power output were in conflict. The strong magnetic field produced just under the coil focal point causes signal dephasing that results in image loss. The effect is voxel-size dependent. Therefore, an increase of the imaging resolution can reduce the extend of the region where signal loss is observed, however at the cost of significantly longer scan time [18].

Furthermore, by using computational modeling we estimated what the net induced E-field of these 3 coil models would be on a patch of motor cortex of a typical brain, corresponding to the 'thumb area', using two orthogonal coil orientations and FEM simulations of a detailed volumetric description of brain tissues. The metric to compute 'neurostimulation' was chosen such that it reflects properties of neurons in the cortical gray matter sheet: the E-field angle with respect to the cortical surface was taken into account such that perpendicular fields lead to maximal stimulation. It was observed that both spiraling coil models had yielded a value of this net field measure that was nearly identical, whereas the idealized circular coil model deviated significantly. Also, realistic effects of TMS coil angle with respect to central sulcus could be reproduced.

We acknowledge the fact that our approach towards modeling a realistic TMS coil, which is characterized by having more complex geometry, can be further improved by incorporating more elaborated current distribution schemes [7] [12]. Instead, we decided to split equally the current between each winding of the spiral coil

as well as each layer of the stacked spiral coil. While this had no influence on the results from our empirical magnetic field measurements it might have underestimated the focality of these two coils in the reported results from the numerical electric field calculations.

Our results help to predict and optimize TMS effects quantitatively, before an actual stimulus is delivered. Given the increasingly important place of TMS in clinical practice [36], such models are needed to accurately deliver TMS induced currents in the desired brain region at the desired dose. Currently, few guidance exists in how detailed the computational model of the TMS coil itself needs to be. Our results clearly demonstrate that a significantly different outcome is achieved when increasing coil detail is taken into account.

The results presented here are among the very few reports of empirical validation of a realistic figure-of-8 coil used for TMS of the human brain. Although the particular coil we investigated is specifically designed to withstand large magnetic fields and comply with MR safety protocols, the only substantial difference we observed from other figure-of-8 coils reported in literature were the ceramic filled casing and the slightly more densely packed wires. Neither of these preclude cross-comparison of other coils to our empirical field measurements.

Similarly to the work by Salinas and colleagues [5], our analysis of the results from the magnetic field measurement demonstrated that the coil geometrical details play a minor role at distances further than 3 cm away from it. Unlike Salinas and colleagues, we observed that the surface area of the coil is the dominant geometrical feature contributing to the discrepancy between simplified (idealistic) and detailed (realistic) models. Salinas and colleagues, however, suggested that wire height (coil depth) rather than wire width (winding turns) is the key differentiating factor. This can be explained by differences in methodology, e.g. our 1x1 mm planar field measurement versus the sampled regularly 5mm hotspot pickup-coil measurements, or the fact they evaluate the E-field while we measure B-field only. It has been suggested [5] that the full electric field, together with secondary effects [10], needs to be considered first before drawing any conclusions in the context of human TMS. We did so using FEM simulation on a realistic human head model with a coil at a distance of 2cm away from the GM cortex. The discrepancy between the simple circular coil versus the detailed spiral coil were exaggerated further by numerical derivation of the complete E-field.

In most previous related TMS studies, when adopting the simplistic circular loop approach towards modeling a figure-of-8 shaped coil, researchers have opted for a

variant of Eqs 2 and 3 where the current through the coil is weighted N times, where N is the number of winding turns. Such an approach additionally contributes to the perceived difference between simplistic and detailed models. In our particular case using 9 (for the number of winding turns) instead of 7 (the ratio in wire length) would have resulted in additional $\sim 23\%$ relative error in approximating the amount of current running through single circular loop coils.

Peres and colleagues [16] also attempted to map the magnetic field of a realistic TMS coil inside an MRI bore, as reported in a conference proceeding. Although that abstract shows that in principle it is possible to map the induced magnetic field with an MR scanner, they did not compare their measurements with a model to assess the validity of both measurements and model. Furthermore, an important limitation of their work is that they were not able, due to technical limitations of their setup, to stimulate with the actual TMS stimulator, but used batteries with direct current (DC) instead. It is therefore hard to evaluate how valid their observations are for estimating the induced field by real TMS coils attached to a real TMS stimulator. With our approach [18], it is possible to stimulate the TMS coil inside a 3T MRI scanner using a real TMS stimulator and a realistic pulse shape, albeit only at low intensities. Although MR phase mapping of a TMS coil is not entirely new, using a real stimulator instead of a battery or other artificial source, also tests assumptions about the temporal characteristics: the assumption that the net DC current under our model biphasic pulse shape is equivalent to induced phase difference is also validated at the same time. In theory discrepancies could have arisen here due to dynamic pulse shape fluctuations might lead to deviating phases, but obviously this did not play a big role.

Our results from the empirical coil validation indicated that at least a coil geometry using spiral winding turns should be used to accurately approximate the induced B-field of a typical TMS coil. However, TMS users generally aim to influence a specific brain area, mostly limited to a structural feature of the cortical surface such as a gyrus or sulcus. For this reason we investigated the effect of TMS on neuronal activation in the motor cortex as EMG measurements from the associated muscles can be used to estimate the amount of activation that is fed into the cortico-spinal tract after a TMS pulse [37]. This way, a TMS user can more easily evaluate the consequences of coil models for predictions in a specific area of the brain that is well investigated, rather than a larger area below the coil. From FEM simulations we observed that the more detailed coils (the two models taking into account spiraling wires) yielded equivalent 'activation', whereas the idealized coil deviated significantly with 15% relative difference. The metric used to approximate 'activation' is based on a simplified scheme of how the total electric fields interact with pyramid cells in the cortical layers,

where the axons perpendicular to the cortical surface are activated maximally for aligned electric fields. For an in-depth review motivating such a scheme, see [1] and [29]. We assessed the validity of this metric by comparing two coil orientations: one with a current induced perpendicularly and another one parallel in respect to the pre-central sulcus. We could generate strong 'activations' for perpendicular coil orientations, and weaker activation for parallel orientations, similar to the findings of neurophysiological experiments [28] and FEM based neurocomputational studies [35]. This finding provide extra confidence in the metric we employed to evaluate neuronal activation, whereas we are aware of the limitations of such a simplified scheme that does not take into account the full complexity of the layers of connected neurons in the cortex.

Conclusions

When modeling a typical figure-of-8 TMS coil the use of an idealized outermost circular contour for each wing was found to be inadequate to accurately compute the total electric field, at a distance from the TMS coil relevant for stimulation of cortical neurons. Instead incorporating realistic wire winding turns resulted in better match to measurements. Both the predicted spatial distribution and magnitude of the field were most accurate in the case where we accounted for the surface area occupied by the spiraling coil wires. To a much lesser extent the wire height and coil thickness were contributing to the magnetic field induced by the coil. The FEM based brain simulations yielded similar results.

Thus, in order to make accurate predictions for the currents induced by TMS in the human brain we not only need to use realistic head properties, but also realistic models of the TMS coil. These models should at least account for the in-plane geometry of the coil, such as the spiraling wires of typical figure-of-8 TMS coils. Such approaches can improve real-time neuronavigation, taking both individual tissue properties and specific TMS coil models into account. This would allow the operator not only to plan injected current with more spatial detail and in individualized patient models, but also gain a certain amount of control over the injected current dose. Current practices are crude and thus unreliable, such as the determination of the 'motor threshold' method [38]. Once achieved, TMS treatment efficacy will improve and the confidence in neurocognitive findings inferred from TMS studies will increase, helping TMS protocols to become more reliable and with less variability between individuals.

Acknowledgment

This work was supported by the DeNeCor project being part of the ENIAC Joint Undertaking. The authors would like to thank Axel Thielscher for sharing with them the human brain 3D tetrahedral model.

References

1. Neggers SFW, Petrov PI, Mandija S, Sommer IEC, van den Berg C a. T. Understanding the biophysical effects of transcranial magnetic stimulation on brain tissue: The bridge between brain stimulation and cognition. *Prog Brain Res.* 1st ed. Elsevier B.V.; 2015; 1–31. doi:10.1016/bs.pbr.2015.06.015
2. Opitz A, Windhoff M, Heidemann RM, Turner R, Thielscher A. How the brain tissue shapes the electric field induced by transcranial magnetic stimulation Supplementary Material. *Neuroimage.* Elsevier Inc.; 2011;58: 849–59. doi:10.1016/j.neuroimage.2011.06.069
3. De Lucia M, Parker GJM, Embleton K, Newton JM, Walsh V. Diffusion tensor MRI-based estimation of the influence of brain tissue anisotropy on the effects of transcranial magnetic stimulation. *Neuroimage.* 2007;36: 1159–70. doi:10.1016/j.neuroimage.2007.03.062
4. Pu L, Liu Z, Yin T, An H, Li S. Simulation of induced electric field distribution based on five-sphere model used in rTMS. *J Xray Sci Technol.* 2010;18: 57–67. doi:10.3233/XST-2010-0241
5. Salinas FS, Lancaster JL, Fox PT. Detailed 3D models of the induced electric field of transcranial magnetic stimulation coils. *Phys Med Biol.* 2007;52: 2879–2892. doi:10.1088/0031-9155/52/10/016
6. De Geeter N, Crevecoeur G, Dupré L. An efficient 3-D eddy-current solver using an independent impedance method for transcranial magnetic stimulation. *IEEE Trans Biomed Eng.* 2011;58: 310–320. doi:10.1109/TBME.2010.2087758
7. Ravazzani P, Ruohonen J, Grandori F, Tognola G. Magnetic Stimulation of the Nervous System: Induced Electric Field in Unbounded, Semi-infinite, Spherical, and Cylindrical Media. 1996;24: 606–616.
8. Miranda PC, Hallett M, Basser PJ. The electric field induced in the brain by magnetic stimulation: a 3-D finite-element analysis of the effect of tissue heterogeneity and anisotropy. *IEEE Trans Biomed Eng.* 2003;50: 1074–1085. doi:10.1109/TBME.2003.816079
9. Laakso I, Hirata A, Ugawa Y. Effects of coil orientation on the electric field induced by TMS over the hand motor area. *Phys Med Biol.* 2014;59: 203–18. doi:10.1088/0031-9155/59/1/203

10. Salinas FS, Lancaster JL, Fox PT. 3D modeling of the total electric field induced by transcranial magnetic stimulation using the boundary element method. *Phys Med Biol*. 2009;54: 3631–3647. doi:10.1088/0031-9155/54/12/002
11. Thielscher A, Kammer T. Electric field properties of two commercial figure-8 coils in TMS: calculation of focality and efficiency. *Clin Neurophysiol*. 2004;115: 1697–708. doi:10.1016/j.clinph.2004.02.019
12. Thielscher A, Kammer T. Linking Physics with Physiology in TMS: A Sphere Field Model to Determine the Cortical Stimulation Site in TMS. *Neuroimage*. 2002;17: 1117–1130. doi:10.1006/nimg.2002.1282
13. Madsen KH, Ewald L, Siebner HR, Thielscher A. Transcranial Magnetic Stimulation: An Automated Procedure to Obtain Coil-specific Models for Field Calculations. *Brain Stimul*. Elsevier Inc.; 2015;8: 1205–1208. doi:10.1016/j.brs.2015.07.035
14. Nieminen JO, Koponen LM, Ilmoniemi RJ. Experimental characterization of the electric field distribution induced by TMS devices. *Brain Stimul*. Elsevier Inc.; 2015;8: 582–589. doi:10.1016/j.brs.2015.01.004
15. Bohning DE, Pecheny a P, Epstein CM, Speer a M, Vincent DJ, Dannels W, et al. Mapping transcranial magnetic stimulation (TMS) fields in vivo with MRI. *Neuroreport*. 1997;8: 2535–2538. doi:10.1097/00001756-199707280-00023
16. Peres A, Souza V. Vector magnetic field mapping of a Transcranial Magnetic Stimulation coil using Magnetic Resonance Imaging: in vitro and in vivo experiments. *World Congr* 2009; 571–574. Available: http://link.springer.com/chapter/10.1007/978-3-642-03885-3_159
17. Hernandez-Garcia L, Lee S, Grissom W. An approach to MRI-based dosimetry for transcranial magnetic stimulation. *Neuroimage*. 2007;36: 1171–1178. doi:10.1016/j.neuroimage.2007.03.064
18. Mandija S, Petrov PI, Neggers SFW, Luijten PR, van den Berg CAT. MR-based measurements and simulations of the magnetic field created by a realistic transcranial magnetic stimulation (TMS) coil and stimulator. *NMR Biomed*. 2016; 1–11. doi:10.1002/nbm.3618
19. Nummenmaa A, McNab JA, Savadjiev P, Okada Y, Hämäläinen MS, Wang R, et al. Targeting of White Matter Tracts with Transcranial Magnetic Stimulation. *Brain Stimul*. Elsevier Ltd; 2014;7: 80–84. doi:10.1016/j.brs.2013.10.001
20. Nummenmaa A, Stenroos M, Ilmoniemi RJ, Okada YC, Hämäläinen MS, Raij T. Comparison of spherical and realistically shaped boundary element head models for transcranial magnetic stimulation navigation. *Clin Neurophysiol*. International

- Federation of Clinical Neurophysiology; 2013;124: 1995–2007. doi:10.1016/j.clinph.2013.04.019
21. Wagner T a, Zahn M, Grodzinsky AJ, Pascual-Leone A. Three-dimensional head model simulation of transcranial magnetic stimulation. *IEEE Trans Biomed Eng.* 2004;51: 1586–98. doi:10.1109/TBME.2004.827925
 22. De Geeter N, Crevecoeur G, Leemans a, Dupré L. Effective electric fields along realistic DTI-based neural trajectories for modelling the stimulation mechanisms of TMS. *Phys Med Biol.* IOP Publishing; 2015;60: 453–471. doi:10.1088/0031-9155/60/2/453
 23. de Weijer AD, Sommer IEC, Bakker EJ, Bloemendaal M, Bakker CJG, Klomp DWJ, et al. A setup for administering TMS to medial and lateral cortical areas during whole-brain fMRI recording. *J Clin Neurophysiol.* 2014;31: 474–87. doi:10.1097/WNP.0000000000000075
 24. Neggers SFW, Langerak TR, Schutter DJLG, Mandl RCW, Ramsey NF, Lemmens PJJ, et al. A stereotactic method for image-guided transcranial magnetic stimulation validated with fMRI and motor-evoked potentials. *Neuroimage.* 2004;21: 1805–1817. doi:10.1016/j.neuroimage.2003.12.006
 25. Kobayashi M, Pascual-Leone A. Transcranial magnetic stimulation in neurology. *Lancet Neurol.* 2003;2: 145–156. doi:10.1016/S1474-4422(03)00321-1
 26. Windhoff M, Opitz A, Thielscher A. Electric field calculations in brain stimulation based on finite elements: an optimized processing pipeline for the generation and usage of accurate individual head models. *Hum Brain Mapp.* 2013;34: 923–35. doi:10.1002/hbm.21479
 27. Thielscher A, Opitz A, Windhoff M. Impact of the gyral geometry on the electric field induced by transcranial magnetic stimulation. *Neuroimage.* Elsevier Inc.; 2011;54: 234–43. doi:10.1016/j.neuroimage.2010.07.061
 28. Brasil-Neto JP, Cohen LG, Panizza M, Nilsson J, Roth BJ, Hallett M. Optimal focal transcranial magnetic activation of the human motor cortex: effects of coil orientation, shape of the induced current pulse, and stimulus intensity. *Journal of clinical neurophysiology: official publication of the American Electroencephalographic Society.* 1992. pp. 132–136. doi:10.1097/00004691-199201000-00014
 29. Fox PT, Narayana S, Tandon N, Sandoval H, Fox SP, Kochunov P, et al. Column-Based Model of Electric Field Excitation of Cerebral Cortex. *Hum Brain Mapp.* 2004;22: 1–14. doi:10.1002/hbm.20006
 30. Krieg TD, Salinas FS, Narayana S, Fox PT, Mogul DJ. Computational and experimental analysis of TMS-induced electric field vectors critical to neuronal

activation. *J Neural Eng.* 2015;12: 46014. Available: <http://stacks.iop.org/1741-2552/12/i=4/a=046014?key=crossref.541e88e57135d992f029061e3a84cc80>

31. Krieg TD, Salinas FS, Narayana S, Fox PT, Mogul DJ. PET-based confirmation of orientation sensitivity of TMS-induced cortical activation in humans. *Brain Stimul.* 2013;6: 898–904. doi:10.1016/j.brs.2013.05.007
32. Rahman A, Reato D, Arlotti M, Gasca F, Datta A, Parra LC, et al. Cellular effects of acute direct current stimulation: somatic and synaptic terminal effects. *J Physiol.* 2013;591: 2563–78. doi:10.1113/jphysiol.2012.247171
33. Berker AO de, Bikson M, Bestmann S. Predicting the behavioral impact of transcranial direct current stimulation: issues and limitations. *Front Hum Neurosci.* 2013;7: 613. doi:10.3389/fnhum.2013.00613
34. Kammer T, Vorwerk M, Herrnberger B. Anisotropy in the visual cortex investigated by neuronavigated transcranial magnetic stimulation. *Neuroimage.* 2007;36: 313–321. doi:10.1016/j.neuroimage.2007.03.001
35. Janssen AM, Oostendorp TF, Stegeman DF. The coil orientation dependency of the electric field induced by TMS for M1 and other brain areas. *J Neuroeng Rehabil.* ???; 2015;12: 1–13. doi:10.1186/s12984-015-0036-2
36. Lefaucheur J-P, André-Obadia N, Antal A, Ayache SS, Baeken C, Benninger DH, et al. Evidence-based guidelines on the therapeutic use of repetitive transcranial magnetic stimulation (rTMS). *Clin Neurophysiol.* 2014;125: 1–57. doi:10.1016/j.clinph.2014.05.021
37. Petersen RNT, Pyndt HS, Nielsen JB. Investigating human motor control by transcranial magnetic stimulation. 2003; 1–16. doi:10.1007/s00221-003-1537-y
38. Schutter DJLG, van Honk J. A standardized motor threshold estimation procedure for transcranial magnetic stimulation research. *J ECT.* 2006;22: 176–178. doi:10.1097/01.yct.0000235924.60364.27

Chapter IV

A validation approach for computational models of TMS induced brain currents using motor evoked potentials

Abstract

The adoption of transcranial magnetic stimulation (TMS) has steadily increased in research as a tool capable of stimulating, safely and non-invasively, the central and peripheral nervous systems. Initial clinical applications were limited to the diagnostic use of TMS and readout signals such as electromyograms (EMG). Subsequently, repetitive TMS (rTMS) was appreciated for its therapeutic benefits as well. However, even after a decade of use of rTMS as an alternative treatment of major depressive disorder in psychiatry, the mechanism of action is still not well understood. Computer models predicting the induced electric field distribution in the brain have been suggested before in the hope to resolve at least some of the uncertainty and resulting variable treatment response associated with the clinical use of TMS.

We constructed a finite element model (FEM) of the head using individual volumetric tissue meshes obtained from an MRI scan and a detailed model of a TMS coil that together can predict the current induced in the head of a patient at any given location with any given coil position and orientation. We further designed several potential metrics of how a TMS-induced current induced neuronal activation in the motor cortex and added this to the model. We validated this model with motor-evoked potentials (MEPs), EMG responses of the hand muscles after TMS on the motor cortex, in an experiment on 9 healthy subjects. We adopted a tailored MEP mapping protocol for model validation, which, unlike traditional grid mappings, varies the TMS machine output intensity between stimulation locations. We further varied coil orientation on each point stimulated to allow exploration of the angular dependency of the model MEPs. Taken together, this approach covers a wide domain and scope of the modeled and measured responses, which are optimally suited for model validation. For each subject, the motor hotspot was manually determined using individual cortical anatomy and BOLD fMRI measurements.

Modeled activation in the motor cortex did not show a good correlation to the observed magnitude of the observed MEPs, for none of the neuronal activation metrics adopted. For an asymmetric activation metric, taking into account induced current direction with respect to the motor cortex sulcal wall, was marginally better than other metrics. Generally all activation metrics based on induced currents performed better than a control metric agnostic of induced electric field magnitude. Our results suggest that one should take into account components of the injected currents and their relationship to the morphology of the underlying motor cortex, but the coarse metrics we used to model the relationship between induced current and neuronal activation probably did not do justice to the complex neuronal circuitry of the cortical sheet. Furthermore, it seemed MEP magnitudes in our experiment are too variable over

subsequent stimulations, which could be mitigated by more repetitions per stimulation location and orientation.

Further efforts to construct validated models predicting TMS effects in individual patient's brains should incorporate microcircuits interactions in the cortical sheet, in addition to induced electrical field models, and take into account the inherent trial-to-trial variability of MEPs.

Introduction

TMS is a non-invasive brain stimulation (NIBS) and modulation technique. Based on the physical principle of electromagnetic induction, it generates magnetic fields, that freely penetrate the skull and can inject relatively focal cortical currents with the appropriate coil design. TMS is increasingly used to treat diseases of the central nervous system, obtain diagnosis after brain trauma, and investigate the organization of the brain [1].

However, how exactly these currents flow and are shaped by non-isotropically conducting brain morphology, and subsequently interact with or modulate neuronal activation, is still an open question. Computer based models predicting TMS-induced currents and subsequent elicited activation have been an active topic of research for more than two decades from which significant progress in understanding TMS effects has been made.

Due to recent advances in computational science, it is now viable, affordable, and possible to model the interaction of electric and magnetic fields with human brain tissue in impressive detail. Initial models of the human cortex were limited to highly idealized geometrical shapes representing the different conductive tissues in the head, and the application of finite element modeling of the incident and induced fields to such compartments. For example, spherical models with superficially derived sub-layers for each major tissue with realistic radius values to account for each tissue thickness have been attempted in the past [2,3]. Later, more sophisticated models were developed where the highly inhomogeneous and anisotropic properties typical for the human brain are captured in sufficient detail, thanks in part to advanced MR imaging. Such models often consist of several separate compartments, segmented automatically or semi-automatically, from T1-weighted anatomical scans generating maps of major brain tissues such as gray matter (GM), white matter (WM), cerebral spinal fluid (CSF), skull, and skin. To approximate the conductive properties of the highly anisotropic white matter, several groups have successfully utilized diffusion-weighted imaging to introduce anisotropic conductivity per mesh element making such models even more realistic [4].

However, despite such progress and the further sophistication of computational modeling of inductively induced currents, only a very small number of such models have been empirically validated. At present, it is unclear what assumptions and simplifications that are unavoidable for any computational model of conductive properties of live tissue, are valid, and which are not. Hence it is not clear to what extent predicted neuronal currents can be relied upon for clinical use. For the incident field or the portion of the electric field induced by the mere geometry of the coil, a few successful validations have been published that confirmed such models at

least partially, including our group. By using elaborate MRI-compatible TMS setups, phase accumulation models based on modeled incident TMS evoked currents were validated quite successfully with deviations of only 1–5% in phase accumulation maps (proportional to incident current magnitude), thus validating this portion of the model for total E-field induced in the head successfully [5]. The situation is much less fortunate for the largest part of such individual TMS-induced activation models. The second part of the total E-field, governed by the inhomogeneity of tissues in the head causing current accumulation and requiring FEM to model, seldom gets empirically validated. A notable exception has been the work of Bungert et al [6–8] where EMG and fMRI were used to validate the responses in the muscle or directly in the brain, respectively. Although some correspondence with measured responses was established, a large portion of unexplained variance remained. Only a small portion of TMS modeling studies have looked into validating their results empirically.

Whereas Bungert et al used varying coil orientations to obtain modeled and measured responses in a varying domain, in their protocols the coil was rotated in small steps while being fixated on one location, and only shifted laterally. Thus missing possible more anterior or posterior coil positions that limits the scope and variability of the modeled versus measured responses. Alternatively, although not used in FEM validations to our knowledge, more classic grid mapping studies using a large number of stimulation locations a rectangular grid in combination with one or a few discreet coil orientations have been published to explore response maps of the motor cortex [9–11]. These studies have provided insights into the spatial distribution of TMS-evoked MEPs but were not used for current model validation. A disadvantage of such experimental designs could be overly long sessions due to the number of TMS discharges required, which would result in MEP amplitude habituation (a.k.a. repetition suppression) [12], making it less suitable for current model validation.

In this study, we developed multi tissues 3D finite element model (FEM) of TMS-evoked currents in the brain, based on a detailed coil model and derived from subject-specific anatomical MR images. To predict the MEP amplitudes at several stimulation locations, we propose several hypotheses (activation ‘metrics’) on how such currents can evoke neuronal activation in the cortical sheet. These metrics include a simple amplitude of the induced current integrated over a certain volume of tissue and several more sophisticated metrics with angular dependencies of local activation on induced current direction (see paragraphs below and the methods section for details). The metrics are motivated by the architecture of the microcircuitry in the cortical sheet. We also tested two ideas on where in the pre-central gyrus MEPs measured at the thumb are primarily evoked: only the posterior wall or the entire gyrus including the premotor cortex. To validate our modeling approach, we conducted experiments with mono-phasic TMS in single pulse mode on the motor cortex (hand area) in combination with EMG on the thumb and index finger abductor muscle (first dorsal interosseous) of each subject.

Importantly, we propose a novel more optimal, and comprehensive approach to probe and map the MEP response from the motor cortex for TMS current modeling validation. In this study we adopted stimulation locations evoking MEPs in a cross-shaped layout, covering Central, Posterior, Anterior, Medial and Lateral locations relative to the hand knob as defined by individual functional fMRI maps of finger movements [13], while probing coil orientation in the four major orthogonal directions. We chose the orientations such that we could investigate possible current direction dependent as well as position effects, covering an optimal domain of spatial parameters.

Many FEM TMS modeling studies produced predicted currents in the shape of 3D maps [14,15], which is not the same as neuronal activation. As discussed above, when validating such models with empirical measures such as TMS-evoked fMRI or MEPs, one needs a metric that reflects neuronal activation as a result of local current estimates, to bridge the gap between the neuronal or muscle responses to TMS and the evoked currents in the brain. Commonly, the maximum electrical field magnitude at each location in a stimulated area is reported in the literature as a proxy for ‘neuronal activation’ [16]. Others have adopted an activation metric proportional to the direction of the electric field relative to the folding cortical surface. Most notably the C3 metric proposed by Fox et al [17], based on a cortical column model, where orthogonal orientation to the outer GM surface fields is suggested as most effective and as such most pronounced to the physiological effect of stimulation. The same model was demonstrated numerically (FEM) and supported with functional ($H_2^{15}O$) PET imaging, as evidence for this hypothesis [18]. Recently, however, such a simplistic generalization of neuronal responses to local current patterns was challenged by the observation that the site of activation is not where we would expect it. Based on FEM models combined with the aforementioned C3 metric [6], albeit through indirect evidence of comparing results from a model to previously reported functional imaging studies, Bungert et al [6] has confronted the notion that any prime component of the E-field relative to the outer cortical layer can be a good estimator alone. Rather they proposed the relative standard deviation (SD) of the product across several coil orientations at a fixed site as a biophysical estimate for the potential MEP response.

We, therefore, did not just focus on this single and challenged metric (C3) but included several potential metrics mimicking the link between local modeled current patterns and compared the results of our FEM EM simulations against all proposed metrics. The metrics we developed take into account the electric field amplitude in combination with its tangential and radial components relative to the targeted cortical surface. Finally, we adopted an additional very simplistic metric not depending on induced current in any way, but only on a distance from the electric field maximum to a stimulation point-target, which can serve as a H_0 -hypothesis. Including such a zero-hypothesis metric allowed us to test the validity of some naive approaches that are completely independent of the induced E-fields, rather they rely on simple distance

from coil to target adjustments to estimate the recommended dosimetry [19]. Previous work by [20], has already challenged such approaches, still, we tried to adequately account for such field-independent predictors in our comparison.

Finally, validation of TMS-evoked current models with MEPs is an indirect approach, even when we manage to establish a good metric for the relationship between induced current models and local neuronal activation. Also, evoked MEPs further rely on assumptions of how the neuronal activation pattern travels from the stimulated motor cortex through the cortico-spinal tract and ultimately innervates the muscles, measured by EMG. We evaluate the numerically produced modeled E-fields on two regions of interest (ROIs) around the hand knob in the motor cortex, one representing the anterior wall of the central sulcus, and the other covering the entire precentral gyrus around the hand knob, also including the pre-motor cortex, similar to Bungert et al [6]. With this, we also tested assumptions about what parts of the tissue in the motor cortex, in which currents are evoked, contribute to the magnitude of the signal arriving at the muscle through the cortico-spinal tract.

Materials and Methods

Participants

For this and another study, a total of 11 subjects were recruited. Data from 9 subjects (4 males and 5 females) were processed and analyzed. The experimental procedure was approved by the medical ethical committee of the University Medical Center Utrecht (UMCU), Utrecht, The Netherlands (protocol 16-469/D).

All participants were included only under written consent and without any counter-indications to TMS reported (personal and/or family history of epilepsy; not currently on any medication). Also, all participants were right-handed. Two of the participants dropped out of the study after failing to follow some of the sessions.

#	Subject	Age	Sex	RMT
1	SU01	21	F	41
2	SU02	34	M	40
	SU03	25	F	39
3	SU04	18	M	34
4	SU05	19	F	40
5	SU06	24	F	38
6	SU07	23	M	40
7	SU08	20	F	41
8	SU09	19	F	42
	SU10	20	F	41
9	SU11	46	M	43

Table 1: Participants and Meshing Parameters

Experimental Setup

MR Image Acquisition

All MR acquisitions were performed with a 3T MR scanner Achieva (Phillips, The Netherlands). Anatomical T1 weighted scan was acquired with a TR/TE of 10.015/4.61ms, a flip angle of 8°, voxel size of 0.75x0.75x0.8mm, scan duration of 677s, 225 slices with a slice gap of 0 mm. For fMRI time series measurements, a single-shot EPI sequence was acquired with 250 dynamics, a TR/TE of 2,000/23ms, a flip angle of 70, a voxel size of 4x4x4 mm, 30 slices with a slice thickness of 3.6mm and a slice gap of 0.4mm.

Electromyography (EMG)

A Neuro-MEP-4 (Neurosoft, Russia) EMG device with 4 channels was used, 20 kHz sampling rate with an amplification gain factor of 1000 (up to 60mV). The software with the device supplies impedance monitoring, which we used to keep impedance low ($<10k\Omega$) in the green zone (green/yellow $<25k\Omega$; yellow/red $<40k\Omega$). We used surface Ag/AgCl electrodes (FIAB, Italy) (REF: F3001ECG), which were placed over the right hand first dorsal interosseous (FDI), abductor digiti minimi (ADM) and extensor carpi radialis (ECR) muscle in a belly-tendon montage and the ground/reference electrode was attached to the wrist of the left hand. For this study, only channel-1 (FDI) traces were processed and analyzed.

Transcranial Magnetic Stimulator (TMS)

The stimulator we used was the Neuro-MS Monophasic TMS (Neurosoft, Russia) with a figure-8 flat coil (Reference: FEC-02-100) in a single pulse mode. All sessions were navigated and EMG MEPs responses were recorded using the Neural Navigator software in the “motor mapping” variant, version 3.1 (Brain Science Tools B.V, The Netherlands). All participants were asked to sit in a relaxed manner on a normal chair with the palm facing upward resting on a table surface, while the head was placed on a chin-support frame supplied by Brain Science Tools BV to constrain head movements.

Extended theoretical background

In chapter 2 we describe the magnetic field evoked by the TMS coil model, how it evokes an incident E-field in the head, how we segment a T1 weighted MRI scan into 5 tissue types and construct a volumetric mesh from those segments. In chapter 2 we also describe the finite element model and induced E-field is provided, and 5 macroscopic models of how an E-field might interact with cortical neuronal tissue to evoke activation. We refer to chapter 2 for all details of the model validated

here, including the neuronal coupling and the metrics of neuronal activation we evaluate later in this chapter.

Activation area ROI

To validate our TMS induced current model with TMS evoked MEPs, we have to first answer two questions on how exactly TMS induced currents lead to a MEP. First, we must have assumptions on how currents generate neuronal activations, and, second, we must define how this neuronal activation contribute to a muscle signal through the cortico-spinal tract. In this section, we explain how we construct two possible regions of interest around the hand knob whose summed neuronal activation could contribute to thumb MEP. In the next section, we hypothesize how ‘activation’ could arise in the neuronal circuits contained in the cortical sheet evoked by the TMS-induced currents.

To obtain the two possible regions of interest (ROIs) in which activation can be expected to contribute to an MEP, inside SCIRun we thresholded the resulting fMRI map until we saw a clear representation in the motor area controlling the hand, anatomically referred to as the “hand knob” (see table 1 for thresholded values). Two surface patches were isolated from the pial surface (the outer gray matter-CSF boundary), see figure 2. The extent of each surface was hand-picked to always span the crown of the precentral gyrus. For the larger ROI-1, the anterior wall of the precentral gyrus facing the precentral sulcus and encompassing the so called ‘premotor’ cortex is included as well as the posterior wall of the precentral gyrus, facing the central sulcus. It hence encompasses the entire pre-central gyrus around the hand knob. For the smaller ROI-2, only the posterior wall of the pre-central gyrus around the hand knob is included, thus encompassing the classical primary motor cortex. See figure 2 for a visualization of ROI-1 and ROI-2 of one of the participants.

In the model validation described in the following sections, the performance of models using either ROI as a ‘MEP generating’ entity is compared, in the hope to observe a better fit for the true MEP generating region of the motor cortex. As MEPs can be evoked from the primary as well as the pre-motor cortex, we think it is important to test this assumption.

For patch isolation of ROI-1 and ROI-2, we developed in-house a new module to SCIRun (Modules::MiscField::SelectMeshROI), which filters triangles based on N-step topological distance from an initial seed element, depicted as a yellow sphere in figure 2.

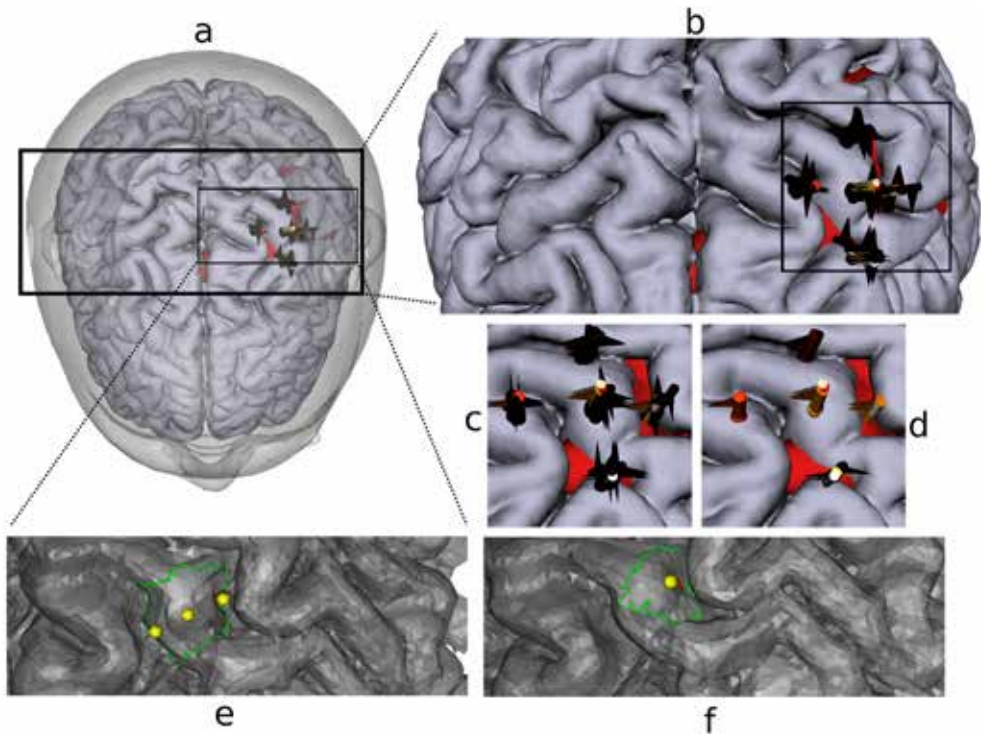


Figure 2: Demonstration of a completed navigation and cross-mapping session with subject SU06 with screen captures from the navigation software we used. (a) an axial from-top view of 3D rendered subject head & cortex. A slightly larger version can be found in (b) and an enlarged centered overview in (c) for all 100 MEPs, and thresholded ($>0.1\text{mV}$) version of the same data in (d). Each flag represents a stimulus nailed at the center of the TMS coil iso-field line intersecting with the cortex during each discharge. The rendering of the M1 area patch for ROI1 is shown in (e) and ROI2 in (f). Seed points for ROI creation are depicted as yellow spheres. Visualizations are obtained from SCIRun.

Experimental protocol

Functional MRI of voluntary thumb movement

During fMRI scanning, the participant was instructed to perform thumb movements with the right thumb upon presentation of an auditory cue. The recording lasted 510 seconds. Thumb movements were measured with ECG electrodes integrated with the MRI system (effectively using them as EMG), attached to the thumb muscle.

Concurrent TMS-EMG

For each subject, individual resting motor threshold (RMT) was determined, starting from 30% MO ramping up in steps of 5% until a detectable MEP was observed, both visually and via NeurosoftMEP software with the criteria of having more than 50mV peak-to-bottom MEP amplitude. Subsequently, intensity was reduced in steps of 1%, until we observed a successful MEP in 5 out of 10 trials [21]. Coil orientation was in AP direction while kept roughly orthogonal to the central motor gyri for each participant.

We conducted MEP mapping on predetermined subject-specific locations, organized roughly in a cross fashion. The procedure involved stimulation in a cross pattern on and around M1 (see figure 2). We relied on an image-based neuro-navigation system to achieve precise cortical targeting, where each coil placement was possible within 3mm spatial accuracy and with <5mm distance to target as a projection on the coil central iso-line (Brain Science Tools BV, The Netherlands). It involved 5 stimulation sites, one on top of M1 (which was determined from individual fMRI BOLD maximum, see section) as well as two locations about 1 cm more medial and lateral along the pre-central sulcus and two locations anterior and posterior from M1. See figure 2 for an impression. Each site was stimulated with 4 orthogonal coil orientations, each repeated 5 times, leading to a total of 100 stimuli (5 positions; 4 orientations; 5 repetitions). The TMS machine output was different for the stimulations directly on M1 (110%RMT) in contrast to the other 4 peripheral locations (120%RMT). This was done in an attempt to roughly match the intensity of the fields injected on all stimuli sites. This way the chance of supra-threshold minimum intensity would not bias in favor of the already anatomically predicted the best location. The orientation of the coil was also picked in a manner that the first orientation always pointed toward M1 ‘cross intersection’.

The order of stimuli was picked in a pseudo-random manner for each subject with a minimum of about 3 seconds inter-stimulus interval (to compensate for potential repetition suppression effects), around 10 seconds interval when changing between the 5 sites. The order of the four major coil orientations was picked in a similar manner per site. A typical session duration took around 15-20 minutes excluding preparation time.

Since our navigation system had an integration with the software package NeurosoftMEP of the EMG manufacturer, it is possible to have a comprehensive session export where each site of stimulation and raw MEP trace is recorded in a human-readable XML format. There are several important parameters exported per stimulus that are crucial for the correct placement of the coil model in the world space of our FEM simulations. The final rigid body transformation was derived as follows:

$NC^{-1}S^{-1}F_1F_2L$, where (N – navigator matrix, based on a mapping between navigator and scanner world space; C – navigator coil generative space; S – navigator

sensor tip offset; F1, F2 and are two flips to compensate for the difference in generative space between SCIRun and the navigation software where L coil thickness offset in Z+ direction along the coil iso-line). This was important to fully reconstruct each single coil position and orientation when running our FEM and activation metric model for each single stimulus (see section for details), to obtain modeled MEP estimates.

Analysis

Functional MRI and BOLD response

To obtain a subject-specific thumb area mapped on each participant's motor cortex we had to post-process the anatomical T1-weighted MR images (see Section) and analyze the functional raw times MRI-EPI series of a trivial voluntary thumb movement task (see Section). For this purpose we used the SPM12 software package [22], which is a freely available toolset for the commercially available Matlab 2014a MATLAB 2014a (The MathWorks, Inc., Natick, Massachusetts, USA). We considered the area corresponding to the thumb movement to be the location with the maximum BOLD response from the statistical activation map as given by SPM12. The statistical activation map was constructed based on event-related generalized linear model (GLM) analysis in a so-called event related analysis, where the thumb movement is modeled as a delta function convolved with the canonical hemodynamic response function (HRF). The timing of the thumb movements (and hence each delta function) was obtained from the EMG recordings that were acquired during MRI acquisition, using custom Matlab code. Two nuisance regressors were involved in the GLM analysis: the average BOLD signal in the WM and the CSF. The final statistical probability images were constructed based on a T-statistic with the T-threshold at $P < 0.05$, family-wise error (FWE) whole-brain corrected [22]. The maps of thumb movement activation around the hand knob in the pre-central gyrus were used to plan the stimulation sites around M1 (see section).

Quantification of MEPs

We evaluated the recorded EMG traces for motor evoked potentials (MEPs) elicited by single-pulse TMS using a straightforward MATLAB routine assessing MEP amplitude as the peak-to-bottom signal difference in the interval 20ms after TMS pulse administration, where MEPs can be expected to occur. Our quantified MEPs were compared to the amplitudes computed by the NeuroMEP software package used to acquire the data, those measures are also based on the same peak to bottom criteria, and found to be nearly equivalent. One of the subjects exhibited relatively low MEP amplitudes ($\leq 0.5\text{mV}$) and the automatic algorithm for onset-peak-bottom detection as part of the NeuroMEP software package failed to register any. This motivated us to write our own quantification routine in MATLAB as explained above, to have better

control and ease of reproducibility of this analysis, rather than the MEP analysis provided by the NeuroMEP software.

Descriptive Statistics

For each stimulus administered with TMS, the 6D position of the coil with respect to the head was stored in MRI native space coordinates by The Neural Navigator for later analysis. From this position, the incident field was computed using piece-wise Biot-Savart as explained above, and then FEM, the activation metrics over the surface patches around M1 were computed (which should be roughly proportional to MEP amplitude). This means we had a simulated and real MEP for each stimulus administered, which could be depicted against each other in a set of 2D points. We computed the correlation coefficient for each point cloud (that is, per metric and ROI) and subject.

Finally, the correlation coefficients were subjected to a 2-way repeated measures ANOVA, where we assessed whether one of the metrics and ROIs yielded a significantly different result compared to the others. If so, subsequent post-hoc tests were performed to test which of the combinations differed significantly. The significance level alpha was set to 0.05.

Results

Physiological EMG recordings

We first present the average observations for the MEPs recorded from the cross-shaped stimulation locations. In figure 4a, a set of sampled MEPs from one responsive position for one subject is presented. In figure 4-b, an overview of average MEP amplitudes for each location and direction is presented. The most optimal coil position seemed to be anterior of the motor hot spot (2.48mV) and the lateral of the motor hot spot (2.0mV) while the most optimal coil orientations were directed medially and anterior. The combination of M-M and A-A (medial location with medial direction and anterior location with anterior orientation, respectively) was most effective in evoking MEPs.

Simulations

We compared the quantified MEPs from the acquired EMG signals for each TMS stimulus, the peak to bottom magnitude, to the modeled 'cMEP'. We calculated based on the suggested activation metrics, the sum/integral over the ROI surface patch weighted by the area (see section Error: Reference source not found).

See figures 4-c and 4-d for the scatter plots of these cMEP x MEP pairwise comparisons, and the calculated correlation coefficients between those measures for one subject (SU06). Table 2 below presents the aforementioned correlation coefficients (CC) for all subjects, ROIs and activation metrics, and their mean and standard deviations. Metric C3 for ROI 1, and C5 for ROI2 had the highest correlation coefficient of modeled vs observed MEPs, i.e. the best correspondence (see table 2). This was confirmed by an omnibus ANOVA of ROI x metric ($F(5, 45) = 8.51; p < 0.005$) implying the correlation coefficient was different for ROIs and metrics in general.

Post hoc paired sample one-sided T-tests were then performed testing (within each ROI) whether these C3 or C5 were indeed different from the C0 or CE, respectively (we tested one-sided as we expected directed metrics such as C3, C4, and C5 to outperform C0 and CE). C0 and CE are the more ‘banal’ zero-hypotheses that do not make any assumptions about the current direction or even current amplitude and are metrics we hoped to outperform. For ROI1, C3 was not significantly different from C0 or CE ($T(8) = 0.80; p = 0.22$ and $T(8) = 0.14; p = 0.45$, respectively). For ROI2, C5 was larger than C0 at trend level ($T(8) = 1.47; p = 0.08$) but not from CE ($T(8) = 1.17; p = 0.13$, respectively). In summary, when taken together, the metrics and ROIs yielded significantly different predictions, with C3 and C5 outperforming other metrics at first sight. However, when specifically tested against much more simplistic metrics C0 and CE, only C5 outperformed the simplest 0-hypothesis C0 at the trend level.

Although C0 was designed to be a naive ‘distance to target’ metric, it was not outperformed by the popular C3 metric, for neither ROI. For the larger ROI2, there was a trend of C5 outperforming C0, but not the other simple metric CE that only takes into account field magnitude at the neuronal interface.

There seems to be a tendency toward better model predictions for those metrics (C4 and C5) taking into account whether injected currents point inward or outward from the orientation of the local cortical sheet. At least, from the correlation coefficients reported in table 2, it is clear that CE and C3 are not forming better than the metrics C4 and C5 that take into account whether currents were directed inward or outward.

In figures 4-c and 4-d the simulated MEP is plotted against the measured MEP for 2 representative subjects. The same figures are provided for all participants in the supplementary material.

ROI Metric	ROI 1						ROI2					
	C0	CE	C2	C3	C4	C5	C0	CE	C2	C3	C4	C5
CC	0.47	0.65	0.66	0.39	0.46	-0.08	0.53	0.66	0.65	0.17	0.37	0.08
	0.32	0.19	-0.12	0.24	0.09	0.19	0.21	-0.13	-0.18	0.21	-0.51	0.32
	0.26	0.09	0.12	0.00	0.33	-0.19	0.25	0.09	0.12	0.03	0.25	-0.15
	0.39	0.49	0.20	0.27	0.51	-0.06	0.34	0.47	0.13	0.22	0.19	0.47
	0.34	0.11	-0.34	0.60	0.02	0.11	0.00	-0.11	-0.36	0.56	-0.75	0.59
	0.02	-0.04	-0.11	0.19	-0.03	-0.02	0.02	0.00	-0.04	0.17	-0.13	0.11
	-0.05	0.52	-0.14	0.50	0.44	0.03	0.00	0.51	0.41	0.52	0.09	0.53
	0.09	0.34	0.33	0.27	-0.05	0.48	-0.10	-0.38	-0.53	0.47	-0.57	0.39
	0.16	0.14	0.11	0.17	0.25	0.01	0.05	0.10	0.07	0.07	-0.35	0.35
Mean	0.22	0.28	0.08	0.29	0.22	0.05	0.14	0.13	0.03	0.27	-0.16	0.30
SD	0.18	0.23	0.30	0.18	0.22	0.19	0.20	0.34	0.37	0.20	0.40	0.24

Table 2: Correlation coefficients for each metric evaluated per cortical ROI patch on each subject individually.

The correlation coefficient per metric, ROI, and subject is presented in table 2 below, along with their means and standard deviations over subjects

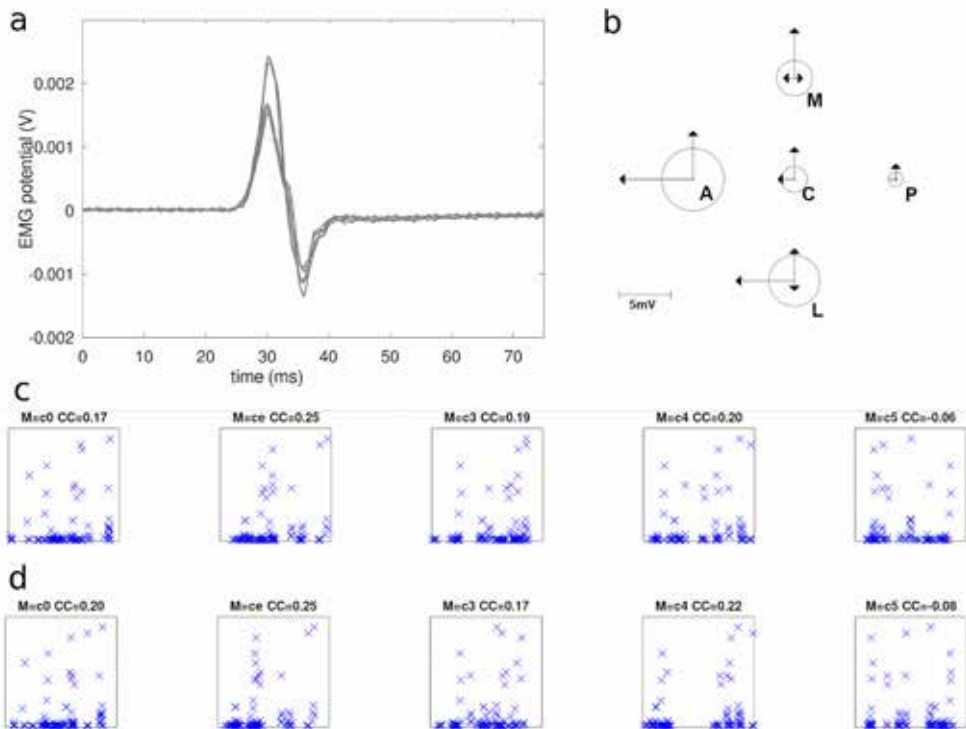


Figure 4:

(a) Average MEP amplitudes are pooled over all subjects and shown separately for each position and orientation of the coil, in a schematic cross and directional arrow and circle graph. The radius of the circles shows the average MEP amplitude per stimulated location.

The length of the arrows denotes the average MEP amplitude for each coil orientation for that location (note that for aesthetic reasons, arrowheads were not plotted when MEP amplitudes were less than 0.8mV). The stimulated locations are denoted as A-anterior, P-posterior, M-medial, L-lateral, C-central according to convention and relative to the central hypothesized ideal hotspot determined from an individual fMRI activation. Orientations were relative to the central sulcus. (b) A subset of MEP traces for one representative subject (SU02), from location A with coil directed in the anterior direction, pointing away from the central sulcus. In this case, all stimuli repetitions caused a clear MEP response. (c) The scatter plots of modeled vs observed responses for subject (SU01) on ROI1. (d) The scatter plots of modeled vs observed responses for subject (SU01) on ROI2.

Discussion

We investigated finite element models of currents in individual heads, and ensuing neuronal activation patterns, induced by a typical TMS figure-of-8 coil by comparing model results with evoked EMG responses in the thumb of nine healthy volunteers. The lack of empirical validation in a growing field of macroscopic computational neuromodulation was one of the motivations to pursue this work.

We obtained reasonable explanatory power for some combinations of ROI and activation metric for about 3 individuals using mainly ROI1 and the C3 metric, and for 5 individuals for the ROI2 and the C5 metric. However, for the group of subjects as a whole, the results were not convincing. Taking into account more sophisticated measures such as coil details, individual head tissue characteristics, and several possible macroscopic neuronal activation metrics, did not systematically explain observed evoked responses better than relatively simple metrics such as CE, which simply reflects local total current magnitude. The main finding was that a FEM model and an activation metric that accounted for asymmetrically directed current interactions with the cortical surface (C5) performed best (at trend level) when accumulating over a larger ROI incorporating the motor cortex (ROI2). For this specific model, we obtained a moderate correlation between observed and modeled MEPs. The C5 metric over ROI2 performed almost equally well as the popular C3 metric over a smaller patch on the anterior bank of the central sulcus (ROI1), covering only primary motor cortex representations of the thumb. However, our rather uninformed metric C0, taking into account only the distance from the stimulated target to the ROI believed to result in MEPs, performed not much worse than C3, and was only outperformed by C5 over ROI2 at the trend level. The other rather naive metric CE taking into account current magnitude modeled with FEM but not the direction of the current relative to the cortical surface performed equally well to both C3 over ROI1 and C5 over ROI2. The other metrics performed less well. Overall, the metrics taking into account induced currents in some way (CE, C2, C3, C4, and C5) together performed better than the uninformed control metric C0, implying that computing currents, in general, are useful.

An important reason for the moderate level of success of combining TMS with EMG to validate results from computational models with observed MEPs is the notorious variability observed in subsequently evoked MEPs. To not make our experiments overly long and to not stress the participants too much, we used 5 repetitions per site where 20 now seems to be the recommended minimum[23].

In our scatter plots in figure 4 this is also clearly visible: while for some larger model-derived responses the individual measured responses tended to increase as well, there was a substantial number of recordings without responses at all, even for those stimuli where one would expect a large response. This might be a habituation effect of repeated TMS stimulation [12], or perhaps modulation of motor responsiveness by other uncontrolled processes going on in the brain (state dependent) [24,25], which reduced the effectiveness of our validation approach. The aforementioned papers on the variability of MEPs largely appeared when the current experiments were already well underway, hence we could not take these recommendations into account. Nevertheless, simply increasing the number of repetitions might not be sufficient, as state-dependency of MEPs would continue to happen and reflect the inherent variability unrelated to the low number of repetitions, and longer trains of identical stimulus might occasionally increase habituation effects.

Empirically, the strongest MEPs were not evoked from stimuli on the central site of the cross pattern of targets we used, focused on M1. Instead, we observed the strongest responses preferentially anterior to the primary motor cortex. In part, this could be explained by the slightly lower intensity applied over the central crossing of our mapping pattern, which corresponds to the subject's hotspot. Similar center-of-gravity (CoG) anterior displacements with respect to the anatomical primary motor cortex have been reported in various grid mapping studies before [9–11,26–28]. This has implications for the current practice of aiming the coil iso-center, which is assumed to be the focal point of stimulation for TMS, to a target of interest. We recently published a thorough study with a 5x5 grid mapping approach, observing the same phenomenon [29]. Another observation worth mentioning is the demonstrated capability of outward injected currents, that is TMS coil pointing away from the target of stimulation, to produce strong responses systematically. The combination of a Medial target and a Lateral to Medial current, and an Anterior and a posterior-anterior directed current were the two most efficient combinations of site and direction.

Our approach for empirically evaluating and optimizing TMS current models is by itself innovative and thorough, in our opinion. Unfortunately, the current data did not allow us yet to unequivocally select an optimal neuronal activation metric or cortical surface patch from which hand MEPs are supposed to be generated. Nevertheless, given the above, several improvements can be suggested for future work, to allow clearer distinction between the predictive value of detailed choices made in such models. Future studies should first and foremost adopt 20 to 30 repetitions per

angulation and position of the coil to obtain an assessment of signal strength going into the cortico-spinal tract to produce an MEP, thus averaging out the uncontrolled variability that plagued our experiments. Even shorter sessions of successive stimuli, perhaps ten in a row, should be considered to avoid the notorious MEP habituation over repetitions, interleaved with brief stretching of hand muscles to avoid habituation. In the same light, a paradigm where location and angle are altered for every single stimulus, perhaps with a robot arm, might further reduce uncontrolled neuronal processes from becoming a dominant factor. This notion is supported by very recent work that demonstrated such randomizations can reduce the number of repetitions needed [30].

Finally, the angle should be varied in steps of 45 degrees rather than 90 degrees as we used, to cover the probed domain in a bit more detail. Steps of 10 degrees are reportedly not changing results significantly [31] and should be considered the lower bound of angle step size.

With such optimizations of the experimental paradigm, it might be possible to make informed choices about how evoked currents induce neuronal activation, and from which part of the motor system, and perhaps also allow for other model optimizations [21,32].

Conclusions

Frameless stereotaxic neuronavigation for TMS in combination with computer-aided dosimetry has the potential to further improve the accuracy, reproducibility and general efficacy of clinical and experimental TMS. Such models would allow for optimization of the evoked current dose and activation pattern through adjusting key parameters, such as pulse intensity, coil placement, and orientation. However, our study challenges the notion that a simple metric based on the induced electric field and cortical surface orientation can predict TMS effects in the brain effectively given the current experimental approach.

There is no compelling reason at the moment to adopt simple metrics for neuronal activation as a result of our comparative analysis. The quality of the predicted motor evoked response was not much better than when using simpler assumptions such as total evoked current in any given region. For larger regions, there was some benefit of computing evoked currents over a mere distance-to-the-coil metric. The direction of the coil was not found to be a clear predictor of the resulting response either. Nevertheless, our experiments demonstrate that both were capable to deliver clear MEPs, and that for a subset of subjects we could explain a substantial part of the variance by taking into account the current direction.

Finally, future validation studies using EMG should adopt larger experiments with more repetitions of stimulation, and attempt to reduce MEP variability by

adopting more optimal randomization of stimulus patterns. Current strategies, such as increasing repetitions, to achieve more robust recordings have the potential to miss subtle differences when it comes to the effects of coil orientation. This further contributes to making validation of FEM EM models of TMS-evoked activation using EMG even more challenging.

References

1. Rossini PM, Rossi S. Transcranial magnetic stimulation: Diagnostic, therapeutic, and research potential. *Neurology*. 2007;68: 484–488. doi:10.1212/01.wnl.0000250268.13789.b2
2. Nieminen JO, Koponen LM, Ilmoniemi RJ. Experimental characterization of the electric field distribution induced by TMS devices. *Brain Stimul*. 2015;8: 582–589. doi:10.1016/j.brs.2015.01.004
3. Nummenmaa A, Stenroos M, Ilmoniemi RJ, Okada YC, Hämäläinen MS, Raji T. Comparison of spherical and realistically shaped boundary element head models for transcranial magnetic stimulation navigation. *Clin Neurophysiol*. 2013;124: 1995–2007. doi:10.1016/j.clinph.2013.04.019
4. Crowther LJ, Porzig K, Hadimani RL, Brauer H, Jiles DC. Realistically modeled transcranial magnetic stimulation coils for Lorentz force and stress calculations during MRI. *IEEE Trans Magn*. 2013;49: 3426–3429. doi:10.1109/TMAG.2013.2247578
5. Petrov PI, Mandija S, Sommer IEC, van den Berg CAT, Neggers SFW. How much detail is needed in modeling a transcranial magnetic stimulation figure-8 coil: Measurements and brain simulations. *PLoS One*. 2017;12: e0178952. doi:10.1371/journal.pone.0178952
6. Bungert A, Antunes A, Espenhahn S, Thielscher A. Where does TMS Stimulate the Motor Cortex? Combining Electrophysiological Measurements and Realistic Field Estimates to Reveal the Affected Cortex Position. *Cereb Cortex*. 2016; 1–12. doi:10.1093/cercor/bhw292
7. Jung J, Bungert A, Bowtell R, Jackson SR. Vertex Stimulation as a Control Site for Transcranial Magnetic Stimulation: A Concurrent TMS/fMRI Study. *Brain Stimul*. 2016;9: 58–64. doi:10.1016/j.brs.2015.09.008
8. Bungert A. TMS Combined with fMRI. PhD Thesis. 2010; 1–253. Available: papers://e10472a9-d7b6-4cc3-b1fd-411b2c1ecba0/Paper/p16030
9. Neggers SFW, Langerak TR, Schutter DJLG, Mandl RCW, Ramsey NF, Lemmens PJJ, et al. A stereotactic method for image-guided transcranial magnetic stimulation validated with fMRI and motor-evoked potentials. *Neuroimage*. 2004;21: 1805–1817. doi:10.1016/j.neuroimage.2003.12.006
10. Phiroz E. Tarapore, M.D.1, Matthew C. Tate, M.D., Ph.D.1, Anne M. Findlay, M.A.2, Susanne M. Honma, B.S.2, Danielle Mizuiri, B.S.2, Mitchel S. Berger, M.D.1,

and Srikantan S. Nagarajan, Ph.D.2Phiroz E. Tarapore, M.D.1, Matthew C. Tate, M.D., Ph.D.1, Anne PD. Preoperative multimodal motor mapping: a comparison of magnetoencephalography imaging, navigated transcranial magnetic stimulation, and direct cortical stimulation. *J Neurosurg.* 2012;117: 354–362. doi:10.1038/jid.2014.371

11. Krieg SM, Picht T, Sollmann N, Bährend I, Ringel F, Nagarajan SS, et al. Resection of motor eloquent metastases aided by preoperative nTMS-based motor maps-Comparison of two observational cohorts. *Front Oncol.* 2016;6: 1–10. doi:10.3389/fonc.2016.00261

12. Löfberg O, Julkunen P, Tiihonen P, Pääkkönen A, Karhu J. Repetition suppression in the cortical motor and auditory systems resemble each other - A combined TMS and evoked potential study. *Neuroscience.* 2013;243: 40–45. doi:10.1016/j.neuroscience.2013.03.060

13. Opitz A, Legon W, Rowlands A, Bickel WK, Paulus W, Tyler WJ. Physiological observations validate finite element models for estimating subject-specific electric field distributions induced by transcranial magnetic stimulation of the human motor cortex. *Neuroimage.* 2013;81: 253–364. doi:10.1016/j.neuroimage.2013.04.067

14. Thielscher A, Opitz A, Windhoff M. Impact of the gyral geometry on the electric field induced by transcranial magnetic stimulation. *Neuroimage.* 2011;54: 234–43. doi:10.1016/j.neuroimage.2010.07.061

15. Opitz A, Paulus W, Will S, Antunes A, Thielscher A. Determinants of the electric field during transcranial direct current stimulation. *Neuroimage.* 2015;109: 140–150. doi:10.1016/j.neuroimage.2015.01.033

16. Thielscher A, Kammer T. Linking Physics with Physiology in TMS: A Sphere Field Model to Determine the Cortical Stimulation Site in TMS. *Neuroimage.* 2002;17: 1117–1130. doi:10.1006/nimg.2002.1282

17. Fox PT, Narayana S, Tandon N, Sandoval H, Fox SP, Kochunov P, et al. Column-Based Model of Electric Field Excitation of Cerebral Cortex. *Hum Brain Mapp.* 2004;22: 1–14. doi:10.1002/hbm.20006

18. Krieg TD, Salinas FS, Narayana S, Fox PT, Mogul DJ. Computational and experimental analysis of TMS-induced electric field vectors critical to neuronal activation. *J Neural Eng.* 2015;12: 046014. Available: <http://stacks.iop.org/1741-2552/12/i=4/a=046014?key=crossref.541e88e57135d992f029061e3a84cc80>

19. Stokes MG. Simple Metric For Scaling Motor Threshold Based on Scalp-Cortex Distance: Application to Studies Using Transcranial Magnetic Stimulation. *J Neurophysiol.* 2005;94: 4520–4527. doi:10.1152/jn.00067.2005

20. Janssen AM, Oostendorp TF, Stegeman DF. The effect of local anatomy on the electric field induced by TMS: evaluation at 14 different target sites. *Med Biol Eng Comput.* 2014;52: 873–883. doi:10.1007/s11517-014-1190-6
21. Schutter DJLG, van Honk J. A standardized motor threshold estimation procedure for transcranial magnetic stimulation research. *J ECT.* 2006;22: 176–178. doi:10.1097/01.yct.0000235924.60364.27
22. Penny W, Friston K, Ashburner J, Kiebel S, Nichols T. *Statistical Parametric Mapping: The Analysis of Functional Brain Images.* Penny W, Friston K, Ashburner J, Kiebel S, Nichols T, editors. *Stat Parametr Mapp Anal Funct Brain Images.* 2007. doi:10.1016/B978-0-12-372560-8.X5000-1
23. Goldsworthy MR, Hordacre B, Ridding MC. Minimum number of trials required for within- and between-session reliability of TMS measures of corticospinal excitability. *Neuroscience.* 2016;320: 205–209. doi:10.1016/j.neuroscience.2016.02.012
24. Bergmann TO. Brain state-dependent brain stimulation. *Frontiers in Psychology.* 2018. pp. 1–4. doi:10.3389/fpsyg.2018.02108
25. Naros G, Lehnertz T, Leão MT, Ziemann U, Gharabaghi A. Brain State-dependent Gain Modulation of Corticospinal Output in the Active Motor System. *Cereb Cortex.* 2019; 1–11. doi:10.1093/cercor/bhz093
26. Hamada M, Galea JM, Di Lazzaro V, Mazzone P, Ziemann U, Rothwell JC. Two Distinct Interneuron Circuits in Human Motor Cortex Are Linked to Different Subsets of Physiological and Behavioral Plasticity. *J Neurosci.* 2014;34: 12837–12849. doi:10.1523/JNEUROSCI.1960-14.2014
27. Hamada M, Murase N, Hasan A, Balaratnam M, Rothwell JC. The role of interneuron networks in driving human motor cortical plasticity. *Cereb Cortex.* 2013;23: 1593–1605. doi:10.1093/cercor/bhs147
28. Opitz A, Zafar N, Bockermann V, Rohde V, Paulus W. Validating computationally predicted TMS stimulation areas using direct electrical stimulation in patients with brain tumors near precentral regions. *NeuroImage Clin.* 2014;4: 500–507. doi:10.1016/j.nicl.2014.03.004
29. Vink JJT, Petrov PI, Mandija S, Dijkhuizen RM, Neggess SFW. Outcome of TMS-based motor mapping depends on TMS current direction. *bioRxiv.* 2018; 371997. doi:10.1101/371997
30. Jonker ZD, van der Vliet R, Hauwert CM, Gaiser C, Tulen JHM, van der Geest JN, et al. TMS motor mapping: Comparing the absolute reliability of digital reconstruction methods to the golden standard. *Brain Stimul.* 2019;12: 309–313. doi:10.1016/j.brs.2018.11.005

31. Janssen AM, Oostendorp TF, Stegeman DF. The coil orientation dependency of the electric field induced by TMS for M1 and other brain areas. *J Neuroeng Rehabil.* 2015;12: 1–13. doi:10.1186/s12984-015-0036-2
32. Rothwell JC, Hallett M, Beradelli A, Eisen A, Rossini P, W P. Magnetic stimulation: motor evoked potentials. *Electroencephalogr Clin Neurophysiol Suppl.* 1999;52: 97–103. doi:10.1016/j.parkreldis.2013.07.017

Chapter V

Validating models of TMS effects with
concurrent TMS/fMRI

Abstract

The exact dose and spatial pattern of brain activation induced by transcranial magnetic stimulation (TMS) are of importance to all applications of TMS, both for clinical and investigational use. How TMS coils induce electrical fields have been investigated and validated by several groups, but models of how evoked currents interact with neuronal tissue and where activation is induced have hardly been validated empirically.

In chapter 2, we have outlined a detailed model of TMS-induced currents in the brain building on our TMS coil models, taking into account various electromagnetic head tissue properties with finite element modeling and several competing macroscopic models of how brain activation is achieved by the TMS induced electrical field. Here, we validate this model using TMS coil discharges administered to the brain of 6 healthy volunteers inside a 3T MRI scanner while acquiring functional MRI scans at the same time.

We conclude that the mere magnitude of the electric field in the cortical gray matter tissue near the stimulation site provides the best metric to predict neuronal activation as measured by BOLD fMRI, whereas models of brain activation taking into account orientation of E-fields relative to the cortical columns and layers do not (yet) yield better predictions of neuronal activation induced by TMS.

This report is relevant for neuronavigated TMS approaches attempting to take into account evoked E-fields and neuronal activation to improve the precision of TMS administration for clinical and investigational purposes.

Introduction

Transcranial magnetic stimulation, a method generating focused magnetic field pulses over the scalp that penetrate the head, is increasingly used to non-invasively investigate brain function, and treat or diagnose conditions affecting the human brain (Rossini & Rossi, 2007). However, many details regarding the exact effect of TMS-induced currents on the underlying brain tissue are poorly understood, hampering the efficient and reliable application of TMS and preventing proper dose control. Hence, TMS treatment attempts and TMS-based brain research can be unreliable.

This gap in our understanding of TMS has spurred several groups to attempt to model the electrical fields induced in the brain by the rapidly changing magnetic field induced by a TMS coil. To this end, realistic models of magnetic fields generated by a TMS coil were developed and empirically validated (Petrov, Mandija, Sommer, Van den Berg, & Neggers, 2017; Salinas, Lancaster, & Fox, 2007). Furthermore, the effect that the electromagnetic properties of the different tissues in the head have on the incident field produced by the TMS coil has now been modeled with finite element modeling (FEM) or boundary element modeling (BEM), thus taking into account the conductive effects of tissues in the head (Opitz, Windhoff, Heidemann, Turner, & Thielscher, 2011; Salinas, Lancaster, & Fox, 2009; Thielscher, Opitz, & Windhoff, 2011), for an overview see our recent review paper (Neggers, Petrov, Mandija, Sommer, & van den Berg, 2015). The total electric field injected by TMS inside an actual human head and brain can hence be assumed to be known to a certain extent.

How this E-field and ensuing electrical currents in the brain then evoke neuronal activation in terms of neuronal depolarization and action potentials is still a matter of considerable debate. It is widely accepted that electric potentials oriented along the main axis of a neuron (from the soma and along the axon), result in the lowest thresholds for depolarization and action potential generation (Day et al., 1989). This has led to the formulation of the macroscopic cortical column cosine (C3) model of neuronal activation by an induced E-field (Fox et al., 2004). The neuronal column is a fundamental principle of neuronal organization within the cortical sheet where the main axes of neurons are oriented in small functional columns perpendicular to the cortical sheet (Hubel & Wiesel, 1979). Hence, it is assumed that E-fields perpendicular to the cortical sheet (wherever they are deployed) are maximally effective in inducing neuronal activation. This is described by activation being proportional to the cosine of the E-field and the normal to the cortical surface at a given location (i.e. with maximally induced activation for E-fields perpendicular to a local patch of cortical sheet). Therefore, activation is based on cortical orientation relative to the induced field and not on whether the local cortical surface is in a sulcus or a gyrus. Gyral crowns are usually oriented in parallel to the scalp and due to the common coil orientation also in parallel to the majority of the applied E field. This dominant orientation of the gyral

crowns relative to the applied fields makes the gyral crowns less susceptible to the TMS E-field. Deeper within a sulcus, the cortical surface is oriented perpendicular to the scalp and the C3 model predicts more activation here (this effect is of course to be regarded on top of the strong reduction of induced field strength further away from the TMS coil, which in turn favors gyral crowns). Some reports claim empirical evidence for such an activation preference for the medial surface deeper in a sulcus with PET and suprathreshold TMS (Fox et al., 2004) or by the ability to explain angular dependency of coil orientation relative to the gyral orientation (Brasil-Neto et al., 1992; Kammer, Vorweg, & Herrnberger, 2007; Petrov et al., 2017). However, the cosine model is also criticized (Bungert, Antunes, Espenhahn, & Thielscher, 2017). A few studies observed that, using subthreshold concurrent TMS/fMRI, the gyral crowns are activated rather than deeper sulci (Takano 2004, Siebner 2001, Bungert 2017 p5092). Some of the most detailed modeling studies of motor cortex activation (Salvador, Silva, Basser, & Miranda, 2011) also do not show a strong preference for sulcal wall activation.

Furthermore, one can argue that the cosine model, despite correctly posing that E-fields oriented along a cortical column of neurons most likely activates those neurons most effectively, ignores the fact that many of the main glutamatergic excitatory neurons in the cortical columns are interconnected horizontally by GABAergic inhibitory interneurons (Tremblay, Lee, & Rudy, 2016). One could speculate that an induced E-field polarizing and hence inhibiting such inhibitory interneurons could contribute to a maximal release of inhibition on and subsequent activation of the disinhibited cortical column neurons. This in turn would predict the opposite of the C3 model, namely activation preferentially in gyral crowns where E-fields are parallel to the main orientation of interneurons, and much less deep in the sulci. We refer to this as the C2 hypothetical activation model.

Finally, it is possible that, due to the complex interplay between cortical columns and horizontally oriented interneurons, there is not a clear preferential influence of the E-field orientation on the neuronal activation in a patch of the cortical sheet, which we refer to here as the 'CE' model. In the present study, we put these 3 possible models of how the orientation of TMS-induced local E-fields evokes neuronal activation in the cortical sheet local to the center of the TMS pulse to the test. We use concurrent TMS with fMRI on healthy volunteers and a pipeline of computational modeling of coil E-fields and induced fields in the brain. First, we describe the MRI image processing and volumetric parcellation to construct proper FEM models of induced currents by TMS and detail the solving of the FEM equations. Then we proceed to elaborate a formal description and implementation of the 3 possible models for locally induced neuronal activation as introduced above. Finally, we describe the empirical concurrent TMS-fMRI technique we developed for this study, the data fMRI analysis, and how we appraise the overlap between empirically observed with computationally derived activation.

Methods

This study contains 2 major sections:

a) constructing a model of a TMS coil and incident evoked E-field, the ensuing induced E-field as approximated by finite element modeling taking into account 5 tissue types in the head, and several crude macroscopic models of brain activation by locally directed E-fields.

b) the empirical validation of the modeled brain activation from the previous section with a dedicated concurrent TMS/fMRI setup in 6 subjects

The first part of this methods section describes the modeling part in detail, whereas the 2nd part describes the experimental and data analysis approach.

Models of TMS evoked brain activation

In chapter 2 we describe the magnetic field evoked by the TMS coil model, how it evokes an incident E-field in the head, and how we segment a T1 weighted MRI scan into 5 tissue types and construct a volumetric mesh from those segments. In chapter 2 we also describe the finite element model (FEM) and induced E-field is provided, and 5 macroscopic models of how an E-field might interact with cortical neuronal tissue to evoke activation. We refer to chapter 2 for all details of the model validated here, except for the models of the neuronal coupling as for the experiments discussed here, some changes apply, which are explained below.

Macroscopic models of brain activation in the cortical sheet

In chapter 2 we outlined 5 potential mechanisms for interaction between the evoked E-field and neuronal activation. Note that 2 of those neuronal coupling models are only relevant for monophasic TMS coils (C4 and C5), as they are asymmetric (respond differently for a reversed current) whereas the MR compatible coil and

stimulator we have available in this experiment has a biphasic pulse shape. This leaves only 3 macroscopic models for the neuronal coupling to use in the current experiments: CE, C2, and C3, as they respond the same way for reversed current directions. Therefore these 3 models are briefly described again below for clarity.

Each ‘metric’ represents a macroscopic model of how the total E-field experienced by a small patch of the cortical sheet acts on pyramid cells within that patch, reflecting knowledge of the microscopic structure of the cortical sheet. Per metric, we also developed a method to implement such metrics on a surface mesh of the cortex. This allows us to experimentally validate these models with concurrent BOLD-fMRI on the same subjects for which the cortical mesh, FEM, and the three metrics suggested.

Figure 1 illustrates each of the metrics of neuronal activation by a locally induced E-field: C3 (activation-induced at descending tracts), C2 (activation induced by interpyramidal connections), and CE (strength of total E-field). Also, the approximation of each activation metric by a triangular surface mesh has been depicted for each metric at several locations on a gyrus.

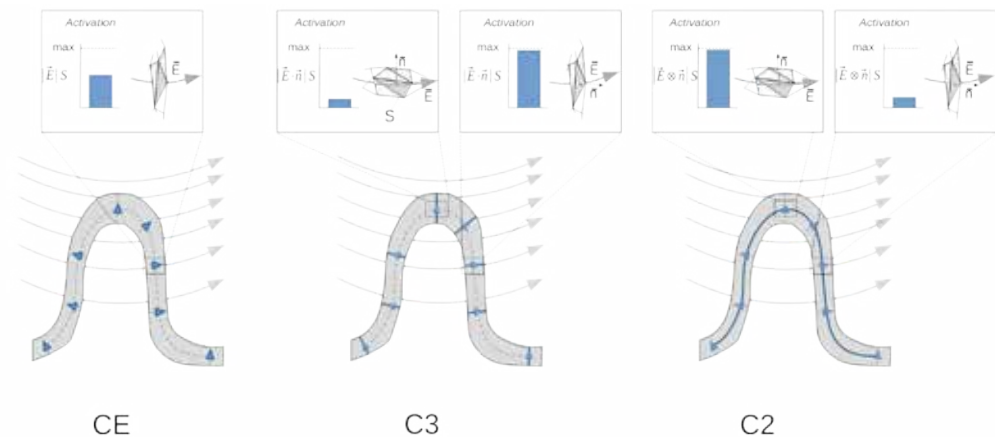


Figure 1: Illustration of the effect of each metric on the final estimate of the effectiveness of stimulation on a highly idealized folded cortical surface of a human cortex in 2D, for one gyrus in 3 situations. The curved grey lines denote the E-field (E) evoked by a TMS stimulus, S is the area of a surface patch, and n is the surface normals. The panels depict the geometrical relationship between a surface polygon normal n and the estimated E-field, given for the center of the polygon.

CE: the activation per surface mesh element equals the size of the E-field times the area of the surface it passes through, independent from the current direction.

C3: for each surface element, the resulting activation is the product of the surface area and the size of the vector product of the E-field and surface normal (size of both vectors times the cosine of the angle between them). This is maximal for a surface patch along the sulcal wall and minimal for a surface patch on the gyral crown.

C2: for each surface element, the resulting activation is the product of the surface area and the size of the cross product of the E-field and surface normal (size of both vectors times the sine of the angle between them). This is minimal for a surface patch along the sulcal wall and maximal for a surface patch on the gyral crown.

Below, each metric is briefly described again. A more detailed description and motivation can be found in chapter 2.

Metric C3. The motivation for this metric is influenced by the fact that neuronal axons oriented perpendicular to the cortical sheet, potentially descending tracts, cause the majority of evoked activations by TMS, and hence are stimulated optimally with currents perpendicularly to the cortical sheet. This has been dubbed the ‘C3’ metric for the relationship between currents and neuronal activation (Fox et al., 2004). See figure 1 for a graphical depiction.

When approximating the cortical surface with a triangular surface mesh, as depicted in figure 1 per metric, a surface patch with a set of triangles would experience the total ‘activation’ of the inner product between the surface normal of each triangle and the total E-field through that triangle (maximal for a local E-field aligned with the surface normal), multiplied by the surface of that triangle S , yielding the term $|\vec{E} \cdot \vec{n}|S$ summed over all triangles in a patch. The absolute value is used because we assume a symmetric interaction for inward and outward E-fields (see below), due to the bi-phasic stimulator we employ

Metric C2. It could also be that local horizontal connections between pyramid cells in the cortex, through inhibitory interneurons (Tremblay et al., 2016), produce most of the activation induced by local fields. In such a case, currents in parallel to a cortical tissue would evoke maximal neuronal activation (or suppress it maximally). This metric we dub C2 is also sketched in figure 1.

For C2, a cortical sheet approximated by a surface with a set of triangles would experience the total ‘activation’ of the length of the outer product between the surface normal of each triangle and the total E-field through that triangle (maximal for a field perpendicular to the normal), again multiplied by the surface of that triangle S , yielding the term $|\vec{E} \otimes \vec{n}|S$ summed over all triangles in a patch. The absolute value is used because we assume a symmetric interaction for inward and outward E-fields (see below).

Metric CE. Finally, we adopt the notion that perhaps the mix of neuron types found in the cortex is too complex for such a simple and crude neuronal metric of activation, and that the best predictor for activation is simply the magnitude of the local E-field without taking into account its direction. We describe this metric as ‘CE’. A surface

patch representing the cortical sheet would for this simple metric contribute $|\vec{E}|S$ per triangle, where S is the surface of each triangle.

Figure 2 depicts how our implementation of these metrics leads to surface-represented predictions of neuronal activation induced by TMS for an actual surface mesh of the cortical sheet of one of our participants.

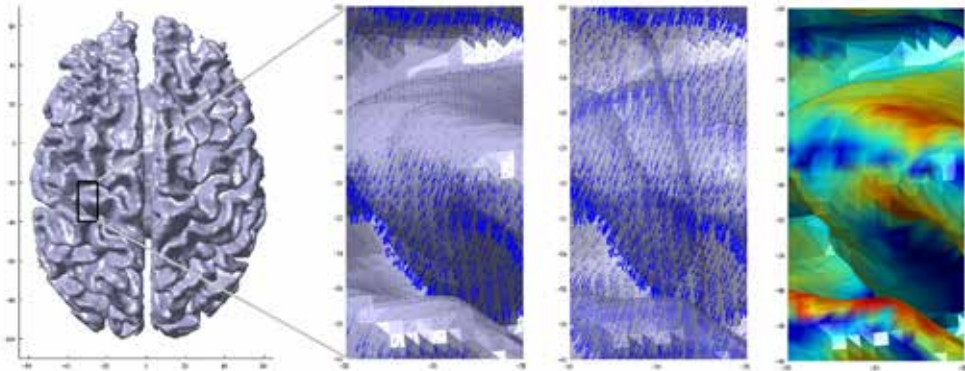


Figure 2: Illustration of the metric computation for one region of the motor cortex. Left panel: surface rendering of the surface halfway through the gray matter sheet (in between the pial surface and GM-WM border). Middle panels: visualization of all surface normals (blue arrows) on a zoomed-in section around the hand knob (right subpanel with transparent gray matter surface). Right panel: same zoomed in section around the hand knob, color-coded with the metric C3 for each patch.

Validation of modeled brain activity patterns with concurrent TMS/fMRI

In 6 healthy individuals, we evoked brain activation with TMS inside a 3T MRI scanner. To this end, a dedicated concurrent TMS/fMRI setup was used. The human primary moto-cortex area-M1 was targeted with single-pulse TMS (spTMS) at 2 intensities, and the ensuing fMRI time series were acquired. It was investigated whether evoked BOLD activation near the stimulation target matches modeled ‘activity’, by using FEM-derived total E-fields based on individual brain morphology as described in the previous section and the 3 aforementioned activation ‘metrics’, confined in the gray matter. It is analyzed which of the metrics results in the best match with measured fMRI BOLD responses to TMS.

Details of the experiment and comparative analysis are provided below.

Participants

6 healthy individuals (1 m, 5 f, mean age 22.8 yr) were included in this study. All participants were screened for contraindications against MRI or TMS, and provided written informed consent. Procedures were approved by the Medical Ethical Committee (METC) of the UMC Utrecht (protocol number 16-469).

Concurrent TMS/fMRI experimental setup.

This section provides a summary of the dedicated concurrent TMS/fMRI setup used in this study. Details can be found in 2 of our previous studies where the same setup was used (de Weijer et al., 2014; Vink et al., 2018).

All MR sequences were performed in a 3T MR scanner (Achieva, Philips Healthcare, Best, The Netherlands).

Experimental design

The experiment consisted of a short intake session ((f)MRI -only) and a TMS session (concurrent TMS-MRI) on a different day.

During the intake session, a normal 8-channel SENSE enabled head coil was used and subjects were placed in a standard position during head scanning. A 3D T1 weighted anatomical scan was acquired with a TR/TE of 10.0/4.6 ms, a flip angle of 8°, voxel size of 0.75x0.75x0.8 mm³, scan duration of 677 s, 225 slices with a slice gap of 0 mm. Next, a single-shot echo-planar imaging (EPI) scan was acquired with 250 dynamics, a TR/TE of 2,000.0/23.0 ms, flip angle of 70°, voxel size of 4x4x4 mm³, a scan duration of 510 s and 30 slices with a slice thickness of 3.6 mm and a slice gap of 0.4 mm. Participants moved the thumb of the right hand after hearing of an auditory cue. The functional data was analyzed to determine the representation of the thumb area in the left M1 as determined with BOLD fMRI. Preprocessing and statistical analysis are described in the data analysis section below. Also during the intake session, the resting motor threshold (RMT) was determined by stimulating the primary motor cortex while increasing the TMS stimulator output until a response in the APB muscle was visible in 5 out of 10 TMS pulses[26].

The TMS session started with neuronavigation to determine the coil position overlying the individual participants M1, using The Neural Navigator by Brain Science Tools BV, the Netherlands (www.brainsciencetools.com). Neuronavigation was

performed outside the MRI scanner in a separate room, and M1 was marked on a bathing cap the participants were wearing. The T1 weighted anatomical scan from the intake session was used for neuronavigation. Based on the 3D brain surface, the M1 target was obtained from the activation map acquired during the intake session and used as a target during neuronavigation. Thereafter, the participant was placed in the MRI scanner with the concurrent TMS/MRI setup and underwent a combined TMS-fMRI sequence in which single TMS pulses were delivered to M1. Finally, a T2-weighted scan was acquired to retrospectively verify TMS coil placement. For details on coil position reconstruction from the T2 weighted MRI, see Vink et al (2018) and De Weijer et al (2013).

After successful TMS coil positioning, two sequences were acquired. First, a T2-weighted scan with a TR/TE of 13,609.0/80.0 ms, flip angle of 90°, voxel size of 2x2x2 mm³, scan duration of 218 s. This was done by attaching 6 custom made markers (small capsules filled with water) to the back of the TMS coil (Fig. 2B), which appear hyper-intense on the T2-weighted scan (Fig. 1). Second, a single-shot EPI sequence was acquired with 500 dynamics, a TR/TE of 2,000.0/23.0 ms, flip angle of 70°, FOV of 256x119.6x208 mm³, matrix of 64x63, voxel size of 4x4x4 mm³, scan duration of 1020 s, 30 slices with a slice thickness of 3.6 mm and a slice gap of 0.4 mm. During the EPI sequence, single pulses of TMS with an intensity of 115% RMT were interleaved with pulses with an intensity of 60% RMT. TMS pulses were delivered with a random interval of 5 to 8 dynamics (10 to 16s) to avoid habituation. It has been shown that the MRI static magnetic field affects the flow of current through the TMS coil, which reduces the TMS magnetic field amplitude[28]. Therefore, we decided to set the RMT at 115% instead of 110% for suprathreshold stimulation.

fMRI data analysis

fMRI time series data were analyzed using SPM12 and several custom Matlab scripts, all running in a Matlab R2014a environment (Mathworks Inc., USA).

First, all EPI volumes were inspected to determine image quality and to identify the presence of potential artifacts. This revealed small random deflections from the baseline signal level in a single slice of a few functional volumes per time series acquired during the TMS session. A small number of artifacts were present in most of the time series data, most likely caused by manually changing the TMS device intensity in between TMS pulses (and hence charging the stimulator capacitors). These deflections are short (one sample) and can only be observed in the vicinity of the TMS coil. All slices of the realigned EPI scans were automatically scanned for the presence

of a sharp peak in the average grey matter signal with a custom algorithm to detect distortions. The distorted slices were then interpolated based on the BOLD signal in the previous and next slice with custom Matlab code. An average of 71 slices were interpolated per participant, out of a total 30 slices and 500 volumes.

Likely, the removal of the large artifacts due to coil charging does not rule out smaller fluctuations that might still be present in the data (see results section).

Next, the fMRI and anatomical MRI data were preprocessed. The functional MRI time series were corrected for head movement using least-square minimization and rigid body transformations (REF). Next, the time series data was coregistered (not resliced) to the T1 weighted anatomical scan using a rigid body transformation and a mutual information registration method from SPM12. The images were then smoothed with 8mm full-width at half maximum.

Next, a GLM approach was adopted to compute the amount of activation observed on average for the 2 intensities of TMS stimulation. The generalized linear model (GLM) included two events: single pulses of 115% RMT and 60% RMT. The BOLD response was modeled with the canonical hemodynamic response function (HRF) and its first-order derivative. Two nuisance regressors were included in the analysis: the average BOLD signal in the white matter and the CSF. BOLD signals were filtered with a high pass filter of 80Hz before the construction of the GLM. Statistical images were constructed based on the contrast between TMS pulses of 115% RMT and TMS pulses of 60% RMT using a T-statistic with a threshold at $P < 0.05$, family-wise error (FWE) corrected [27].

Finally, the activation maps (T-maps and contrasts) were resliced to the lattice of the T1-weighted anatomical scan for proper comparison with the model values, also expressed in this lattice (see below).

Note that the above analysis does not include a normalization to MNI space, the data stays represented in so-called ‘native space’ as they were oriented in the MRI scanner. This was needed as the coil, FEM, and activation metric modeling described above had to be performed in native space as well, and it is our goal to compare BOLD activation with models. As the participants had to maintain a tilted head angle in contrast to the normal posture to allow for placement of the TMS coil (see ‘experimental setup’ above). This native space data is less suitable to display activation maps graphically as slicing would be under an oblique angle. The activation maps and anatomical scan were normalized to MNI space using the normalization parameters from the unified segmentation step described in the session on volumetric meshes above. This was purely done for visualization purposes of the fMRI BOLD data, all analyses are performed in native space.

Comparison of fMRI activation maps with modeled brain surface ‘activation’

fMRI activation maps, analyzed as the GLM regression coefficients (contrast maps) reflecting relative signal change induced by TMS as described above (high intensity versus low intensity), need to be compared to the surface triangulation-based modeled ‘activation’ maps described in the previous section. The fMRI maps are expressed in a rectangular grid compliant with the Nifti v1.1 data specifications (according to the T1-weighted anatomical scan because of the reslicing, see the previous section), but the modeled ‘activation’ comes as a value per triangle on the extracted brain surface. Hence, we need to convert the modeled activation from a triangular surface representation to a matching rectangular grid. We accomplished this as follows. While iterating over all triangular faces representing the brain surface and having an associated model ‘activation’, we computed for each triangle which grid points in the lattice of the T1 weighted anatomical scan are closer than 1.5mm to the triangle (shortest orthogonal distance to the triangle). Those lattice points (voxels) were given the value of the model ‘activation’ associated with that triangle as explained in the previous section. All voxels not in the vicinity of any triangle are given the value zero.

This way, we obtain an ‘activation’ map in the same image lattice as the analyzed fMRI bold activation maps so they can be compared. In this created image, all activation values are constrained in the gray matter by virtue of the above procedure. An example of such a model activation map is given in figure 3 below.

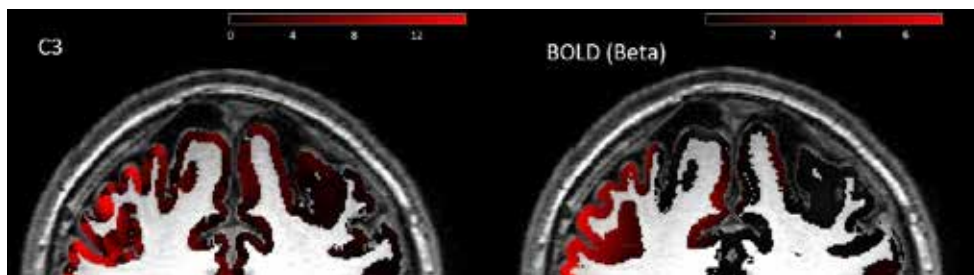


Figure 3: ‘Activation’ maps as assessed in the gray matter portion of a coronal slice of a participant MRI image, in the same rectilinear image lattice for the analyzed fMRI bold activation maps (right panel) and the C3 metric (left image) that is originally obtained on a surface mesh, allowing direct comparison. In this created image, all activation values are constrained in the gray matter by virtue of the processing pipeline discussed in this section.

For a proper comparison, the fMRI activation maps, represented by the contrast between high and low-intensity stimulation (difference between β_{high} and β_{low}), are also masked by the gray matter indexed map obtained from tissue segmentation (see the section on ‘Models of TMS evoked brain activation’) such that

voxels outside the gray matter are set to 0. This procedure assures the modeled ‘activation’ can be compared to the measured BOLD activation in a rectangular lattice (a ‘voxel based’ comparison).

The overlap between the measured BOLD activation map and the modeled activation (for each metric) forced into a rectangular lattice representation as described above is assessed as follows. First, both the BOLD fMRI activation map and the modeled ‘activation’ map are thresholded at a ratio of 0.3 (30%) of the maximum activation value, where values below the threshold are set to 0 and above the threshold to 1. Then, the Dice Sørensen coefficient (DSC) is used to compute the overlap between the two images. This DSC index originally stems from agriculture, and was used to compare vegetation on fields, and has later been adopted for comparing binarized medical tissue images in segmented images, including brain segmentations (Baselice, Ferraioli, & Pascazio, 2015; Zou et al., 2004). This index is straightforward, and computes the fraction of overlapping voxels (3D image pixels) between 2 binarized images X and Y in relation to the total volume of the segmented image, as follows:

$$DSC = \frac{2|X \cap Y|}{|X| + |Y|}$$

This index yields a maximum of 1 when the two images compared are identical, and 0 when they are completely non-overlapping.

DSC’s are computed for the following 3 comparisons:

$$X = T(\beta_{\text{high}} - \beta_{\text{low}}); Y = T(A_{\text{CE}});$$

$$X = T(\beta_{\text{high}} - \beta_{\text{low}}); Y = T(A_{\text{C3}});$$

$$X = T(\beta_{\text{high}} - \beta_{\text{low}}); Y = T(A_{\text{C2}});$$

where $\beta_{\text{high}} - \beta_{\text{low}}$ is the contrast between high and low TMS-induced BOLD activation, A_{CE} is the model activation for the CE metric (total field) as explained in the section on modeling above. T is a thresholding function where:

$$T(x) = \begin{cases} 0 & : x \leq t \\ 1 & : x > t \end{cases}$$

The threshold value t equals 0.3 x the maximum value of the map that is thresholded. The DSC is computed for voxels within a spherical region of interest (ROI) around the location of maximum activation in the CE model. This is done to exclude voxels in regions further away from the motor cortex, that might be activated

through connections or auditory signals due to the fact that the supra-threshold TMS pulse still evokes a louder clicking sound than the sub-threshold TMS pulse. This way, the most direct comparison possible is made between directly activated cortical layers and modeled activation in cortical layers.

Results

TMS induced BOLD activation

For 6 participants, the TMS BOLD activation was analyzed as described in the methods section. The regression coefficients for high and low TMS machine output were contrasted and overlaid on the anatomical MRI of each participant. In figure 4, the fMRI activation for high versus low machine output TMS is presented in a slice through the motor cortex for 2 participants.

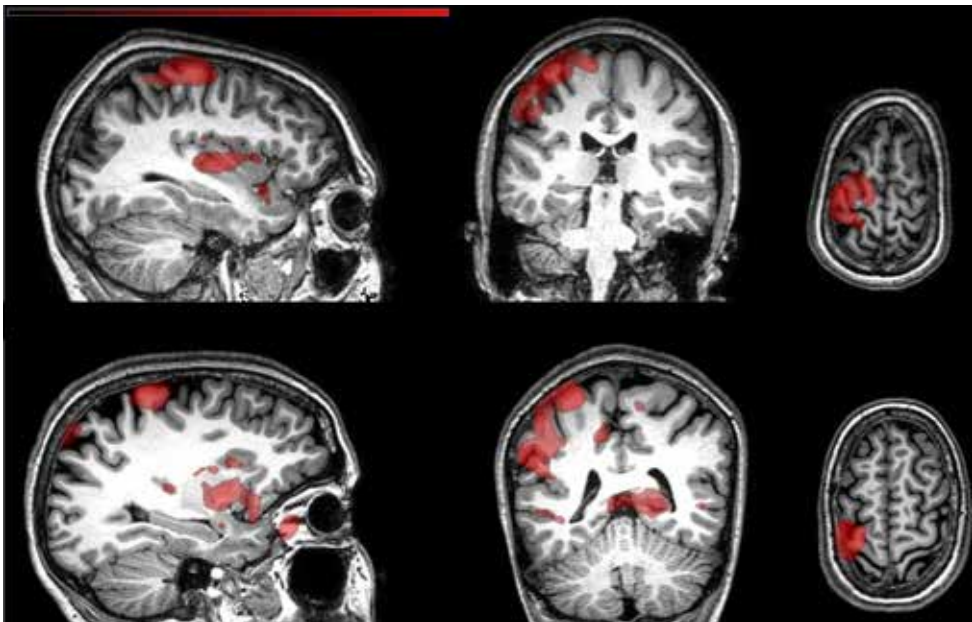


Figure 4: TMS-induced BOLD activation maps for high versus low machine output TMS overlaid on the T1 weighted MRI for 2 participants (top panels denote one participant, bottom panel another participant), in sagittal, coronal and axial view (from left to right).

There is an area of activation near the targeted region for most participants. Targeting was not always successfully maintained while the setup was in the MRI bore, sometimes regions near but not exactly on the motor cortex were targeted with the isocenter of the TMS incident field (also see figure 5 with 3D renderings). Activation

in the targeted motor cortex area tends to be in the more superficial parts of the cortical sheet (the gyral crowns) and not so much in the deeper parts of the sulci.

Also, in the left temporal lobe, there is a larger cluster of activation for some participants, that extends into non-neuronal tissue outside the brain. We believe this is an artifact due to the manual alteration of intensity during the experimental session, as explained in the methods section ('fmri activation analysis'). In the 3D renderings of BOLD activation below, it can be seen that these potential artifacts are close to the coil wing near the temporal lobe, especially when the coil deviated from its ideal position parallel to the scalp. For this reason, the BOLD activation was only evaluated within a ROI of 4cm around the maximum model activation (generally near the maximal field center line of the coil, see methods section), largely excluding this artifact from the assessment.

Comparison of model and BOLD activation patterns

As described in the methods section, the DSC was computed to compare the overlap of the model and BOLD activation for each of the 3 metrics. See figure 5a and 5b below for 2 participants, where a cortical rendering is presented of TMS-evoked BOLD activation and modeled activation for the 3 metrics. In the title, the DSC overlap coefficient between measured BOLD and modeled activation is given for each metric. The cortical renderings for all other participants are provided in the supplementary material.

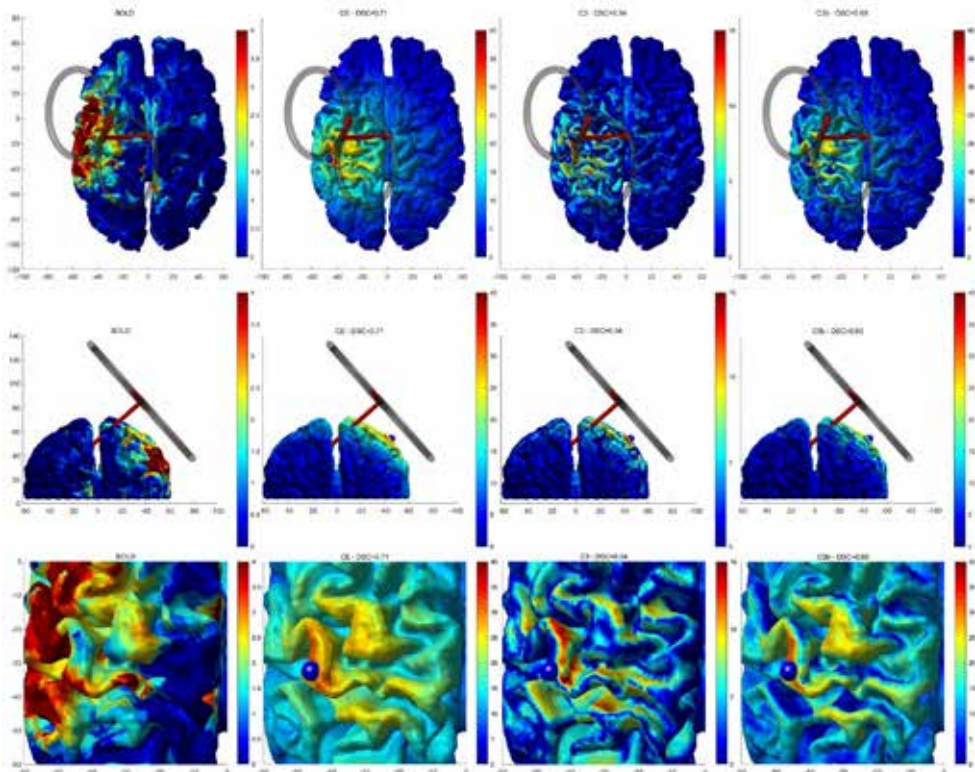


Figure 5-a: Cortical renderings of TMS evoked BOLD activation (left panels) and modeled activation for the CE, C3 and C2 metrics (from left to right). In the title, the DSC overlap coefficient between measured BOLD and modeled activation is given for each metric. Top panels and middle panels provide a top and middle view of the entire cortex, with an idealized TMS coil rendered at the reconstructed TMS coil position (from the T2 weighted MRI, see methods) and coil B-field isocenter. The bottom panels provide a zoomed-in version of the same data. The blue sphere was the center of the ROI for which the analytical comparison between observed activation (left panels) and the model activations (other panels) was computed.

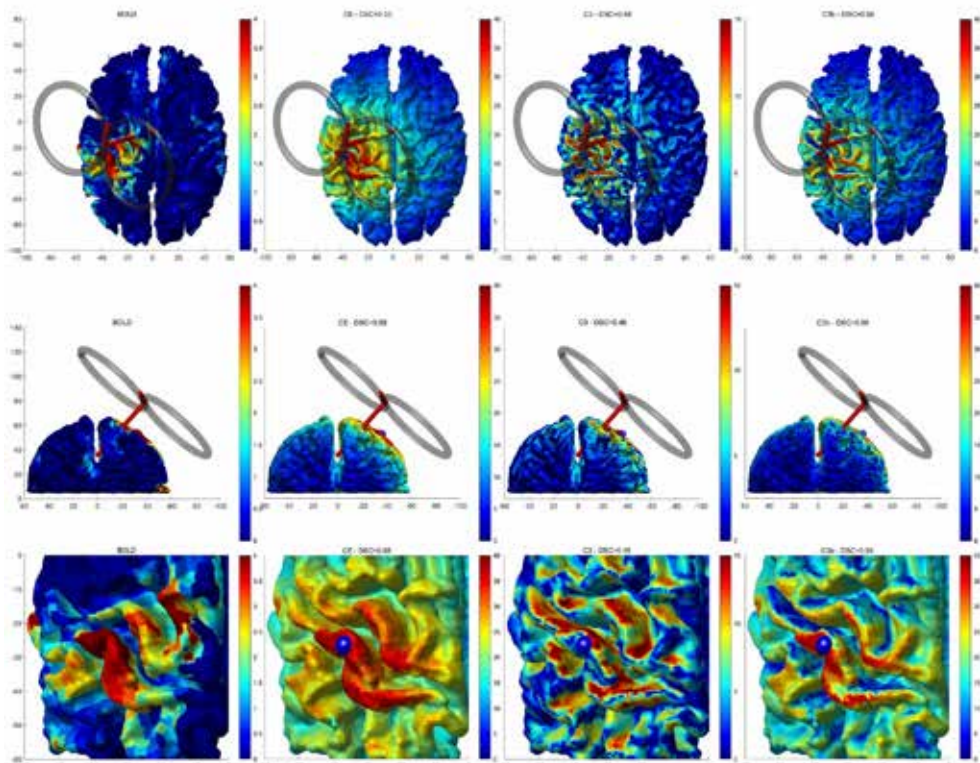


Figure 5-b: Same data as for Figure 5a, but for another participant.

As it can be seen from figure 5, for both subjects there is some spatial resemblance between the BOLD activation and especially the activation following the ‘total induced field’ metric CE and the ‘parallel’ activation metric C2 model, that all show activation primarily in the gyral crown. The C3 metric results in ‘activation’ that has maximal values somewhat deeper inside the sulci. This pattern of resemblance is reflected in a lower DSC for the comparison of activation following the C3 metric with respect to the BOLD activation.

In table 1 below, the DSC coefficients for all 6 participants are given for all 3 metrics. There is a trend for a lower DSC for overlap between measured BOLD activation and modeled activation due to C3 as compared to the other 2 metrics ($T=1.722$, $p=0.058$).

DSC	CE	C3	C2
S1	0.7108	0.5392	0.6487
S2	0.5453	0.4757	0.5634
S3	0.4685	0.4416	0.3245
S4	0.4849	0.4594	0.4303
S5	0.5849	0.4672	0.5211
S6	0.4482	0.4083	0.4064

Discussion

We managed to successfully stimulate 6 participants with TMS on or near the motor cortex while acquiring BOLD fMRI data. Observed BOLD activation tends to be primarily focused around the more superficial parts of the cortical sheet, the gyral crowns.

After segmentation and volume meshing of the anatomical T1 weighted MRI scan, calculation of the incident field of the TMS coil, and estimation of a Finite Element Model, we obtained a realistic individual total induced field pattern for the same 6 participants. We applied 3 putative models of induced E-field $\langle \rangle$ neuronal activation following different assumptions on cell types that are sensitive to TMS-induced fields: the well-known C3 cosine model assuming neurons oriented along cortical columns perpendicular to the cortical field attribute the majority of the activation, an alternative model C2 where horizontally directed interneurons contribute most to the activation or a simpler model CE where the magnitude of the total induced E-field activates neurons, irrespective of the direction of the induced E-field.

When directly comparing the observed activation with modeled activation in the cortical sheet, the most overlap was found for the CE model where no directional preference was observed. A lower overlap was found for the C2 metric of neuronal activation, and the worst-performing metric was the well-known C3 metric based on cortical column orientation.

When inspecting the measured BOLD activation and the modeled activation patterns on the cortical surface, as depicted in figure 5, the above finding seems to be largely explained by the fact that the BOLD observation is constrained to the more superficial part of the gyral crowns, rather than deeper in the sulci. Both the CE and C2 models predict more superficial ‘activation’, and hence show the most overlap with the measured BOLD activation. The CE and C2 models did not differ substantially from each other.

These findings seem to match the findings of (Bungert et al., 2017; Opitz et al., 2011, 2011) best. Their brain modeling results also exhibited the strongest

superficial rather than sulcal induced currents, which they attributed not only to the incident field strength decaying rapidly below the coil surface, but also the resistance caused by the narrow passages between the gyral crowns and the inner side of the dura mater that constrains the flow of cerebral spinal fluid. It has to be noted here that in the aforementioned studies, induced currents were assessed directly, and not through macroscopic neuronal activation metrics as attempted here. Although Bungert et al did not directly compare their modeling results to functional MRI activation in the same subjects as the present study attempted, they did analyze functional MRI literature on motor activation and concluded from that literature that indeed fMRI activation tends to be more superficial than deeper within the sulci for motor-related paradigms. The assessment by us was somewhat hampered by the necessity to use MNI space averages and infer sulcal activation maps from such reported coordinates, which can be quite different from native space non-normalized brain space, the results point in the same direction as the present study that did compare modeling work with activation directly in 6 participants.

The present study had several important limitations that need to be discussed. First, the BOLD fMRI experiments were, for some subjects, plagued by artifacts that seemed related to the manual alterations of TMS machine output during the experiment. We were able to remove the larger spikes but some more subtle activation that correlated with the super versus subthreshold stimulation paradigm adopted here, was still present in the activation contrast as can be seen in figure 5. This artifact mainly occurred near the temporal lobe directly below one coil wing. For the BOLD and model activation overlap assessment, we focused on activation near the motor cortex using a spherical region of interest approach to exclude the artifact from our results.

Second, for computational reasons, we merged the skin and skull tissue segments. This greatly simplified the volumetric meshing of those tissue volumes as the boundary between them was noisy in our data, and unsuitable for FEM. We might, however, have overestimated the secondary currents as modeled by FEM (right-most expression in equation [1]) as a result.

Third, the overlap assessment of BOLD with modeled ‘activation’ by the DSC value is probably simplistic, for several reasons. The first reason is that BOLD activation evoked by TMS reflects the full pattern of neuronal activation, both local to the TMS evoked maximal field, as well as local and distal responses to such neuronal activation through connections, through secondary activations caused by TMS such as auditory or somatosensory signals (even though we contrasted high vs low-intensity TMS there still is a difference between both conditions), and possibly through reafferent activation from evoked muscle activation due to suprathreshold stimulation. The modeled activation on the other hand only reflects directly activated cortical tissue, and completely disregards activation through local and distal connections.

Nevertheless, one can safely assume that also the BOLD activation at least reflects the same type of direct neuronal activation as the modeled direct activation, and hence shows a larger degree of overlap for correctly modeled activation.

In conclusion, the present study observed that at the moment total TMS-evoked electric field assessments as modeled by FEM are sufficient to describe neuronal activation that occurs mainly in the gyral crowns, for both BOLD fMRI and modeled activation. Activation preference for currents running in parallel with the cortical surface performed equally well, but the well-known C3 metric where the orientation of cortical columns perpendicular to the gyral wall is supposed to explain the largest part of TMS-evoked activation (Fox et al., 2004), performed worst of all 3 activation models tested. Further research with higher resolution imaging techniques should be able to better discriminate between total electric field and currents parallel to the cortical sheet, or more detailed cortical layer models.

Acknowledgments

Acknowledgements: This work was supported by the ENIAC grant entitled DeNeCor 'Devices for NeuroControl and NeuroRehabilitation'.

References

- Ashburner, J., & Friston, K. J. (2005). Unified segmentation. *NeuroImage*, 26(3), 839–851. <https://doi.org/10.1016/j.neuroimage.2005.02.018>
- Baselice, F., Ferraioli, G., & Pascazio, V. (2015). A Novel Statistical Approach for Brain MR Images Segmentation Based on Relaxation Times. *BioMed Research International*, 2015. <https://doi.org/10.1155/2015/154614>
- Brasil-Neto, J. P., Cohen, L. G., Panizza, M., Nilsson, J., Roth, B. J., & Hallett, M. (1992). Optimal focal transcranial magnetic activation of the human motor cortex: effects of coil orientation, shape of the induced current pulse, and stimulus intensity. *Journal of Clinical Neurophysiology: Official Publication of the American Electroencephalographic Society*, 9(1), 132–136.
- Bungert, A., Antunes, A., Espenhahn, S., & Thielscher, A. (2017). Where does TMS Stimulate the Motor Cortex? Combining Electrophysiological Measurements and Realistic Field Estimates to Reveal the Affected Cortex Position. *Cerebral Cortex (New York, N.Y.: 1991)*, 27(11), 5083–5094. <https://doi.org/10.1093/cercor/bhw292>
- Day, B. L., Dressler, D., Maertens de Noordhout, A., Marsden, C. D., Nakashima, K., Rothwell, J. C., & Thompson, P. D. (1989). Electric and magnetic stimulation of human motor cortex: surface EMG and single motor unit responses. *The Journal of Physiology*, 412, 449–473.
- de Weijer, A. D., Sommer, I. E. C., Bakker, E. J., Bloemendaal, M., Bakker, C. J. G., Klomp, D. W. J., ... Neggers, S. F. W. (2014). A setup for administering TMS to medial and lateral cortical areas during whole-brain fMRI recording. *Journal of Clinical Neurophysiology: Official Publication of the American Electroencephalographic Society*, 31(5), 474–487. <https://doi.org/10.1097/WNP.0000000000000075>
- Fox, P. T., Narayana, S., Tandon, N., Sandoval, H., Fox, S. P., Kochunov, P., & Lancaster, J. L. (2004). Column-based model of electric field excitation of cerebral cortex. *Human Brain Mapping*, 22(1), 1–14. <https://doi.org/10.1002/hbm.20006>
- Hubel, D. H., & Wiesel, T. N. (1979). Brain mechanisms of vision. *Scientific American*, 241(3), 150–162.
- Kammer, T., Vorweg, M., & Herrnberger, B. (2007). Anisotropy in the visual cortex investigated by neuronavigated transcranial magnetic stimulation. *NeuroImage*, 36(2), 313–321. <https://doi.org/10.1016/j.neuroimage.2007.03.001>
- Neggers, S. F. W., Petrov, P. I., Mandija, S., Sommer, I. E. C., & van den Berg, N. A. T. (2015). Understanding the biophysical effects of transcranial magnetic stimulation on

- brain tissue: the bridge between brain stimulation and cognition. *Progress in Brain Research*, 222, 229–259. <https://doi.org/10.1016/bs.pbr.2015.06.015>
- Opitz, A., Windhoff, M., Heidemann, R. M., Turner, R., & Thielscher, A. (2011). How the brain tissue shapes the electric field induced by transcranial magnetic stimulation. *NeuroImage*, 58(3), 849–859. <https://doi.org/10.1016/j.neuroimage.2011.06.069>
- Petrov, P. I., Mandija, S., Sommer, I. E., Van den Berg, C., & Neggers, S. F. (2017). *How much detail is needed in modeling a transcranial magnetic stimulation coil: measurements and brain simulations.*
- Rossini, P. M., & Rossi, S. (2007). Transcranial magnetic stimulation: diagnostic, therapeutic, and research potential. *Neurology*, 68(7), 484–488. <https://doi.org/10.1212/01.wnl.0000250268.13789.b2>
- Salinas, F. S., Lancaster, J. L., & Fox, P. T. (2007). Detailed 3D models of the induced electric field of transcranial magnetic stimulation coils. *Physics in Medicine and Biology*, 52(10), 2879–2892. <https://doi.org/10.1088/0031-9155/52/10/016>
- Salinas, F. S., Lancaster, J. L., & Fox, P. T. (2009). 3D modeling of the total electric field induced by transcranial magnetic stimulation using the boundary element method. *Physics in Medicine and Biology*, 54(12), 3631–3647. <https://doi.org/10.1088/0031-9155/54/12/002>
- Salvador, R., Silva, S., Basser, P. J., & Miranda, P. C. (2011). Determining which mechanisms lead to activation in the motor cortex: a modeling study of transcranial magnetic stimulation using realistic stimulus waveforms and sulcal geometry. *Clinical Neurophysiology: Official Journal of the International Federation of Clinical Neurophysiology*, 122(4), 748–758. <https://doi.org/10.1016/j.clinph.2010.09.022>
- Thielscher, A., Opitz, A., & Windhoff, M. (2011). Impact of the gyral geometry on the electric field induced by transcranial magnetic stimulation. *NeuroImage*, 54(1), 234–243. <https://doi.org/10.1016/j.neuroimage.2010.07.061>
- Tremblay, R., Lee, S., & Rudy, B. (2016). GABAergic interneurons in the neocortex: From cellular properties to circuits. *Neuron*, 91(2), 260–292. <https://doi.org/10.1016/j.neuron.2016.06.033>
- Vink, J. J. T., Mandija, S., Petrov, P. I., van den Berg, C. A. T., Sommer, I. E. C., & Neggers, S. F. W. (2018). A novel concurrent TMS-fMRI method to reveal propagation patterns of prefrontal magnetic brain stimulation. *Human Brain Mapping*, 39(11), 4580–4592. <https://doi.org/10.1002/hbm.24307>
- Zou, K. H., Warfield, S. K., Bharatha, A., Tempany, C. M. C., Kaus, M. R., Haker, S. J., ... Kikinis, R. (2004). Statistical Validation of Image Segmentation Quality Based on a Spatial Overlap Index. *Academic Radiology*, 11(2), 178–189. [https://doi.org/10.1016/S1076-6332\(03\)00671-8](https://doi.org/10.1016/S1076-6332(03)00671-8)

Chapter VI

Temporal control of events in a novel
concurrent TMS-fMRI setup tested on TMS of
the prefrontal cortex

Abstract

Repetitive transcranial magnetic stimulation (rTMS) has been applied increasingly to treat severe mental disorders over the last 2 decades. For example, rTMS applied over the left dorsolateral prefrontal cortex (DLPFC) provides a safe and effective treatment for selected patients with treatment-resistant major depressive disorder (MDD). Little is known, however, about the mechanisms of action of TMS in the brain, which might lead to the unreliable outcome often observed.

To better understand the mechanism of action of TMS, we devised a new setup capable of studying the effects of TMS in-vivo using TMS concurrently with functional MRI. This setup overcomes several technical hurdles present in discharging a TMS coil inside a 3T MRI environment, such as mechanical forces acting on the coil and mounts to the MRI bed, the exact timing of TMS with respect to MRI readout gradients, leaking of currents to the MR bore from a charging TMS device, and the challenge of placing the coil to frontal and lateral sites and monitoring its position. This paper describes the setup in detail and elaborates on how the specific challenges are overcome.

To test the feasibility of the approach, we applied single-pulse TMS to the left DLPFC in 10 healthy participants using this unique TMS-fMRI set-up, in which we could record the direct effects of TMS in the brain.

Stimulation of the DLPFC triggered activity in a number of connected brain regions, including the subgenual anterior cingulate cortex (sgACC) in 4 out of 9 participants. The sgACC is of particular interest because regulating the activity in this region has shown to relief some patients with depression symptoms.

We conclude that this improved concurrent fMRI-TMS method allows investigations into the neural mechanisms behind putative TMS treatment effects, and can elucidate the relevant pathways. Several future improvements are proposed based on the current study.

Introduction

Major depressive disorder (MDD) is a complex disorder characterized by a depressed mood and/or loss of interest or pleasure in (almost) all activities (American Psychiatric Association, Association, others, & American Psychiatric Association, 2013). It affects 4.7% of the global population and is the second leading cause of disability worldwide [1] [2].

MDD is currently treated by means of antidepressant medication, psychotherapy (often behavioral therapy), or some combination of these two. Treatment-resistant patients are treated with electro-convulsive therapy or, in rare cases, with deep brain stimulation.

rTMS is a targeted non-invasive brain stimulation method, with only mild side effects and has proven to be effective in the treatment of MDD [3], and has recently obtained FDA approval for its application in MDD [4].

TMS is a means of using electromagnetic induction to stimulate a brain region. Repetitive delivery of TMS pulses (rTMS) to a brain region modulates the excitability of the stimulated cortical area, inducing changes in neural plasticity [5] (Allen, Pasley, Duong, & Freeman, 2007). These neuroplastic changes outlast the duration of stimulation and are believed to be induced through long-term potentiation/depression mechanisms [6]. High (> 5 Hz) or low (< 5 Hz) frequency stimulation results in a lasting increase or decrease in excitability, respectively [7][8]. Stimulation is applied to a focal region in the brain, but the effects of TMS are not limited to the stimulated brain region but can spread to other cortical areas [9] [10][11].

Although already applied clinically, little is known about the mechanism of action of high-frequency stimulation of the DLPFC. Over the last decades, neuroimaging studies have investigated the depressed brain intensively and several neuroanatomical regions have been found to exhibit abnormal activity in patients with MDD, with the subgenual anterior cingulate cortex (sgACC) attracting the most attention. Neuroimaging studies have shown that baseline metabolic activity in the sgACC is increased in patients with MDD and that normalization of the sgACC activity correlates with relief of depressive symptoms [12][13][14][15]. It is hypothesized that rTMS of the DLPFC induces an antidepressant effect through direct or indirect neuromodulation of the abnormal activity in the sgACC [16]. MRI functional connectivity studies show that treatment outcome positively correlates with functional connectivity strength between the sgACC and the DLPFC, providing some evidence for this hypothesis [16] [17]. However, the evidence is limited and a relationship between resting state functional connectivity and the propagation of activity evoked by TMS has not been established yet.

Therefore, we designed an improved method that can be used to investigate the propagation pattern of TMS-induced activity after stimulation of the left DLPFC and other target regions relevant for TMS treatment. Because TMS effects are strongly affected by TMS coil placement (with respect to individual brain morphology), we also investigated the effect of TMS coil placement on propagation patterns of TMS-induced activity [18] [19].

Other research groups, Bohning et. al. , have preceded us in exploring concurrent TMS/fMRI. Some of the first approaches by [20], [21] with an open birdcage MR receive coil and echo-planar imaging sequences demonstrated for the first time that this technique was feasible. Later improvements by other groups included the prevention of currents from the recharging TMS stimulator (after a TMS pulse) and other high-frequency noise from outside the MRI room to leak into the MR bore, potentially heavily distorting imaging quality [22] [23], improvements of the pulse sequence and shimming techniques used [23], improved coil placement and location monitoring [24], and several more. The improved setup presented here builds upon a previous paper from our group where a new open coil array was used allowing medial as well as lateral coil placement, as more space is available to maneuver the TMS coil while still recording whole-brain EPI images, introducing this particular approach [9]. The present study adds an improved pulse sequence and improved synchronization of TMS pulse timing with respect to the MRI readout gradients using a custom-built dedicated electronics unit, which facilitates image stability and allows specific phase mapping applications described elsewhere [25].

To test the feasibility and performance of this improved setup for the investigation of treatment-relevant TMS effects in the brain, we applied single pulses of TMS to the left DLPFC during a functional MRI recording in 10 healthy participants. To assess the performance of the current setup compared to previous work, and to investigate the ability to investigate a well-known brain network, we also investigated stimulation of the thumb motor area M1, which has been studied in the majority of aforementioned studies.

We assessed whole brain network activity evoked by comparing TMS pulses at an intensity above the motor threshold with pulses below the motor threshold. We also carefully monitored TMS coil location relative to DLPFC to assess the effects of variability in coil location on evoked activation.

(The material and methods section is further extended to cover in detail the custom in-house developed electronics (sync box), allowing for precise temporal decoupling/synchronization of MR with TMS. You are reading an adaptation of the original text with additional emphasis on the setup employed in the study.)

Materials and methods

Participants

The experimental procedure was approved by the medical ethics committee of the University Medical Center Utrecht (UMCU), Utrecht, The Netherlands. All participants provided written informed consent and were screened for MRI and TMS exclusion criteria. MRI data were acquired from 10 right-handed participants (Table I). One participant had to be excluded due to unavailability for the follow-up session. During the experimental procedure, we strictly adhered to the guidelines and recommendations for TMS endorsed by the International Federation for Clinical Neurophysiology [26].

Table I. Participant details. The MNI coordinates of the normalized center of gravity (COG) of the TMS area are shown for each participant. The TMS area is based on initial TMS coil placement and corrected for subsequent head motion during image acquisition. The maximum displacement of the TMS target from the center of gravity reflects the effect of head movement on the displacement of the TMS coil isocenter.

Participant number	Sex	Age	RMT [%MO]	Comment	COG of TMS area			Max displacement from the COG (mm)	TMS-MRI of M1
					X	Y	Z		
1	F	21	66		-43	23	45	4.4	Yes
2	M	34	73		-25	18	62	3.3	No
3	F	25	76	Excluded	-	-	-	-	-
4	M	18	58		-29	41	37	6.1	No
5	F	19	83		-33	25	47	5.2	Yes
6	F	24	83		-30	33	41	5.0	Yes
7	M	23	80		-29	28	52	2.1	Yes
8	F	20	78		-35	25	47	3.6	Yes
9	F	19	83		-33	22	57	2.9	Yes
10	F	20	82		-30	14	51	2.5	No

Experimental Setup

Our concurrent TMS-fMRI setup has previously been used to successfully detect TMS-induced activity in the motor network in response to TMS pulses delivered to the primary motor cortex (M1) of healthy participants [9]. The main changes are the improved synchronization of the TMS pulse administration with MR readout gradients, and the pulse sequence.

Overview

The setup we devised consists of a relay box preventing leakage currents from the stimulator from distorting the MRI image acquisition, consisted of MR compatible TMS coil, a safety box, a 3T MRI scanner, and finally a connected synchronization box to operate and synchronize the relay box and the TMS device with MRI acquisition

Figure 1 below presents an overview of the entire setup where arrows denote the flow of connectivity between each component. There were two key control pathways responsible for controlling the relay box CS2 and triggering the TMS machine CS1.

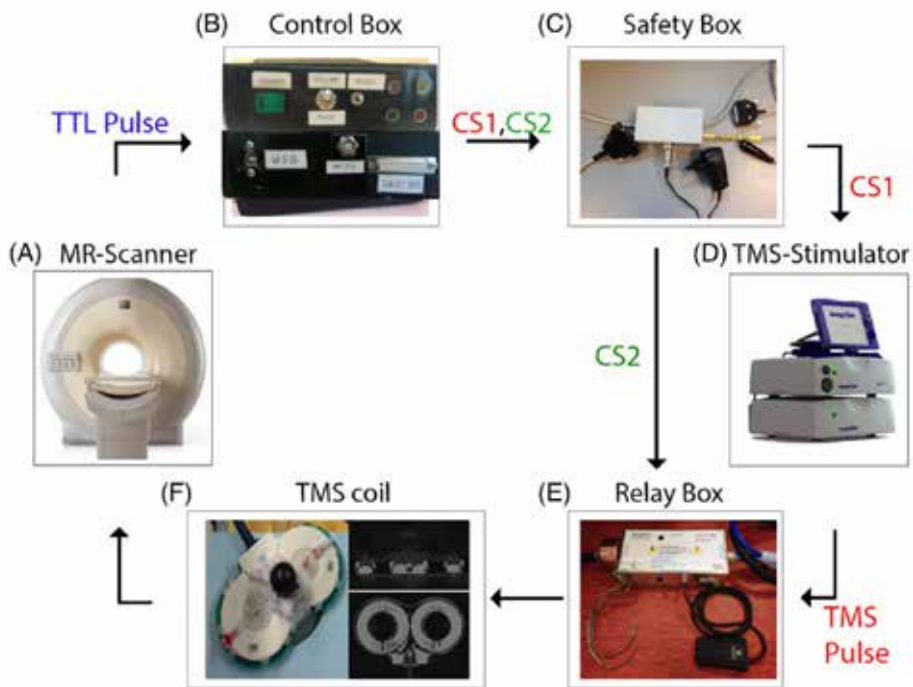


Figure 1: The integrated transcranial magnetic stimulation (TMS)-MRI setup: A, 3-T MR scanner (Achieva, Philips, Best, the Netherlands); B, control box; C, safety box; D, TMS stimulator (Magstim Rapid2, Whitland, Carmarthenshire, UK); E, filter box (Magstim Rapid2); F, MR-compatible TMS coil (Magstim Rapid2); X-ray images were obtained using a C-arm (BV29, Philips) Adaptation from original published work of Mandija et. al. Figure1 [25]

TMS stimulator and MR-compatible coil

A bi-phasic Magstim Rapid2 magnetic stimulator and an MR-compatible TMS coil were used. We measured the pulse shape with an oscilloscope, the results are displayed in Figure 2-A. Multiple measurements were conducted starting from 1% to

17% using a circular (2cm) pick-up coil at 3cm from coil iso-center. In Figure 2b you can see an X-ray of the coil where the wiring is visible.

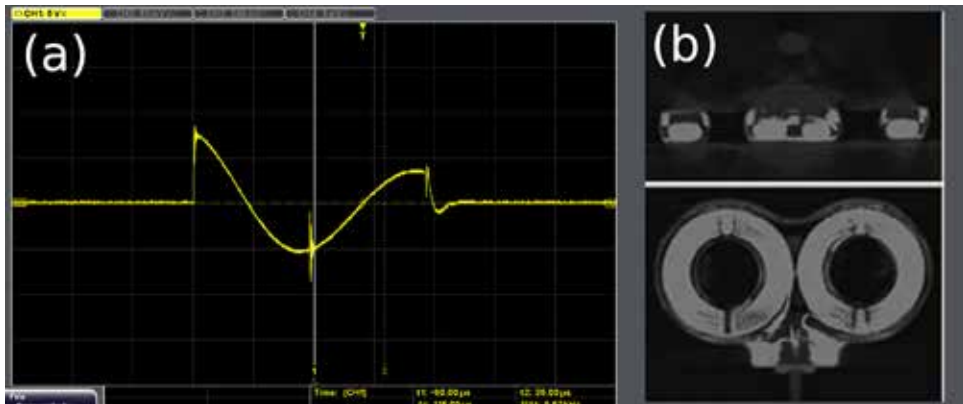


Figure 2: On the left (a) screen export from the oscilloscope device, plotting the induced voltage in a pick-up coil 3cm from coil surface iso-center using 17% TMS MO. On the right (b) the bottom and side-way X-ray scan

RF filter box with leakage relay

The TMS filter box manufactured by Magstim Inc., UK was used between the TMS stimulator and the MR-compatible TMS coil, mounted on and earthed with the waveguide tube in the wall of the MRI room. It operates a relay that is closed only during the TMS pulse, and open otherwise, thus preventing leakage of currents induced during re-charging of the large capacitor-bank in the TMS stimulator. It also filters out RF noise from outside the MRI room. Its function is described in detail elsewhere [22]. A drawing of the main circuits inside the filter box (taken from Weiskopf et al) is provided in Figure 3.

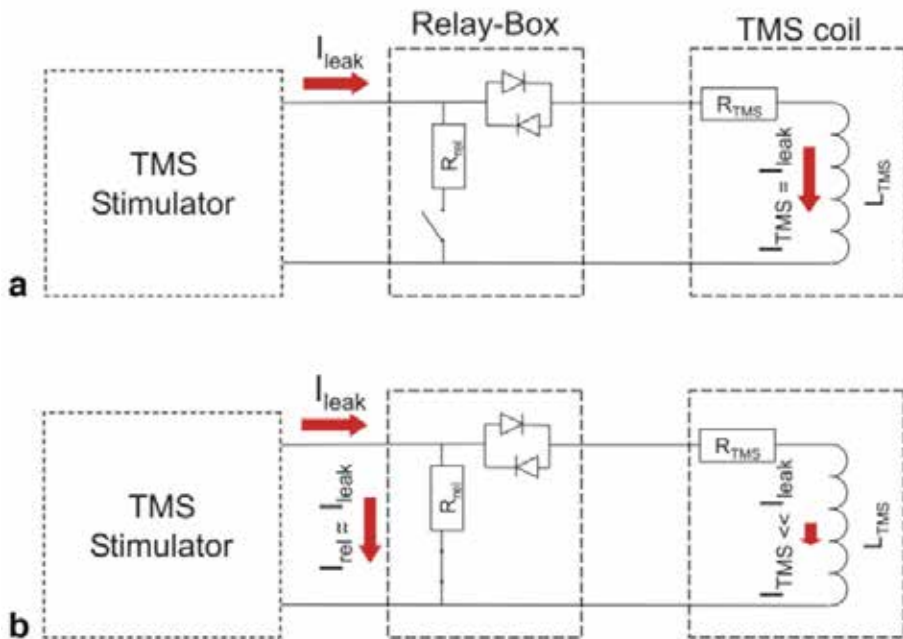


Figure 3: Minimizing leakage currents through the TMS coil. (a) Low-frequency leakage currents I_{leak} are only limited by the low resistance R_{TMS} of the TMS coil. Therefore, even small residual voltages can cause significant leakage currents I_{TMS} flowing through the TMS coil. (b) To minimize I_{TMS} , a relay with minimal resistance R_{rel} is inserted in parallel to the TMS coil and two high-voltage diodes are inserted in series. The diode arrangement ensures that the effective coil resistance R_{TMS} is very large ($>100\text{ k}\Omega$) when the voltage across the coil and diodes is less than 0.5 V. When the relay is closed it shorts the leakage current, preventing it from flowing through the TMS coil. (Figure 1 in the original publication [22])

Synchronization box

An important addition to the previous setup is a greatly improved synchronization between the TMS pulse, the MR readout gradients and the opening and closing moment of the filter box relay (see section), using the so called ‘sync box’ designed especially for this setup. The sync box input is the TTL pulse arriving from the MR scanner indicating the moment of the RF excitation pulse, and the outputs are connected to the filter box and the TTL trigger input of the TMS main unit. It is fully programmable and operates at microsecond precision. The main purpose of the sync box is to guarantee the triggering of the TMS pulse at a fixed interval after the MRI TTL pulse, and precise closing and opening of the relay in the filter box to prevent leakage currents from entering the MRI room.

The timing should be precise (milliseconds) to be able to conduct imaging modalities such as phase accumulation where temporal precision is of critical importance. Phase mapping sequence used to measure magnetic field patterns of a TMS coil in the MRI bore, by exploiting the fact that phase shifts are proportional to incident field strengths evoked by a TMS pulse. For such unique measurements, a TMS discharge must be exactly triggered at the start of the MR readout gradient onset, with microsecond precision. Details of this application can be found in a previous paper from our group [27]. Also for EPI (fMRI) the slow time response of the relay (15-17ms) limits the potential window of opportunity and narrows the tolerance to error. The previously based PC control via COM port control [9] was considered inadequate to provide reliable millisecond resolution based on the software timers of the OS. Options varied from complex real-time OS (RTOS) to expensive real time IO cards, instead, we decided to experiment with PSoC solutions popular in the car industry to achieve basic automation. PSoC stands for programmable system on chip and incorporate an FPGA (programmable field matrix) with onboard ARM Cortex M0 processor for control and many auxiliary discrete components on the same silicon chip (e.g. IO and serial communication). Instead of going through the effort of programming the FPGA directly, there is free IDE software with ready available library of common digital&analog components. At the same time we still benefit of FPGA properties low latency and high fidelity implementation with the only drawback of initial small (<1s) boot time when powering on. Manufacturer: Cypress Electronics; Prototyping board: CY8CKIT-049-4200 family PSoC 4 chip.

The sync box allows for two modes of operation in regard to adjusting timings with the scanner to perform either single slice or volume acquisition. When in single-slice mode the TMS is triggered on every incoming TTL pulse from the scanner, otherwise in volume mode it is triggered on every N slice based on the span of the volume. The mode can be switched from the front panel of the device (Figure 1-B) however it does require reprogramming to change N for the number of slices in volume mode. Single slice mode was used for phase accumulation experiments mentioned before and published elsewhere [25][28]. The volume mode was designed for the study described here, and allows 1 TMS trigger per EPI volume, and the skipping of EPI volumes to accommodate the acquisition of the slow fMRI BOLD response (see section). In Figure 1-B we can see that the control box gets its input from the MR scanner and provide two outputs, one for closing the relays and another for triggering the TMS itself, provided as control outputs CS1 and CS2 responsible for triggering the TMS and closing the relay respectively.

A schematic drawing of the sync box internals, its in- and output pins and other components is given in Figure 4. The input from the scanner is connected via BNC coax cable on input pin PI_MRI_TTL on the MCU and further routed to component Counter_TTL. A digital pulse counter is used only in volume mode to wait for N scans before triggering. The timer element PWM_RELAY determines the timing

for starting opening the relay (CS2 pathway in Figure 1) on pin PO_RELAY and PWM_SAFETY provides an extra 20ms time window to allow for the relay to close completely. Finally, PWM_TMS is the delay for triggering the TMS (CS1 pathway in Figure 1) on digital output pin PO_TMS. There is also one extra PWM depicted in Figure 4, namely PWM_TEST, which is intended for developers only, allowing for quick testing by mimicking the input TTL pulse expected from the scanner.

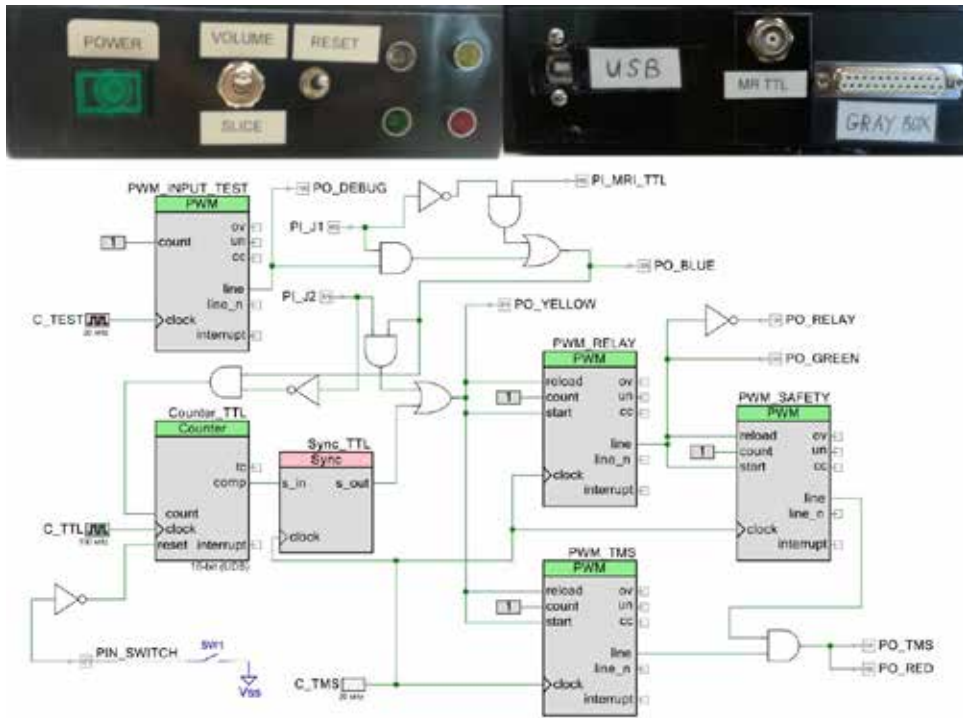


Figure 4: Top: photo of the front and back panel of the sync box. Bottom: Schematics of the sync/control box, direct screen from PSoC Creator 3.4, where each 4x PWM (pulse width modulators) and 1x Counter components are interconnected along a common digital bus along auxiliary logical gates AND, OR and INVERSE. (PO stands for Output Pin and PI for Input pin)

There are 4 LEDs on the front panel of the sync box, see the top photo Figure 4. They are intended as visual feedback for the user, and although hard to interpret directly they are still informative to whether the currently running sequence is expected or not. On every MR-TTL pulse, the blue LED blinks and the yellow LED lights during the complete time frame of the synchronization period. The yellow LED will be enabled for each blink of the blue LED in single-slice acquisition mode and every N blinks otherwise during volume acquisition. Finally, the green LED will light up for the duration of 20ms, the time for the relay to completely close, followed by abrupt red LED blink to signify the brief moment (5ms time frame) where the 0.5ms long TMS pulse is discharged.

The back panel of the sync box, as shown in Figure 4, accommodates all of the necessary cable plugs, such as USB 2.0 power and data (MCU programming/flashing); BNC connection to the MRI; LTP port connection to the gray box.

The input to the sync box is coming directly from the scanner, MRI-TTL, TTL standing for transistor level logic (3-5V) and it is handled as a high impedance input at MCU level (PI_MRI_TTL Figure 4). Although the moment of the TTL pulse is adjustable, the scanner will signal at the end of each image sequence, by default. In the case of a single slice acquisition, this will always denote the end of imaging, however, in the case of volume acquisition, this often requires several acquisitions to form a volume. A switch on the front panel of the sync box allows us to switch between the two main modes of operation. When set to single slice mode the switch effectively bypasses the counter Counter_TTL in Figure 4, when in volume mode the counter is programmed to expect some number of pulses from the scanner before proceeding with the relay and TMS trigger timing offsets via PWM_RELAY and PWM_TMS. In Figure 5 below we illustrate a complete EPI sequence with a TMS trigger at the end, the image is not up to scale. Such EPI volumes with TMS were interspersed with volumes without TMS to allow the slow BOLD response to a TMS pulse to evolve completely before stimulating again. See section for details.

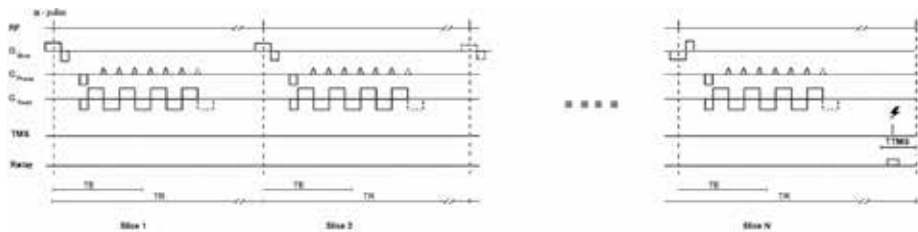


Figure 5: A schematic drawing of the EPI pulse sequence used in this study. The RF excitation (a -pulse), slice selection gradient (G_{slice}), phase encoding gradient (G_{phase}) and readout gradient (G_{read}), the TMS pulse trigger and relay control signal are shown. 1st, 2nd and last slice are shown. After the last slice, extra time ($TTMS$) of 300ms was added to allow for the TMS pulse and closing and opening of the relay to prevent leakage currents from reaching the MR room. $TR=2000$ ms, $TE=23.0$ ms. Note: this figure is only a schematic to elucidate the main principle used, timings and magnitudes are not to scale as this is not an exact log of the pulse sequence.

Setup Safety Measures

To operate the setup safely and to prevent permanent damage to the relays of the RF filter box we must ensure the TMS is never discharged when they are open. The relays are exposed to high currents driven by quick high voltage ramps that can easily

arc and yield the connector pins together, at worst even catching fire, thus it is very important to prevent such a situation. The gray/safety box in Figure 1-C is preventing exactly that. In addition, it provides an independent, current boosted/amplified power source to the control line of the relay/filter box.

Similar logic for safety is also built into the FPGA logic of the control/sync-box. In Figure 4 you can see a binary digital logic AND-gate between PWM_TMS and PWM_SAFETY pulse width modulators used for timing. The latter is adjusted to trigger at 20ms after the relay control signal is turned on to prevent the TMS trigger before the relay is settled.

Final (third level) safety precaution is built inside the relay box itself in the form of an air-pressure safety pedal that prevents discharge unless pressed to avoid any accidental triggering when handling any of the equipment and not in an active session.

MRI equipment and pulse sequence

All MR sequences (MRI-only and concurrent TMS-MRI) were performed in a 3T MR scanner (Achieva, Philips Healthcare, Best, The Netherlands).

The pulse sequence used here is an adapted EPI sequence where an additional silent time of around 300ms was inserted after the readout and phase encoding gradient completed their sweep of K-space. This resulted in a 2D EPI sequence with the following parameters: TR/TE of 2,000.0/23.0 ms, flip angle of 70°, FOV of 256x119.6x208 mm³, matrix of 64x64, voxel size of 4x4x4 mm³, scan duration of 17 min, 30 slices with a slice thickness of 3.6 mm and a slice gap of 0.4 mm. The TTL pulse triggering the sync box was set at the same time as the RF excitation pulse (the sync box then builds in a wait time such that the TMS pulse is scheduled 40 ms later (during the extra silent time)).

Mechanical setup

The setup where the coil was mounted and in which the participant head and the MR FLEX receive coils were placed is identical to the setup described in De Weijer et. al. [9] and is demonstrated in Figure 5.

The main advantage of this setup was that the head of the participant can be tilted away from the normal position along the main axis of the B₀ field that is commonly adopted in MRI scanners, due to the FLEX coils that can be spaced further apart than standard bird-cage MR receive coil arrays. This allows space for the TMS coil to be placed also in more lateral positions on the scalp, and it allows the plane of the TMS coil to stay closer to the perpendicular orientation relative to the B₀ field of the MRI bore, which minimizes Lorentz forces acting on the TMS coil when

discharging in a 3T MRI field. This greatly increases the safety of the participants as such Lorentz otherwise poses a risk for the coil to become damaged during operation.

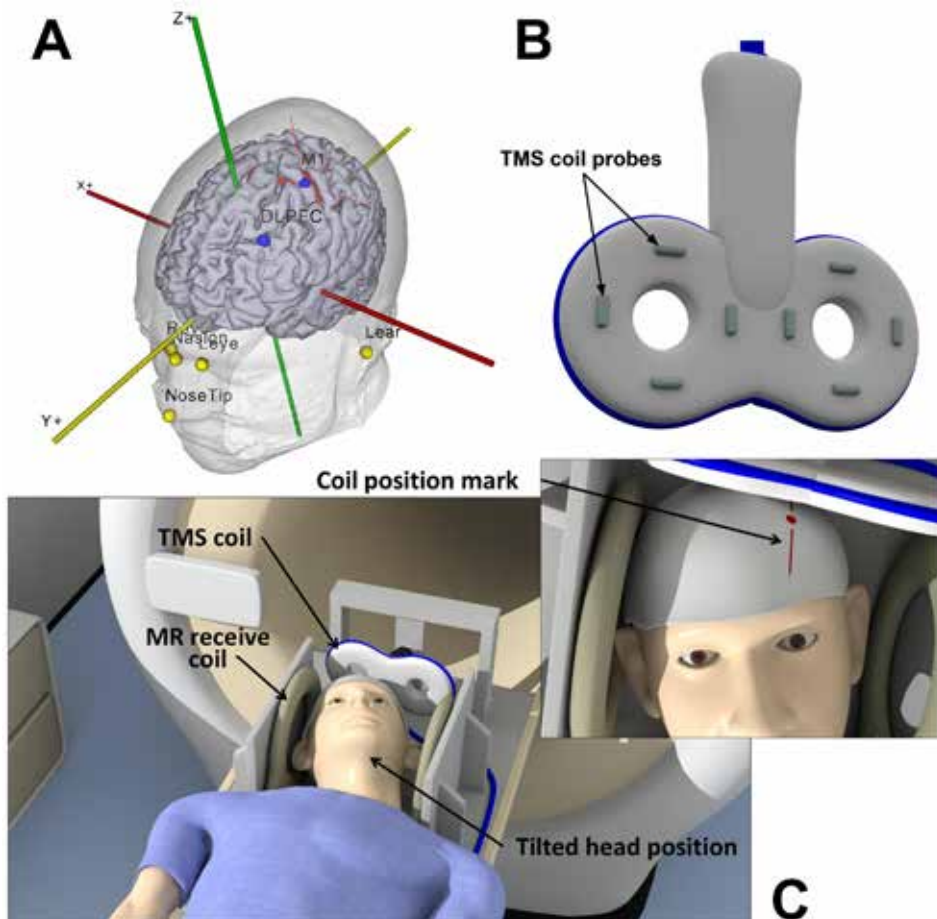


Figure 6: Panel A Location of facial markers and TMS targets in the Neural Navigator. Facial markers: the tip of the nose; nasion, left and right inner eyelid; left and right upper and lower ear. TMS targets: the primary motor cortex (M1); dorsolateral prefrontal cortex (DLPFC). The DLPFC is located in the middle frontal gyrus, 3cm anterior to the premotor area. Panel B. TMS coil probes. The probes can be visualized in a T2-weighted scan to determine their location with respect to the head. Panel C. Participant is lying on the MR bed with the head positioned in between two MR receive coils and the TMS coil located over the cranium. The TMS coil is oriented perpendicular to the static magnetic field of the MRI scanner to minimize Lorentz forces in the coil. The head is tilted in order to position the TMS coil over the left DLPFC. (In the published variant: Figure 2)

Experimental protocols

The experiment was divided into two parts: an intake session (MRI-only) with a standard 8-channel head coil, and a TMS session (concurrent TMS-MRI). These sessions are described below.

Intake sessions

First, a 3D T1 weighted anatomical scan was acquired with a TR/TE of 10.0/4.6 ms, a flip angle of 8°, voxel size of 0.75x0.75x0.8 mm³, scan duration of 11.3 min, 225 slices with a slice gap of 0 mm. This scan was used for neuronavigation during the TMS session and other visualization purposes.

Next, a single-shot echo-planar imaging (EPI) scan was acquired with 250 dynamics, a TR/TE of 2,000.0/23.0 ms, a flip angle of 70°, a voxel size of 4x4x4 mm³, a scan duration of 8.5 min and 30 slices with a slice thickness of 3.6 mm and a slice gap of 0.4 mm. During this scan, participants were instructed to move the thumb of the right hand upon presentation of an auditory cue. This scan was used to validate our concurrent TMS-fMRI setup by comparing voluntarily induced motor network activity with TMS-induced network activity in response to TMS of the primary motor cortex. Preprocessing and statistical analysis are described in the data analysis section.

TMS session

For each participant, the T1 weighted image acquired during the intake session was segmented with SPM12 to obtain skin, skull, cerebrospinal fluid (CSF), white matter, and grey matter (GM) masks [29]. The segmentations were used to visualize the 3D brain and skin surface in the Neural Navigator (Brain Science Tools, The Netherlands, www.neuralnavigator.com). The location of M1 was obtained from the statistical map acquired during the intake session and marked on the 3D brain surface. The DLPFC target was placed 3 gyri (i.e. 3cm) anterior to the premotor gyrus within the middle frontal gyrus, corresponding to the border between Brodmann areas 46 and 9 [30]. Eight facial markers were used to align world space with the MRI coordinates: the upper and lower left and right ear, the left and right inner eyelid, the tip of the nose, and the nasion (Figure 6-A). Neuronavigation was then used to determine the TMS coil position for stimulation of M1. The TMS coil was oriented with the TMS coil handle perpendicular to the orientation of the precentral gyrus and pointing in the posterior direction. Markings were made on the bathing cap to be able to replicate the TMS coil position inside the scanner since neuronavigation could not be performed inside the MRI scanner room. These markings were also made for the DLPFC. For the DLPFC, the TMS coil handle was oriented perpendicular to the orientation of the middle frontal gyrus with the handle at 90 degrees with the midline.

Next, the TMS coil was placed over the left M1 guided by neuronavigation to determine the resting motor threshold (RMT). This was done by applying single pulses of TMS (with an inter-stimulus interval of 7s) to the primary motor cortex while increasing the TMS stimulator output until a response in the APB muscle was visible in 5 out of 10 TMS pulses [31].

The concurrent TMS-MRI session was divided into two parts: In the first part TMS was applied to M1 and in the other part TMS was applied to the DLPFC. For the concurrent TMS-MRI experiments, a custom-made setup was used. The head was positioned in a custom designed setup between 2 MR receive coils (Figure 6-C). The TMS coil was attached to a custom made mount which was positioned over the participant's cranium, eliminating potential TMS coil movement. Additionally, to minimize Lorentz forces on the TMS coil wings, the angle between the TMS coil plane and the MRI static magnetic field was limited to 25 degrees. The head was tilted backward and rotated slightly to match the coil position with the markings on the bathing cap. The head and neck of the participant were supported to increase comfort and minimize head movement during the scan.

After TMS coil positioning, two scans were acquired. First, a T2-weighted scan with a TR/TE of 13,609.0/80.0 ms, flip angle of 90°, voxel size of 2x2x2 mm³, scan duration of 3.6 min. The purpose of this scan was to visualize the coil location and orientation relative to the head. This was done by attaching 6 custom made markers (small capsules filled with water) to the back of the TMS coil (Figure 6-B), which appear hyper-intense on the T2-weighted scan. Second, a single-shot EPI sequence was acquired with 500 dynamics, a TR/TE of 2,000.0/23.0 ms, flip angle of 70°, FOV of 256x119.6x208 mm³, matrix of 64x64, voxel size of 4x4x4 mm³, scan duration of 17 min, 30 slices with a slice thickness of 3.6 mm and a slice gap of 0.4 mm. We acquired 500 dynamics to make sure that we had sufficient power to detect the effects of single pulses of TMS. During the EPI sequence, single pulses of TMS with an intensity of 115% RMT were interleaved with pulses with an intensity of 60% RMT. TMS pulses were delivered with a random interval of 5 to 8 dynamics (10 to 16s) to avoid habituation.

Specifically, an EPI volume with a TMS pulse immediately after the last slice during an additional time window without readout constituted the 'TMS volume'. In between TMS volumes, there were 5 to 8 EPI volumes of the same duration without a TMS pulse. The total number of EPI volumes with a TMS pulse was 100 out of 500 in total. See Figure 5 for details.

Data analysis

Analysis of the structural and fMRI data was performed with custom scripts and SPM12 [29] in the Matlab R2014a environment (Mathworks Inc., USA).

The T1-weighted image was segmented with SPM through unified segmentation with 6 tissue type priors to obtain a grey matter, white matter, and CSF mask.

All EPI volumes were inspected to determine image quality and to identify the presence of potential artifacts. This revealed small random deflections from the baseline signal level in a single slice of a few functional volumes per time series acquired during the TMS session. A small number of artifacts were present in most of the time series data. These deflections were short (one sample) and could only be observed in the vicinity of the TMS coil. All slices of the realigned EPI scans were automatically scanned for the presence of a sharp peak in the average grey matter signal with a custom algorithm to detect distortions. The distorted slices were then interpolated based on the BOLD signal in the previous and next slice with custom Matlab code. 15 to 70 slices were interpolated out of 30 slices and 500 volumes depending on the participant.

All EPI volumes were realigned and normalized using the non-linear normalization parameters obtained from the segmentation of the T1-weighted scan. The EPI volumes were subsequently resliced at a resolution of 4x4x4 mm³ and smoothed with an FWHM of 8mm.

Based on the location of the TMS coil markers in the T2-weighted scan, we were able to reconstruct the TMS coil position and isocenter, as described in detail in [9]. Thereafter, the EPI volumes were realigned using SPM12. Next, the mean EPI scan was co-registered to the T1-weighted scan. The inverse of the EPI to T1 affine transformation and the inverse of the EPI realignment affine transformations were used to create a head movement-corrected reconstruction of the location of the TMS coil isocenter. Thereafter, the center of gravity (COG) of the TMS coil isocenter was calculated by calculating the average of the 3D coordinates of the TMS coil isocenter over all volumes.

For the functional data obtained during the intake session, the thumb movements were modeled with the canonical hemodynamic response function (HRF) and its first-order derivative in a standard event-related GLM analysis with 2 nuisance regressors: the average BOLD signal in the white matter and the CSF. Statistical images were constructed based on an F-statistic with the F-threshold at $P < 0.05$, family-wise error (FWE) corrected [29].

We performed a standard event-related GLM analysis in SPM12. The generalized linear model (GLM) included two events: single pulses of 115% RMT and 60% RMT. The BOLD response was modeled with the canonical hemodynamic response function (HRF) and its first-order derivative. The mechanism through which TMS induces brain activity is different from conventional MRI tasks which investigate voluntary brain activity. The inclusion of the first-order derivative allows more

variability in the hemodynamic response, which allows more accurate modeling of the BOLD response during TMS pulse delivery. Two nuisance regressors were included in the analysis: the average BOLD signal in the white matter and the CSF. BOLD signals were filtered with a high pass filter of 80Hz before the construction of the GLM. Statistical images were constructed based on the contrast between TMS pulses of 115% RMT and TMS pulses of 60% RMT using an F-statistic with a threshold at $P < 0.05$, family-wise error (FWE) corrected [29].

Results

Voluntary versus TMS-induced motor activity (M1 session)

Voluntary movement of the right thumb results in observable activity in, among other regions, the left primary motor cortex (M1) and supplementary motor area (SMA), the right hemisphere of the cerebellum and the bilateral putamen and thalamus ($P < 0.05$, FWE corrected; Figure 7-B). Because the participants were instructed to move their thumbs based on auditory cues, activity was also observed in the primary auditory cortex (A1).

During the concurrent TMS-fMRI session, the TMS coil isocenter was located slightly medio-anterior to the maximum BOLD response in the precentral gyrus, with a limited displacement of the TMS coil isocenter due to head movement during the session (Figure 7-A). The TMS-induced activity was defined as the contrast between TMS pulses of 115% RMT and 60% RMT. The participant reported thumb movement in response to high-intensity TMS pulses throughout the majority of the session and reported no thumb movements for low-intensity TMS pulses. Some TMS-induced activity was observed in the bilateral M1 and thalamus, the left SMA and putamen, and the right hemisphere of the cerebellum ($P < 0.05$, FWE corrected; Figure 7-C). Because TMS pulse delivery is accompanied by an auditory ‘click’, activity can also be observed in A1. Additionally, TMS-induced activity was observed in the bilateral primary visual cortices.

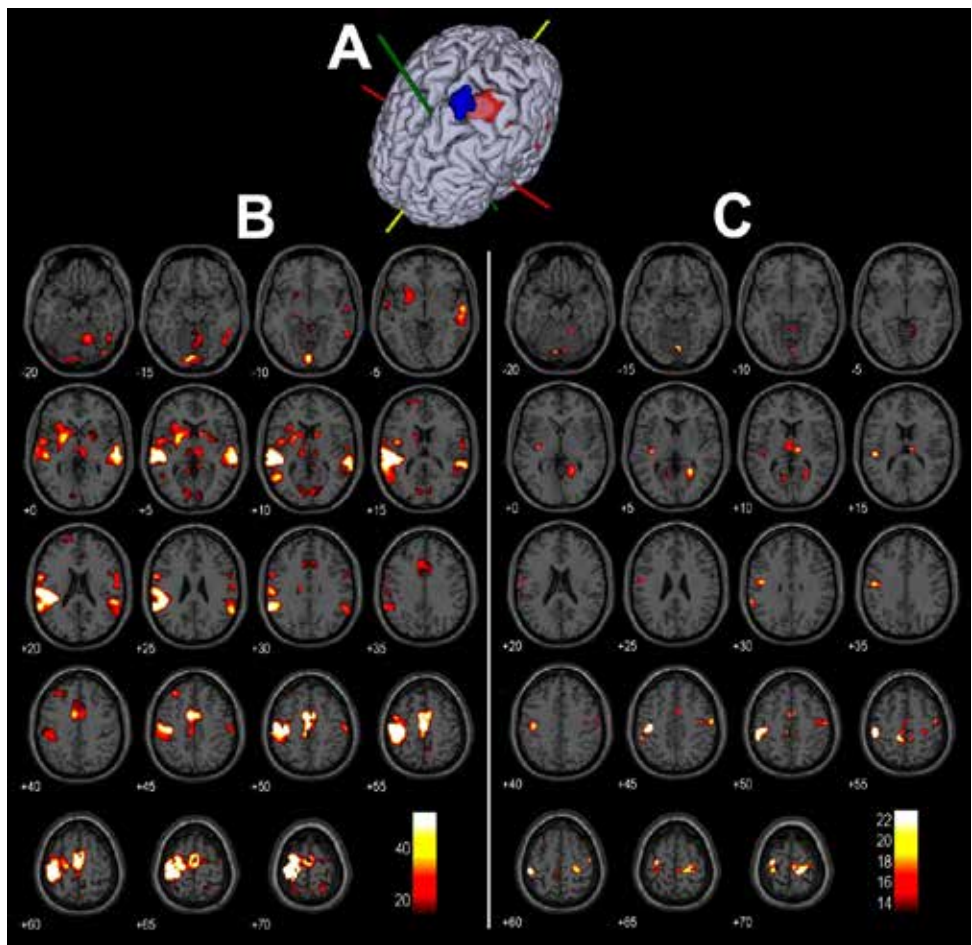


Figure 7. Panel A. Activity in the primary motor cortex in response to voluntary thumb movements (in red) and the location of the TMS coil isocenter during the TMS-fMRI session is shown (in blue). Panel B. Activity in response to voluntary thumb movements contrasted with baseline activity ($P < 0.05$, FWE corrected). Axial slices of an MNI brain are shown (left = left). Panel C. TMS-induced activity in response to TMS pulses of 115% RMT contrasted with baseline activity ($P < 0.05$, FWE corrected). The same slices are shown in panel B.

TMS target (DLPFC session)

The following sections describe the results of the DLPFC session. The locations of the COG of the TMS coil isocenters were located well within the anatomical landmarks of the DLPFC in all participants (Figure 8-A). The TMS coil isocenter remained within the DLPFC for the majority of the session in all participants, despite small head movements. Head movement resulted in a maximum displacement of the TMS coil isocenter from the COG of 2.1 mm to 6.1 mm (mean: 4 mm) depending on the participant, which shows that TMS coil placement was accurate and

head movement was limited. In the majority of the participants, the TMS coil isocenter was located in the posterior part of the DLPFC, while the TMS coil isocenter was located in the anterior part of the DLPFC for participants 4 and 6. The normalized COGs of the TMS coil isocenter cluster in the left DLPFC (Figure 8-B), with the COGs of participants 2 and 4 located on the edges of the middle frontal gyrus.

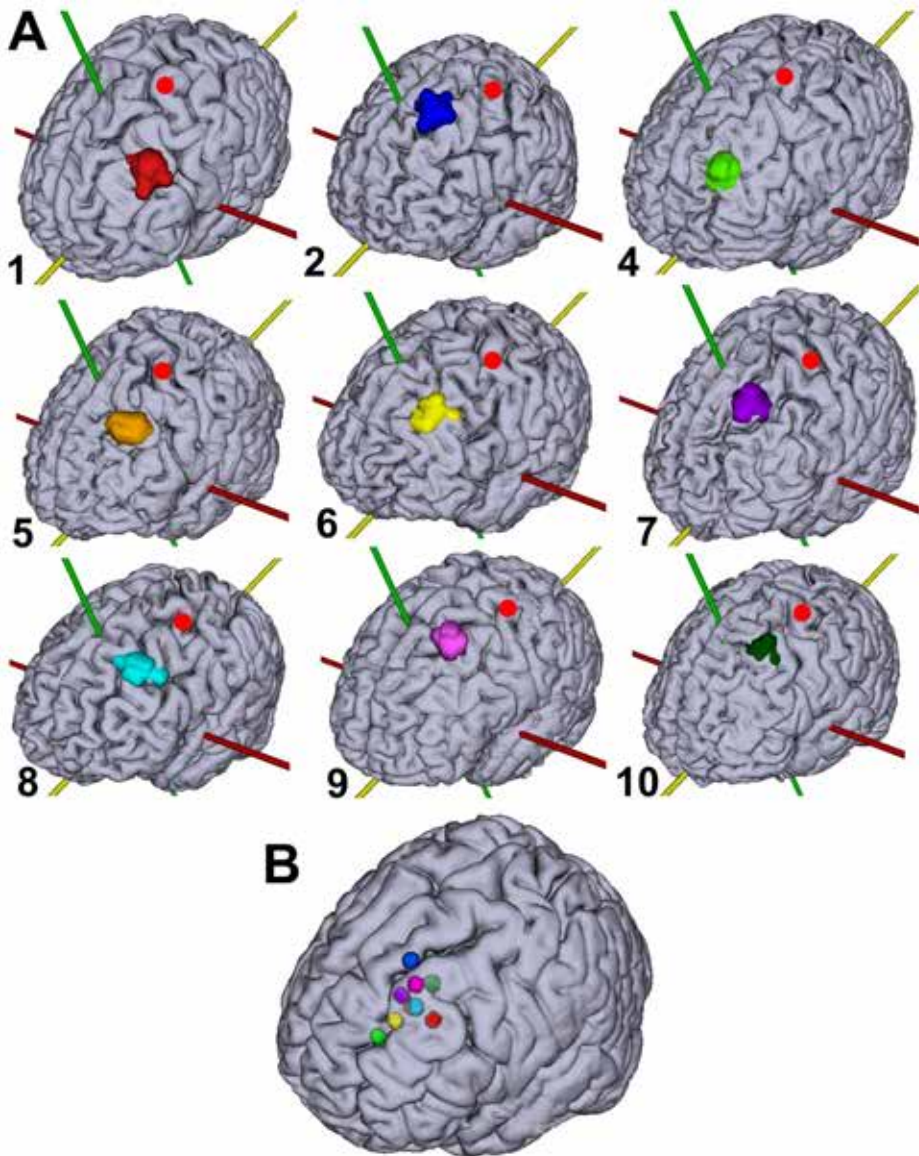


Figure 8. Panel A. TMS targets projected onto individual brain surfaces. The numbers refer to the participant numbers in table I. The red dot indicates the location of the hand area in the primary motor cortex (M1) as determined through fMRI. Panel B. The normalized center of gravity of each individual TMS target is projected onto an MNI brain.

The TMS targets are based on initial TMS coil placement (as determined through a T2-weighted scan) and corrected for subsequent head movement during image acquisition (as determined through realignment of the EPI volumes). Corresponding colors are used in panels A and B and table I.

TMS-induced activity (DLPFC + M1 session)

An overview of neuroanatomical regions that showed TMS-induced activity in response to TMS pulses delivered to the left DLPFC is shown for all participants (Table II). Highlights of TMS-induced activity are shown on four slices of an MNI brain for each participant (Figure 9). These slices showed activity in response to TMS pulses of 115% RMT contrasted with TMS pulses of 60% RMT ($P < 0.05$, FWE corrected). The observed propagation patterns of TMS-induced activity showed substantial variation between participants. However, all participants showed TMS-induced activity in one or more subdivisions of the left prefrontal cortex. Interestingly, TMS-induced activity was generally absent in the right hemisphere (contralateral to the stimulation site). Although TMS-induced activity was predominantly present in the left prefrontal area, it also propagated to distant areas: including parietal and temporal areas.

Table II. Summary of TMS-induced activity observed in individual participants. DLPFC: Dorsolateral prefrontal cortex; VLPFC: Ventrolateral prefrontal cortex; APFC: Anterior prefrontal cortex; MPFC: medial prefrontal cortex; PM: Premotor cortex; OFC: Orbitofrontal cortex; S1: Primary somatosensory cortex; sgACC: subgenual anterior cingulate cortex; SPL: superior parietal lobule; Temp: Temporal lobe.

#	DLPFC	VLPFC	APFC	MPFC	PM	OFC	S1	sgACC	SPL	Temp
1	Left									
2	Left	Left	Left		Left					Right
3	-	-	-	-	-	-	-	-	-	-
4		Left			Left					
5	Left	Left	Left	Left	Left	Bi		Left		Right
6	Left	Left					Left			
7	Left	Left	Left	Left				Left		
8		Left					Left	Left		
9	Left	Left	Left	Left	Left		Left	Left		
10	Left								Left	Bi

Figure 10 shows TMS-induced activity evoked by stimulation of the left M1 and DLPFC of participant 9. Stimulation of the left M1 resulted in TMS-induced activity in the bilateral M1 and premotor cortex. The activity could also be observed in

the left SMA. Application of TMS to the left DLPFC led to activity in a large part of the left prefrontal cortex and a small cluster in the left M1 and S1.

Figure 11 shows TMS-induced activity in the limbic region, specifically focusing on activity in the sgACC. The delivery of TMS pulses to the DLPFC caused activity in the sgACC in 4 out of 9 participants, all of whom showed activity in the left (ipsilateral to stimulation) sgACC (Table II). However, participant 7 shows TMS-induced activity on the boundary between the subgenual ACC and the neighboring ACC. No activity was not observed for stimulation of M1 and is therefore specifically related to DLPFC stimulation.

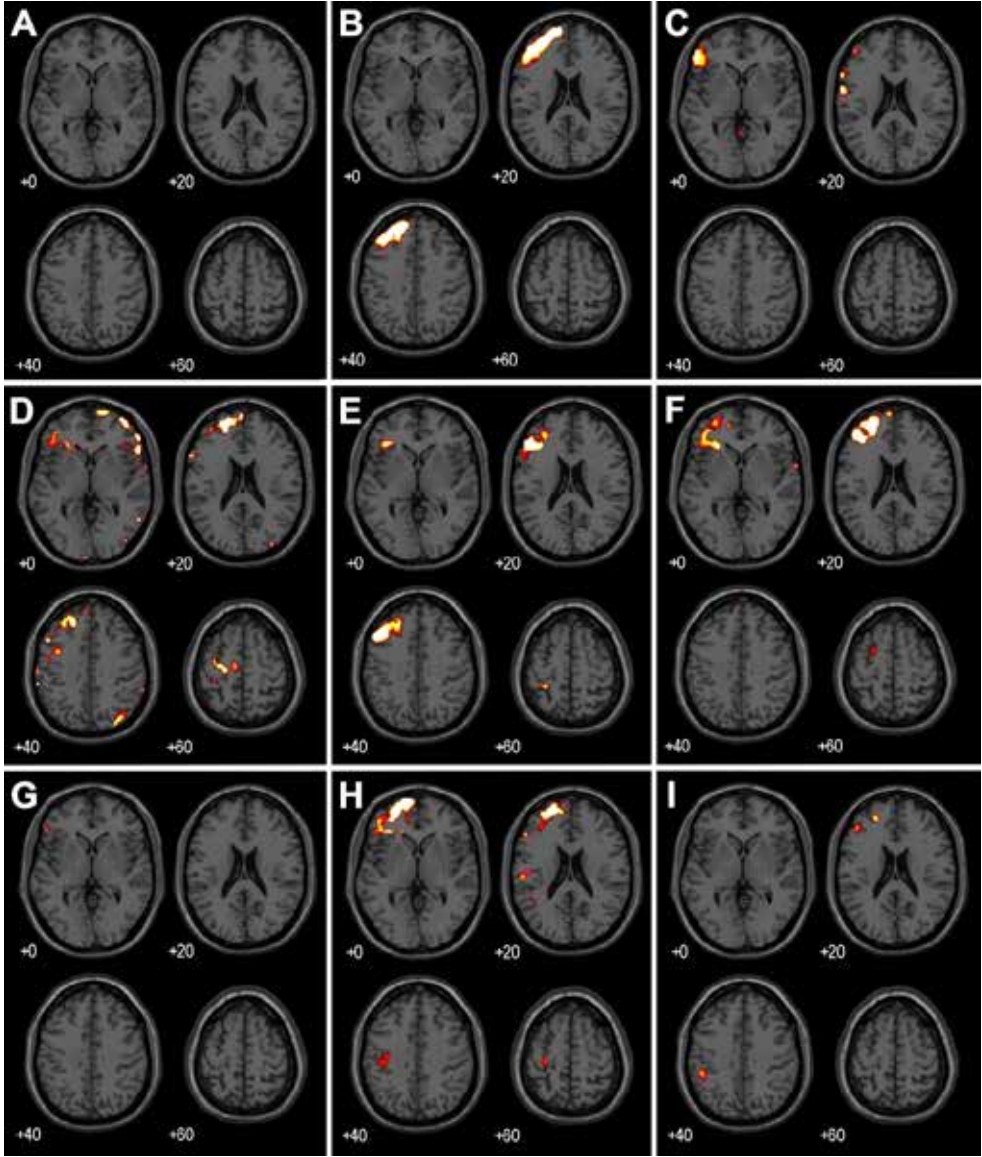


Figure 9. TMS-induced activity in response to TMS pulses of 115% RMT contrasted with TMS pulses of 60% RMT ($P < 0.05$, FWE corrected). Axial slices of an MNI brain are shown (left = left). Panels A to I show the TMS-induced activity of participants 1, 2, and 4 to 10.

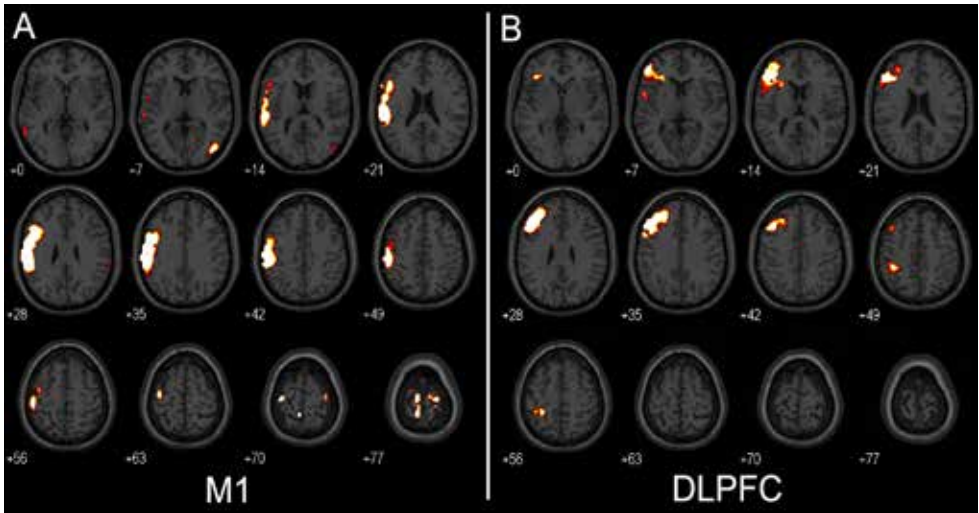


Figure 10. TMS-induced activity in response to TMS pulses of 115% RMT contrasted with TMS pulses of 60% RMT ($P < 0.05$, FWE corrected). Axial slices of an MNI brain are shown (left = left). Panels A and B show TMS-induced activity in two different participants in which the TMS target was very similar. Left is left. Panel A. TMS-induced activity of participant 9. Panel B. TMS-induced activity of participant 10.

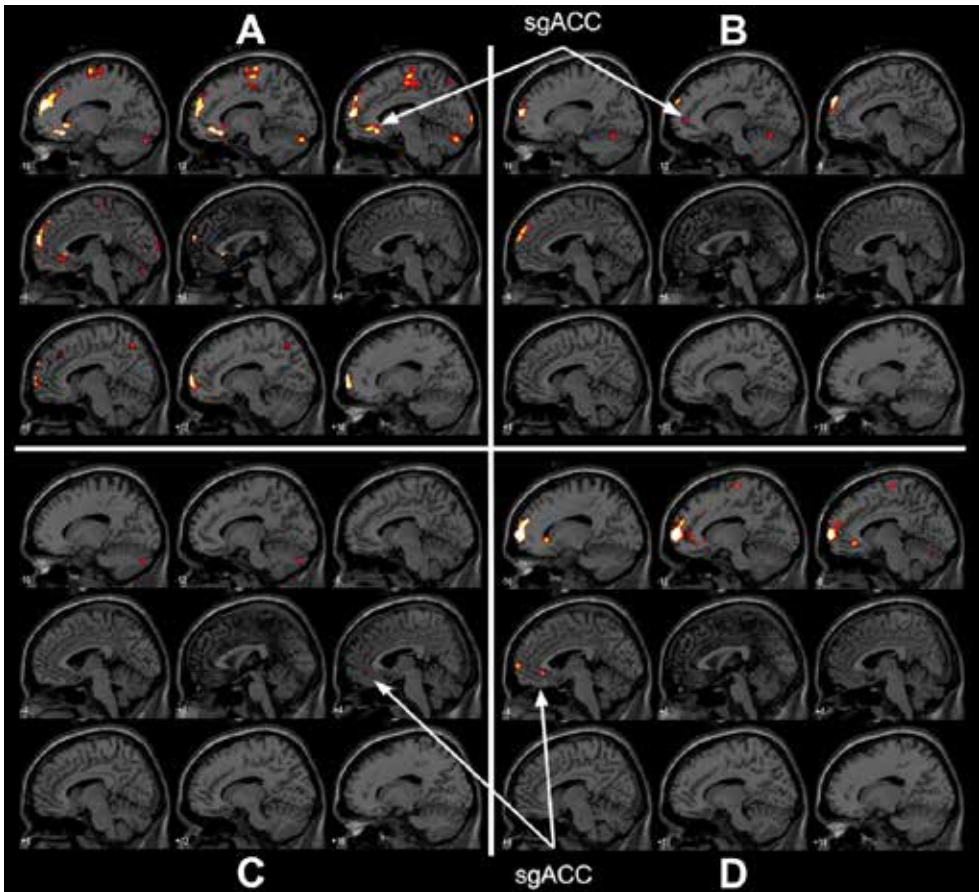


Figure 11. TMS-induced activity in response to TMS pulses of 115% RMT contrasted with TMS pulses of 60% RMT ($P < 0.05$, FWE corrected). Sagittal slices of an MNI brain are shown (first slice = left side; last slice = right side). Panel A. TMS-induced activity of participant 5. Panel B. TMS-induced activity of participant 7. Panel C. TMS-induced activity of participant 8. Panel D. TMS-induced activity of participant 9.

Discussion

Using a novel concurrent TMS-MRI setup, we investigated the propagation patterns of TMS-induced activity after stimulation of the left DLPFC and left M1. We found that TMS delivered to the DLPFC results in activity in the sgACC in about half of the participants, while TMS delivered to the left M1 does not result in sgACC activity. This indicates that TMS-induced activity evoked by TMS of the left DLPFC has the ability to, directly or indirectly, propagate from the DLPFC to the sgACC. The existence of such a pathway was already suggested indirectly by others who investigated the mechanisms of action of rTMS of the left DLPFC in MDD by exploring resting state functional connectivity in healthy individuals [16] [17]. Our observations provide the first direct evidence that TMS-induced activity can propagate to the sgACC (at least in some individuals).

Our concurrent TMS-MRI setup also reliably showed TMS-induced network activity in the network normally activated during voluntarily induced motor network activity (Figure 7). For M1 stimulation, we observed TMS-induced activity in neuroanatomical regions which are strongly associated with motor activity, like M1, SMA, putamen, thalamus, and cerebellar subregions, and most of those regions were also observed in other concurrent TMS-fMRI studies [9]. Importantly, we did not observe activity in the sgACC for M1 stimulation, which shows that TMS-induced activity in the sgACC is specific for stimulation of the DLPFC. The activation of known motor regions for stimulation of M1, and the specificity of sgACC activity for stimulation of the DLPFC provide adequate evidence that concurrent single pulse TMS-fMRI can be used to investigate individual propagation patterns.

Our findings are in agreement with prior literature, which indicates that propagation of evoked activity is a complex process that, similar to functional connectivity, varies significantly between individuals [32][33][34]. Consequently, the ability of rTMS to modulate specific brain regions, the antidepressant effect, is likely to depend on the state of the individual brain network. Concurrent TMS-fMRI allows the identification of the present individual structural and functional brain organization and connectivity, related to stimulation of a specific area of interest, such as the DLPFC. This concept can potentially be used to predict treatment outcome or to increase treatment efficacy of repetitive stimulation of the DLPFC in MDD. For example, by targeting treatment at the functional region near the DLPFC that leads to individual

sgACC activation, assuming the pathway from the prefrontal cortex to sgACC is the mechanism of action of the antidepressant effect of rTMS, as has been suggested [16][17]. In this way, future studies can investigate whether the propagation of TMS-induced activity to sgACC is an accurate predictor of beneficial response to rTMS treatment of the DLPFC in a clinical population of patients with MDD.

Finally, TMS-evoked activity consists of the activity of interest and confounding activity, such as auditory and somatosensory activity induced by the ‘clicking’ sound of the TMS coil and the superficial stimulation of the skin respectively[35]. We attempted to minimize confounding brain activity by contrasting TMS pulses of 115% RMT with TMS pulses of 60% RMT. However, a contrast with low-intensity TMS does not sufficiently eliminate confounding activity. Consequently, somatosensory and auditory activity should be interpreted with caution.

TMS-induced activity

The TMS-induced activity was generally observed in the TMS target area. However, 2 participants did not show activity in the vicinity of the TMS coil for stimulation of the left DLPFC. The absence of TMS-induced activity in the TMS target area has been reported previously [36][37][9]. A possible explanation is that in some cases the TMS-induced currents depolarize the descending white matter tracts, rather than the cell bodies, bypassing synaptic transmission in the TMS target area. As synaptic transmission appears to make up the majority of the hemodynamic signal measured using fMRI, concurrent TMS-fMRI appears to be predominantly sensitive to synaptic transmission evoked by TMS [38].

Image artifact

The application of concurrent TMS-fMRI is challenged by numerous technical difficulties, a few of which have already been addressed in other works [10][39]. A technical issue that was not previously described is that we observed short deflections (one sample) in baseline activity in a single slice in the vicinity of the TMS coil in EPI volumes during the inspection of the BOLD signal (section). These artifacts were only observed during sessions in which TMS intensity was changed during the experiment and was absent when the machine output was kept constant. This suggests that currents leaked in the TMS coil, creating a local magnetic field around the TMS coil. This local magnetic field perturbed the MRI static magnetic field during image acquisition, resulting in image distortions. Unfortunately, the cause of the artifact could not be identified with complete certainty.

Fortunately, the observed artifacts on the measured activation responses were negligible, as only a few slices were affected per participant (in less than 0.5% of all acquired slices per participant) and the artifact in these slices could effectively be

removed through interpolation. However, TMS-induced activity in the vicinity of the TMS coil should be interpreted with caution.

Conclusions

In conclusion, our improved concurrent TMS/fMRI setup has the potential to reveal activated networks when stimulating primary motor areas in the whole brain, proving its efficacy. Also, the enhanced timing precision allows for precise phase mapping of TMS coils as shown earlier by our group [25].

Furthermore, TMS pulses delivered to the left DLPFC induce activity in a number of connected brain regions, including the sgACC in some of the participants. This indicates that the modulatory effect of repetitive stimulation of the left DLPFC has the ability to propagate to the sgACC, depending on individual structural connectivity, providing a potential mechanism for its antidepressant effect. This demonstrates the clinical usefulness of this improved technical setup in uncovering and studying neuronal mechanisms behind rTMS treatment effects of neuropsychiatric disorders, with the ultimate goal of optimizing rTMS targeting and parameters in modulating the brain networks of interest and hence for the desired treatment outcome.

Acknowledgment

This work was supported by the Netherlands Organization for Scientific Research awarded to R. M. Dijkhuizen (VICI 016.130.662), and the DeNeCor project as part of the ENIAC Joint Undertaking (ENIAC131003; <http://eniac.eu>) awarded to CAT van den Berg and SFW Neggers.

References

- [1] A. J. Ferrari *et al.*, “Burden of Depressive Disorders by Country, Sex, Age, and Year: Findings from the Global Burden of Disease Study 2010,” *PLoS Med.*, vol. 10, no. 11, p. e1001547, Nov. 2013.
- [2] A. J. Ferrari *et al.*, “Global variation in the prevalence and incidence of major depressive disorder: a systematic review of the epidemiological literature,” *Psychol. Med.*, vol. 43, no. 3, pp. 471–481, Mar. 2013.
- [3] M. S. George *et al.*, “Daily left prefrontal transcranial magnetic stimulation therapy for major depressive disorder: A sham-controlled randomized trial,” *Arch. Gen. Psychiatry*, vol. 67, no. 5, pp. 507–516, 2010.
- [4] J. P. O’Reardon *et al.*, “Efficacy and Safety of Transcranial Magnetic Stimulation in the Acute Treatment of Major Depression: A Multisite Randomized Controlled Trial,” *Biol. Psychiatry*, vol. 62, no. 11, pp. 1208–1216, 2007.
- [5] E. A. Allen, B. N. Pasley, T. Duong, and R. D. Freeman, “Transcranial Magnetic Stimulation Elicits Coupled Neural and Hemodynamic Consequences,” *Science* (80-.), vol. 317, no. 5846, pp. 1918–1921, 2007.
- [6] S. Ishikawa *et al.*, “Effect of theta burst stimulation over the human sensorimotor cortex on motor and somatosensory evoked potentials,” *Clin. Neurophysiol.*, vol. 118, no. 5, pp. 1033–1043, May 2007.
- [7] S. K. Esser, R. Huber, M. Massimini, M. J. Peterson, F. Ferrarelli, and G. Tononi, “A direct demonstration of cortical LTP in humans: A combined TMS/EEG study,” *Brain Res. Bull.*, vol. 69, no. 1, pp. 86–94, Mar. 2006.
- [8] A. Valero-Cabré, B. R. Payne, and A. Pascual-Leone, “Opposite impact on 14C-2-deoxyglucose brain metabolism following patterns of high and low frequency repetitive transcranial magnetic stimulation in the posterior parietal cortex,” *Exp. Brain Res.*, vol. 176, no. 4, pp. 603–615, Jan. 2007.
- [9] A. D. de Weijer *et al.*, “A setup for administering TMS to medial and lateral cortical areas during whole-brain fMRI recording,” *J. Clin. Neurophysiol.*, vol. 31, no. 5, pp. 474–87, 2014.
- [10] S. Bestmann, J. Baudewig, H. R. Siebner, J. C. Rothwell, and J. Frahm, “Functional MRI of the immediate impact of transcranial magnetic stimulation on cortical and subcortical motor circuits,” *Eur. J. Neurosci.*, vol. 19, no. 7, pp. 1950–1962, 2004.

- [11] A. Rahman *et al.*, “Cellular effects of acute direct current stimulation: Somatic and synaptic terminal effects,” *J. Physiol.*, vol. 591, no. 10, pp. 2563–2578, 2013.
- [12] P. Videbech, “PET measurements of brain glucose metabolism and blood flow in major depressive disorder: a critical review,” *Acta Psychiatr. Scand.*, vol. 101, no. 1, pp. 11–20, Jan. 2000.
- [13] H. S. Mayberg *et al.*, “Regional metabolic effects of fluoxetine in major depression: serial changes and relationship to clinical response,” *Biol. Psychiatry*, vol. 48, no. 8, pp. 830–843, Oct. 2000.
- [14] H. S. Mayberg *et al.*, “Deep Brain Stimulation for Treatment-Resistant Depression,” *Neuron*, vol. 45, no. 5, pp. 651–660, Mar. 2005.
- [15] S. H. Kennedy *et al.*, “Changes in Regional Brain Glucose Metabolism Measured With Positron Emission Tomography After Paroxetine Treatment of Major Depression,” *Am. J. Psychiatry*, vol. 158, no. 6, pp. 899–905, Jun. 2001.
- [16] M. D. Fox, R. L. Buckner, M. P. White, M. D. Greicius, and A. Pascual-Leone, “Efficacy of Transcranial Magnetic Stimulation Targets for Depression Is Related to Intrinsic Functional Connectivity with the Subgenual Cingulate,” *Biol. Psychiatry*, vol. 72, no. 7, pp. 595–603, Oct. 2012.
- [17] J. P. Lefaucheur *et al.*, “Evidence-based guidelines on the therapeutic use of repetitive transcranial magnetic stimulation (rTMS) (2018 UPDATE),” *Clin. Neurophysiol.*, vol. 125, no. 11, pp. 2150–2206, 2014.
- [18] P. B. Fitzgerald *et al.*, “A Randomized Trial of rTMS Targeted with MRI Based Neuro-Navigation in Treatment-Resistant Depression,” *Neuropsychopharmacology*, vol. 34, no. 5, pp. 1255–1262, Apr. 2009.
- [19] A. T. Sack, R. Cohen Kadosh, T. Schuhmann, M. Moerel, V. Walsh, and R. Goebel, “Optimizing Functional Accuracy of TMS in Cognitive Studies: A Comparison of Methods,” *J. Cogn. Neurosci.*, vol. 21, no. 2, pp. 207–221, 2009.
- [20] D. E. Bohning *et al.*, “Mapping transcranial magnetic stimulation (TMS) fields in vivo with MRI,” *Neuroreport*, vol. 8, no. 11, pp. 2535–2538, Jul. 1997.
- [21] D. E. Bohning *et al.*, “Combined TMS / fMRI Study of Intensity-Dependent TMS Over Motor Cortex,” *Ratio*, vol. 45, no. 4, pp. 385–394, 1999.
- [22] N. Weiskopf *et al.*, “Image artifacts in concurrent transcranial magnetic stimulation (TMS) and fMRI caused by leakage currents: modeling and compensation,” *J. Magn. Reson. Imaging*, vol. 29, no. 5, pp. 1211–7, May 2009.
- [23] A. Bungert, C. D. Chambers, M. Phillips, and C. J. Evans, “Reducing image artefacts in concurrent TMS/fMRI by passive shimming,” *Neuroimage*, vol. 59, no. 3, pp. 2167–2174, 2012.

- [24] D. E. Bohning, S. Denslow, P. . Bohning, J. . Walker, and M. . George, "A TMS coil positioning/holding system for MR image-guided TMS interleaved with fMRI," *Clin. Neurophysiol.*, vol. 114, no. 11, pp. 2210–2219, Nov. 2003.
- [25] S. Mandija, P. I. Petrov, S. F. W. Neggers, and P. R. Luijten, "Noninvasive Electric Current Induction for Low-Frequency Tissue Conductivity Reconstruction: Is It Feasible With a TMS-MRI Setup?," *Tomography*, vol. 2, no. 3, pp. 203–214, 2016.
- [26] S. Rossi, M. Hallett, P. M. Rossini, and A. Pascual-Leone, "Safety, ethical considerations, and application guidelines for the use of transcranial magnetic stimulation in clinical practice and research," *Clin. Neurophysiol.*, vol. 120, no. 12, pp. 323–330, 2012.
- [27] S. Mandija, P. I. Petrov, S. F. W. Neggers, P. R. Luijten, and C. A. T. van den Berg, "MR-based measurements and simulations of the magnetic field created by a realistic transcranial magnetic stimulation (TMS) coil and stimulator," *NMR Biomed.*, no. August, pp. 1–11, 2016.
- [28] S. Mandija, P. I. Petrov, S. F. W. Neggers, A. D. de Weijer, P. R. Luijten, and C. A. T. van den Berg, "MR based TMS field measurements and electromagnetic simulations," *Proc. 23rd Sci. Meet. Int. Soc. Magn. Reson. Med. Toronto, Canada 2015*, vol. 0931, 2015.
- [29] W. Penny, K. Friston, J. Ashburner, S. Kiebel, and T. Nichols, "Statistical Parametric Mapping: The Analysis of Functional Brain Images," *Stat. Parametr. Mapp. Anal. Funct. Brain Images*, 2007.
- [30] R. Ahdab, S. S. Ayache, P. Brugières, C. Goujon, and J.-P. Lefaucheur, "Comparison of 'standard' and 'navigated' procedures of TMS coil positioning over motor, premotor and prefrontal targets in patients with chronic pain and depression," *Neurophysiol. Clin. Neurophysiol.*, vol. 40, no. 1, pp. 27–36, 2010.
- [31] D. J. L. G. Schutter and J. van Honk, "A standardized motor threshold estimation procedure for transcranial magnetic stimulation research.," *J. ECT*, vol. 22, no. 3, pp. 176–178, 2006.
- [32] M. D. Fox, M. Corbetta, A. Z. Snyder, J. L. Vincent, and M. E. Raichle, "Spontaneous neuronal activity distinguishes human dorsal and ventral attention systems," *Proc. Natl. Acad. Sci.*, vol. 103, no. 26, pp. 10046–10051, Jun. 2006.
- [33] D. A. Handwerker, V. Roopchansingh, J. Gonzalez-Castillo, and P. A. Bandettini, "Periodic changes in fMRI connectivity," *Neuroimage*, vol. 63, no. 3, pp. 1712–1719, Nov. 2012.
- [34] P. Sauseng, W. Klimesch, C. Gerloff, and F. C. Hummel, "Spontaneous locally restricted EEG alpha activity determines cortical excitability in the motor cortex," *Neuropsychologia*, vol. 47, no. 1, pp. 284–288, Jan. 2009.

- [35] S. H. Lisanby, D. Gutman, B. Luber, C. Schroeder, and H. A. Sackeim, "Sham TMS: intracerebral measurement of the induced electrical field and the induction of motor-evoked potentials," *Biol. Psychiatry*, vol. 49, no. 5, pp. 460–463, Mar. 2001.
- [36] J. Baudewig *et al.*, "Functional MRI of cortical activations induced by transcranial magnetic stimulation (TMS)," *Neuroreport*, vol. 12, no. 16, pp. 3543–3548, Nov. 2001.
- [37] S. Bestmann, J. Baudewig, H. R. Siebner, J. C. Rothwell, and J. Frahm, "BOLD MRI responses to repetitive TMS over human dorsal premotor cortex," *Neuroimage*, vol. 28, no. 1, pp. 22–29, Oct. 2005.
- [38] M.-A. Tagamets and B. Horwitz, "Interpreting PET and fMRI measures of functional neural activity: the effects of synaptic inhibition on cortical activation in human imaging studies," *Brain Res. Bull.*, vol. 54, no. 3, pp. 267–273, Feb. 2001.
- [39] C. C. Ruff *et al.*, "Distinct Causal Influences of Parietal Versus Frontal Areas on Human Visual Cortex: Evidence from Concurrent TMS-fMRI," *Cereb. Cortex*, vol. 18, no. 4, pp. 817–827, Apr. 2008.

Chapter VII

Design and evaluation of a rodent-specific
TMS coil: an in silico and in vivo validation
study

Abstract

Background: Rodent models are fundamental in unraveling cellular and molecular mechanisms of transcranial magnetic stimulation (TMS)-induced effects on the brain. However, proper translation of human TMS protocols to animal models have been restricted by lack of rodent-specific focal TMS coils.

Objective: We aimed to improve TMS focalization in rodent brain with a novel small, cooled, rodent-specific TMS coil.

Methods: A rodent-specific 25-mm figure-of-eight TMS coil was developed. Stimulation focalization was simulated *in silico* for the rodent coil and a commercial human 50-mm figure-of-eight TMS coil. Both coils were also compared *in vivo* by measurement of brachialis motor evoked potential (MEP) responses to TMS at different brain sites in anesthetized rats (n=6). Focalization was determined from the coils' level of stimulation laterality.

Results: *In silico* simulation results deemed the human coil insufficient for unilateral stimulation of the rat motor cortex, whereas lateralized electrical field induction was projected attainable with the rodent coil. Cortical, *in vivo* MEP amplitude measurements from multiple points in each hemisphere, revealed unilateral activation of the contralateral brachialis muscle, in absence of ipsilateral brachialis activation, with both coils.

Computer simulations motivated the design of a smaller rodent-specific TMS coil; however they came short in explaining the capability of a larger commercial human coil to induce unilateral MEPs *in vivo*. Lateralized TMS, as demonstrated for both TMS coils, corroborates their use in translational rodent studies, to elucidate mechanisms of action of therapeutic TMS protocols.

Introduction

Transcranial magnetic stimulation (TMS) is a non-invasive brain stimulation technique that has been widely used to modulate cortical excitability and to study central nervous system physiology in healthy subjects and patients [1]. Repetitive TMS (rTMS) protocols have shown therapeutic potential in several neurological and psychiatric disorders [2], however the cellular and molecular mechanisms underlying TMS-induced neurorecovery remain poorly understood [3]. These mechanisms could be systematically studied in rodent models; however, there is a lack of rodent-specific TMS coils [4].

TMS studies in rodents have regularly made use of commercial human coils [5]. Due to their relatively large size, these coils induce a broad volume of electrical current, resulting in widespread stimulation in small rodent brain [3,5], which limits the translational relevance to human TMS applications [5]. Nevertheless, Rotenberg and colleagues (2010) have shown that a commercial human TMS coil can be used to reliably generate unilateral MEPs from the forelimb of the rat [6]. The authors accomplished this by laterally positioning the coil over a rat brain hemisphere. This coil position only allows a fraction of the electromagnetic field to be applied to a single hemisphere, resulting in focal stimulation and unilateral MEPs.

Although smaller rodent-specific TMS coils would theoretically improve focalization of brain stimulation, development of miniature TMS coils has been challenging due to increased resistance, overheating, and coil rupture [7]. Parthoens and colleagues (2016) have shown that coil size can be significantly reduced, however they were unable to demonstrate improved focalization, evidenced by the lack of MEP laterality during motor threshold (MT) determination [8]. Other studies have shown that rodent-specific coils with reduced stimulation intensity have greater focality [4,9,10]. However, the effects induced by these low-intensity stimulation coils, may not be representative of the changes induced by high-intensity stimulation coils as used in human TMS studies [11]. Furthermore, a recent study by Meng and colleagues (2018) has proposed the design of a figure-0 shaped coil with a ferromagnetic core [12]. This design requires less power to achieve similar magnitudes of the induced electric field compared to the more common no-core coil designs. The authors demonstrated a novel mechanism to shift the induced magnetic field and thus create more focal stimulation than traditionally possible with such circular shaped coil designs. Although this coil improves focality, it is designed in the form of tightly packed coil wirings that will unlikely withstand more demanding rTMS protocols. Consequently, there is a need for small animal coils that can deliver TMS and rTMS at intensities similar to human studies, whilst maintaining a good degree of focality. This could facilitate studies in animal models of disease to develop, test and guide TMS-based therapies for clinical use [5].

Therefore, in this study we first modeled the stimulation focality of a commercial human figure-of-eight coil (50 mm), by employing the finite element modeling method (FEM) in electro-magnetic computer simulations to a 3D anatomical magnetic resonance imaging (MRI) dataset of the rat brain. Based on these *in silico* simulation results, we developed a small, rodent-specific figure-of-eight coil (25 mm). Subsequently, we tested whether these coils could focally stimulate the rat primary motor cortex, from *in silico* simulation of the field profiles and *in vivo* measurement of brachialis MEP responses in the rat. We hypothesized that a smaller rodent coil would allow more focal stimulation of cortical rat brain tissue than a large commercial human TMS coil.

Material and Methods

In silico experiments

Computer Simulation

Computer simulations were conducted using the free open source software package SCIRun 4.7+ (A Scientific Computing Problem Solving Environment (Scientific Computing and Imaging Institute, SCI, Utah, USA)). Two additional modules were developed, namely one for generating the geometry of thin wire coils and another for solving their respective induced electromagnetic fields based on the Biot-Savart law (see Petrov et al (2014) [13], see also Chapter 2 of this thesis).

Head Model

A 3D rat brain model, consisting of white matter-, gray matter- and cerebrospinal fluid-labeled voxels was constructed from a high-resolution MRI template, as described in the Appendix (see Material and Methods, Head model). The MRI template and tissue segmentations are available for download [14].

The generation of a 3D mesh from the segmented image, 168x137x273 matrix size and 94 μm resolution, was done with the Cleaver 2, a free multi-material tetrahedral meshing tool developed by the NIH Center for Integrative Biomedical Computing at the University of Utah Scientific Computing and Imaging (SCI) Institute (<https://github.com/SCIInstitute/Cleaver2/releases>) [15].

We generated an adaptive mesh using the following input parameters: sizing field 2.0, sampling resolution 1.0, and Lipschitz/grading 3.0. Preprocessing was applied to the initial binary segmentation where each compartment was isolated and iteratively smoothed via multiple steps of inflate-deflate (smooth parameter = 0.5, see BioMesh3D (part of SCIRun4 <https://www.sci.utah.edu/cibc-software/scirun/biomesh3d.html>, step 1 and 2 only)). The procedure resulted in a mesh with 628,897 nodes and 3,551,606 elements. The following conductivity properties were set for each relevant tissue compartment: gray matter 0.33 s/m [8,16]; white matter 0.25 s/m; CSF 1.7 s/m, the values are similar to human conductivities at low frequency <10 kHz. No anisotropic properties were captured, which were relevant for the white matter only.

Coil models

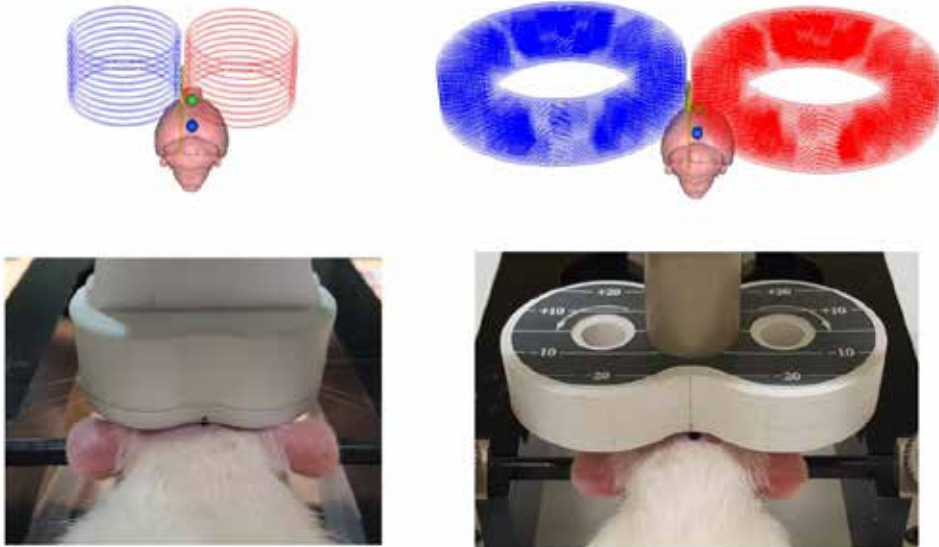


Figure 1: Finite element modeling (FEM) simulation and experimental coil setup. In the top and bottom rows, the simulation and experimental setup of coil orientation and positioning are demonstrated for the small (left) and large (right) TMS coils, respectively. The bottom row shows the initial central positioning of the coils in the middle of the rat head. The center of the figure-of-eight coils were placed above the midpoint of the interaural line. From this position, the coil was moved anterolaterally to position the center of each coil over the forelimb region of the motor cortex.

Two figure-of-eight coil models were constructed (see figure 1), namely one coil with a diameter of 50 mm (equivalent to a readily available commercial human coil by Neurosoft, Ltd., Ivanovo, Russia), and a second coil with a 25 mm diameter. Initial simulation results suggested that induced currents from the 25 mm coil were

mainly unilaterally focalized. Therefore, we requested Neurosoft to manufacture this coil. Due to its small size, and our ambition to use this coil for rTMS studies, the coil also had to be equipped with cooling which was achieved with silicone oil. To maintain efficient cooling, the design of the smaller coil was based on sparser wire distribution (winding) compared to the larger uncooled coil. This resulted in coil heights of 24 mm and 18.5 mm for the small and large coil, respectively.

The geometric generation of the coils were implemented in additional modules to SCIRun 4.7 (see Appendix, Material and Methods, table 1S for coil parameters) [13]. The same procedure as explained by Petrov and colleagues was used to derive the peak current driven through the coil for the bi-phasic Neurosoft TMS stimulator at 100% machine output (MO) [13]. This resulted in current values of 64×10^6 A/s (80% MO) for the small coil and 36×10^6 A/s (45% MO) for the large coil.

Cortical region of interest

We constructed a small region of interest (ROI) patch in the form of a lattice 3D mesh ($16 \times 17 \times 2$ voxels, $8 \times 8.5 \times 1$ mm³ size, resolution 0.5 mm), placed superficially (~1 mm depth) on each hemisphere of the rat cortex in the mesh obtained from the segmented image. The area corresponding to the forelimb region of the rat's primary motor cortex was masked in accordance with the mapping study of Fonoff et al. [17]. Their study provides an accurate (0.5 mm resolution grid, same as our ROI) functional map of the primary motor cortex in relation to bregma, determined from microelectrodes and electromyography (EMG) MEPS.

To place each ROI patch in our model, we defined lambda in relation to the interaural line, from which bregma was allocated at 8.34 mm anterior to lambda. The patch was visually aligned, in orthogonal view, with the outer/superior gray matter surface. The distance of 8.34 mm was derived from the linear regression formula: $Y = bX + a$ (Y = distance of the interaural line to bregma, X = rat weight, a and b are constants) as suggested by Whishaw et al. [18] and the average body weight of the MRI-scanned rats. Considering this formula, the discrepancy with our experimental rat population (average weight: 413 g) (see below) was found to be around 5.5% (< 0.5 mm), hence we attempted no compensation in modeling.

In vivo experiments

Animals

Six naïve adult male Sprague Dawley rats (413 ± 21 g (mean \pm SD); Charles River, Sulzfeld, Germany) were used. Experiments were approved by the Animal Ethics Committee of the University Medical Center Utrecht, The Netherlands, and were conducted in agreement with Dutch laws ('Wet op de Dierproeven', 1996) and

European regulations (Guideline 86/609/EEC). Animals were housed in pairs under controlled environmental conditions (12h-light/dark cycle, temperature 20-24°C, 45-65% humidity), with ad libitum access to food and water, and with a Perspex tube as cage enrichment.

Animal preparation and anesthesia

Rats were briefly anesthetized with a mixture of medical oxygen and isoflurane (5% induction, 2.5% maintenance) for the placement of a lateral tail vein catheter preloaded with heparinized saline (50 U.I./ml), followed by the continuous infusion of propofol (40 ± 2 mg/kg/h; Fresenius Kabi, The Netherlands). Propofol anesthesia was used during MEP recordings, because at low propofol doses, stable MEP responses can be measured over a period of 4 hours [19].

Isoflurane was maintained at 2.5% during the first 5 minutes of propofol infusion, whereafter isoflurane delivery was discontinued. A 20 minute washout period of isoflurane was endorsed, before the onset of MEP measurements, to limit the suppressive effect of isoflurane on MEPs [20,21]. Meanwhile, the rat's head was shaved (to ensure close contact of the TMS coil with the skull) and the animal was fixed in a stereotactic frame. During the entire experimental procedure, the body temperature of the animals were maintained at 37 °C using a rectal temperature feedback probe connected to a circulating water-heated pad system.

Electromyography

MEPs were recorded from the forelimbs of the animals with monopolar, 28G stainless steel needle electrodes (Neuroline, Ambu), inserted into the belly of each brachialis muscle. The location of the brachialis muscle was determined by palpation of the forelimb in the extended position. The needle electrodes were presoaked in saline (0.9% NaCl, Braun) before insertion, to ensure low impedance [22]. After insertion, the electrodes were secured and held in place by adhesive tape. A reference electrode was positioned distally in the footpad of the forelimb. Each animal was electrically grounded with a single disposable subdermal needle electrode (Technomed, Europe), inserted into the base of the tail. The EMG signal was band-pass filtered between 5 and 10 kHz, and amplified by a factor of 164 in the range of up to 60 mV (Neuro-MEP-4 system, Neuro-MEP software, Version 3.4.25.0, Neurosoft Ltd., Ivanovo, Russia). EMG signal was digitized with a 20 kHz sampling rate and traces were stored in XML files for further analysis using Matlab.

Transcranial magnetic stimulation

All animals were stimulated with a biphasic Neuro-MS/D stimulator using a small (25 mm) and a large (50 mm) figure-of-eight TMS coil, manufactured by Neurosoft, Ltd., Ivanovo, Russia (see section 'Coil models' above for details). During stimulation, each coil was fixed horizontally in the posterior-anterior orientation into a manipulator and secured to the stereotactic frame (see Appendix, Material and Methods, figure 1). This allowed movement of the coil along three axes.

To conduct the TMS-MEP measurements in a consistent manner, the anterior-posterior coordinates of bregma were calculated relative to the interaural line, as described by Whishaw and colleagues [18]. The central point of the interaural line was used as a zero reference point for positioning the center of the coil over the forelimb region of the rat's motor cortex. Firstly, the posterior end of the coil was positioned on the zero reference point. Secondly, the coil was moved posteriorly to position the center of the coil over bregma. Finally, from bregma the coil was moved anterolateral above the cortical forelimb region. The center of the forelimb region was estimated to be 1 mm anterior and 2.5-3 mm lateral to bregma based on functional mapping of the rat motor cortex [17]. Small differences in coil center positioning reflected minor variances in skull width and snout curvature.

Motor threshold determination

The MTs for the left and right hemispheres were determined independently for each coil. Single pulses were administered to the left motor cortex, followed by stimulation of the right motor cortex, or vice versa. MEPs were recorded with Neuro-MEP software (Version 3.4.25.0, Neurosoft Ltd., Ivanovo, Russia).

To determine the location over the motor cortex where MEPs could be reliably measured, the coil was moved both anteroposteriorly and mediolaterally over the left and right hemispheres in steps of 1 mm. At each location, an approximation of the MT was obtained by starting stimulation at 20% (large coil) or 50% (small coil) of the maximum MO and increasing the intensity in steps of 5% until a positive MEP response was recorded. A positive MEP response was defined as a MEP with a peak-to-peak amplitude of at least 50 μ V. Due to signal noise and the polymorphic nature of the MEPs we often observed MEP amplitudes of ≥ 0.1 mV. The estimated MT was regarded as the minimum intensity at which minimally five of ten consecutive trials resulted in positive MEPs [23]. To exclude the possibility of low frequency rTMS-induced effects, we allowed a minimum of 10 seconds between stimulation pulses [24,25].

Additional MEPs were recorded at four adjacent locations in each hemisphere, namely: 1 mm medial, 1 mm anterior, 1 mm lateral and 1 mm posterior to the central

location. At each location, including the central location, we stimulated at 100% of the approximated MT for each hemisphere and recorded 10 EMG traces. Similar grid measurements in humans are typically done at 110-120% of the MT, but because of the larger MEP amplitudes that we recorded (≥ 0.1 mV vs 0.05 mV in humans), we used a lower stimulation intensity for these grid measurements.

Data analysis

Each EMG trace was analyzed in Matlab (MATLAB and Statistics Toolbox Release 2012b, The MathWorks, Inc., Natick, Massachusetts, United States.). The MEP amplitude was determined from the difference between the minimum and maximum EMG reading values between 7 ms and 25 ms after the TMS discharge. No dynamic analysis was performed to detect the time points of MEP onset and end, or the maximum and minimum amplitudes, as the shape of the MEPs were quite variable over coils and rats, and generally had a complex polyphasic morphology [26,27] (see Appendix, Results, figure 2), which was less reproducible as compared to human MEPs [16].

We performed a visual inspection of all trials and verified that the automated MEP amplitude detection was accurate. In five rats, a few single recordings were excluded because of ripple-like spurious signals (see Appendix, Results, figure 2 C and D). From one rat all recordings were excluded because of a high degree of spontaneous EMG activity, probably caused by anesthesia problems.

First, average MEP amplitudes for each forelimb, calculated from ten consecutive EMG traces, were determined for every stimulation location (5 per hemisphere), for each coil. Next, differences in MEPs were statistically analyzed with a repeated-measures, within-subjects, ANOVA (2 x COIL TYPE, 3 x LOCATION, 2 x HEMISPHERE, 2 x FORELIMB) using IBM SPSS statistics (version 20, IBM, NY, USA). Values were classified as statistically significantly different if $p < 0.05$.

Results

MS coil laterality

In silico validation

To evaluate the incident electric field, namely the primary electric field produced by the coil alone, we considered a surface plane (10x10 cm) positioned at different offsets (z-offset) along the coils' iso-centers. In particular we compared the fields of the small coil (figure 2: B1, B3) to those of the large coil (figure 2: B2, B4) at

a depth z-offset of 5 mm below their surface, where we defined 100 V/m as a reference threshold value for successful neuronal activation [28]. The simulation results (figure 2: A1 – A4) were obtained with a MO of 80% and 45% for the small and large coils, respectively. These intensities were selected as the most representative MO for each coil from our in vivo experiments. In figure 2 (B3 and B4), the half power region (HPR) is depicted as a measure of focality, defined as the area where the total electric field, E , obeys the condition $|E| > |E_{\text{maximum}}| = 100\text{V}/\sqrt{2}$ [28], with a small to large coil ratio of 32:60 mm². Although these results are indicative of better focal stimulation in favor of the small coil, it also hints at possible power impotence in comparison to the large coil, consequently having an effect on the capability of the small coil to sufficiently stimulate neuronal populations involved in eliciting MEPs. This predicament can be supported further when considering the depth decay of the fields of each coil at an individually fixed MO. The field of the large coil drops by 20% from $z = 5$ mm to $z = 10$ mm, and by 35% from $z = 10$ mm to $z = 20$ mm, whereas the small coil drops by 27% and 40%, respectively. In addition, using the same approach, we validated the magnetic field for each coil at a distance of 20 mm and 100% of the MO to values/plots provided by the manufacturer (see Appendix, Results, figure 3).

The computer simulations of the complete electrical field for the large coil showed similar values in ipsi- and contralateral homologous regions, despite lateralized positioning of the coil center. This was demonstrated for three different locations on each side of the cerebrum (-4, -3, -2, 2, 3 and 4 mm from midline) evaluated on the ROI patches (figure 2, A1: small coil overview; A2: large coil overview; A3 and A4: isolated rendering of the patches alone for the small coil and large coil, respectively). The slight asymmetry in the electrical field between the hemispheres can be explained by the small anatomical asymmetry of white matter in our sample of rat brain images. An integral of the electrical and current density vector fields on each side of our predefined ROI grids (see Methods, ‘Cortical region of interest’) is shown in relation to MEP recordings in figure 3 (top panel) for each of the 3 simulated coil positions on each side (for each hemisphere).

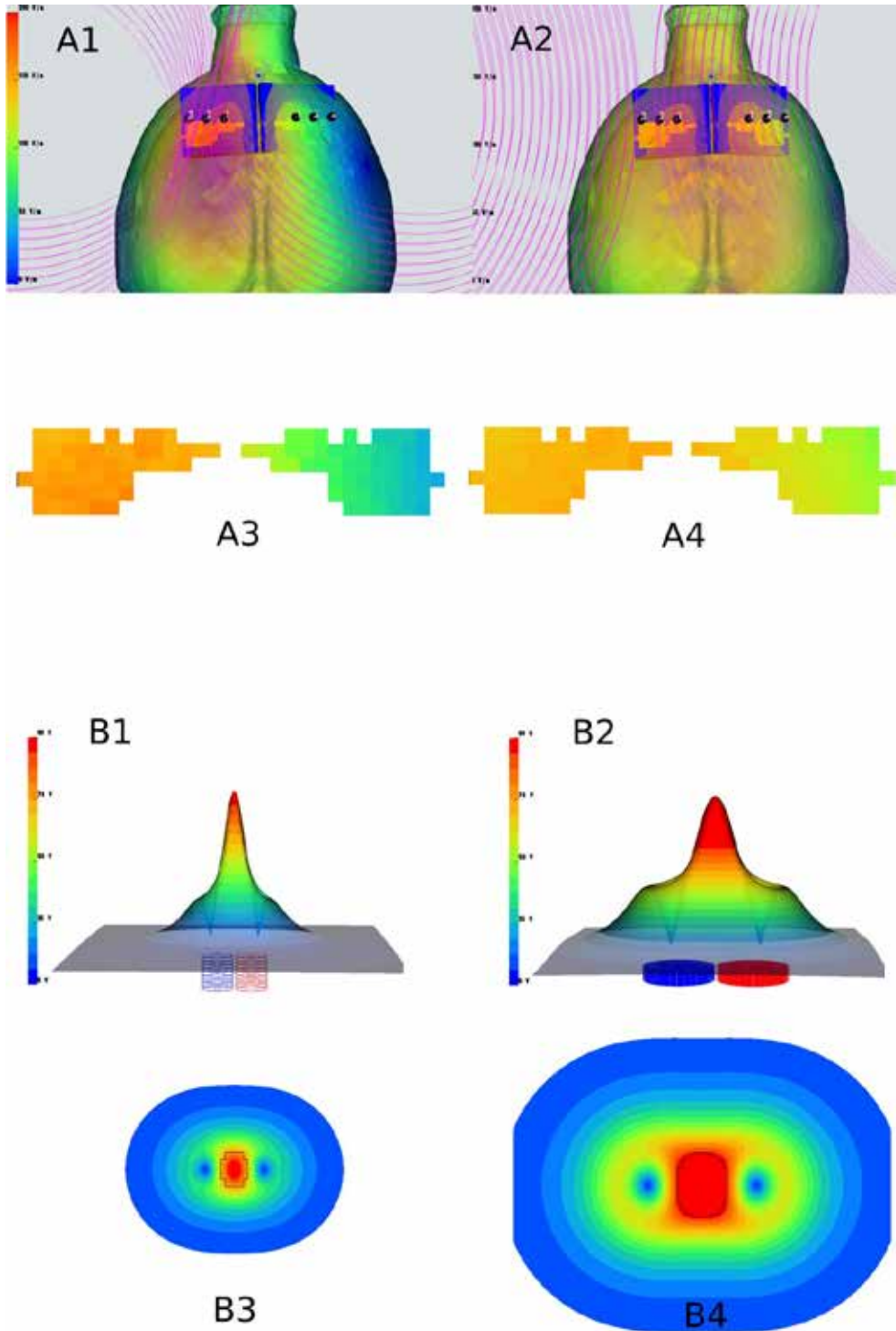


Figure 2: Simulation results for the brain model ROIs and coil electric fields alone. Top view (A): Rendering of the total electric field, as a transparent overlay (10% opacity) over the outer cortex boundary of the FEM 3D model, for the small (A1) and large (A2) coils.

Black spheres mark the 3 locations on each hemisphere where coil positions were sampled, the results are shown only for the coils positioned at the outer left position. The isolated ROI patches are shown separately for the small (A3) and large (A4) coils. Bottom view (B): Primary electric field (coil contribution only) visualization for the small (B1, B3) and large (B2, B4) coils. The inflated surface in the aforementioned figures is simply a z-axis inflated square mesh with a factor of $z=z+0.1*|Et|/\max(|Et|)$; where Et is the final total electric field (the primary coil and secondary FEM derived electric fields combined). Additionally, the top view of these surfaces is shown in rendering B3 and B4. The distance between the surface of each coil and the square mesh is 5 mm, a relevant anatomical depth around which we expect the strongest cortical stimulation possible. The black line, outline (iso-line) in B3 and B4, depicts the extent of the half power region (HPR). ROI/s = region/s of interest.

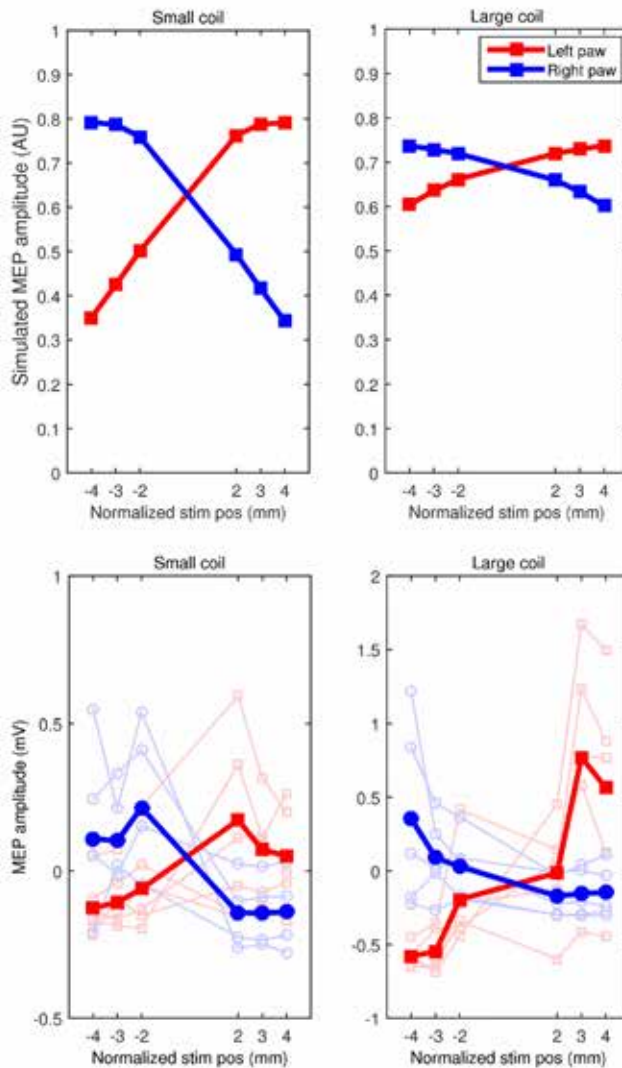


Figure 3: TMS coil laterality plots; *in silico* and *in vivo* validation. Top view: *In silico* simulations of the small coil showed a substantial difference in motor evoked potential (MEP) amplitudes when either stimulating the left (-) or right (+) hemispheres independently. This laterality was not obvious for the large coil.

Bottom view: MEP amplitudes measured *in vivo* for the small and large TMS coils. Stimulation of one hemisphere with either the small or the large TMS coil resulted in a clear difference between the MEP responses detected in the contralateral (higher MEP amplitude) and ipsilateral forelimbs (lower MEP amplitude), respectively, indicative of TMS laterality for both coils.

The horizontal axis (mm) gives the relative position of TMS at three positions in either the left (-) or right (+) hemisphere. The three stimulation positions in each hemisphere correspond to the relative motor hotspot position (-3/ 3), and positions 1 mm medial (-2/ 2) and lateral (-4/ 4) to the hotspot. The vertical axis (mV) gives the rectified MEP amplitude. The bold lines in the graphs depict the average MEP responses for 5 animals, while the non-bold lines represent average MEPs for each rat individually (bottom view). TMS = transcranial magnetic stimulation, pos = position.

In vivo validation

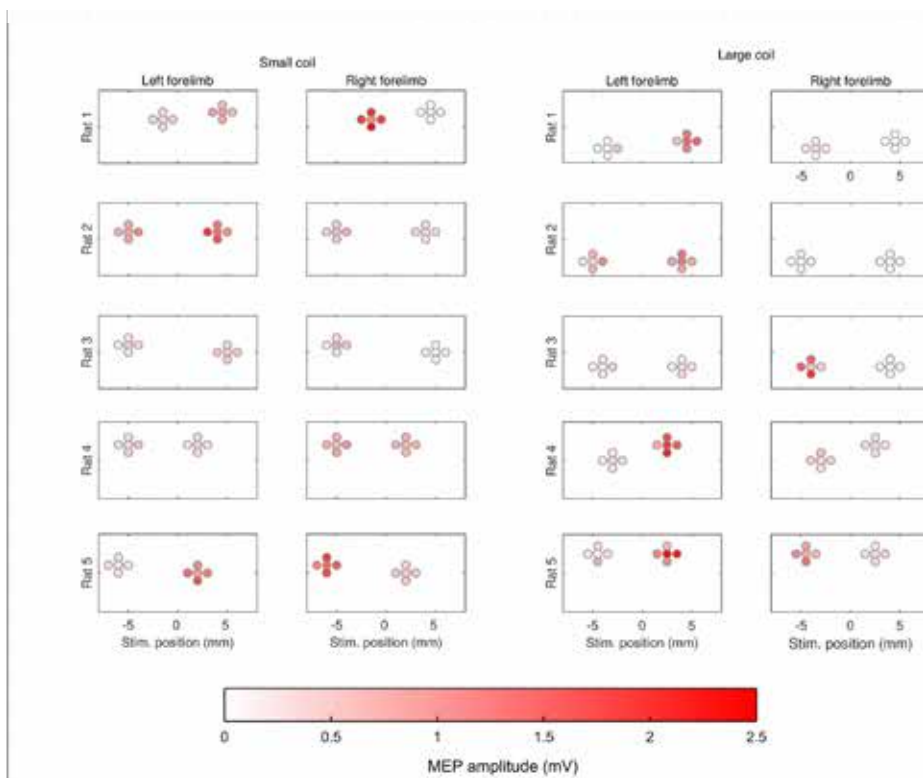


Figure 4: Five-point TMS-MEP grid map of the forelimb region of the rat motor cortex. Averaged MEP responses recorded for the left and right forelimb in five rats, using a small rodent-specific TMS coil (left) and a large commercial human TMS coil (right). Horizontal axis (mm) informs on the five-point stimulation positions in the lateral-medial (midline: 0)

plane on the left (-) and right (+) hemispheres, respectively. The central grid point position was regarded as the MEP hotspot location, with the surrounding four grid-points being 1 mm anterior, medial, posterior or lateral from the hotspot position. TMS = transcranial magnetic stimulation, MEP = motor evoked potential.

In vivo TMS experiments revealed that the small coil needed about double the amount of MO intensity compared to that of the large coil to generate MEPs and to determine the MTs (see Appendix, Results, table 2). The average MTs for the small coil were: $73 \pm 8\%$ MO (right hemisphere) and $81 \pm 4\%$ (left hemisphere). Whereas, the average MTs for the large coil were: $42 \pm 3\%$ MO (right hemisphere) and $45 \pm 4\%$ MO (left hemisphere). For both TMS coils, the intensity of the MT varied with 0-10% between hemispheres. In one animal we observed a 25% MO intensity difference between hemispheres for the small coil.

Coil laterality was evaluated from averaged MEP amplitudes, recorded bilaterally from the left and right forelimbs, evoked from five stimulation positions over each hemisphere, i.e. a central location of the motor cortex, and locations at 1 mm anterior, medial, posterior and lateral of the central location, respectively (figures 3 and 4). The MEP amplitude maps showed that clear lateralization can be observed for both the large and the small TMS coils, different from the in silico results where the large coil hardly exhibited lateralization (figure 3). Both TMS coils induced small MEP responses in the ipsilateral forelimb, but the largest MEP responses were observed in the contralateral forelimb. Interestingly, the relative hotspot (center of motor cortex) area did not always yield the highest MEP responses.

To further validate coil laterality statistically, MEP amplitude data from three lateral stimulation positions in each hemisphere (POS = 6 stimulation positions) were plotted (figure 3, bottom panel). A significant interaction between TMS stimulation position and forelimb channel on MEP amplitude [POS x LIMB: (F(5, 4) = 13.965, p=0.01)], statistically confirmed the main lateralization effect (larger responses in the forelimb contralateral to the stimulated hemisphere). A significant difference was observed in MEP amplitude when considering the interaction between coil size, stimulation position and forelimb channel [COIL x POS x LIMB: (F(5, 4) = 8.212, p = 0.014)]. The latter seems to reflect a stronger lateralization for the large coil, which may be explained by the larger MEP amplitudes for the large coil.

Discussion

The aim of the present study was to evaluate the focality of a conventional figure-of-eight TMS coil and a rodent-specific miniaturized figure-of-eight TMS coil. FEM simulations predicted that the large conventional TMS coil would be unable to achieve lateralized focal stimulation of the rat motor cortex. Therefore, we hypothesized that the small rodent-specific TMS coil would more focally elicit lateralized MEPs compared to the large coil. However, unexpectedly, our *in vivo* data showed that both TMS coils were able to elicit unilateral MEPs from the contralateral forelimb of the rat.

In contrast to some recently designed rodent-specific TMS coils [4,8], our small figure-of-eight coil successfully induced focal stimulation and elicited MEPs. Previously, reduction in coil size has been hampered by physical difficulties such as overheating and deformation, due to increased resistance and larger currents needed to produce an effective magnetic field [29]. However, through effective silicone oil cooling, our small coil could deliver focal stimulation pulses at intensities similar to conventional TMS coils.

Lateralized MEPs were also recorded in response to stimulation with the large TMS coil, consistent with the findings of Rotenberg and colleagues who used a similarly sized commercial TMS coil to stimulate the rat motor cortex [6]. This was inconsistent with our *in silico* simulations, in which the incident electrical fields for the large TMS coil were only marginally different between the left and right motor cortex. However, it is possible that our cortical ROI is under representative of the full population of neurons that is involved in a typical rat MEP response.

Overall, the strong lateralization of the majority of MEPs in our study suggests that signals originated from one hemisphere. In agreement with other studies that measured cortically derived MEPs induced by direct electrical stimulation and TMS in rats, MEPs had a complex polyphasic morphology, signifying a cortical origin, with a relatively long onset latency of 7-25 ms, which is caused by the summation of excitatory post-synaptic potentials mediated by several descending motor tracts [6,26,27]. According to Nielsen and colleagues, the size and latency of MEPs in rats critically depend on coil position and stimulation intensity, as these parameters determine the relative contribution of differently activated motor tracts on MEP morphology. Therefore, the broad range of MEP onset latencies observed in our study could reflect the activation of multiple descending motor tracts, including the cortico- and reticulospinal tracts, which might have contributed to MEP morphology in varying degrees. Furthermore, the observed variability in hemispheric MTs and hotspot MEP amplitudes may also be explained by differences in the contribution and number of activated motor tracts during stimulation.

MEP amplitudes produced with the large coil were approximately twice as high as those elicited by the small coil. While the small coil had better focality and deeper field penetration, due to the superior power decay curve, the applied stimulation intensities might have been insufficient to excite the relevant physiological area in its entirety. Additionally, this could explain the sporadic MEPs with multiple volleys/ripples, and highly variable and relatively long latencies, after the TMS pulse (see Appendix, Results, figure 2 C and D). Nielsen and colleagues reported similar long-latency (20-30 ms) MEPs, recorded in the biceps brachii of rats, that were elicited by weak TMS stimulus intensities just above MEP threshold [27]. In addition, it is possible that the power used for the small coil was not always sufficient to elicit stable suprathreshold MEPs. However, increasing MO intensity above 85% poses challenges and limitations with regard to heating, particularly for rTMS protocols, even under active cooling.

Conclusions

In this study we have combined in-vivo and in-silico experiments to guide the design of an optimal small rodent TMS coil capable of inducing a strong enough electric field in relatively confined cortical regions. In silico simulations suggested favorable ability of this coil in comparison to larger commercially available human coils. Our in vivo data showed that reliable MEP asymmetry can be achieved with the novel TMS coil, although this was also feasible with a larger conventional TMS coil. Our study demonstrates that focal TMS stimulation can be accomplished in translational rodent studies. The apparent discrepancy between our in silico and in vivo results is an important consideration for follow-up studies.

Acknowledgements

Funding: This work was supported by the Netherlands Organization for Scientific Research [VICI 016.130.662] and by the DeNeCor project being part of the ENIAC Joint Undertaking.

Supporting Information

Material and Methods

In silico experiments

Head model

A 3D rat brain template was constructed from 48 postmortem male Wistar rat (13 weeks old, average weight of 330 g) brain scans acquired at a 9.4T horizontal bore MR system with a 90 mm-diameter 1000 mT/m gradient coil (Agilent, Santa Clara, CA, USA) using a radio-frequency transmit and receive birdcage coil (Millipede, Agilent, Santa Clara, CA, USA). The paraformaldehyde-fixed extracted brains were placed in a custom-made holder and immersed in a non-magnetic oil (Fomblin, Solvay Solexis, Weesp, The Netherlands). Anatomical images were acquired with a 3D gradient-echo scan [repetition time (TR) / echo time (TE) = 6.87 / 3.34 ms; flip angle 15 degrees; 64 averages] at an isotropic voxel resolution of 94 μm . Diffusion-weighted images were acquired with a diffusion-weighted 8-shot spin-echo Echo Planar Imaging scan [TR / TE = 2700 / 28 ms; 128×128 matrix; field-of-view 25×25 mm²; 55 slices of 0.2 mm; 8 averages; b-value 3174 s/mm²; 60 diffusion-weighted images in non-collinear directions; 6 b₀ images]. Fractional anisotropy parameter maps were constructed from voxel-wise estimates of the diffusion tensor after eddy current corrections. Images were averaged after linear (affine) and nonlinear (diffeomorphic demons) alignment. Tissue segmentation in white matter, gray matter and cerebrospinal fluid was done with K-means classification based on input from the anatomical MRI, fractional anisotropy maps and average diffusion-weighted MRI.

Coil models

Table S1: Parameters for coil modeling and generation (SCIRun::CreateTMScoil)

Coil models

Table S1: Parameters for coil modeling and generation (SCIRun::CreateTMScoil)

Coil Parameters	Small coil	Large coil
Machine output (MO)	80%	45%
max dl/dt	6.4x10 ⁶ A/s	3.6x10 ⁶ A/s
Windings	2	17
Radius inner	9.5 mm	14.5 mm
Radius outer	10.5 mm	23.5 mm
Distance outer	1 mm	1 mm
Stacks	10	10
Stack step	1.5 mm	1 mm
LOD	2	2

In vivo experiments

Transcranial magnetic stimulation

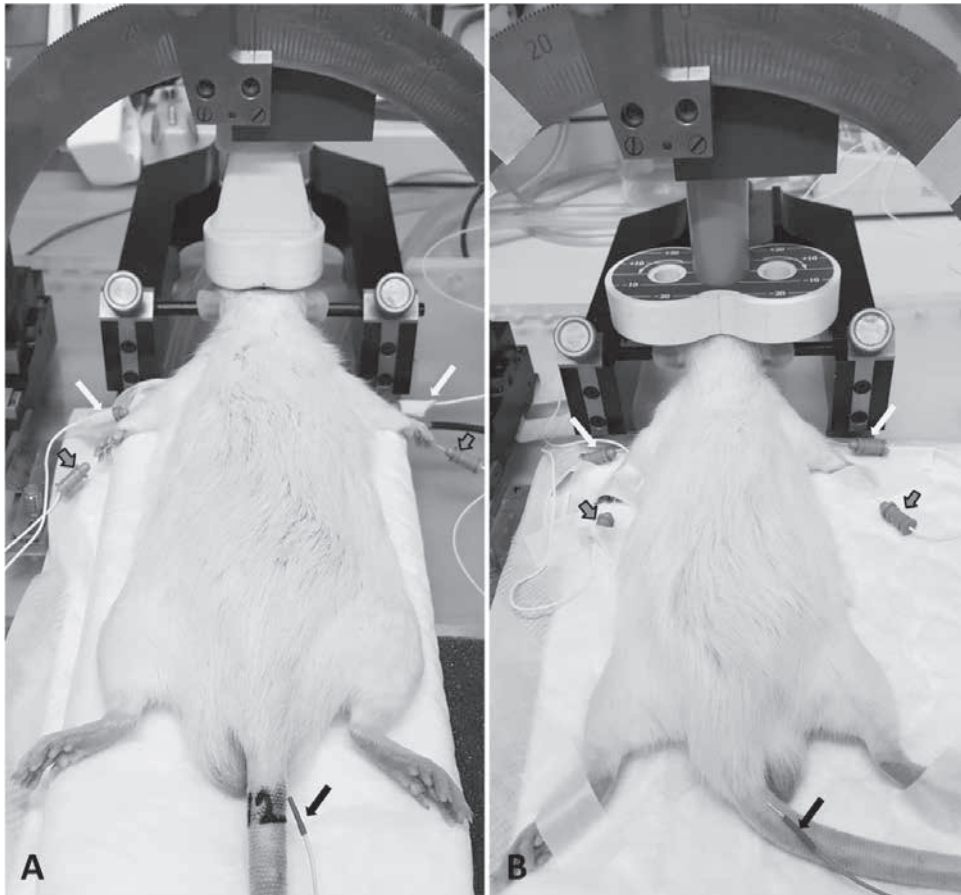


Figure S7: Experimental setup for in vivo TMS of rat brain. Propofol-anesthetized rats were placed in a rodent stereotactic head frame. The TMS coils, small (A) or large (B), were fixed to an arm of the stereotactic frame which allowed sub-mm movements in three directions. Using EMG, motor evoked potentials (MEPs) were recorded bilaterally from each forelimb (brachialis muscle), while applying TMS over the contralateral forelimb region of the motor cortex. Active (white arrows), reference (grey arrows) and ground (black arrows) electrodes are indicated in the pictures. TMS = transcranial magnetic stimulation; EMG = electromyography; MEPs = motor evoked potentials.

Results

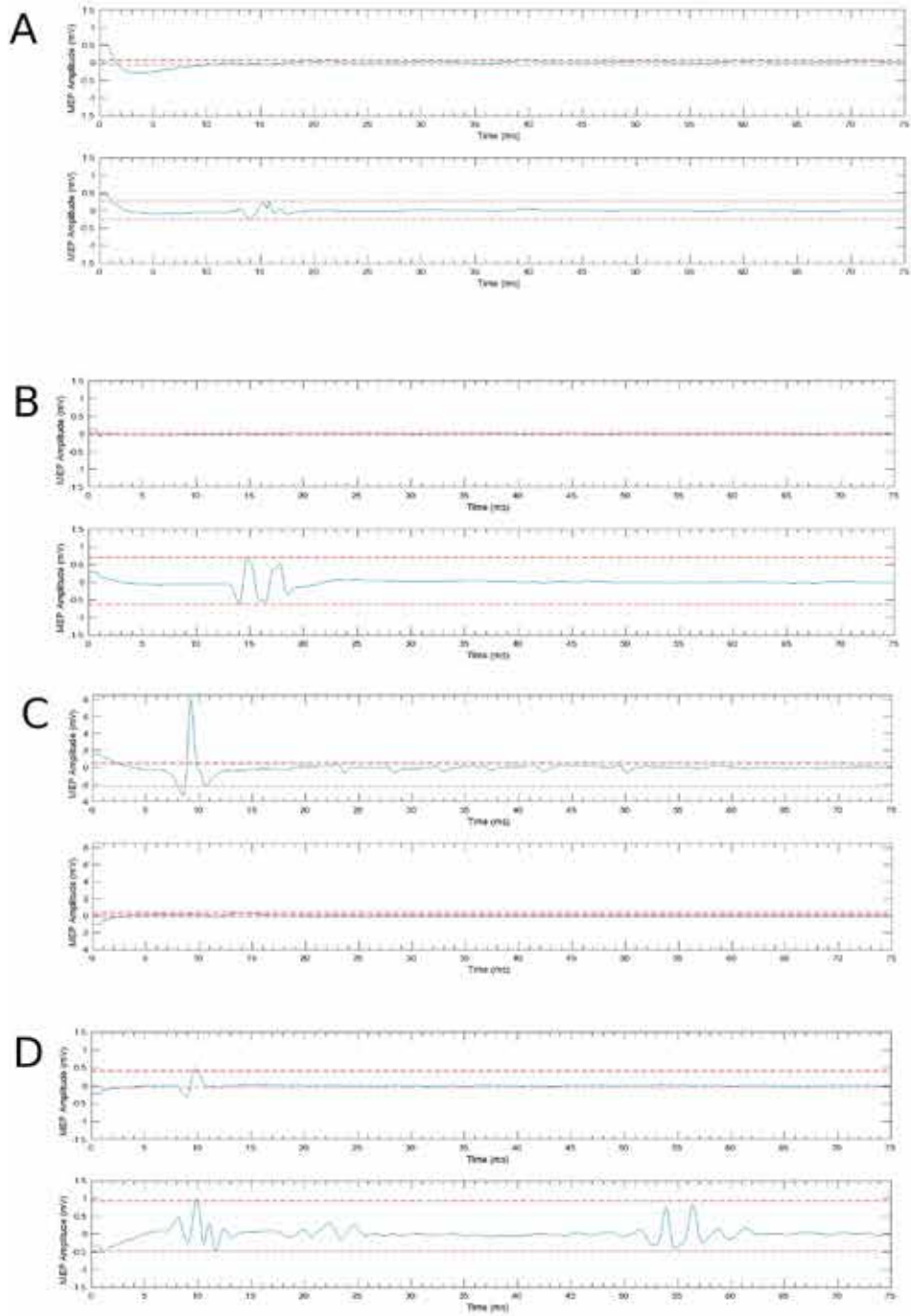


Figure S8: Representative individual electromyography (EMG) traces with TMS-induced motor evoked potentials (MEPs). EMG traces (in mV) recorded from ipsi- and contralateral forelimbs as a function of time (in ms) after unilateral TMS over the motor

cortex with a small (panel A) or large (panel B) TMS coil. (C, D) Spurious signals detected in EMG data when using the small TMS coil. Continued twitches are visible in the signal, which seems to be unrelated to the TMS pulse. The dotted lines indicate the minimum and maximum amplitudes of the EMG reading between 7 ms and 25 ms after the TMS stimulus. The difference between these two time points was taken as the MEP amplitude in mV. TMS = transcranial magnetic stimulation.

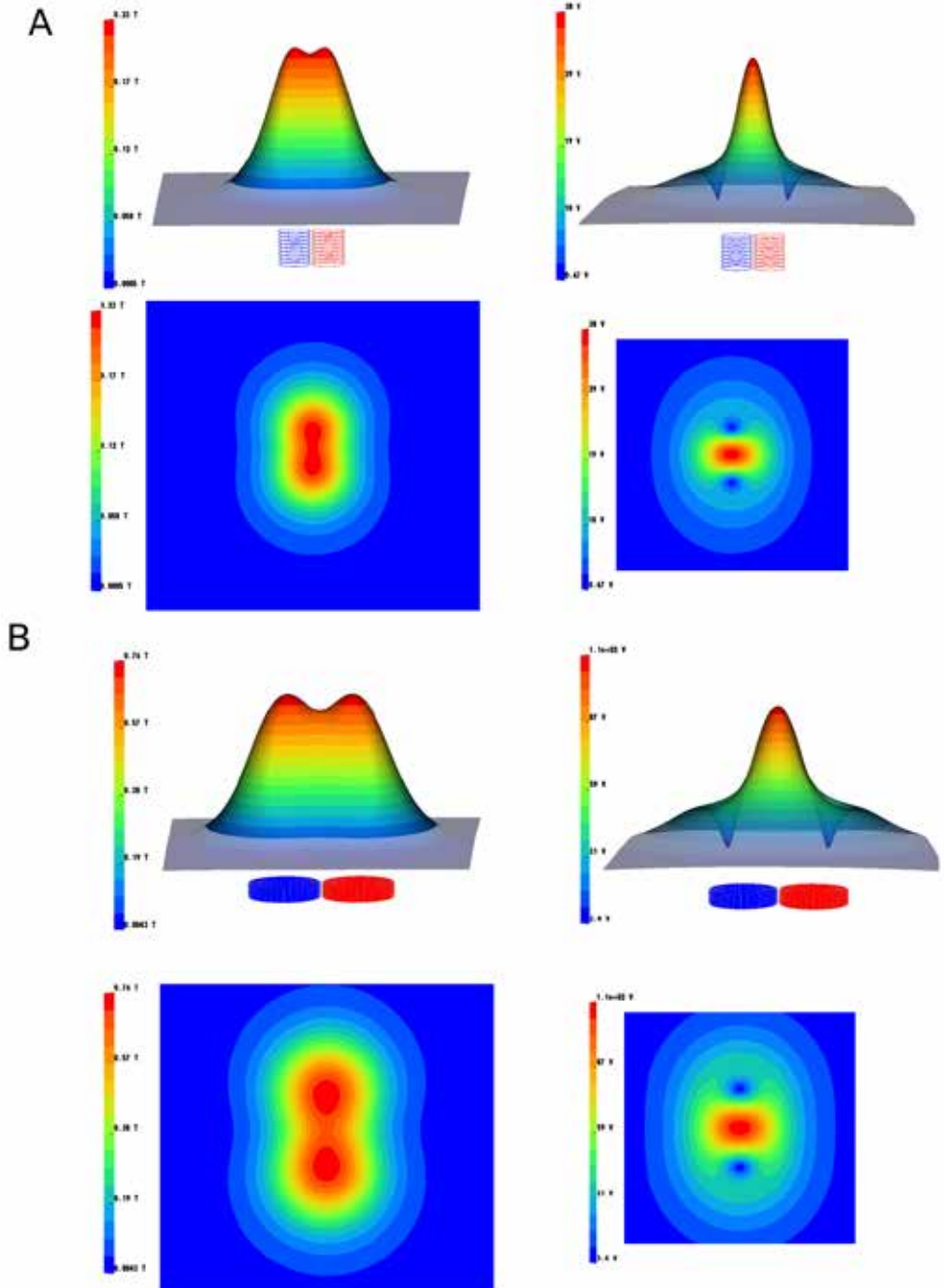


Figure S3: The simulated electrical and magnetic fields produced by the small and large TMS coils. Visualization of the magnetic vector potential (left) and magnetic fields (right) for the small (A) and large TMS coils (B). The measured location is a plane positioned as 2.0 cm offset from primary coil surface. The 3D visualization is an artificially inflated triangular surface to depict the general shape of each field, the degree of deformation along the primary axis is promotional to the magnitude map depicted below (grid of 128x128 for a size of 10x10cm). TMS = transcranial magnetic stimulation.

Table S2: Motor thresholds (MTs) generated for each hemisphere with the small and large TMS coils

Rat	Small coil		Large coil	
	Right hemisphere MT (% MO)	Left hemisphere MT (% MO)	Right hemisphere MT (% MO)	Left hemisphere MT (% MO)
1	75%	75%	40%	50%
2	80%	80%	45%	45%
3	60%	85%	40%	45%
4	75%	85%	45%	45%
5	75%	80%	40%	40%
Mean	73%	81%	42%	45%
SD	8%	4%	3%	4%

References

- [1] Dayan E, Censor N, Buch ER, Sandrini M, Cohen LG. Noninvasive brain stimulation: from physiology to network dynamics and back. *Nat Neurosci* 2013;16:838–44. doi:10.1038/nn.3422.
- [2] Lefaucheur J-P, André-Obadia N, Antal A, Ayache SS, Baeken C, Benninger DH, et al. Evidence-based guidelines on the therapeutic use of repetitive transcranial magnetic stimulation (rTMS). *Clin Neurophysiol* 2014;125:2150–206. doi:10.1016/j.clinph.2014.05.021.
- [3] Tang A, Thickbroom G, Rodger J. Repetitive transcranial magnetic stimulation of the brain: Mechanism from animal and experimental models. *Neuroscientist* 2015;23:82–94.
- [4] Tang AD, Lowe AS, Garrett AR, Woodward R, Bennett W, Canty AJ, et al. Construction and evaluation of rodent-specific rTMS coils. *Front Neural Circuits* 2016;10:1–10. doi:10.3389/fncir.2016.00047.
- [5] Vahabzadeh-Hagh AM, Muller PA, Gersner R, Zangen A, Rotenberg A. Translational neuromodulation: approximating human transcranial magnetic stimulation protocols in rats. *Neuromodulation* 2012;15:296–305. doi:10.1111/j.1525-1403.2012.00482.x.
- [6] Rotenberg A, Muller PA, Vahabzadeh-Hagh AM, Navarro X, López-Vales R, Pascual-Leone A, et al. Lateralization of forelimb motor evoked potentials by transcranial magnetic stimulation in rats. *Clin Neurophysiol* 2010;121:104–8. doi:10.1016/j.clinph.2009.09.008.
- [7] Cohen D, Cuffin BN. Developing a more focal magnetic stimulator. Part I: Some basic principles. *J Clin Neurophysiol* 1991;8:102–11. doi:10.1097/00004691-199101000-00013.
- [8] Parthoens J, Verhaeghe J, Servaes S, Miranda A, Stroobants S, Staelens S. Performance characterization of an actively cooled repetitive transcranial magnetic stimulation coil for the rat. *Neuromodulation* 2016;19:459–68. doi:10.1111/ner.12387.
- [9] Rodger J, Mo C, Wilks T, Dunlop SA, Sherrard RM. Transcranial pulsed magnetic field stimulation facilitates reorganization of abnormal neural circuits and corrects behavioral deficits without disrupting normal connectivity. *FASEB J* 2012;26:1593–606. doi:10.1096/fj.11-194878.
- [10] Makowiecki K, Harvey AR, Sherrard RM, Rodger J. Low-Intensity Repetitive Transcranial Magnetic Stimulation Improves Abnormal Visual Cortical Circuit Topography and Upregulates BDNF in Mice. *J Neurosci* 2014;34:10780–92. doi:10.1523/JNEUROSCI.0723-14.2014.

- [11] Grehl S, Viola HM, Fuller-Carter PI, Carter KW, Dunlop SA, Hool LC, et al. Cellular and molecular changes to cortical neurons following low intensity repetitive magnetic stimulation at different frequencies. *Brain Stimul* 2015;8:114–23. doi:10.1016/j.brs.2014.09.012.
- [12] Meng Q, Jing L, Badjo JP, Du X, Hong E, Yang Y, et al. A novel transcranial magnetic stimulator for focal stimulation of rodent brain. *Brain Stimul* 2018;11:663–5. doi:10.1016/j.brs.2018.02.018.
- [13] Petrov PI, Mandija S, Sommer IEC, Van Den Berg CAT, Neggers SFW. How much detail is needed in modeling a transcranial magnetic stimulation figure-8 coil: Measurements and brain simulations. *PLoS One* 2017;12. doi:10.1371/journal.pone.0178952.
- [14] Otte WM, Dijkhuizen RM. Rat brain template. *Open Sci Framew* 2018. <https://osf.io/epy5d/> (accessed April 6, 2018).
- [15] Bronson JR, Sastry SP, Levine JA, Whitaker RT. Adaptive and unstructured mesh cleaving. *Procedia Eng* 2014;82:266–78. doi:10.1016/j.proeng.2014.10.389.
- [16] Chang WH, Fried PJ, Saxena S, Jannati A, Gomes-Osman J, Kim YH, et al. Optimal number of pulses as outcome measures of neuronavigated transcranial magnetic stimulation. *Clin Neurophysiol* 2016;127:2892–7. doi:10.1016/j.clinph.2016.04.001.
- [17] Fonoff ET, Pereira JF, Camargo LV, Dale CS, Pagano RL, Ballester G, et al. Functional mapping of the motor cortex of the rat using transdural electrical stimulation. *Behav Brain Res* 2009;202:138–41. doi:10.1016/j.bbr.2009.03.018.
- [18] Whishaw IQ, Cioe JDD, Previsich N, Kolb B. The variability of the interaural line vs the stability of bregma in rat stereotaxic surgery. *Physiol Behav* 1977;19:719–22. doi:10.1016/0031-9384(77)90304-3.
- [19] Luft A, Kaelin-Lang A, Hauser T-K, Cohen L, Thakor N, Hanley D. Transcranial magnetic stimulation in the rat. *Exp Brain Res* 2001;140:112–21. doi:10.1007/s002210100805.
- [20] Haghghi SS, Madsen R, Green KD, Oro JJ, Kracke GR. Suppression of motor evoked potentials by inhalation anesthetics. *J Neurosurg Anesthesiol* 1990;2:73–8.
- [21] Haghghi SS, Green KD, Oro JJ, Drake RK, Kracke GR. Depressive effect of isoflurane anesthesia on motor evoked potentials. *Neurosurgery* 1990;26:993–7.
- [22] Wiechers DO, Blood JR. EMG needle electrodes: Electrical impedance. *Arch Phys Med Rehabil* 1979;60:364–9.
- [23] Rossini P, Barker A, Berardelli A, Caramia M, Caruso G, Cracco R, et al. Non-invasive electrical and magnetic stimulation of the brain, spinal cord and roots: basic

principles and procedures for routine clinical application. Report of an IFCN committee. *Electroencephalogr Clin Neurophysiol* 1994;91:79–92. doi:10.1016/0013-4694(94)90029-9.

[24] Vaseghi B, Zoghi M, Jaberzadeh S. Inter-pulse interval affects the size of single-pulse TMS-induced motor evoked potentials: A reliability study. *Basic Clin Neurosci* 2015;6:44–51.

[25] Thomson RH, Maller JJ, Daskalakis ZJ, Fitzgerald PB. Blood oxygenation changes resulting from trains of low frequency transcranial magnetic stimulation. *Cortex* 2012;48:487–91. doi:10.1016/j.cortex.2011.04.028.

[26] Schlag MG, Hopf R, Redl H. Serial recording of sensory, corticomotor, and brainstem-derived motor evoked potentials in the rat. *Somatosens Mot Res* 2001;18:106–16. doi:10.1080/135578501012006219.

[27] Nielsen JB, Perez MA, Oudega M, Enriquez-Denton M, Aimonetti JM. Evaluation of transcranial magnetic stimulation for investigating transmission in descending motor tracts in the rat. *Eur J Neurosci* 2007;25:805–14. doi:10.1111/j.1460-9568.2007.05326.x.

[28] Salvador R, Miranda PC. Transcranial magnetic stimulation of small animals: a modeling study of the influence of coil geometry, size and orientation. *Conf Proc . Annu Int Conf IEEE Eng Med Biol Soc IEEE Eng Med Biol Soc Annu Conf* 2009;2009:674–7. doi:10.1109/IEMBS.2009.5334070.

[29] Weissman JD, Epstein CM, Davey KR. Magnetic brain stimulation and brain size: relevance to animal studies. *Electroencephalogr Clin Neurophysiol Potentials Sect* 1992;85:215–9. doi:10.1016/0168-5597(92)90135-X.

Chapter VIII

Summary and general discussion

Discussion

In this final chapter, we will summarize the results of our experimental work involving healthy human subjects and rodents, using well-established single-pulse TMS protocols. The main aim of this thesis was to validate computational models that predict electric fields from FEM models for a given coil position and ensuing neuronal responses using measurements of physiological responses following the administration of single-pulse TMS. For that purpose, we looked into two measures that were previously successfully combined with TMS and were demonstrated to be safe and compatible: motor-evoked potentials (the EMG response to TMS) and the BOLD response using concurrent TMS/fMRI. We will cover the shortcomings and limitations of both approaches and suggest alternatives. In addition, we will explore methodological considerations regarding the interpretation of each type of measurement.

The modeling aspect behind computer guidance of TMS and in particular the potential of a dosimetry estimate derived from E-field is the central and by far the most complex methodological aspect of our experiments. Therefore, as a reflection on the outcome of the chapters presented so far, we will revisit each major part required to achieve a virtual TMS electric-field simulation, namely, the need to model the coil-induced field per specific stimulator parameters and then the need to numerically derive the additional secondary field governed by the dielectric properties of the stimulated medium (i.e., the brain). In our case, the secondary E-field was provided by a 3D compartmentalized model of the 5 relevant tissue types of the head. A final and crucial part was the derivation of an activation metric that could serve as a crude predictor of the neuronal stimulation once the E-field prediction for a TMS stimulus has been derived, allowing validation of the model with observed physiological responses.

We will continue to discuss future developments in the application of TMS and elaborate on their possible implications in the context of modeling. Our focus will be on suggestions for improvement of the practical value of such models. Also, we will acknowledge some alternatives and emerging imaging modalities as potential tools for in-vivo model validation. Finally, we will cover the broader application and usability of FEM EM models with a focus on computer-guided dosimetry of TMS.

TMS Model Construction

TMS Coil Modeling

In this section, we will reflect on the experience gained during TMS coil modeling. Various numerical methods and approaches for that purpose have been suggested. The extent to which they could correctly approximate the shape and magnitude of the induced field has received less attention in the literature [1]. Instead, most coil modeling studies have concentrated on suggesting novel TMS coil designs with a focus on primary field energy, focality, and depth optimizations [2] [3].

The importance of accurate TMS coil models is supported by the theory from chapter 2. We can see that inaccuracies in the approximation of the primary E-field (governed by the coil geometry) will be further propagated to the estimate of the secondary field (governed by the medium). This by itself already served as a motivation to develop an in-house implementation of the coil-geometry generator and field solver. This way the model could be easily adjusted to allow for calibration against measurements. We conducted magnetic-field mapping of the coil under very low intensity (4% MO) inside a 3T MR scanner. Such a low intensity was picked intentionally. Higher intensities were simply not achievable due to the inherent physical limits of the technique [4].

Additionally, in chapter 3, we managed to evaluate the effect of the total electric field on a realistically shaped human head (courtesy of [5]). The most critical geometrical detail of the coil contributing to spatial accuracy is the coil surface area, which is bound by the difference between the outer versus inner radius of the copper wire windings. In contrast, the model thickness influenced the final results to a much lesser extent and at a significant computational cost. We found highly idealized single-wire loop models to overestimate the focality of figure-8 coil when evaluated in a realistic scenario over the cortical M1 area. The findings of chapter 3 motivated the development of coil models used for the remainder of the modeling and model validation work presented in this thesis (chapters 2, 4, and 5), being a model with realistic spiral windings but infinitesimally thin.

The coil models that we proposed were based on the piece-wise BiotSavart method of deriving the EM field of coils. This method has the advantage of being straightforward to implement in the form of integration over an arbitrary curved profile. It is flexible and allows capturing the form and shape of any arbitrary coil. However, even when using a modern parallel CPU, the direct calculation of the field of a realistic head model could take up to half an hour compared to 5 minutes for the linear system FEM solver.

An alternative approach, avoiding the need for modeling entirely, has been suggested with which a computer database is maintained of precise field measurements

in the form of 3D sampled vector fields (60x45cm with 0.4mm resolution) [1]. This eliminates the need to model each combination of coil shapes employed in practice, especially if we consider each combination of manufacturer and coils offered per device. However, the endeavor of building and maintaining such an all-inclusive dataset is equally if not even more demanding. An additional benefit of the model-less approach is the possibility to achieve better accuracy. The spatial accuracy of the field approximations is governed by the detail of the coil geometry, which is particularly prone to tuning errors, especially when trying to balance the inner current distribution in more complex shapes. Also numerically quantifying the magnitude is problematic when too close to the coil, a fundamental limitation of the BiotSavart law. In contrast, the inaccuracy due to the measuring equipment is expected to be lower, largely determined by the interpolation and extrapolation strategy between probe positions. We should acknowledge, however, that deriving reliable instrumental measurements near the coil might also prove to be a hardly trivial task.

Nevertheless, we adopted a similar approach to optimizing coil simulation time, that is, using a pre-calculated field of a particular coil model and then simply applying the transformation to place it correctly in place and then interpolate the vector field to the head model (nodes or elements of the FEM mesh). This technique was crucial for the undertakings described in chapter 4, where 100 simulations were required per subject, that is, for each position stimulated on the actual subject's head. The required approximately 25 minutes for the calculation of a single stimulus coil field alone results in almost 2 days of additional computational simulation time; instead, with our method, interpolation took less than 3 minutes per stimulus. This is all possible due to the relatively homogeneous permeability of the human head, similar to that of free space μ_0 .

Human Head Modeling

Besides a good model of the incident E-Field of a TMS coil, we need a good volumetric geometrical model of a human brain for each major tissue with distinct electrical conductive properties. Furthermore, such a 3D head model needs to be derived from individual MR images. As it turned out, this was one of the hardest problems to tackle in the context of the larger body of work presented in this thesis. Previous studies have tested the possibility to generalize the induced E-field maps on a group level using a standard brain and concluded that the complex and individual human morphology simply prevents using generic head models to predict TMS dosimetry in a subject-specific head model [6].

The derivation of subject-specific 3D FEM volumetric meshes that are anatomically correct and suited for numerical processing at the same has been challenging due to several complicating factors. Despite our best efforts, a completely automatized processing was not practically achieved, which we found to be a common

struggle among other researchers in the field. Except for a few subjects, most MRI image segmentations required manual adjustments in the classification of tissue types that could prove tedious and time-consuming. Most notably, within sulci, the ‘sulcal walls’ of the cortical sheet could ‘kiss’, that is, merge above the cleft that a sulcus forms (see chapter 2). Volumetric irregular tetrahedral meshes are critical for FEM accuracy, while strictly requiring both smooth and veridical boundaries between compartments in the case of heterogeneous domains (see chapter 2). Those two requirements combined lead to conflicting outcomes in the case of thin highly convoluted interfaces, such as the CSF–GM boundary. While imaging-smoothing operations could be successful in removing small discontinuities along the surface, they could as easily introduce unwanted holes and other topological artifacts into the final mesh that will negatively affect FEM solvers and lead to inaccurate local current estimates.

The complex morphology of the GM, characterized by its intricate folding of the gyri, sometimes leads to CSF interfaces that are less than 1mm thick. Such interfaces form predominantly around tightly packed gyri with narrow gaps in the folds of the cortical surface, and sometimes along areas of skull thickening on top of the gyral crowns. Layers of CSF with a resolution below 1mm fall just under the imaging resolution of the MRI images that we obtained for each participant, which makes voxel classification fundamentally ambiguous and vulnerable to several partial volumes effects [7] [8]. Higher-resolution T1-weighted MRI (at sub-millimeter resolution) might help better distinguish thin CSF compartments, while potentially presenting a new problem – the need for dura-matter classification. This could be a challenge because at a higher resolution, the dura-matter tissue surrounding the cortex becomes distinguishable, and it has similar voxel intensities to GM. Most head models of TMS omit the dura-matter since its significance for field distribution is considered small and to a large extent an unwanted artifact. It remains to be seen whether such assumptions are correct. Higher-resolution segmentations could also lead to an increased number of elements in the final mesh unless smart adaptive-parameter strategies are included. An alternative approach that ensures water-tight surfaces is the deformable-mesh approach [9].

In short, the 3D meshing of MRI images of individual participants appeared to be computationally very demanding, easily requiring a day per participant for some algorithms. Moreover, full automation is almost impossible to achieve in a universal, robust manner that could guarantee some level of consistent quality. At best we could hope for an iterative trial-and-error process with a minimum need for manual processing.

We managed to develop a pipeline that was effective in meshing the individual subject MRIs for subsequent use in FEM (see chapter 2), but it required manual intervention and verification, which was tedious at best. This process will eventually

produce meshes with a magnitude in the millions of elements, to accurately describe the head tissue types needed for the work at hand. Easy, on-demand meshing pipelines creating fully automatic individual meshes generated from MRI images are required for TMS-induced E-field modeling to eventually be adopted in clinical workflows [5]. It is identified here as a key impediment to the adoption of E-field modeling in clinical settings at the moment, requiring further research and development before computational neuro-stimulation can be used to control TMS dosimetry in clinical practice [10].

White Matter Relevance

As stated in chapter 2, we decided on modeling the WM-tissue conductivity as isotropic scalar quantity instead of the more realistic conductivity tensor ratio of 1:3 derived from DTI post-processing. We also partially motivated our decision based on several studies concluding a minor effect of taking into account white matter conductive anisotropy on the E-field distribution and magnitude (10%) [11]. Despite our skepticism in including DWI-based FEM modeling of WM as a passive conductor, we must defend the implication of WM tractography in identifying structural connectivity among brain areas and its relevance to TMS dosimetry and especially to subsequent signal propagation. The study of the human connectome and the possibility to derive a connective probability map for the general healthy population to further assist the application of TMS based on signal propagation have been already explored [12].

The capability of TMS to induce activity in brain regions distal from those directly stimulated has been demonstrated before [13] [14]. We also observed similar causality in our experiments (see chapter 6). The implications of TMS being able to probe and intervene in active human brain networks in a controllable and observable manner are numerous. It has been postulated that the origin of many psychological disorders, including MDD, is ultimately some type of network disorder [15][16]. Rather than dismissing the importance of connectivity in the context of TMS, we opted for not including anisotropy in our modeling of the WM tissue, as it has shown to have limited influence on the outcome of E-fields alone.

Tissue Dielectric Properties

Another critical aspect of delivering reliable estimates of the total E-field induced by a TMS coil is the accuracy of the adopted DP of the tissues in the head. Reported DP values from physiological recordings in the literature are sparse and often dated (<http://niremf.ifac.cnr.it/tissprop/>) (<http://niremf.ifac.cnr.it/docs/DIELECTRIC/Report.html>) [17]. Finding accurate DP

values for tissues in principle remains challenging for the computational E-field modeling community, including the models presented in this thesis.

Biological tissues exhibit a diverse range of conductivity and permittivity, which are themselves also highly sensitive to variations in the frequency of the administered EM stimulation. In the low-frequency regime (LF; 1–10 kHz), which includes typical TMS stimulation patterns in the ~4KHz range, the human head remains highly heterogeneous when we account for some of the major tissue types.

Initial insights into the uncertainties surrounding the variability of tissue conductivity can be derived from an experiment on rat cadaver brains that has revealed a striking difference in conductivity properties when compared to in-vivo tissue [18]. When considering the effect of temperature on electrical tissue properties, on the 14th-day postmortem, the aforementioned study reported a temperature-dependent linear E-field strength decrease of 38% when the temperature changed from 4° C to 37° C. Similar observations of above 100% discrepancies in tissue conductivity were reported when comparing in-vivo against ex-vivo values, interestingly with a 36% increase in the conductivity ratio between GM and WM [19]. Such a drastic change could be attributed to the rapid loss of temperature that bodily fluids undergo after death, being a limiting factor to both ion mobility and general tissue atrophy. Specifically for CSF conductivity, the difference between room and body temperature of 25°–37° C might lead up to a 44% difference in sigmas (1.45–1.79 S/m) [20]. Other biological factors, such as aging, have been implicated in altering conductivity, as reported in experiments conducted on rodents [21]. Interestingly, in rTMS depression treatment, age has been identified as a key predictor of treatment response, due to the larger prefrontal cortical entropy among the elderly population, more often requiring higher rTMS intensities [22]. This might be related to the altered conductivity with age mentioned before.

One fundamental problem with ex-vivo measurements is that, once a sample is taken from a deceased animal, its cellular structure might degenerate rapidly, leading to drastic changes on a micro level, such as the break of the cellular membrane. In turn, this has a strong impact on determining the macro dielectric properties of particular tissues under LF stimulation, whereas, in the case of HF the membrane usually remains impermeable to externally currents. Therefore, both composition and structure become critically important when we consider the LF regime.

The difference between in-vivo and ex-vivo values has motivated attempts to map non-invasively the dielectric properties of tissues in-vivo. Two principal approaches have been explored varying in the way that the external currents are introduced: (1) direct-current injections via surface electrodes and (2) inductively, through an electromagnetic coil. Methods relying on surface electrodes, such as traditional Electrical Impedance Tomography (EIT), suffer from low sensitivity at sites away from the electrodes [23]. Taking advantage of modern MR, the MR-EIT technique was introduced which can achieve better sensitivity in depth [24]. However,

the power and the duration required to obtain good SNR might exceed the maximal current limits dictated by noninvasive safety standards (SAR; ICNIRP2020 IEEE2005) (https://standards.ieee.org/standard/C95_1-2005.html) (<https://www.icnirp.org/en/activities/news/news-article/ef-guidelines-2020-published.html>). The effect of tissue heating is complex when we consider highly inhomogeneous brain areas, which are typical of the complex organization of the folded human cortex. Alternatively, utilizing the gradient coils of an MR machine, we can inductively induce currents. Unfortunately, this approach was found to have significant limitations in that while it is possible in theory to decouple the phase contribution arising from RF currents (MHz) with respect to the phase from LF currents (kHz), the latter phase component is below the noise level of typical MRI acquisitions [25]. In collaboration with another group, we investigated TMS as a possible method of current injection inside the MRI scanner, in order to estimate the electrical properties of tissue compartments in the heads of our participants. We relied on the same concurrent TMS/MRI setup presented in chapter 6. While this is a very promising novel technique, capable of stronger magnetic-field (0.4T) injections, the MR gradient coil capable of 10mT/m made it impossible to reconstruct tissue conductivity values near the TMS coil [26] due to the strong dephasing of the excited proton-spin magnetic resonance. This work was part of the thesis of a partner project in the same consortium, which, had it been successful, would have aided our modeling attempts tremendously by providing individual-tissue-conductivity values, which, however, no one has yet accomplished.

Having acknowledged the lack of reliable conductivity values and the impediments to obtaining in-vivo measurements, we should turn our attention to the degree to which FEM predictions are affected by assumed conductivity values. Outcomes from several studies looking at the possible impact on accuracy are encouraging. After careful analysis of the uncertainty and sensitivity of dielectric tissue properties in the case of TMS and tDCS, one group has made several intriguing claims [27]. First, in general, FEM modeling for TMS stimulation is less affected by assuming conductivity values that are off to some extent than for example tDCS. Second, only the magnitude of the induced E-field is affected rather than the current orientation and the general distribution of the induced E-field. This can be expected, as the direction and distribution of the induced E-field are driven mainly by tissue geometry and the 3D meshes constructed to describe it. Third, the two dominant tissue types driving the uncertainty for TMS were found to be GM (75%) and WM (23%). Fourth, higher uncertainties were reported in the sulcal walls (20–25%) compared to the gyral crown (5%).

Another computational study, involving a complex DWI-driven model of dielectric tissue properties, tested the tissue frequency response on human-head tissues and concluded that sensitivity to either conductivity or permittivity is smaller than that to frequency [28].

Despite all the aforementioned points regarding the uncertainty involved in determining accurate LF dielectric properties of living tissue, we are still confident in our underlying assumptions and trust the results from our models. To the best of our knowledge, the values that we used (see chapter 2) are commonly adopted in the community.

TMS Model Validation

Macroscopic Metrics of Activation

One of the main motivations for our investigation was the need for better interpretation and empirical validation of the numerically predicted TMS-induced E-fields from EM models. For this purpose, we needed to define the quantitative relationship between locally induced currents and neuronal activation in the cortical sheet, as empirical validation of such computed E-fields often involves measures of neuronal activations or consequences thereof (such as overt movement). In our attempt to derive macroscopic metrics of the net neuronal activation of a single pulse of TMS, we looked at the direction of the injected currents relative to the direction of the normal on the cortical sheet as a prime differentiating factor, which is inversely related to the tangential component of the E-field. In particular, we looked into the general angle formed in relation to the surface of the cortical GM sheet, and its tangential and radial components. Functional PET imaging in combination with TMS has revealed a site of activation deeper in the sulcus wall where the E-field is orthogonal to the cortical surface [29], justifying such distinctions.

Combined TMS with EMG

In chapter 4, we validated the complete model of the effects of a single pulse of TMS as described in chapter 2; this was achieved in an experiment on 9 volunteers, who underwent stimulations of several locations near the thumb motor hotspot while 4 channels of EMG from hand muscles were being recorded. We simulated the motor cortex and ensuing hand MEP responses for the same coil positions and orientations, using individually derived FEM models and cortical activation measures, and compared those with the observed empirical MEPs.

We observed high variability in the responses to single-pulse TMS, for example around 60% of TMS discharges resulted in no response at all. This hindered our attempt to establish a relationship between at least one of our TMS models and

observed responses to a larger extent than expected. One general limitation of EMG is that MEPs are an indirect measurement of cortical excitability that further involves interaction with the cortical-spinal tract and to some extent might depend on specific muscle physiology. The responses are also influenced by the neuronal activation state in other connected regions, habituation and arousal effects, and other uncontrolled variables. This finding complicates the analysis because it introduces several sources of variability that are not under experimental control. In our cross-mapping protocol, discharges sometimes resulted in a response and other times not, despite nearly identical stimulation intensities, site, and coil direction [30]. The high variability in MEP response is well known, and some recommendations for achieving robust response were already taken into consideration in our experimental design, but not sufficiently so.

The number of repetitions needed to obtain robust MEP readings as well as the inter-stimulus interval needed to minimize any repetition suppression due to habituation [31] had to be chosen carefully, and several conditions had to be taken into account. We managed to realize a minimum of 3s inter-stimulus interval and a pseudo-random order of site and coil direction. However, as it appeared after our experiments were conducted, our 5 repetitions per site and coil orientation fell short of the number of repetitions that are recommended for reliable MEP estimates: 25–30 [32] [33] and 30–40 [34]. The reason for keeping the number of repetitions low was in line with our motivation for keeping the session relatively short (<25min), which in retrospect was made achievable thanks to the advanced software that we used. Our goal was namely to prevent fatigue and lack of motivation and arousal, which would hamper reliable MEP recordings. Still, it constitutes a major limitation of the experiments thus conducted, partially due to concerns about the duration of the sessions (METC approval). For future work of this type, we intend to substantially increase the number of repetitions per site and coil orientation, preferably executed in pseudo-random order.

In conclusion, we observed that neuronal-activation metrics taking into account induced current magnitude in general outperformed simpler activation metrics, but we could not establish a clear advantage of a certain region of interest in MEP generation, nor of a specific activation metric in explaining observed MEP magnitudes. The findings described in the chapter, however, have demonstrated the potential benefits of the approach with an improved experimental design. On a related note, the combination of TMS E-field models with EMG has the potential to improve current MEP mapping techniques [35].

Combined TMS and fMRI

In chapter 3, the full model of single-pulse TMS effects from chapter 2 was validated by deploying TMS inside the bore of a 3T MRI scanner during the

acquisition of fMRI data in a special setup (see chapter 6) on 6 healthy volunteers. A biphasic stimulator was used.

This setup allowed the comparison of modeled activation patterns for 3 of the neuronal activation metrics outlined in chapter 2: the CE metric taking into account only the locally induced electric fields, the C3 metric favoring currents perpendicular to the sulcal wall, and the C2 metric with maximal local responses for E-fields parallel to the sulcal wall. Note that the inward and outward activation metrics could not be considered, as the bidirectional pulse shape affecting each induced current direction equally would have yielded the same predictions.

It was observed that the CE metric, taking into account the magnitude of the electric field in the local cortical tissue near the TMS stimulation area site, demonstrated the closest match with the measured BOLD fMRI. Taking into account the local orientation of E-fields did not improve the correspondence of the model with observed BOLD data.

Although there is only limited empirical data available on how and where a TMS pulse invokes currents in the cortical surface that is targeted, a few recent studies did compare their FEM modeling results to the published neuroimaging literature. Notably, Bungert et al. came to similar conclusions as we did [36]. Their model also showed the largest currents superficially rather than in the sulcus. They cited concurrent TMS-PET and TMS-fMRI literature that also exhibited superficial activation foci and considered this as evidence in support of their results.

This experiment encountered problems in that changing TMS machine output in between discharges caused artifacts for some participants, resulting in a smaller number of participants than originally planned. Nevertheless, it did show evidence supporting one of the metrics.

Image-guided TMS practices could benefit from these findings, as it seems advisable to take into account evoked E-fields and ensuing activation patterns to improve the dose control for TMS applications in clinical and investigatory use of TMS.

Summary of the validation results

Initially, we postulated the existence of a strong direction sensitivity in response to injected currents relative to the folding of the cortical sheet and we conducted a multi-modal approach toward testing the validity of such hypothesis. Unfortunately, our results were inconclusive in the support of a such hypothesis. While activation metrics such as C3, showcasing the advantage of currents orthogonal to the cortical sheet, proved better for one of the modeled motor cortex regions, they fell short for the other. It is worth mentioning that no inverse correlation was observed for any metric that might otherwise suggest some sort of pure inhibition effect, for

example in situations implying the advantage of the C3 hypothesis. In that case, we would expect any current tangential to the cortical sheet to be inhibitory in nature, under normal TMS conditions arising at the crown of the gyri. In fact, when validated with MEP, it was the magnitude of the E-field alone that provided an improved prediction as compared to the intensity agnostic C0 metric (see chapter 5). The activation metrics yielding more superficial activation were the ones with the best performance, as validated with a TMS-induced fMRI BOLD response (see chapter 5).

Such discrepancies among the best-performing activation models could be partially explained by the differences between BOLD and MEP measurements, from a physiological and mechanistic point of view. Additionally, the idealized design of the activation metrics could explain why no clear preference for one of them emerged. We took into account only two principal neuronal interactions within the cortical sheet (parallel and orthogonal) and two polarities (inward and outward). We ignored mixtures of such interactions and other known microscopic organizational principles in the cortical sheets [37], and we fully ignored local and distal interactions between patches of the cortical sheet. While we still stand by our initial premise of a strong direction-sensitive effect of TMS, the level at which we simplify the complexity of the underlying microstructure of the cortical sheet might just not be sufficient to explain the complex interactions between injected currents and the observed neuronal activation patterns.

Applications

In the following subsections, we highlight the most prominent way in which the models presented in this thesis can improve, influence, or otherwise help with the general understanding and application of TMS.

Improvements in the concurrent TMS/fMRI setup

Chapter 6 of this thesis was exclusively dedicated to the elaborate experimental setup required to achieve robust and safe results when combining concurrent MR with TMS. Some additional content is presented as an extension only to the material and methods section, while the rest remained identical to the original published work [38].

We successfully managed and controlled most of the previously reported complications that might arise in the attempt to combine TMS with MRI: temporal decoupling (100ms before EPI) synchronization [39], image artifacts [40], and general safety [41]. The low SNR, caused by the need to use soft RF receive coils instead of the traditional head cage, was the main problem that we faced in our study. A custom-tailored TMS coil with an integrated RF MR coil has recently shown the potential to

alleviate the issue [42]. The lack of compatible navigation was another hindrance, which made it hard to position the coil for a large part of our subject population. Neither an optic nor a magnetic tracking system could easily be applied. As part of our coil validation, we looked into quick planar EPI images in an attempt to assess the spread of the magnetic field and reconstruct the coil position, which has been suggested before [43]. The progress toward a more integrated system will certainly resolve the main impediment to the current setup, namely it still being too complex. Chapter 6 was exclusively focused on our experimental setup, covering some particularities and technical challenges in the effort to combine TMS with MRI.

The utility of TMS with fMRI is not limited to E-field modeling and is relevant as a tool for investigating any causality between remote regions in response to TMS by providing functional connectivity maps, which further advance our understanding of the human connectome. We already mentioned that it could be beneficial for TMS applications in general. Brain activity is organized in functional networks; in particular, dysfunctions in the SN, crucial for cognitive control and response inhibition, and the VMN, part of the classic reward circuit, are implicated in a wide range of psychiatric disorders [44]. In the case of depression, a connection has been established with dLPFC and ACC in healthy subjects [45].

Model-driven rodent coil design

Chapter 7 presented a novel coil design for the differential stimulation of a single hemisphere of a rodent. Rodent TMS is emerging as an important preclinical model to study the potential therapeutical benefits of TMS on brain recovery after stroke.

Building the physical coil prototype together with a project partner was preceded by a series of computer FEM simulations on an anatomically correct MR-derived model. The purpose of those virtual iterations was to optimize the size and dimension of the coil to achieve sufficient penetration with minimum amount of spread, which would lead to the most optimal configuration.

Furthermore, the insight that we gained from the work described in chapter 3 on the level of geometric detail required to model TMS coils for human-size cortex was crucial. The few studies that have explored the discrepancy between simplified and more realistic coil models have revealed that the level of detail is indeed relevant for human-brain stimulation, and is especially significant for rodents [46]. This is due to several factors that further complicate the modeling of coils used for rodents compared to coils used for humans – the ratio of the coil to head size (with increasing head volume, the TMS-induced E-field in the brain first gets stronger and then weaker following an exponential function) and the distance from scalp to the cortex [46], [47]. Both numerically deriving and experimentally measuring the field magnitude near the

coil have traditionally been challenging, as discussed in the more theoretical chapter 3. Therefore, there is an inherent level of additional uncertainty and large space for error when evaluating a magnetic field numerically close to the source and especially when targets are of similar size.

The main technical challenge encountered while working with initial prototypes of the rodent coil was the extreme heat accumulation under rTMS protocols (see chapter 7). The minute size of the coil in combination with the thicker wires (and thus higher impedance) required higher MO (80%) while providing less opportunity for cooling. It is also expected that inter-wire forcing after each discharge will contribute negatively to the lifespan (counted in a number of discharges) under higher operational temperatures. Therefore, we can positively recommend for future coil models that they incorporate thermal and mechanical calculations, similar to [48]. Overheating issues under rTMS protocols were the main engineering problem to overcome in the initial prototypes of the coil.

Preventing side effects

Although TMS is noninvasive and considered safe, without long-term side effects, this is not to say that it comes without some downsides. One commonly reported side effect is a transient headache shortly after a session [49]. It is expected that the scalp muscles just under the coil surface will experience the strongest current, due to their proximity to the coil wrings and the relatively high conductivity of the scalp. This serves as a motivation to keep sessions short, especially during rTMS. Single-pulse discharges might be problematic too. In particular when targeting a more anterior cortex area near the facial muscles, as is the case with DLPFC and TPJ, sessions are prone to causing exceptionally high levels of pain and even jaw contractions. We had to cancel one of our experiments involving concurrent TMS with fMRI on DLPFC exactly because of such complaints after just a handful of discharges. In that case, the precision of the coil placement was limited, and subjects had to assume an awkward pose in the scanner (with their head tilted).

The modeling presented so far in this thesis has the potential to aid in addressing such scalp-related unintended, and highly undesired, direct muscle stimulations. It constitutes an alternative use of the methods we employ in this thesis, outside the context of correct dosimetry. Computer TMS models can be utilized in at least two ways. It is possible to come up with an innovative coil that minimizes the effect of prolonged (rTMS) sessions in the context of headaches [50]. It is equally possible to come up with some type of heuristic metric of certain scalp positions for optimal orientation, to spare certain facial muscle groups.

Future Directions

In the following two subsections, we not only propose one promising way forward for computational TMS models but also suggest an additional modality to help us validate them.

Combined TMS and EEG

One alternative imaging modality in particular deserves more attention, namely, EEG. It is by far the second most adopted method, just after EMG, when studying the effects of spTMS and rTMS. One major advantage of EEG in comparison to both EMG and fMRI is the ability to measure directly the neuronal firing without the need of a proxy, thus avoiding the need for any further biological interpretation, such as the nontrivial cortico-spinal tract interaction and the slow metabolic neuronal reaction to oxygen depletion BOLD. Much like fMRI, it allows for global brain imaging and has been demonstrated in combination with TMS, simultaneous reading (online effect) [51]. However, the spatial resolution of modern MR systems is increasing, while there persists some physical limitations to what is spatially possible with EEG (~5mm). Even high-density EEG caps are not potent enough to capture in sufficient detail the effects exerted by TMS in an area of roughly 2x4 cm. The method is known to suffer from several shortcomings concerning source localization: known as the mathematically ill-posed inverse type of problem [52], the effects of skull anisotropy near electrodes might ultimately compromise accuracy [53] [54]. Finally, some impediments specific to the combination of EEG with TMS might need to be addressed too – e.g., TMS artifacts filtering due to TMS pulse discharge [55] and auditory-sensory TEPs [56].

All these limitations diminish the attractiveness of the combined EEG approach for E-field model validation and spTMS. Nevertheless, the superior resolution of EEG in combination with TMS makes it an exceptionally suitable tool to probe the timing of signal propagation and the complex interactions of inhibitory versus excitatory global networks. In that respect, the combination of TMS with EEG remains an ideal tool to probe active functional connectivity [57]. Furthermore, the TEPs' responses have shown good reliability across sessions, making them a stable bio-marker of neuronal excitability [58].

One relatively recent trend in combining EEG and TMS is potentially even more relevant for dosimetry alone. The close-loop EEG-guided TMS application based on brain state is gaining traction among researchers. The idea is that TMS can be applied in phase synchrony with the natural rhythms of the brain [59]. Large-scale neuronal populations – which are known to fire in synchrony and form typical natural rhythms oscillating in distinct frequency bands, alpha (8–12Hz), beta (13–20), and

beta/gamma(21–50Hz) – have been reported in response to TMS [60]. The idea that phase-dependent stimuli will have a discernible modulation effects on responses coincides with what we intuitively connect with the pendulum effect: the notion that, when influencing a dynamic system, the moment of the application of force might be more important than just the amount. An emerging technique, TMS combined with neuro-feedback EEG, has introduced the concept of ‘neuronal entrainment’ by demonstrating TMS frequency-dependent oscillation modulation or otherwise making it possible to modify the timing of the spikes of neurons on a group level [61], also shown with alternating-current stimulation [62].

Multi-scale neuronal population models

Following the inconclusive results from our optimistic attempt to simplify the effect of neuronal activation on the macro level using crude metrics, we are inclined to suggest a more comprehensive approach toward modeling the response to exogenous electric fields. Such an approach will inevitably involve biologically plausible modeling of the human cortical structure, drawing from our current knowledge of neurology and neural physiology.

Akin to methods already applied for functional image reconstruction (fMRI, EEG, MEG), using a physiologically plausible mechanism of action makes it possible to adapt those advanced imaging techniques to explain the neuronal response to electrical as well as sensory stimulation (see dynamic causal modeling [63]). With DCM, scientists are trying to fit a model to the data to better explain an observation. Similarly, we can try to identify a simple yet effective model of response to electric stimulation on the level of micro cortical circuits.

Employing DCM in physiological studies involves plausible neural mass and neural field models. Often referred to as regions, each including several neuronal sub-populations, representing key constituents of the cortex. However, the complexity of interactions and the amount of detail might vary significantly between studies. Most populate each region with some excitatory pyramidal (output) neurons, inhibitory interneurons, and excitatory spiny (input) neurons. Often intrinsic (within a single source) connections are estimated per region, while extrinsic connections (between sources) are subdivided into forward, backward, and lateral. Forward connections arrive at the input population, backward connections arrive at both the output and the interneuron populations, and lateral connections arrive at all three populations. All extrinsic afferents are projecting from the output pyramidal population [64] [65] [66] [67]. If we were to adapt this approach to our needs of TMS model validation, we should inverse input and output, having inputs to pyramidal cells and output from spiny cells. It is also important to realize that these different regions are treated as distinct processing units, following the principle of ‘functional segregation’, enhanced with the

idea of ‘functional integration’, according to which those regions need to communicate with each other to ultimately cause a complex behavior.

It follows from our brief outline of DCM that a high level of approximation of relatively large-scale neuronal populations, as well as knowledge from the sphere of modern neurology, determines which behavior we shape exactly. However, we can also start from a single neuron and hope to invoke equally plausible behavior on a population level. In principle, this would be a more straightforward building block, although, depending on the sought level of detail, it could be even more challenging to model a single neuron.

Single neuron models based on Hodgkin–Huxley model are nothing new, the most common computational models being those of single-compartment neurons in the form of a cylinder with fixed diameter and length and slight variations of the membrane-potential equation to derive a final transverse polarization, in other words, cable equations [68]. The parameters of the equation depend mainly on the type of cell, morphology, and ratio of the different ion-gated channels [69]. Some studies have gone as far as modeling the Tuft dendrites of L5 pyramidal cells and their mechanism of interaction (local feedback circuits to L5) [70][71]. The effect of myelination has been explored computationally too, revealing unmyelinated axon thresholds above the capabilities of conventional TMS [72]. More elaborate multi-compartmental neuronal computational models exist, in which several different cell types are included, with realistic morphology and complex axon arbors [73].

To gain even greater physiological insight into the underlying molecular and cellular mechanism of action, the so-called multilevel models have been recently introduced. One study in particular focused on the synaptic plasticity of hyperpolarization-gated neurons in the MVN [74]. It involved an elaborate multiscale model incorporating both electrophysiological and biochemical signaling at the vestibular nerve synapses on proximal dendrites of the neuron. In another study, a comprehensive set of L1 of L5 type neurons of rats and humans, spanning almost a complete cortical column, were incorporated in a local uniform DC and DC-pulsed E-field 3D virtual simulator [73]. Multi-scale models involving realistic 3D FEM with motor cortex patches with the dense neuronal cortical columns of L2/L3 and L5 pyramidal neurons are arguably the most relevant for the work presented here [75]. Even more reminiscent of the FEM models demonstrated here is a multiscale subject-specific model, albeit limited to pyramidal neurons (the NEURON project) [76]. We expect the natural progression of 3D FEM work to include such a multiscale approach. In one recent publication, we already found a clear example of such a model on similar ROIs on M1 with a complete representation of L1–L6 cortical columns [77]. The same research group reported their preference for the E-field magnitude instead of the (C3-metric) component orthogonal to the cortical surface of the E-field.

Those studies come to a similar conclusion: the mode of neuronal depolarization dependent on various morphological features of the axonal arbor, including myelination, diameter, and branching, is very preferential. Overall, the outcomes were reported to be similar to those of other experimental physiological studies, such as the whole cell patch-clamp recording under uniform E-field in-vivo and in-vitro in rodents [78]. Even more remarkably, thanks to further experiments with multi-scale models with the more realistic M1 patch, some of the authors have claimed proposed a novel hypothesis to explain the latency between I-waves and D-waves, entirely based on a synthetic computational model [79][80].

Final Remarks

The theoretical approach presented in this thesis, and the empirical and practical work presented to validate the approach and demonstrate its usefulness for research and clinical applications, demonstrate that computational approaches to predict the effect of non-invasive brain stimulation are worthwhile, can be validated, and have great potential. Several limitations were observed, that might be resolved soon. Our approach could guide such studies, and present a unified framework for the formulation, empirical validation, and application of computational neurostimulation methods.

References

- [1] K. H. Madsen, L. Ewald, H. R. Siebner, and A. Thielscher, “Transcranial Magnetic Stimulation: An Automated Procedure to Obtain Coil-specific Models for Field Calculations,” *Brain Stimul.*, vol. 8, no. 6, pp. 1205–1208, 2015.
- [2] L. Gomez, S. Goetz, and A. V. Peterchev, “Design of Transcranial Magnetic Stimulation Coils with between Depth, Focality, and Energy,” *J. Neural Eng.*, vol. 15, no. 4, pp. 1–31, 2018.
- [3] C. C. Sánchez, J. M. G. Rodriguez, Á. Q. Olozábal, and D. Blanco-Navarro, “Novel TMS coils designed using an inverse boundary element method,” *Phys. Med. Biol.*, vol. 62, no. 1, pp. 73–90, 2017.
- [4] S. Mandija, P. I. Petrov, S. F. W. Neggers, P. R. Luijten, and C. A. T. van den Berg, “MR-based measurements and simulations of the magnetic field created by a realistic transcranial magnetic stimulation (TMS) coil and stimulator,” *NMR Biomed.*, no. August, pp. 1–11, 2016.
- [5] M. Windhoff, A. Opitz, and A. Thielscher, “Electric field calculations in brain stimulation based on finite elements: an optimized processing pipeline for the generation and usage of accurate individual head models.,” *Hum. Brain Mapp.*, vol. 34, no. 4, pp. 923–35, Apr. 2013.
- [6] M. Iwahashi, J. Gomez-Tames, I. Laakso, and A. Hirata, “Evaluation method for in situ electric field in standardized human brain for different transcranial magnetic stimulation coils,” *Phys. Med. Biol.*, vol. 62, no. 6, pp. 2224–2238, 2017.
- [7] J. Tohka, A. Zijdenbos, and A. Evans, “Fast and robust parameter estimation for statistical partial volume models in brain MRI.,” *Neuroimage*, vol. 23, no. 1, pp. 84–97, Sep. 2004.
- [8] J. V Manjón, J. Tohka, and M. Robles, “Improved estimates of partial volume coefficients from noisy brain MRI using spatial context.,” *Neuroimage*, vol. 53, no. 2, pp. 480–90, Nov. 2010.
- [9] S. M. Smith, “Fast robust automated brain extraction.,” *Hum. Brain Mapp.*, vol. 17, no. 3, pp. 143–55, Nov. 2002.
- [10] A. Thielscher, A. Antunes, and G. B. Saturnino, “Field modeling for transcranial magnetic stimulation: A useful tool to understand the physiological effects of TMS?,” *Proc. Annu. Int. Conf. IEEE Eng. Med. Biol. Soc. EMBS*, vol. 2015-Novem, pp. 222–225, 2015.

- [11] M. De Lucia, G. J. M. Parker, K. Embleton, J. M. Newton, and V. Walsh, "Diffusion tensor MRI-based estimation of the influence of brain tissue anisotropy on the effects of transcranial magnetic stimulation.," *Neuroimage*, vol. 36, no. 4, pp. 1159–70, Jul. 2007.
- [12] A. Opitz, M. D. Fox, R. C. Craddock, S. Colcombe, and M. P. Milham, "An integrated framework for targeting functional networks via transcranial magnetic stimulation.," *Neuroimage*, vol. 190, pp. 443–9, 2015.
- [13] S. Bestmann, C. C. Ruff, F. Blankenburg, N. Weiskopf, J. Driver, and J. C. Rothwell, "Mapping causal interregional influences with concurrent TMS–fMRI," *Exp. Brain Res.*, vol. 191, no. 4, pp. 383–402, 2008.
- [14] C. C. Ruff *et al.*, "Distinct Causal Influences of Parietal Versus Frontal Areas on Human Visual Cortex: Evidence from Concurrent TMS–fMRI," *Cereb. Cortex*, vol. 18, no. 4, pp. 817–827, Apr. 2008.
- [15] S. Bestmann and E. Feredoes, "Combined neurostimulation and neuroimaging in cognitive neuroscience: Past, present, and future," *Ann. N. Y. Acad. Sci.*, vol. 1296, no. 1, pp. 11–30, 2013.
- [16] S. H. Siddiqi, S. F. Taylor, D. Cooke, A. Pascual-Leone, M. S. George, and M. D. Fox, "Distinct symptom-specific treatment targets for circuit-based neuromodulation," *Am. J. Psychiatry*, vol. 177, no. 5, pp. 435–446, 2020.
- [17] C. Gabriel, C. Gabriel, S. Gabriel, S. Gabriel, E. Corthout, and E. Corthout, "The dielectric properties of biological tissues: I. Literature survey.," *Phys. Med. Biol.*, vol. 41, no. 11, pp. 2231–49, 1996.
- [18] A. Opitz, A. Falchier, G. S. Linn, M. P. Milham, and C. E. Schroeder, "Limitations of ex vivo measurements for in vivo neuroscience," *Proc. Natl. Acad. Sci.*, vol. 114, no. 20, pp. 5243–5246, 2017.
- [19] J. A. Latikka, J. A. Hyttinen, T. A. Kuurne, H. J. Eskola, and J. A. Malmivuo, "The conductivity of brain tissues: Comparison of results in vivo and in vitro measurements," *Annu. Reports Res. React. Institute, Kyoto Univ.*, vol. 1, pp. 910–912, 2001.
- [20] S. B. Baumann, D. R. Wozny, S. K. Kelly, and F. M. Meno, "The electrical conductivity of human cerebrospinal fluid at body temperature," *IEEE Trans. Biomed. Eng.*, vol. 44, no. 3, pp. 220–225, 1997.
- [21] C. Gabriel, "Dielectric properties of biological tissue: Variation with age," *Bioelectromagnetics*, vol. 26, no. SUPPL. 7, pp. 12–18, 2005.
- [22] D. Antonenko, U. Grittner, G. Saturnino, T. Nierhaus, A. Thielscher, and A. Flöel, "Inter-individual and age-dependent variability in simulated electric fields

- induced by conventional transcranial electrical stimulation,” *Neuroimage*, vol. 224, no. September 2020, p. 117413, 2020.
- [23] L. Koessler *et al.*, “In-vivo measurements of human brain tissue conductivity using focal electrical current injection through intracerebral multicontact electrodes,” *Hum. Brain Mapp.*, vol. 38, no. 2, pp. 974–986, 2017.
- [24] M. Chauhan, R. Vidya Shankar, N. Ashok Kumar, V. D. Kodibagkar, and R. Sadleir, “Multishot echo-planar MREIT for fast imaging of conductivity, current density, and electric field distributions,” *Magnetic Resonance in Medicine*, vol. 82, pp. 71–82, 2017.
- [25] S. Mandija *et al.*, “A geometrical shift results in erroneous appearance of low frequency tissue eddy current induced phase maps,” *Magn. Reson. Med.*, vol. 00, pp. 1–8, 2015.
- [26] S. Mandija, P. I. Petrov, S. F. W. Neggers, and P. R. Luijten, “Noninvasive Electric Current Induction for Low-Frequency Tissue Conductivity Reconstruction: Is It Feasible With a TMS-MRI Setup?,” *Tomography*, vol. 2, no. 3, pp. 203–214, 2016.
- [27] G. B. Saturnino, A. Thielscher, K. H. Madsen, T. R. Knösche, and K. Weise, “A principled approach to conductivity uncertainty analysis in electric field calculations,” *Neuroimage*, vol. 188, no. December 2018, pp. 821–834, 2019.
- [28] N. De Geeter, G. Crevecoeur, L. Dupré, W. Van Hecke, and a Leemans, “A DTI-based model for TMS using the independent impedance method with frequency-dependent tissue parameters,” *Phys. Med. Biol.*, vol. 57, no. 8, pp. 2169–88, Apr. 2012.
- [29] P. T. Fox *et al.*, “Column-Based Model of Electric Field Excitation of Cerebral Cortex,” *Hum. Brain Mapp.*, vol. 22, no. 1, pp. 1–14, 2004.
- [30] L. D. Gugino *et al.*, “Effect on Evoked Compound Muscle Action Potentials,” *Clin. Neurophysiol.*, vol. 112, no. 10, pp. 1781–1792, 2001.
- [31] O. Löfberg, P. Julkunen, P. Tiihonen, A. Pääkkönen, and J. Karhu, “Repetition suppression in the cortical motor and auditory systems resemble each other - A combined TMS and evoked potential study,” *Neuroscience*, vol. 243, pp. 40–45, 2013.
- [32] M. R. Goldsworthy, B. Hordacre, and M. C. Ridding, “Minimum number of trials required for within- and between-session reliability of TMS measures of corticospinal excitability,” *Neuroscience*, vol. 320, pp. 205–209, 2016.
- [33] K. Cuypers, H. Thijs, and R. L. J. Meesen, “Optimization of the transcranial magnetic stimulation protocol by defining a reliable estimate for corticospinal excitability,” *PLoS One*, vol. 9, no. 1, 2014.

- [34] M. Biabani, M. Farrell, M. Zoghi, G. Egan, and S. Jaberzadeh, "The minimal number of TMS trials required for the reliable assessment of corticospinal excitability, short interval intracortical inhibition, and intracortical facilitation," *Neurosci. Lett.*, vol. 674, no. February, pp. 94–100, 2018.
- [35] M. Pitkänen, E. Kallioniemi, P. Julkunen, M. Nazarova, J. O. Nieminen, and R. J. Ilmoniemi, "Minimum-Norm Estimation of Motor Representations in Navigated TMS Mappings," *Brain Topogr.*, vol. 30, no. 6, p. 723, 2017.
- [36] A. Bungert, A. Antunes, S. Espenhahn, and A. Thielscher, "Where does TMS Stimulate the Motor Cortex? Combining Electrophysiological Measurements and Realistic Field Estimates to Reveal the Affected Cortex Position," *Cereb. Cortex*, no. September, pp. 1–12, 2016.
- [37] S. F. W. Neggers, P. I. Petrov, S. Mandija, I. E. C. Sommer, and C. a. T. van den Berg, "Understanding the biophysical effects of transcranial magnetic stimulation on brain tissue: The bridge between brain stimulation and cognition," *Prog. Brain Res.*, no. Comput. Neurostimulation, pp. 1–31, 2015.
- [38] J. J. T. Vink, S. Mandija, P. I. Petrov, C. A. T. van den Berg, I. E. C. Sommer, and S. F. W. Neggers, "A novel concurrent TMS-fMRI method to reveal propagation patterns of prefrontal magnetic brain stimulation," *Hum. Brain Mapp.*, vol. 39, no. 11, pp. 4580–4592, 2018.
- [39] S. Bestmann, J. Baudewig, and J. Frahm, "On the synchronization of transcranial magnetic stimulation and functional echo-planar imaging," *J. Magn. Reson. Imaging*, vol. 17, pp. 309–316, 2003.
- [40] N. Weiskopf *et al.*, "Image artifacts in concurrent transcranial magnetic stimulation (TMS) and fMRI caused by leakage currents: modeling and compensation.," *J. Magn. Reson. Imaging*, vol. 29, no. 5, pp. 1211–7, May 2009.
- [41] L. J. Crowther, K. Porzig, R. L. Hadimani, H. Brauer, and D. C. Jiles, "Realistically modeled transcranial magnetic stimulation coils for Lorentz force and stress calculations during MRI," *IEEE Trans. Magn.*, vol. 49, no. 7, pp. 3426–3429, 2013.
- [42] L. I. Navarro De Lara *et al.*, "A novel coil array for combined TMS/fMRI experiments at 3 T," *Magn. Reson. Med.*, vol. 74, no. 5, pp. 1492–1501, 2015.
- [43] M. Moisa, R. Pohmann, L. Ewald, and A. Thielscher, "New coil positioning method for interleaved transcranial magnetic stimulation (TMS)/functional MRI (fMRI) and its validation in a motor cortex study," *J. Magn. Reson. Imaging*, vol. 29, no. 1, pp. 189–197, 2009.

- [44] K. Dunlop, C. A. Hanlon, and J. Downar, “Noninvasive brain stimulation treatments for addiction and major depression,” *Ann. N. Y. Acad. Sci.*, vol. 1394, no. 1, pp. 31–54, 2017.
- [45] M. Tik *et al.*, “Towards understanding rTMS mechanism of action: Stimulation of the DLPFC causes network-specific increase in functional connectivity,” *Neuroimage*, vol. 162, no. May, pp. 289–296, 2017.
- [46] F. S. Salinas, J. L. Lancaster, and P. T. Fox, “Detailed 3D models of the induced electric field of transcranial magnetic stimulation coils.,” *Phys. Med. Biol.*, vol. 52, no. 10, pp. 2879–2892, May 2007.
- [47] R. Salvador and P. C. Miranda, “Transcranial magnetic stimulation of small animals: a modeling study of the influence of coil geometry, size and orientation.,” *Conf. Proc. IEEE Eng. Med. Biol. Soc.*, vol. 2009, pp. 674–7, Jan. 2009.
- [48] S. D. March *et al.*, “Thermal and mechanical analysis of novel transcranial magnetic stimulation coil for mice,” *IEEE Trans. Magn.*, vol. 50, no. 9, 2014.
- [49] O. Durmaz, M. A. Ateş, and M. G. Şenol, “Repetitive transcranial magnetic stimulation (rTMS)-induced trigeminal autonomic cephalalgia,” *Noropsikiyatri Ars.*, vol. 52, no. 3, pp. 309–311, 2015.
- [50] S. F. Cogan, K. A. Ludwig, C. G. Welle, and P. Takmakov, “Tissue damage thresholds during therapeutic electrical stimulation,” *J. Neural Eng.*, vol. 13, no. 2, p. 021001, 2016.
- [51] R. J. Ilmoniemi and D. Kičić, “Methodology for combined TMS and EEG,” *Brain Topogr.*, vol. 22, no. 4, pp. 233–248, 2010.
- [52] R. Grech *et al.*, “Review on solving the inverse problem in EEG source analysis,” *J. Neuroeng. Rehabil.*, vol. 5, pp. 1–33, 2008.
- [53] M. Fernandez-Corazza, S. Turovets, P. Luu, N. Price, C. H. Muravchik, and D. Tucker, “Skull modeling effects in conductivity estimates using parametric electrical impedance tomography,” *IEEE Trans. Biomed. Eng.*, vol. 65, no. 8, pp. 1785–1797, 2018.
- [54] V. Montes-restrepo, H. Hallez, P. Van Mierlo, and S. Staelens, “Influence of skull modeling on EEG source localization : Inhomogeneities , geometry and noise sensitivity,” *Brain Topogr.*, vol. 1, no. 27, pp. 95–111, 2016.
- [55] R. J. Ilmoniemi *et al.*, “Dealing with artifacts in TMS-evoked EEG,” *Proc. Annu. Int. Conf. IEEE Eng. Med. Biol. Soc. EMBS*, vol. 2015-Novem, no. August 2016, pp. 230–233, 2015.
- [56] V. Conde *et al.*, “The non-transcranial TMS-evoked potential is an inherent source of ambiguity in TMS-EEG studies,” *Neuroimage*, vol. 185, pp. 300–312, 2019.

- [57] M. Bortoletto, D. Veniero, G. Thut, and C. Miniussi, “The contribution of TMS-EEG coregistration in the exploration of the human cortical connectome,” *Neuroscience and Biobehavioral Reviews*, vol. 49. Elsevier Ltd, pp. 114–124, 2015.
- [58] M. Hallett *et al.*, “Contribution of transcranial magnetic stimulation to assessment of brain connectivity and networks,” *Clin. Neurophysiol.*, vol. 128, no. 11, pp. 2125–2139, 2017.
- [59] C. S. Herrmann, D. Strüber, R. F. Helfrich, and A. K. Engel, “EEG oscillations: From correlation to causality,” *Int. J. Psychophysiol.*, vol. 103, pp. 12–21, 2016.
- [60] M. Rosanova, A. Casali, V. Bellina, F. Resta, M. Mariotti, and M. Massimini, “Natural frequencies of human corticothalamic circuits,” *J. Neurosci.*, vol. 29, no. 24, pp. 7679–7685, 2009.
- [61] C. J. Wilson, M. H. Higgs, D. V. Simmons, and J. C. Morales, “Oscillations and Spike Entrainment,” *F1000Research*, vol. 7, no. 0, p. 1960, Dec. 2018.
- [62] R. F. Helfrich, T. R. Schneider, S. Rach, S. A. Trautmann-Lengsfeld, A. K. Engel, and C. S. Herrmann, “Entrainment of brain oscillations by transcranial alternating current stimulation,” *Curr. Biol.*, vol. 24, no. 3, pp. 333–339, 2014.
- [63] J. Kahan and T. Foltynie, “Understanding DCM: ten simple rules for the clinician,” *Neuroimage*, vol. 83, pp. 542–9, Dec. 2013.
- [64] R. J. Moran, K. E. Stephan, T. Seidenbecher, H. C. Pape, R. J. Dolan, and K. J. Friston, “Dynamic causal models of steady-state responses,” *Neuroimage*, vol. 44, no. 3, pp. 796–811, 2009.
- [65] R. J. Moran, M. Symmonds, K. E. Stephan, K. J. Friston, and R. J. Dolan, “An in vivo assay of synaptic function mediating human cognition,” *Curr. Biol.*, vol. 21, no. 15, pp. 1320–1325, 2011.
- [66] A. M. Bastos, W. M. Usrey, R. A. Adams, G. R. Mangun, P. Fries, and K. J. Friston, “Canonical Microcircuits for Predictive Coding,” *Neuron*, vol. 76, no. 4, pp. 695–711, 2012.
- [67] S. J. Kiebel, M. I. Garrido, and K. J. Friston, “Dynamic causal modelling of evoked responses: The role of intrinsic connections,” *Neuroimage*, vol. 36, no. 2, pp. 332–345, 2007.
- [68] B. Wang, A. S. Aberra, W. M. Grill, and A. V. Peterchev, “Modified cable equation incorporating transverse polarization of neuronal membranes for accurate coupling of electric fields,” vol. 15, no. 2, pp. 1–42, 2019.

- [69] M. Pospischil *et al.*, “Minimal Hodgkin-Huxley type models for different classes of cortical and thalamic neurons,” *Biol. Cybern.*, vol. 99, no. 4–5, pp. 427–441, 2008.
- [70] M. E. Larkum, T. Nevian, M. Sandier, A. Polsky, and J. Schiller, “Synaptic integration in tuft dendrites of layer 5 pyramidal neurons: A new unifying principle,” *Science (80-.)*, vol. 325, no. 5941, pp. 756–760, 2009.
- [71] F. Aspart, M. W. H. Remme, and K. Obermayer, *Differential polarization of cortical pyramidal neuron dendrites through weak extracellular fields*, vol. 14, no. 5. 2018.
- [72] B. Wang, W. M. Grill, and A. V. Peterchev, “Coupling Magnetically Induced Electric Fields to Neurons: Longitudinal and Transverse Activation,” *Biophys. J.*, vol. 115, no. 1, pp. 95–107, 2018.
- [73] A. S. Aberra, A. V. Peterchev, and W. M. Grill, “Biophysically realistic neuron models for simulation of cortical stimulation,” *J. Neural Eng.*, vol. 15, no. 6, p. 066023, 2018.
- [74] Y. Xie, M. Kazmierczyk, B. P. Graham, M. B. Dutia, and M. I. Stefan, “A multi-scale model reveals cellular and physiological mechanisms underlying hyperpolarisation-gated synaptic plasticity,” *Submitt. Prepr. bioRxiv*, p. 418228, 2018.
- [75] H. Seo, N. Schaworonkow, S. C. Jun, and J. Triesch, “A multi-scale computational model of the effects of TMS on motor cortex,” *F1000Research*, vol. 5, no. May, p. 1945, 2016.
- [76] B. D. Goodwin and C. R. Butson, “Subject-Specific Multiscale Modeling to Investigate Effects of Transcranial Magnetic Stimulation,” *Neuromodulation*, vol. 18, no. 8, pp. 694–703, 2015.
- [77] A. S. Aberra, B. Wang, W. M. Grill, and A. V. Peterchev, “Simulation of transcranial magnetic stimulation in head model with morphologically-realistic cortical neurons,” *Brain Stimul.*, vol. 13, no. 1, pp. 175–189, 2019.
- [78] T. Radman, R. Ramos, J. Brumberg, and M. Bikson, “Role of Cortical Cell Type and Morphology in Sub- and Suprathreshold Uniform Electric Field Stimulation,” *Brain Stimul.*, vol. 2, no. 4, pp. 215–228, 2009.
- [79] C. V. Rusu, M. Murakami, U. Ziemann, and J. Triesch, “A model of TMS-induced I-waves in motor cortex,” *Brain Stimul.*, vol. 7, no. 3, pp. 401–414, 2014.
- [80] J. Triesch, “Modeling TMS-induced I-waves in human motor cortex,” *Comput. Neurostimulation*, vol. 34, pp. 289–312, 2015.

Chapter IX

Nederlandse Samenvatting

Directe elektrische stimulatie van neuronen met behulp van micro-elektroden heeft een lange geschiedenis in de neurowetenschappen (sinds circa 1070). De gerelateerde indirecte stimulatie via het inductieprincipe van Faraday heeft een veel recentere oorsprong. In 1985 demonstreerde Anthony T. Barker voor het eerst een modern apparaat dat werkt via een platte cirkelvormige spoel die het menselijke perifere en centrale zenuwstelsel kan stimuleren vanaf de buitenkant van het hoofd. Tegenwoordig kennen we deze uitvinding onder de naam “TMS” (Transcranial Magnetic Stimulation), waarbij transcranieel staat voor “door de schedel”. De naam impliceert het belangrijkste werkingsprincipe. Door middel van relatief sterke maar kortdurende magnetische pulsen kan het apparaat door de schedel heen met weinig tot geen verzwakking een stroom opwekken in het brein. Vervolgens zullen zich in de hersenoppervlakte (cortex) kortstondig geïnduceerde secundaire elektrische stromen vormen en zowel prikkelende als remmende effecten veroorzaken in een relatief lokaal gebied met een doorsnede van 2 x 4 cm, tot 2,5 cm onder het oppervlak van de spoel. Het meest aansprekende is dat de methode niet-invasief is, relatief pijnloos met af en toe hoofdpijn als de meest voorkomende bijwerking, gecombineerd met zeer zeldzame incidenten van geïnduceerde epileptische aanvallen. De toediening van TMS, meestal in de variant genaamd repetitieve TMS (rTMS) waarbij meerdere pulsen snel achter elkaar worden toegediend, wordt in het algemeen goed verdragen terwijl het een diverse klinische werkzaamheid vertoont bij een indrukwekkend scala aan neurologische en psychiatrische aandoeningen.

De praktische toepassing van TMS is nog steeds grof en vaak onnauwkeurig, zonder rekening te houden met individuele morfologische verschillen in menselijke neocortex, die wordt gekenmerkt door een zeer unieke vouwing van de GM (grijze stof). Moderne medische beeldvorming met hoge ruimtelijke resolutie (zoals MRI)

heeft ons in staat gesteld om de toepassing van TMS te bevorderen met de introductie van zogenaamde 'neuro-navigatie' waarbij de TMS-spoel wordt gevolgd en geleid naar specifieke neuroanatomisch doelen met millimeterprecisie. Het is echter nog steeds een open vraag hoe de intensiteit en, nog belangrijker, de richting van de door stimulatie opgewekte stroom kan worden gecontroleerd om de werkzaamheid van TMS te optimaliseren per individu. Sommige onderzoeken hebben gebruik gemaakt van anatomisch nauwkeurige computermodellen om fysiek realistische elektromagnetische velden te simuleren in een poging om de neurofysiologische respons in het brein van een persoon te voorspellen, en op die manier te optimaliseren voor het beoogde klinische doel.

Mijn proefschrift focust op verbeterde computermodellen om door TMS geïnduceerde hersenstromen te voorspellen, en vooral om deze empirisch te valideren, wat vaak is nagelaten in publicaties in dit nog jonge veld. In die geest heb ik in dit proefschrift veldmodellen gemaakt van de geïnduceerde elektrische velden in het hoofd, volgend op TMS-ontlading. Hiertoe heb ik op specifieke 3Dhoofdmodellen gemaakt die afgeleid zijn van individuele MRI scans van personen, en gebruikt in zogenaamde "Eindige elementen (Finite Element) Modellen", gecombineerd met realistische en gevalideerde spoelgeometrieën en stimulatorparameters. Het meer technische aspect van de opbouw van de modellen met uitgebreide theoretische achtergrond is te vinden in hoofdstuk 2.

De focus van ons onderzoek lag niet op het modelleren, maar veeleer op de empirische validatie van die modellen. We hebben eerst de vereiste geometrische details onderzocht die nodig zijn om een van de meest gebruikte spoelen (in de vorm van een 8) te modelleren, zie hoofdstuk 3. In dit geval hebben we intern homogeen geleidende fantoom modellen ontwikkeld voor gebruik in een MRI scanner, die we

gebruikten om de nauwkeurigheid van het primaire magnetische veld in onze modellen te valideren. Onze model voorspellingen hebben we vergeleken met gemeten MR-faseaccumulatiebeelden (EPI).

Vervolgens hebben we een multimodale benadering ontwikkeld om het meer complete spoel- en hoofdmodel van de geïnduceerde elektrische velden op gezonde proefpersonen te testen. Daarvoor rekruteerden we een tiental vrijwilligers voor een eerste screening en twee vervolgssessies. Tijdens de intake sessie kregen we een snel (<15min) anatomisch T1 gewogen MR-beeld, gebruikt voor het bouwen van 3D FEM-modellen. De experimentele sessie met EMG omvatte een zorgvuldige selectie van verschillende spoelrichtingen gesitueerd rond het duimgebied in de motor cortex (met BOLD fMRI gelokaliseerd) van de proefpersoon. De TMS-geïnduceerde spierpotentialen (MEP's) werden vervolgens vergeleken met de genoemde stromen die gegenereerd werden door ons computermodel in de motorcortexmodelstromen zoals beschreven in hoofdstuk 2. In tegenstelling tot eerder voorgestelde preferentiële activering met stromen loodrecht op de oppervlakte van de cortex, vonden we geen sterkere correlatie tussen model en observatie dan dan een model wat simpelweg de sterkte van het elektrische veld berekende. De orientatie van de locale corticale morfologie leek geen rol te spelen. Zie hoofdstuk 4 voor details.

We kunnen vergelijkbare conclusies trekken uit onze gelijktijdige TMS met fMRI-experimenten zoals beschreven in hoofdstuk 5, waar we TMS hebben toegediend in een MRI scanner in een speciaal door ons ontworpen opstelling, waarbij tijdens TMS functionele MRI (fMR) beelden werden opgenomen. We namen waar dat het BOLD-signaal van fMRI, een proxy-signaal voor de metabole processen in neuronen, een goede overlap heeft met het maximale elektrische veld uit onze computerelectrisch veld simulaties (verkregen uit FEM modellen). Bovendien leverde de voor het hele

brein opgenomen fMRI beelden een duidelijk bewijs dat de effecten van TMS niet beperkt zijn tot het tussenliggende gebied van maximale stimulatie-intensiteit onder de spoel. In plaats daarvan nemen we duidelijke subcorticale en soms interhemisferische activeringspatronen waar als resultaat van toediening van TMS pulsen.

In hoofdstuk 6 geven we aanvullende informatie over de technische details van de MR-compatibele TMS opstelling die we speciaal voor het onderzoek hebben ontwikkeld.

Tot slot werden de door ons ontwikkelde modellen met succes gebruikt om een zeer kleine TMS spoel voor gebruik op knaagdieren te ontwerpen en te verbeteren, die in staat is om selectief alleen de linker of rechter hersenhelft te stimuleren. Zie hoofdstuk 7. Dit demonstreert een alternatief gebruik voor onze computermodellen zoals beschreven in hoofdstuk 2, die ook toepasbaar blijken op veel kleinere schaal dan de menselijke. Deze spoelen zijn vervolgens ingezet voor translationeel onderzoek naar herstelprocessen na herseninfracten. Hoewel TMS op zichzelf niet-invasief is, stelt translationeel onderzoek met knaagdieren ons in staat anderszins invasieve procedures uit te voeren waarbij een kunstmatig geïnduceerde beroerte betrokken is. en mogelijk sneller herstel met behulp van rTMS.

In hoofdstuk 8 ga ik in op huidige en toekomstige ontwikkelingen rondom computationele neurostimulatie en zijn toepassingen. Toekomstig onderzoek op het gebied van computerondersteunde TMS-dosimetrie zou de structurele organisatie van de menselijke cortex in meer detail moeten onderzoeken. De neuronale respons op externe prikkels, zoals TMS, is complex en niet altijd gemakkelijk te voorspellen op macroschaal. Multischaalmodellen die zowel elektrofysiologische als biochemische signalering bevatten, zijn veelbelovend en hebben al een indrukwekkende nauwkeurigheid aangetoond bij het voorspellen van cortico-spinale motorische reacties.

Chapter X

Dankwoord

My own story with UU dates back to the year 2007. When choosing a graduate school at age 24 little did I know how I would become a cliché case of 'you cannot escape destiny'. Having applied officially to both UCL (bio-graphics) and UU (computer games and multimedia) I ended up with an MSc thesis on the topic of bio-electricity and FEM modeling.

Huge thanks and deep appreciation to my two supervisors SWF Neggers and CAT van der Berg, who introduced me to neuroscience and MR imaging and Geertjan Huiskamp to bio-electricity. Also, I wish to express my deepest gratitude to both UU (Faculty of Informatics) and UMCU (Rudolf Magnus Brain Center) for the one-of-a-lifetime opportunity to grow in such an exciting and impactful field as neuroscience and computer science.

Big thanks to Stefano Mandija, the partner in MR crime, for being a never-ending stream of excitement. I will equally cherish the time spent in front of monitors as well as in the lab. It was always funny and productive at the same time. I still remember how his enthusiasm was only outmatched by the scheduled maintenance of the MR room.

Thanks to Jord Vink and Stefano Mandija for having my back for some of the human experiments, during the most intense years as a PhD candidate. Those were some turbulent years where along with the research I was leading the software engineering of a medical startup. My graduation could have easily turned into a mirage if not for you too.

Thanks to the 7T lab crew for assisting me with the space and occasional expertise in building phantoms for imaging and electronic devices for our experiments. In particular, I want to thank Ingmar Voogt for his assistance in building experimental phantoms.

Some very 'special' thanks go to central IT for wiping my work PC, twice. I don't know who you are and where you are but I certainly hope karma catches up to you one day. Sarcasm aside, two people deserve credit for helping me address any IT needs I ever had during my UMCU employment. Those are the local IT support guy Ton Mokveld, who was always proactive and thus helpful. Also, Yumas Hankuri, for setting up a grid computing server for generating 3D meshes. The latter was of great significance for the initial attempt of running image processing pipelines.

One of the most remarkable exchanges I had was with the biology students. I appreciated the patience of Wim Otte for explaining in a long email thread that by

'striping' he meant the physical striping of a brain and not a fancy image post-processing algorithm. I appreciate even more Julia Boonzaier for handling the strangest hardware of them all, the rodents. She has my deepest respect and to some extent my sympathies. Needless to say, I started to appreciate computers even more.

Last but not least, I want to thank my first promotor Rick Dijkhuizen, for allowing me to experience the real side of life science, which can be dirty and unpredictable at the same time. I will never forget my first visit to his office, in the animal research facility, which brought an eerie feeling as if I were in a computer game with all the red and blue pipes running along the hallways.

Great gratitudes go to my parents, for their constant nagging and persistent pushing for me to finish this manuscript. Without you, this thesis might have never seen the light of day. I dedicated it to you.

Chapter XI

Publications

Neggers, S.F., Petrov, P.I., Mandija, S., Sommer, I.E. and van den Berg, N.A., 2015. Understanding the biophysical effects of transcranial magnetic stimulation on brain tissue: the bridge between brain stimulation and cognition. *Progress in brain research*, 222, pp.229-259.

Vink, J.J., Mandija, S., Petrov, P.I., van den Berg, C.A., Sommer, I.E. and Neggers, S.F., 2018. A novel concurrent TMS-fMRI method to reveal propagation patterns of prefrontal magnetic brain stimulation. *Human brain mapping*, 39(11), pp.4580-4592.

Petrov, P.I., Mandija, S., Sommer, I.E., Van Den Berg, C.A. , Dijkhuizen, R.M., and Neggers, S.F., 2017. How much detail is needed in modeling a transcranial magnetic stimulation figure-8 coil: Measurements and brain simulations. *PloS one*, 12(6), p.e0178952.

Petrov, P.I., Mandija, Vink, J.J., S., Sommer, I.E., Van Den Berg, C.A. ,Dijkhuizen, R.M., and Neggers, S.F., 2023. A validation approach for computational models of TMS induced brain currents using motor evoked potentials. *bioRxiv*

Petrov, P.I., Mandija, Vink, J.J., S., Sommer, I.E., Van Den Berg, C.A. and Neggers, S.F., 2023. Validating models of TMS effects with concurrent TMS/fMRI. *BioRxiv*

Mandija, S., Petrov, P.I., Vink, J.J., Neggers, S.F. and van den Berg, C.A., 2021. Brain tissue conductivity measurements with MR-electrical properties tomography: an in vivo study. *Brain topography*, 34(1), pp.56-63.

Boonzaier, J., Petrov, P.I., Otte, W.M., Smirnov, N., Neggers, S.F. and Dijkhuizen, R.M., 2020. Design and evaluation of a rodent-specific transcranial magnetic stimulation coil: An in silico and in vivo validation study. *Neuromodulation: Technology at the Neural Interface*, 23(3), pp.324-334.

Mandija, S., van Lier, A.L., Katscher, U., Petrov, P.I., Neggers, S.F., Luijten, P.R. and van den Berg, C.A., 2016. A geometrical shift results in erroneous appearance of low frequency tissue eddy current induced phase maps. *Magnetic Resonance in Medicine*, 76(3), pp.905-912.

Mandija, S., Petrov, P.I., Neggers, S.F., Luijten, P.R. and van den Berg, C.A., 2016. MR-based measurements and simulations of the magnetic field created by a realistic transcranial magnetic stimulation (TMS) coil and stimulator. *NMR in Biomedicine*, 29(11), pp.1590-1600.

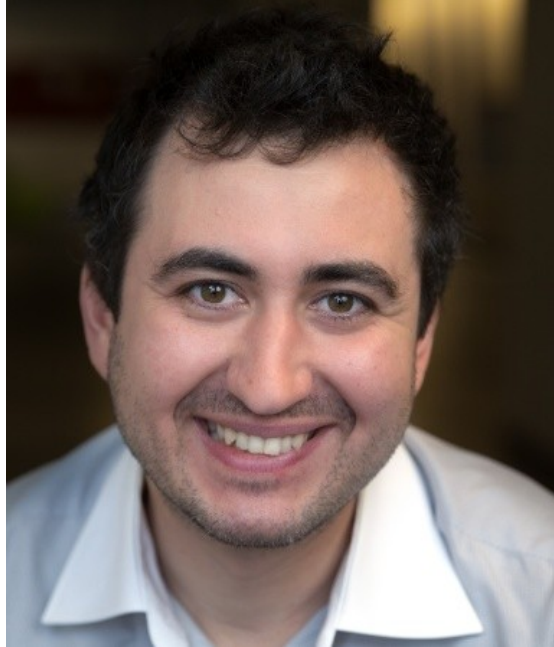
Boonzaier, J., van Tilborg, G.A., Straathof, M., Petrov, P.I., Van Heijningen, C.L., Van Vliet, G., Smirnov, N., Van Der Toorn, A., Neggers, S.F. and Dijkhuizen, R.M., 2017. Differential outcomes of rtms and anesthesia effects on functional connectivity in the rat brain. *Brain Stimulation: Basic, Translational, and Clinical Research in Neuromodulation*, 10(2), p.418.

Mandija, S., Petrov, P.I., Neggers, S.F., Luijten, P.R. and van Den Berg, C.A., 2016. Noninvasive electric current induction for low-frequency tissue conductivity reconstruction: is it feasible with a TMS-MRI setup?. *Tomography*, 2(3), pp.203-214.

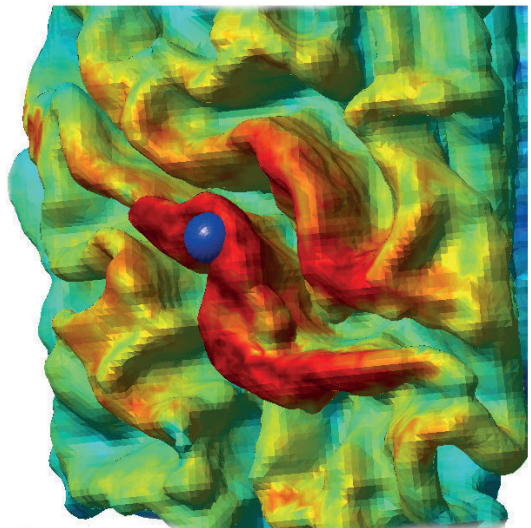
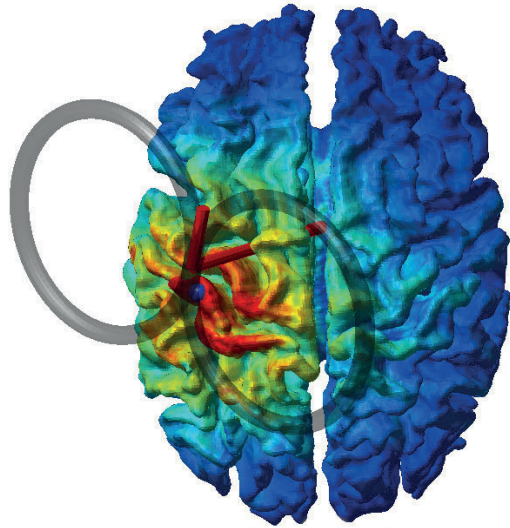
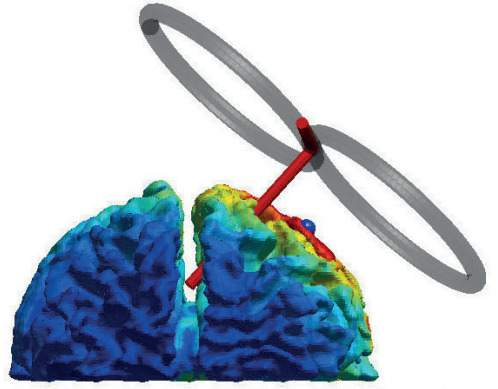
Vink, J.J., Petrov, P.I., Mandija, S., Dijkhuizen, R.M. and Neggers, S.F., 2018. Outcome of TMS-based motor mapping depends on TMS current direction. *bioRxiv*, p.371997.

Chapter XII

Curriculum Vitae



Petar Ivanov Petrov was born on September 10th, 1982 in the city of Plovdiv (Philippopolis), Bulgaria. He completed a vocational high school in electronics with a focus on microprocessors. Then, decided to pursue a bachelor's degree from a liberal art college with a major in Computer Science and a minor in Math, AUBG Blagoevgrad, Bulgaria. After spending a few years in private software developing companies he decided to look for a grad school. In 2007, after being accepted into both UCL in London and UU in Utrecht, he decided to go for the latter in the hope to complete a degree in GMT (Games and Media Technology) and following life long dream to join the gaming industry. Instead, picking a topic closer to lifesciences for his MSc thesis, led to a career in bio-electricity and computer modeling (FEM). In late 2013 he commenced a Ph.D. project to further extend, improve and empirically validate physical models of electro-magnetism and the effects of TMS on the human cortex. In parallel, he was involved in various technical aspects concerning the development of commercial medical device software. His role as lead engineer in the newly founded start-up company Brain Science Tools B.V. was and still is crucial today. In the years 2022 and 2023 he calibrated the 10th anniversary of the company and the long-awaited completion of his Ph.D. track. Currently, he is involved in collaborative R&D between BST B.V. and Philips Medical Systems B.V. regarding the possibility of real-time TMS coil tracking inside an MR machine. Shortly he will take part in future neuro-stim research as part of SynMech – A synaptic mechanogenetic technology to repair brain connectivity (EU Horizon Pathfinder Challenges).



ISBN 9789493289208



9 789493 289208

NUR 981